Highf requency optoelectronic devices in the mid infrared wavelength region.

Zahra Sadat Asghari

Université Paris Diderot - Paris 7
Université Sorbonne Paris Cité

Doctorat de Physique

High frequency optoelectronic devices in the mid-infrared wavelength region

Zahra Asghari

Laboratoire Matériaux et Phénomènes Quantiques (MPQ)

Présentée et soutenue publiquement à Paris le 22 Mars 2019

Président du jury: Yann Gallais, Professeur des universités, Université Paris 7

Directeur de thèse: Carlo Sirtori, Professeur des universités, Ecole normale supérieure Paris

co-Directrice de thèse: Maria Amanti, Maitre de conférences, Université Paris 7

Rapporteurs: Sophie Bouchoule, Directeur de recherche, Université Paris 11 Paris-SUD
Roland Teissier, Directeur de recherche, Université Montpellier 1

Membres: Alexandre Delga, Ingénieur de recherche, THALES
Guillaume Ducournau, Maitre de conférences, Université de Lille
Eva Monroy, Ingénieure de recherche, CEA

A Boubi...

Abstract:

Keywords : Mid infrared, optoelectronic, intersubband devices, semiconductors, photodetectors, RF communications

Mid infrared (MIR) covers the region of the electromagnetic spectrum between optics and THz ranges. This frequency range is of great interest for applications in spectroscopy and free space optical communications. The progress on unipolar devices based on intersubband transitions, has introduced in the MIR a new family of semiconductor lasers and detectors. These optoelectronic devices are indeed based on optical transitions between electronic states in the conduction band of a complex sequence of quantum wells. Their characteristic lifetime is of the order of picoseconds and therefore intersubband devices have a great potential for wideband ultrafast applications.

The aim of this work is the design of a system for high data bit rate free space optical communications in the mid infrared spectral region, with all the components operating at room temperature. To this end, we investigate the high frequency performances of quantum cascade detectors (QCD) and lasers (QCL).

Firstly, we carefully explore the electrical and optical characteristics of QCD at 4.9 μm operating at room temperature. A detailed study of the band structure and charge distribution at different operating temperature and under different applied bias is reported. We demonstrate a background limited infrared photodetector (BLIP) temperature of 135 K and a detectivity at this temperature of 2×10^{11} $Jones$, which is at the state of the art.

We then focus on QCD response to high frequency modulation. We engineered and realized an electronic system compatible with high frequency operation. We report an optical response up to 5.4 GHz with a 50×50 $(\mu m)^2$ square mesa using a gold air-bridge technology. Thanks to rectification measurements, we show that the band-pass is limited by the specific detector bandstructure. For the high frequency modulation of QCLs, we develop a plug and play system with an optimization on the injection contact that allows the demonstration of a cut off frequency of 10 GHz, limited by the photodetector.

Finally, we present a proof of principle demonstration of a free space optical communication experiment using a QCL and a quantum well infrared photodetector (QWIP) at 4 Gb/s. We use a Binary Phase-Shift Keying (BPSK) modulation technique and we obtain a bit error rate of 10^{-5}.

Résumé:

Mots-clef : Moyen infrarouge, optoéléctronique, dispositifs inter-sous-bandes, semiconducteurs, photodetecteurs, communication RF

La région moyen-infrarouge se situe entre les domaines de l'optique et du THz du spectre électromagnétique. Cette région a un intérêt particulier dans les applications spectroscopiques et la communication dans l'espace libre.

Grâce à des avancées technologiques sur la fabrication de dispositifs unipolaires basés sur des transitions inter-sous-bandes, la région du moyen-infrarouge est devenue accessible par une nouvelle famille de lasers et détecteurs à base de semiconducteurs. Ces dispositifs optoélectroniques sont basés sur des transitions optiques entre les états électroniques de la bande de conduction d'une structure composée d'une succession de puits quantiques. Leur temps de vie caractéristique est de l'ordre du picosecondes et ainsi, les dispositifs inter-sous-bandes disposent de propriétés de dynamique ultra rapides intéressantes dans le développement des applications à hautes fréquences.

L'objectif de cette thèse est la conception d'un système prêt à l'emploi pour la communication dans l'espace libre à haut débit dans le moyen-infrarouge, avec tous les composants qui fonctionnent à température ambiante. Dans ce but, nous avons étudié les performances hautes fréquences d'un système composé de détecteurs et de lasers à cascade quantiques.

Dans un premier temps, nous avons caractérisé les propriétés électriques et optiques d'un détecteur à cascade quantique à 4.9 μm à température ambiante. La structure de bande ainsi que la distribution des charges a été étudié en détails dans différentes conditions de température et de tensions appliquées aux bornes du détecteur. Nous avons montré une température limite de détection de 135 K avec une detectivité à cette température de 2×10^{11} $Jones$, nous situant dans l'état de l'art.

Par la suite, nous nous sommes concentrés sur la réponse en modulation à haute fréquence du détecteur à cascade quantique. Nous avons, en premier lieu, optimisé le système électronique afin qu'il soit compatible avec des mesures hautes fréquences. Avec ce système, nous avons mesuré une détection optique jusqu'à 5.4 GHz en utilisant un détecteur à cascade quantique de taille 50×50 $(\mu m)^2$ avec son pont suspendu en or adapté en impédance avec tout le reste du montage expérimental. Grâce à des mesures de rectification, nous avons montré que la fréquence de coupure est limitée par la structure de bande du détecteur en soit. Nous avons ensuite développé un système prêt à l'emploi pour les modulations hautes fréquences du laser à cascade quantique, ce dernier étant optimisé grâce une étude sur son contact d'injection. Nous montrons ainsi une fréquence de coupure optique de 10 GHz, limitée par le photo-détecteur.

Enfin, comme preuve de concept, nous avons réalisé une communication dans l'espace libre de 4 Gb/s à l'échelle du laboratoire en utilisant un laser à cascade quantique et un photo-détecteur infrarouge à puits quantiques. Pour cela, nous avons utilisé une modulation par changement de phase binaire et nous avons obtenu un taux d'erreur de 10^{-5}.

Remerciements:

La réussite de cette thèse n'a été possible qu'avec l'entourage technique, administratif, professionnelle, amical et familial dont j'ai pu bénéficier.

Je souhaite ainsi remercier en premier lieu mon directeur de thèse Carlo SIRTORI et ma codirectrice de thèse Maria AMANTI. Carlo a été mon référent technique et manager de projet. Malgré ses fonctions de directeur de laboratoire, il a su être disponible pour moi et m'a permis de m'affirmer dans le monde scientifique. Je tiens à le remercier pour toutes ces années d'enrichissement à ses côtés. Maria est l'une des plus belles rencontres que j'ai pu avoir au laboratoire. Je l'ai connue durant mon stage et nous avons fini par faire des essais cryogéniques jusqu'à tard le soir en laboratoire. Je ne la remercierai jamais assez pour le soutien moral qu'elle a su m'apporter.

En deuxième lieu, je souhaite remercier les rapporteurs qui ont très minutieusement lu mon manuscrit et dont leurs remarques m'a permis de compléter ce manuscrit : M. Roland TEISSIER, Mme Sophie BOUCOULE, merci. Ensuite, je souhaite remercier mon parrain scientifique, Giuseppe LEO ainsi que mon tuteur scientifique Takis KONTOS, qui ont donné de leur temps et m'ont guidé tout le long de ma thèse. Je souhaite de plus remercier les autres membres du jury pour leur présence ainsi que les échanges de très bonne qualité que nous avons pu avoir durant ma soutenance, M. Alexandre DELGA (un remerciement spécial à lui pour le soutien technique et la collaboration que nous avons pu avoir sans laquelle ma thèse n'aurai pas pu avoir cette qualité), M. Guillaume DUCOURNAU et Mme Eva MONROY, merci. M. Yann GALAIS, merci d'avoir présidé ma séance de soutenance.

Je remercie également mon équipe au laboratoire MPQ de Paris Diderot: Angela, Yanko et tout particulièrement Djamal qui a été très présent pour moi lors de mes manipulations au laboratoire et qui fut pour moi une très belle rencontre en dehors du travail.

Tout docteur scientifique se souviendra toujours de ces quelques années de thèse remplies de hauts et de bas. Ce qui nous revient toujours à l'esprit est la cohésion, le soutien, le support, l'aide, et les bons moments passés avec les autres étudiants en thèse et postdocs. Je souhaite remercier toutes ces personnes qui m'ont supporté surtout avec mes séances de conférences scientifiques organisé à 9h du matin : Alireza, Etienne, Allegra, Azzura, Etienne, Chérif, Sébastien, Mathieu, Sofia, Margaux, Gael, Jako, Alice, Rishav, Ouafi, Biswarup et ceux que j'ai pu oublier, à vous tous, Merci !

Je souhaite remercier mes ingénieurs de salle blanche préférés dont leurs techniques et astuces m'ont permis de fabriquer des échantillons de très bonne qualité. Votre bonne humeur en salle blanche et les moments de fou rires me resteront toujours à l'esprit ; Stéphane, Pascal et Christophe, Merci. Je souhaite remercier aussi Martial qui m'a toujours usiné ce que je voulais malgré « mes talents de dessinateur ».

Anne, notre chère responsable administratif, merci pour ton aide dès mon arrivée au laboratoire, merci d'avoir toujours soutenu les étudiants en thèse dans leurs moments difficiles et merci pour les bonbons à ton bureau. Sandrine et Jocelyne, merci pour toute votre aide administrative durant toute ma période de thèse et Dieu sait comme je ne suis pas douée à ça. Merci pour votre sourire dès le matin, vos bonjours et vos éclats de rire qui donnaient de la joie à tout l'étage.

Je tiens enfin à remercier les personnes les plus chères à mon cœur ; mes amis qui ont pu se déplacer pour ma soutenance et ceux qui m'ont envoyé tout leur soutien de loin : Nazgol, Atefeh, Fatemeh, Nahid, Maedeh, Arefeh, Niknaz, Maryam, Zeinab, Sahar, Zeinab, Farnoosh, Maryam, Fatemeh, Sareh, Sina, Nima, Mohammad, Farah, Mina; et bien sûr ma famille, en France et en Iran qui ont toujours été fiers de moi, ce qui constitue ma plus grande fierté. Tout particulièrement, maman Khadijeh, papa Mehdi, Amirsina mon petit frère et ma petite soeurette Sana, un énorme merci.

Contents

Outline of the manuscript:

Nowadays, reliable fast data communication is a primary requirement to respond to the increasing demand to reduce usage of environmental capital and support sustainable economic development. The aim of this work is to validate the building blocks of a high frequency plug and play system for high frequency free space optical communication in the mid-infrared spectral region, compatible with room temperature operation.

This work is organized into 4 chapters.

In chapter 1 we present an overview of the principal applications in the mid-infrared (MIR) region of the electromagnetic spectrum, with particular interest in optical communication. We introduce also the optoelectronic devices based on intersubband transitions and discuss the state of the art of such devices. Our focus is mostly on detectors and mainly on QWIP (quantum well infrared photodetector) and QCD (quantum cascade detector). We note that the research on high frequency QCD is a quite immature field despite of their performances at room temperature and their ultra-short lifetime.

In chapter 2 we present the working principle of QCD operating in the MIR range of the electromagnetic spectrum. We study a detector based on III-V ternary heterostructure made of GaInAs quantum wells sandwiched between AlInAs barriers operating at 4.9 μm. We perform detailed electrical and optical characterization of the QCD in a mesa geometry. We demonstrate a background limited infrared photodetector (BLIP) temperature of 135 K and a detectivity at this temperature of 2×10^{11} $Jones$. In the last part of the chapter we investigate the characteristics of the QCD under reverse bias.

In chapter 3 we present ultra-fast response of a QCD integrated in a co-planar waveguide adapted to 50 Ω impedance. We present rectification and optical high frequency measurements. We measured the detector modulation bandwidth up to 11 GHz for the 10 μm device in rectification experiments and 3 GHz for the 50 μm one in the optical set up. In the last part we discuss the origin of cut off frequency for QCD operating at room temperature and we relate it to device band structure.

A free space optical communication experiment is presented in chapter 4. In the first part we present the design of an optimized quantum cascade laser (QCL) to be employed as source in communication protocols. We demonstrate the improvement of optical high frequency modulation with a cut off frequency of around 10 GHz. In addition, we present the generation of a comb in the mid-infrared for a plug and play mounted laser and locking of its inter-mode frequency over 2.5 MHz. Using an externally provided QWIP we demonstrate free space communication in laboratory at 4 $Gbps$ using a Binary Phase-Shift Keying (BPSK) modulation technique with a bit error rate of 10^{-5}.

1 Introduction

Contents

In this chapter we present an overview of the principal applications in the mid infrared region of the electromagnetic spectrum, with particular interest in free space optical communications. We then focus on the physics of intersubband transitions which are the mid-infrared optical transitions exploited in all optoelectronic devices that we discuss in this thesis. These transitions originate between confined electronic states in the conduction band of semiconductor quantum wells. Thanks to the technology of epitaxial growth, it is possible to engineer complex sequence of quantum wells suitable for source and detectors operating in the mid-infrared. We present the state of the art for devices operating in this spectral region with particular interest in their high frequency performances. We focus on detectors and mainly on QWIP and QCD. Since their first demonstration, QWIPs have presented high performances in MIR detection, such as high detectivity and responsivity, as well as ultra-fast modulation performances (tens of GHz). We identify the research on high frequency QCD as a quite immature field despite of their ultrashort lifetime, that make them ideal for wide band frequency response. This aspect will be deeply studied in this thesis and it will be presented in chapter 2 and 3.

1.1 Mid infrared

The infrared (IR) is the range of the electromagnetic spectrum between the visible and the microwave(see Figure 1.1). The IR region can be divided into three different regions: the near infrared (NIR) with wavelength between 750 nm and 2,5 μm, the mid infrared (MIR) between 2,5 μm and 30 μm and the far infrared (FIR, known also as terahertz domain) between 30 μm and 1 mm. Above IR, there is the microwave part of the electromagnetic spectrum.

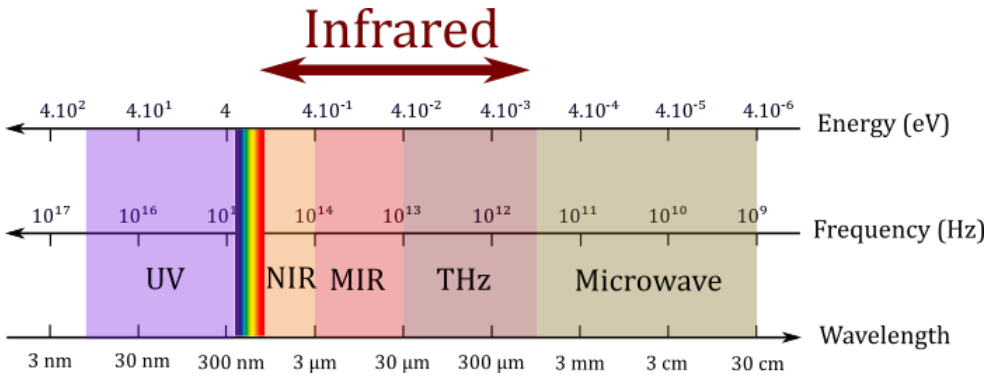

Figure 1.1: Electromagnetic spectrum

Sir Frederick William Herschel was the first scientist to "see" invisible light [Barr, 1961], the infrared. In 1800, by mean of prisms and thermometers, he was able to measure the temperature of the different colors of the diffraction light from the prism. Measuring a variation of temperature from the violet to red, he decided to measure the temperature beyond red color. He surprisingly (at that time of course) could measured a radiation in this range. He thus discovered new radiation at higher wavelength than the visible light.

However, the term of infrared light appears in the 1900 when another scientist, Max Planck, discovered the relation between the temperature of a body and the intensity of the radiation that it emits [Planck and Masius, 1914]. He introduced the concept of blackbody, that is an ideal absorber and a radiator in the whole electromagnetic spectrum with a spectral energy distribution depending on its temperature. The emission spectrum of a blackbody is presented in figure 1.2.

Despite the visible domain, where the light is diffused from primary sources (like the sun or lamps), in the infrared, each body acts as a source due to its temperature.

It was at the end of the XIX century that the first measurement of photocurrent coming from IR light absorption was observed by the physics Nobel prize, Antoine Becquerel.

In this thesis, we mainly focus on the MIR of the electromagnetic spectrum. In this region a large number of organic molecules rotational and vibrational transitions occur. Spectroscopy measurements such as pollutant detection [Kosterev et al., 1999], toxic gas detection, or even gas detection for diseases analysis [Henderson et al., 2018] are examples of applications in the MIR range. More spectroscopy applications in the MIR domain will be detailed in the following.

At the same time, there are two interesting atmospheric windows in the MIR range: the bands between $3-5$ μm and $8-14$ μm [Howard and Garing, 1962] Due to a minimum of atmospheric absorption, these bands are the working range for many

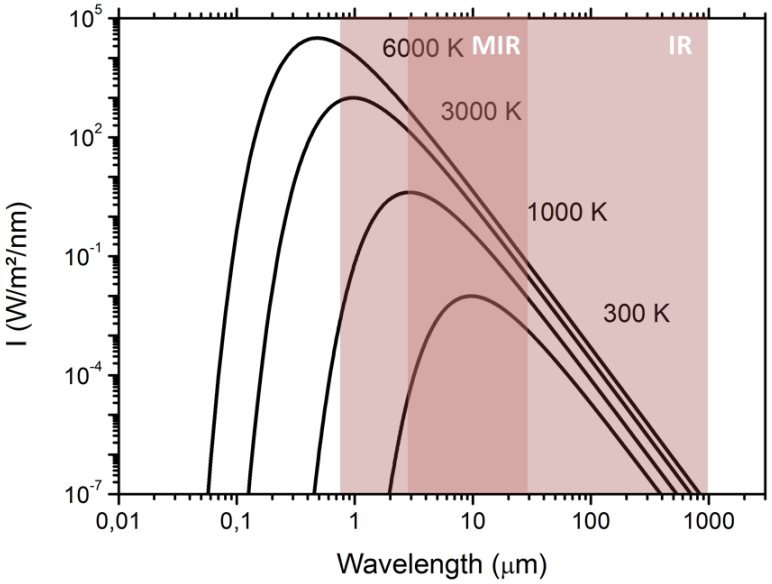

FIGURE 1.2: Planck's law for different temperatures. We can see that a body at room temperature has its emission in the mid infrared domain.

applications such as thermal imaging or spectroscopy measurements. Figure 1.3 shows atmospheric transmission where the two transparency windows are visible.

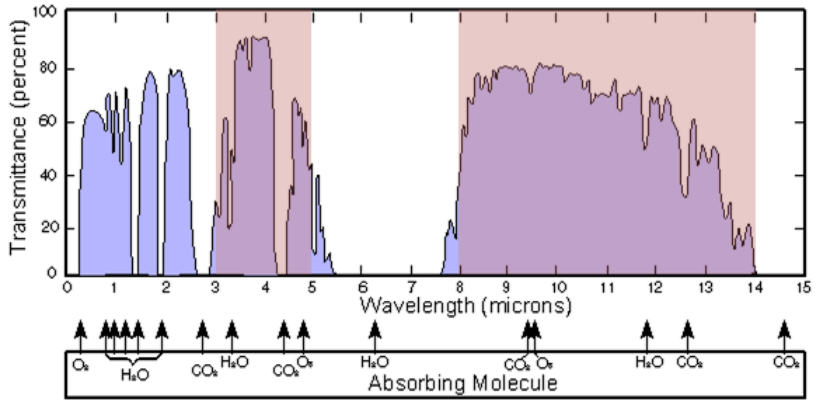

FIGURE 1.3: Atmospheric transmittance in the mid infrared range. We can identify the two atmospheric windows between 3–5 μm and 8–14 μm, interesting for different applications in this range.

1.1.1 General Applications in the IR

IR radiation and detection have various applications in both civilian and military domain. They have been studied extensively over the past century. Because of important improvements in the performances of the quantum cascade laser (QCL) as a continuous-wave, powerful and wavelength tunable source in the MIR, an increase in the applications has been seen in the last years. An overview of them is presented by Tittel and Richter in the book of Sorokina [Tittel et al.] and also the publication of Kosterev [Kosterev et al., 1999].

Here we present some examples of applications of the IR radiation:

- In ecological point of view, IR imaging helps to determine heat losses in buildings [Balaras and Argiriou, 2002]. It gives additional information to already existing techniques in order to quantify potential energy savings. Figure 1.4 shows an image of a house taken with a commercial IR camera.

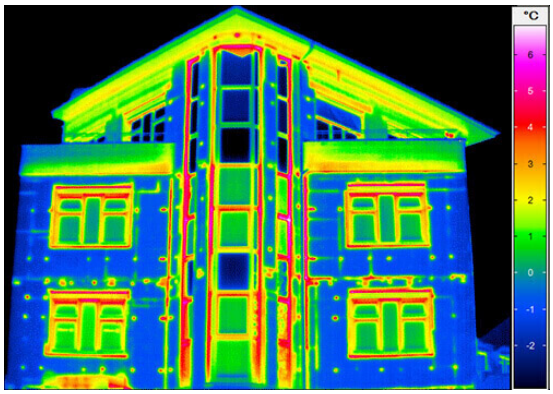

FIGURE 1.4: Thermography image of a building. The color bar represents the temperature measured with the camera. We can see that for example, the temperature on windows border is higher that other places of the house due to a lack of isolation (source: Infratec).

  Moreover, in meteorology and climatology, temperature of oceans is constantly measured by infrared satellites in order to provide data regarding global warming (El Nino events [Browning and Gurney, 1999]).

- In the security domain, cameras based on infrared detection are used by police and in the army for night vision. Missiles can be guided in night towards their targets (usually planes) thanks to thermal emission of the planes motors. Cameras are also used by fireman to localize living body caught in smoke, or even to prevent catastrophic event by localizing earlier the seat of fire.

- In medicine, IR technology is used for fast, passive, non-contact and non-invasive analysis of body tissues, known as medical infrared thermography [Lahiri et al., 2012], [Hildebrandt et al., 2010], [Flesch, 1983]. It has been successfully used as an adjunctive for diagnosis of breast cancer [Ng, 2009], diabetic subjects [Bharara et al., 2012], dentistry applications [Snekhalatha et al., 2018], kidney treatments [Unger et al., 2006], heart operations [Manginas et al., 2007] and many others [Lahiri et al., 2012].

- In archaeology, infrared imaging has helped to discover ancient footprints of vanished civilizations [Casana et al., 2017]. Radiometric thermal cameras implanted in small drones monitored by smartphone, take aerial thermography images that are complementary tools for researcher.

- Spectroscopy

  IR spectroscopy is by far the most important application in this range of the electromagnetic spectrum. IR spectroscopy is thus performed in FIR, MIR and NIR. However, spectroscopy in the MIR range has some specificities that is worth to investigate.

  Molecules transitions As said previously, numerous molecules possess their rotational and vibrational transitions in the MIR region. Detection of molecular

vibrational and rotational modes by means of IR absorption is known as vibrational spectroscopy. Spectra in the MIR permit to obtain unique information with higher sensitivity compared to other spectroscopy techniques. Indeed, the fundamental vibrational bands active in the MIR region have stronger line strengths than the harmonic and combination bands, typically used in the visible and near-IR regions. Because MIR radiation has lower energy compared to near infrared or visible, it excites fundamentals vibrational rather than the overtones. Moreover, the absorption lines corresponding to each molecules are more separated within the spectrum, enabling selective spectroscopic detection of a large number of molecules. MIR spectroscopy is thus an extremely useful region for providing spectral fingerprints, in order to identify and characterize materials. Here are some examples of spectroscopy in the MIR:

- The non destructive characteristic of the MIR spectroscopy is used to control materials quality in industry. For example in medical and pharmaceutical industry, MIR spectroscopy is used to test and identify the inbound raw materials used for medicine [Sun et al., 2016],[Guo et al., 2016],[Eerdenbrugh and Taylor, 2011].
- In agriculture, MIR spectroscopy is used for soil classification [Linker], safety and quality analysis of the food for costumer need [Wilson and Tapp, 1999] as well as food composition analysis [Luna et al., 2013],[Kim et al., 2016],[Culbert et al., 2015],[Kemsley et al., 1992].
- In environmental field, pollutant gas detection such as carbon monoxide (CO) and carbon dioxide (CO_2) [Dong et al., 2018]; methane (CH_4) and ethane (C_2H_6) [Ye et al., 2016] are performed using MIR spectroscopy.
- In order to prevent natural disaster such as volcanic eruption, fluxes and ratios of different volcanic gas species (e.g., SO_2, HCl, CO_2, etc.) can be measured to interpret magmatic processes at depth [Richter et al., 2002].

1.1.2 Optical communication

Optical communication is by definition, the use of light as a mean of data transfer for communication. Nowadays, reliable fast data communication is a primary requirement to respond to the increasing need of a better use of infrastructure.

In the following we present the historical origins of optical communication. We will focus on the two main types of optical communication, the free space optical communication and fiber-optic, with particular attention to their applications in the IR. In the last part of the paragraph, we present an overview of emitters and receivers for optical communication.

Optical communication from the Greek to Li-Fi including Graham Bell's photophone

Optical communication is one of the oldest way of communication between humans. Both Greek and Romans communicate messages over long distances by turning on and off torches [Forge, 2008]. First invented device based on optical telecommunication was the photophone [Bell, 1880]. The photophone was invented by Alexander Graham Bell in 1880. According to him, the photophone is his best invention (even greater than the telephone). The principle behind the optical communication of the photophone is really simple. Image 1.5 presents the principle detailed in the following:

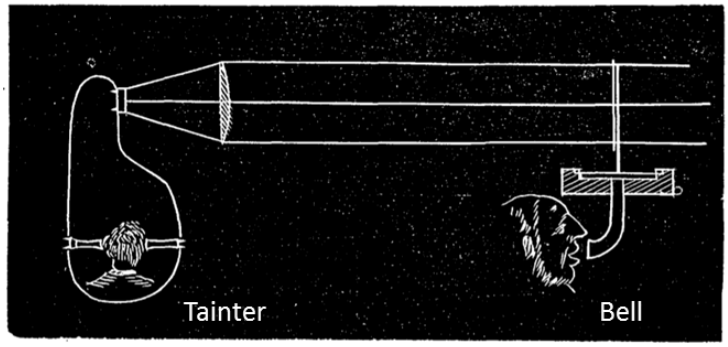

FIGURE 1.5: First illustration of photophone transmission data made by Bell in his publication [Bell, 1880]

Tainter (A.G. Bell assistant) speaks on a microphone, his voice is amplified and directed toward a plane silvered mirror of thin glass (thus flexible). As words were spoken, they cause the mirror to oscillate from convex to concave position. The mirror is also positioned in a way to reflect sunlight on a second mirror that is positioned near Bell. The sunlight is thus modulated by Tainter's sound wave as it is more or less reflected by the mirror. In Bell's first demonstration, the distance between the two mirrors was about 213 m, from the rooftop of the Franklin school to the window of Bell's laboratory. This second flexible mirror receives the modulated light and thanks to a selenium cell, the modulation light is converted back into sound waves which are then amplified and can be heard by Tainter. When Tainter heard Bell's voice, he waves his hat from the window of his laboratory to notify Bell that the signal has been transferred. However we will never know what were the first phrases that have been transferred "wirelessly".

It is important to add that this demonstration was realized years before radio communication. It is in fact the first demonstrated wireless communication. The photophone invention was not really well welcomed at that time. An article on it in the NYtimes[1] mention how "ordinary people" were not completely convinced about a wireless communication. However, Alexander Graham Bell was really optimist and also futurist about this invention. He said: "Can imagination picture what the future of this invention is to be?".Nevertheless, after invention of radio communication 19 years later, the light communication has been cast aside. It is only in the last decades that the optical communication using light has gain interest, mostly after the development of LEDs in the 70s. At present, Li-Fi (Light Fidelity) communication technology is considered to be the continuity of photophone invention. Since 2005, Li-Fi uses visible light (480 *nm* and 650 *nm*) to transfer data in tens of meters [Svilen Dimitrov, 2015].

Free space optical communication

Free Space Optical Communication (FSO) is an emerging technological solution for ever increasing data throughput requirements of communication links to remote assets at sea, air or space [Hemmati, 2006]. Virtually unlimited bandwidth and unregulated frequency spectrum makes FSO superior to radio frequency (RF) communications. In addition, low probability of detection and interception are particularly

[1] https://www.nytimes.com/1880/08/30/archives/the-photophone.html

attractive for defense applications. FSO communication has wide range of application: inter satellite links, links between satellite and spacecraft, links between satellite and the Earth, last mile applications, building to building connections, extending fiber optics to nearby building, etc. Figure 1.6 shows a schematic of the different applications for FSO communication. Current commercial efforts are based on advanced lasers and detectors in the 1.55 μm wavelength regime with high bandwidth (2.5 Gb/s) as well as long distance (4 km) links [Szajowski et al., 1999].

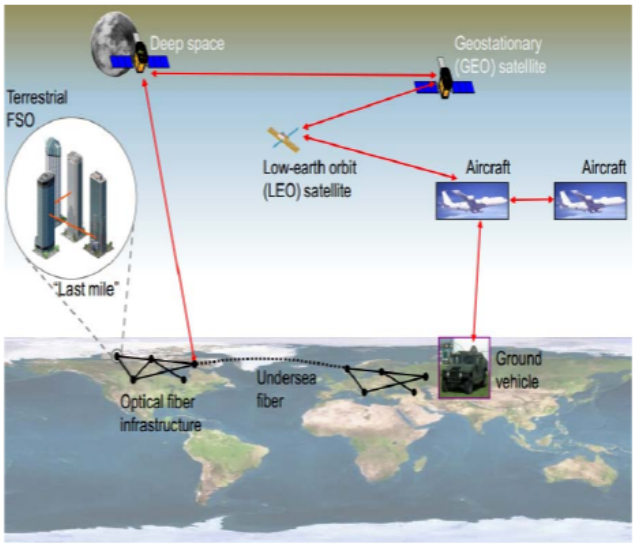

Figure 1.6: Schematic of different applications of free space optical communication [Jain et al., 2013]

In FSO communication, data are transferred from the optical source to a detector via the electromagnetic field in the "free space". Free space is by definition the surrounding environment area that can be the vacuum or the atmosphere. FSO communication is particularly advantageous when the connection is needed for a limited time or when major obstacles have to be crossed. It can be easily used for data transfer from different buildings on Earth, without the need of heavy infrastructure. Moreover, this can also replace the already existing communication system between spacecrafts (space stations) and between spacecraft and the Earth. At present, communication technology for these systems is the use of radio waves enabling orbital broadcasts to transmit hundreds of megabits of information per second. Lasers, which operate at higher frequencies, could replace microwave sources to increase the data transmission speed with rate of gigabits per second in such applications.

Sources and detectors operating between 750 nm and 1600 nm are mature devices frequently used in fiber optics. Consequently, FSO communication has been developed in this range. Moreover, using standard components for fiber based systems is important for interfaces and connecting to existing networks.

Limitations

- Main limitations of FSO communication are adverse weather conditions and atmospheric particulates, generated naturally or by human pollution. They interfere with laser data link due to absorption and strong scattering of light

by suspended particles known as Rayleigh scattering. The Rayleigh scattering is proportional to the inverse of the laser wavelength to the power of four :

$$Rayleigh \propto \frac{1}{\lambda^4} \tag{1.1}$$

- For weather conditions, such as fog, where particles in the atmosphere have bigger dimension, a more general scattering effect known as Mie scattering plays a role during the diffusion. Fog perturbs the transmission mainly because of absorption and scattering through the water particles. The Mie scattering depends on the size particle, liquid water content, fog temperature and the humidity [Plank et al., 2012]. It is reduced for wavelengths greater than the average diameter of atmosphere particles (typically 1 μm) [Capasso et al., 2002].

  Figure 1.7 summarizes some previously published experimental results of atmospheric attenuation as a function of the wavelength [Chen, 1975], [Pavelchek et al., 2004]. It shows a consistent and significant advantage from $3-5$ μm and $8-14$ μm.

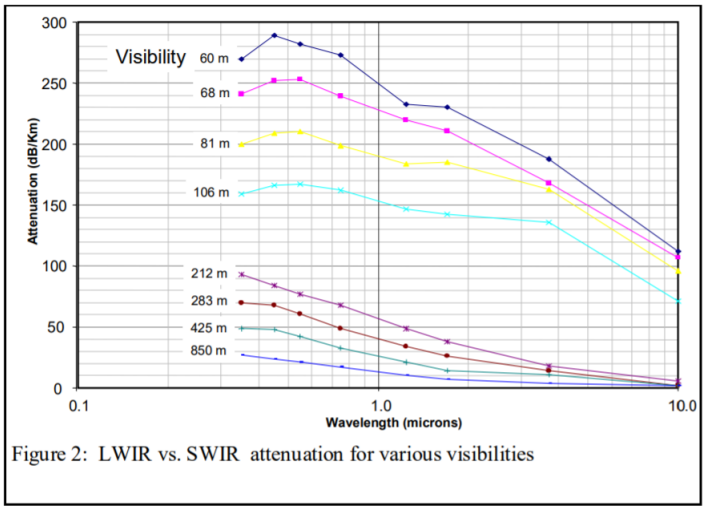

FIGURE 1.7: Attenuation of electromagnetic radiation as a function of wavelength for different visibility length [Pavelchek et al., 2004].

- In addition, when solar radiation illuminates in the field of view of the detector, small refractive index variation can affect the FSO communication performances. A variance calculation known as Rytov variance [Larry C. Andrews, 2005] indicates the scintillation effects and its dependency on the operating wavelength:

$$(1/\lambda)^{7/6} \tag{1.2}$$

  Nearly one hundred times lower losses can be expected in the second atmospheric window ($8-14$ μm) in comparison to the first atmospheric widonw ($3-5$ μm) transmission for clear weather conditions (i.e. 10 km visibility) [Zuev, 1976]. For lower visibility conditions this advantage is even greater.

- Eye safety is another important aspect where MIR links are favorable over those of shorter wavelengths. MIR terminals can transmit more power and

stay below Maximum Permissible Exposure (MPE) threshold to avoid damaging biological effects within the eye or skin[2]. MPE is a characteristic parameter for laser safety and is measured at the cornea of the human eye for a given exposure time and wavelength.

In order to overcome these limitations of free space communication it is important to develop reliable sources and detectors in the tens of μm range.

Despite the substantial investments into development of longer wavelengths systems back in the 1980s, those systems were bulky, inefficient and expensive (e.g. CO2 lasers [Reiland et al., 1986]). The recent accelerated advances in Quantum Cascade Lasers (QCLs) as well as progress in mercury cadmium telluride photo-diodes enable low Size, Weight and Power (SWaP) and therefore cost efficient optical systems operating in MIR spectra [Razeghi et al., 2007].

Experimental realizations of FSO in MIR have been demonstrated using a QCL. They show improved performances respect to NIR in adverse conditions with reduced visibility [Corrigan et al., 2009].

Fiber-optic communication

Thanks to the development of low-loss optical fibers in the 1970s, optical communication has became the most popular system used for communication. The importance of fiber-optic communications was highlighted when Charles Kao was awarded the Nobel Prize in Physics in 2009 for his remarkable work on transferring light to fibers[3]. At present, the overall fiber deployment has exceeded 4 billion kilometers[4]. The amount of globally deployed optical fiber has been growing at a rate of 15% per year since 2000 [Winzer et al., 2018]. Figure 1.8 shows all the optical fibers links installed under the sea. A map showing all the cables on earth would be really messy and countries would not be recognizable!

In today's telecommunication technology, fibers are frequently used in wavelength of 850 nm, 1300 nm and 1550 nm. An important development on sources and detectors working at room temperature with high efficiency at these wavelengths has permitted a fast improvement on this technology. Optical fibers are optimized concerning losses, guiding properties, dispersion, and nonlinearities. Depending on the transmitter technology and fiber length, data rates up to hundreds of Gbit/s are reported. This rate has been increased up to Tb/s by using multi channel fibers called wavelength division multiplexing (WDM). WDM capacities in single-mode fiber of up to 115 Tb/s have been reported [Renaudier et al., 2017].

A main drawback of this communication system is the infrastructure cost. Indeed, digging cables in earth and even under the sea cost a lot. Repairing and changing damaged cables is also a time and money consuming process. Fiber installation is also a long process. It is predicted that in 2030 France will be connected to fiber optics by 100%. However the project will cost around 35 billion euros. [5]

[2] ANSI Z136.1—2007, American National Standard for Safe Use of Lasers, March 16, 2007

[3] https://www.nobelprize.org/prizes/physics/2009/summary/

[4] It could be wrapped around the globe approximately 100,000 times!

[5] http://www.lefigaro.fr/secteur/high-tech/2017/01/31/32001-20170131ARTFIG00096-la-fibre-optique-va-couter-15-milliards-de-plus-que-prevu-a-la-france.php

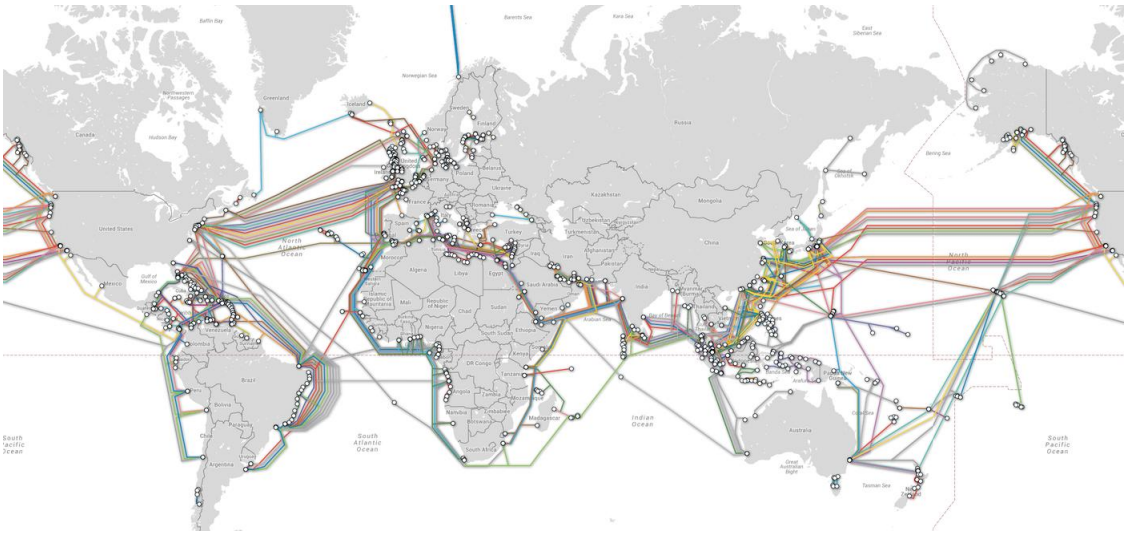

FIGURE 1.8: Submarine cable routes used by fiber optics ref: https://mapscaping.com/blogs/geo-candy/interactive-submarine-cable-map

Emitters in optical communication

Optical transmitters must have specific properties such as being compact, efficient and reliable. They have to be able to be modulated fast enough to transmit data. Having the ability to operate over a wide temperature range, without major performance degradation is also an advantage for outdoor applications. The two main types of optical transmitters that are used today are both based on semiconductor technology: light-emitting diodes (LEDs) and laser diodes.

- **Light-emitting diodes: LEDs**

  LEDs are in a most common shape, a simple forward biased p-n junction (see figure 1.9). LEDs commonly used for communications are made from Indium gallium arsenide phosphide (InGaAsP) or GaAs, with operating wavelength of respectively 1.3 μm and 0.8 μm. The emission of light is based on electroluminescence. As it is a spontaneous emission, the emitted light is incoherent and it has a wide spectrum (spectral width 30-60 nm) which results also to a low output optical power.

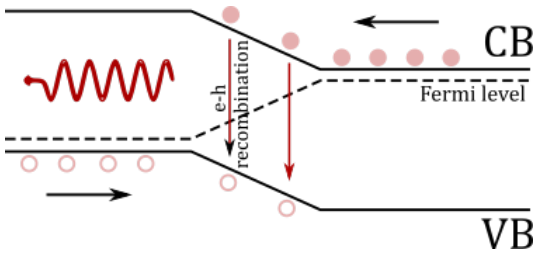

FIGURE 1.9: LED pn junction

  These characteristics make LEDs not suitable for long distance FSO communication and they are more interesting for fiber optics communication in local area network applications. They are also nowadays widely produced and their manufacturing technology is now well mastered which makes them useful for low cost applications.

Optical communication using LEDs in fiber optics are used for a bit rate of 10-100 Mbit/s and a transmission distance of a few kms [Webster and Eren, 2017]. In wireless communications, they are used for short distance applications for example data transfer (internet connection) through the reading lamp (LED) installed for each passenger in an airplane [Hou and Zhang, 2015].

- **Diode Lasers**

  The difference between LEDs and laser diodes is that LEDs produce incoherent light, while laser diodes produce coherent light. The principle of light emission in lasers is no more due to spontaneous emission, but it is a stimulated emission. This stimulated emission results in higher output power compared to LEDs. Moreover, the output of lasers is more directional which on one side leads to a better coupling for fiber optics ($\approx$ 50% of coupling efficiency) and on the other side a better and easier light collection in free space optical communication. Furthermore, semiconductor lasers can be modulated directly by electrical injection. The most commonly used classes of semiconductor lasers for optical communication are Fabry-perot Lasers (FP), Distributed feedback lasers (DFB) and Vertical cavity surface emitting lasers (VCSEL). Their working principle is briefly detailed in the following:

  – Vertical cavity surface emitting lasers (VCSEL)
  VCSELs have been presented by Soda *et.al* in 1979 [Soda et al., 1979]. Their structure is particularly different from other lasers. The active region is sandwiched between two highly reflective mirrors (99.5 to 99.9% of reflectivity) that actually consist on distributed Bragg reflectors (DBRs). VCSELs based on GaAs have been extremely studied and they start to obtain interest as an optical transmitter thanks to their high reliability and high speed modulation (10 Gbit/s) [Mederer et al.].

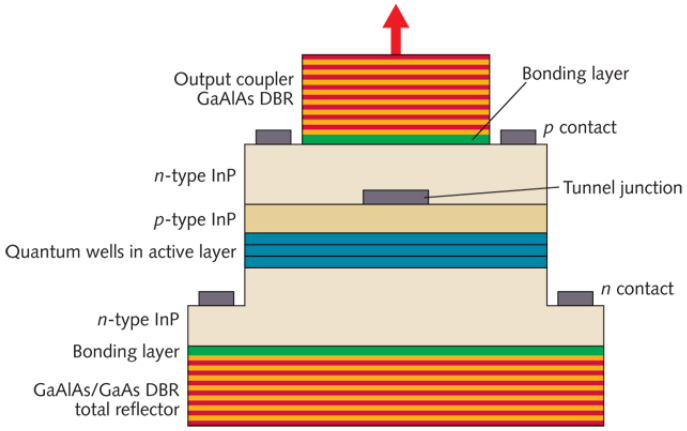

FIGURE 1.10: Design of one type of VCSEL (source : [Kapon and Sirbu, 2009])

VCSELs together with LEDs are the most cost efficient source for optical communication. VCSELs have low power emission, because of high reflectivity of the DBRs mirror which led to low quantum efficiency [Iga, 2000]. The optical power in VCSEL is in the order of tens of mW at room temperature [Yoshikawa et al.] for short wavelength (850 nm) and have to be engineered in order to increase the output. That's why, they are mostly used for short distance and short wavelength FSO communication [Zaidi, 2016].

– Fabry-perot Lasers (FP)

This laser diode consists of two partially reflecting mirrors facing the cleaving plane of the crystal. The stimulated emitted rays use the cavity to travel back and forth between the two mirrors forming a standing wave until they exit from the device. For FP laser much higher value of radiation power and multi-mode operation is obtained [Bugajski et al., 2013]. In pulsed operation (with pulse length up to 300 ns), the peak power reaches even a few watts. But increase in pulse duration can cause a significant laser structure damage due to an increased temperature in the structure.

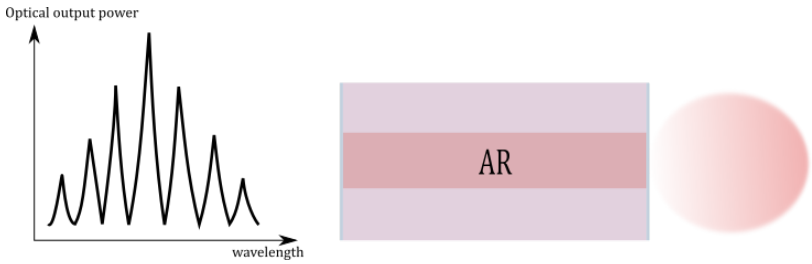

FIGURE 1.11: Schematic diagram of a FP laser (right) and its corresponding spectrum (left) (multi-mode)

– Distributed feedback lasers (DFB)

A DFB is a laser where the feedback function is ensured by a periodic grating etched directly on the cavity (Figure 1.12). The grating is a Bragg reflector. Thank to this grating, a single longitudinal mode is selected which leads to a single mode laser. DFB laser has been first demonstrated in 1970 by Herwig Kogelnik. For DFB lasers, emitted radiation is characterized by the power level up to hundreds of mW. FSO communication up to 40 Gb/s using DFB laser at 1.5 μm has been reported [Tsai et al., 2015].

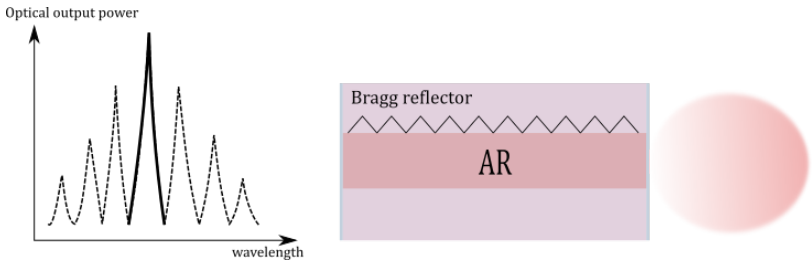

FIGURE 1.12: Schematic diagram of a DFB laser (right) and its corresponding spectrum (left) (single-mode)

Receivers in optical communication

Optical receivers convert the optical signal to electrical signal. They thus recover the transmitted data. They must have low noise and high gain at the operating wavelength. Moreover, a fast response time is essential for the high frequency optical communication.

There are different types of photodetectors: Photodiodes, phototransistors, photon multipliers, photo resistors

Photodiodes are widely used as photodetectors. They are made of semiconductors in a p-n (positivie-negative) and p-i-n (positivie-intrinsic-negative)configurations similar to LED emitters. Avalanches photodiodes (APD) and metal-semiconductor-metal (MSM) photodetectors are also used as a receiver for optical communication.

PIN photodetctors can be extremely wideband and they are commercially available with DC to 50+ GHz response. The high frequency response of pin semiconductor photodiodes is mainly limited by the carrier transit time, the junction capacitance and the photodetector size. Moreover, high thermal noise reduces the performances of pin detectors. To reduce the thermal noise, transimpedance amplifiers can be used which paying the price of reduced bandwidth of the system.

In photon counting detectors, each detected photon generates a digital output signal. They have been realized up to Gbit/s data rates. However, photon counting receivers are limited to detect at most one photon per reset time. The detector is thus rapidly blinded after a detection until the reset. Moreover, dark counts reduce the efficiency of this type of detector.

Avalanche photodiodes (APD) have better performances compared to PIN detectors as they provide internal gain within the detection process. The photcurrent is internaly multiplied by a factor $M > 1$. Thus, the different noise contribution are reduced compare to PIN detectors which leads to higher signal to noise ratio (SNR).

MSM detectors are alternative photodeteors with fast response times and larger active area. However, their availability and cost, but also restricted fabrication size, constraints their use in FSO applications.

1.2 Intersubbands transitions

In previous section, we presented the interest of MIR in different applications and more specifically for fast free space communications.This range of the electromagnetic spectrum became accessible since the advent and development of devices based on intersubbands transitions. In the following, we present the main characteristics of these transitions and their comparison with interband transitions.

A quantum well (QW) is made of a semiconductor sandwiched between another semiconductor with higher energy gap. Figure 1.13 shows a scheme of a QW with the corresponding energy gap. In order to obtain a perfect interface between the different layers, only semiconductors that have compatible lattice constants can be used [Liu, 2000], [Sze and Ng, 2006], [Harrison, 2011]. Within QWs, due to energy quantification, we can observe energy transitions between the subbands of the valence band (VB) and the conduction band (CB) which is named interband transition (IB) or between two subbands of the same band (either CB or VB) named intersubband transitions (ISB).

In this section we will give a brief historical approach to the theory an the experiment toward intersubband transitions. Then a very basic introduction to QW energy levels and their intersubband transitions is given together with a short comparison with the interband transitions.

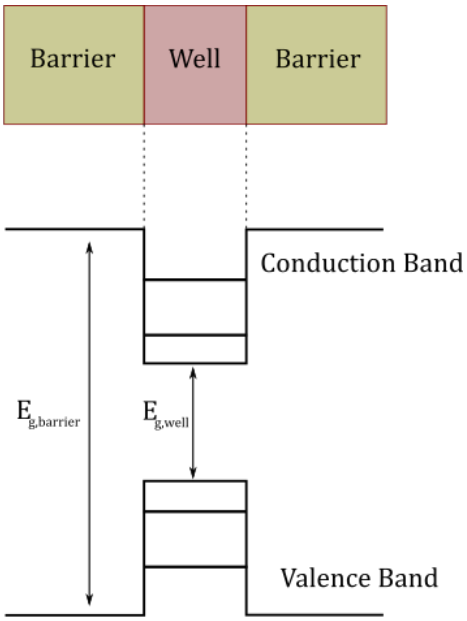

FIGURE 1.13: Schematic QW (top) with the corresponding energy bands (bottom)

1.2.1 Historical review of Intersubband

In 1985, West and Eglash [West and Eglash, 1985a] have been the first group to experimentally demonstrate the existence of intersubband transition within semiconductors. They have observed an absorption at Brewster angle in QWs made of GaAs/AlGaAs.

Later, development of growth techniques such as molecular beam epitaxy (MBE) (developed in the late 1960s at Bell Telephone Laboratories by J. R. Arthur and Alfred Y. Cho [Arthur, 1968], [Cho and Arthur, 1975]) and metalorganic chemical vapor deposition (MOCVD) has lead to more controllable growth within the single atom scale. Figure 1.14 shows a transmission electron microscopy (TEM) image of the active region of a QCL grown by MBE [WALTHER and KRYSA, 2017]. The scale in the image shows the nanometric thickness of different layers and thus the growth performances developed nowadays in epitaxial techniques.

In 1987, Levine and co-workers at AT & T Bell Laboratories were the first group to fabricate a detector based on intersubband transition, the quantum well infrared photodetector (QWIP) [Levine et al., 1987]. They have later on successfully demonstrated the first bound-to-continuum QWIP operating at 10 μm [Levine, 1993]. We will detailed this photodetector in section 1.3.2.

Intersubband based sources have first been introduced by the population inversion theory in a superlattice structure made by Kazarinov and Suris in 1971 [Kazarinov and Suris, 1971]. The first luminescence based on intersubband has been demonstrated by Helm and coworkers in 1989 [Helm et al., 1989]. The emission was observed in the FIR and it was due to resonant tunneling in a superlattice structure. However, only in 1994 the first experimental realization of intersubband laser has been reported [Faist et al., 1994]. This was a QCL operating in pulsed regime at 4.2 μm developed by Faist, Capasso, Sirtori and co-workers again in the AT&T Bell Laboratories.

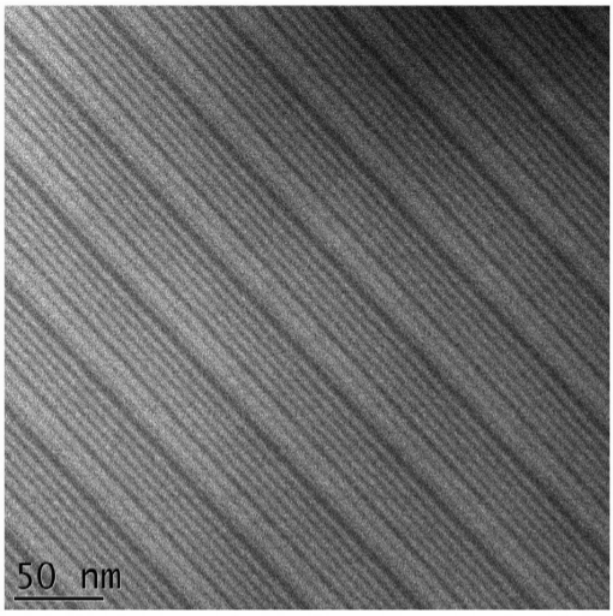

FIGURE 1.14: Transmission electron microscopy image of a QCL. The dark lines represent the AlGaAs barriers and the lighter lines the GaAs wells [WALTHER and KRYSA, 2017].

1.2.2 Energy levels and wavefunctions in QWs

To model a QW, we follow the envelope function approximation developed by Gerald Bastard [Bastard, 1988]. In this formalism, the electron wavefunction $\Psi_n(\mathbf{r})$ is expressed as the product of a Block function $u_n(\mathbf{r})$, that has the same periodicity than the crystal, and an envelope function $f_n(\mathbf{r})$ that varies slowly with respect to the scale of the lattice potential. Thus, the electron wavefunction is expressed as:

$$\Psi_n(\mathbf{r}) = f_n(\mathbf{r})u_n(\mathbf{r}) \tag{1.3}$$

with n the band energy level (subband) index and $\mathbf{r}$ the position vector of the electron within the band.

Assuming a similar Block function for both of the semiconductor, the Schrödinger equation can be expressed using only the envelope function. The Schrödinger equation to be solved in order to obtain the electronic states in the semiconductor QW is expressed as:

$$\frac{-\hbar^2}{2m^*}\vec{\nabla} f_{n,k}(\mathbf{r}) + [V_b(\mathbf{r}) + V_{ext}(\mathbf{r})] f_{n,k}(\mathbf{r}) = E_{n,k} f_{n,k}(\mathbf{r}) \tag{1.4}$$

where $\mathbf{k}$ corresponds to the electron wavevector, $\hbar$ yields for the reduced Planck's constant, m^* the effective mass of the electrons, E_n the eigenvalues and $V_b(\mathbf{r})$ the conduction band profile potential and $V_{ext}(\mathbf{r})$ the contribution of an external potential that can be for instance the electrostatic potential due to electrons and ionized impurities or an external electric field applied to the heterostructure.

The QW exists only in the growth direction, normal to the layers :i.e the electrons are essentially free to move in the planes of the QW layers ((x,y) planes) and their energy is quantified in the the growth direction along the z axis. Thus, the different contribution can be separated and the envelope function can be rewritten as:

$$f_{n,\mathbf{k}_{(x,y)}}(\mathbf{r}) = \frac{1}{\sqrt{S}} e^{i\mathbf{k}_{(x,y)}.r} \phi_n(z) \tag{1.5}$$

where S stands for the in-plane normalization area. Thanks to this simplification, we can rewrite the equation 1.4 by considering $\phi_n(z)$ as the solution of the one dimensional Schrödinger equation:

$$\frac{-\hbar^2}{2}\frac{d}{dz}\left(\frac{1}{m^*}\frac{d\phi_n(z)}{dz}\right) + [V_b(z) + V_{ext}(z)]\phi_n(z) = E_n\phi_n(z) \tag{1.6}$$

Solutions to this equation is:

$$E_{n,\mathbf{k}_{(x,y)}} = E_n + \frac{\hbar^2 k^2_{(x,y)}}{2m^*} \tag{1.7}$$

The solution is the sum of the eigenenergies E_n and the kinetic energies $\frac{\hbar^2 k^2_{(x,y)}}{2m^*}$ that is associated to the free movement of electron in the plane parallel to the semiconductor layers.

The eigenenergies E_n depend on the potential shape. If we consider an infinite barrier potential (i.e $V_b \to \infty$) with a QW with a width equal to L (along the growth direction z), and using the boundary conditions $\phi_n(0) = \phi_n(L) = 0$, the solutions to the equation 1.6 have the following form:

with the eigenstates:

$$\phi_{n,even}(z) = \sqrt{\frac{2}{L}} sin(n\frac{\pi z}{L}) \tag{1.8}$$

or

$$\phi_{n,odd}(z) = \sqrt{\frac{2}{L}} cos(n\frac{\pi z}{L}) \tag{1.9}$$

and eigenvalues:

$$E_n|_{V_b\to\infty} = \frac{\hbar^2\pi^2}{2m^*L^2}n^2 \tag{1.10}$$

The energy separation between two consecutive subbands is assumed to be constant in k-space. To ensure this property, the effective mass is considered to be independent of the energy. This energy separation between the fundamental level ($n = 1$) and the next energy level ($n = 2$) is equal to:

$$E_2 - E_1 = \frac{3\hbar^2\pi^2}{2m^*L^2} \tag{1.11}$$

From equation 1.10 we can see two important dependencies of the subbands energy:

- **QW's width: L**

  Smaller is the width of the QW, higher will be the difference in energy between the energy levels.

- **Quantum number: n**

  The energy levels evolved quadratically with the quantum number n.

However, in our work, in order to study the intersubband transition in the QWs, we need to define a finite barrier height V_b. Moreover, we will assume only two states with energy levels inferior to the barrier height. Thus,the wavefunctions for the first and second eigenstates become:

$$\phi_1(z) = C_1 \begin{cases} e^{x_1(z+L/2)} cos(k_1 L/2) & if z < -L/2 \\ cos(k_1 z) & if -L/2 < z < L/2 \\ e^{-x_1(z-L/2)} cos(k_1 L/2) & if z > L/2 \end{cases} \tag{1.12}$$

$$\phi_2(z) = C_2 \begin{cases} -e^{x_2(z+L/2)} sin(k_2 L/2) & if z < -L/2 \\ sin(k_2 z) & if -L/2 < z < L/2 \\ e^{-x_2(z-L/2)} sin(k_2 L/2) & if z > L/2 \end{cases} \tag{1.13}$$

with

$$C_1 = \frac{1}{\sqrt{L/2 + (V_b/x_1 E_1)}} cos^2(k_1 L/2) \tag{1.14}$$

$$C_2 = \frac{1}{\sqrt{L/2 + (V_b/x_2 E_2)}} sin^2(k_2 L/2) \tag{1.15}$$

with the two transcendental equation:

$$tan(k_1 L/2) = \frac{m_b^* k_1}{m^* x_1} tan(k_2 L/2) = -\frac{m_b^* k_2}{m^* x_2} \tag{1.16}$$

where $k_{1,2} = \sqrt{2m^* E_{1,2}}/\hbar$, $x_{1,2} = \sqrt{2m^*(V_b - E_{1,2})}/\hbar$, m^* and m_b^* are respectively the well and the barrier effective mass and E_1 and E_2 respectively the first (ground) and the second eigenstate energy. In order to solve equation for the finite barrier case, we consider a fictitious-box above the barrier potentials that have a width much larger than the barrier ($L_{box} >> L$). Thus, in the box, there are delocalized eigenstates which can have even or odd parity. We will consider only the odd parity continuum states as we will see in the next section that these are the only states that contribute to the the intersubband transitions. The solutions are:

$$\phi_{odd}(z) = \sqrt{\frac{2}{L_{box}}} \begin{cases} sin(k'(z + L/2) - \beta_1) & if z < -L/2 \\ \beta_2 sin(kz) & if -L/2 < z < L/2 \\ sin(k'(z - L/2) * \beta_1) & if z > L/2 \end{cases} \tag{1.17}$$

where $k = \sqrt{2m^* E}/\hbar$, $k' = \sqrt{2m_b^*(E_{odd} - V_b)}/\hbar$, E_{odd} is the energy associated to the odd-nth eigenstate, β_1 is given by $tan(\beta_1) = tan(m^* k'/m_b^* k)$ and $\beta_2 = (sin(kL/2) + \frac{m_b^* k}{m^* k'} cos(kL/2))^{-1/2}$. These parts are explained in more details in the books of Schneider *et.al* [Schneider and Liu, 2007] and Rosencher *et.al* [Rosencher et al., 2002] and D.Palaferri thesis.

A program has been developed in our team by A. Vasanelli, in order to solve these equations numerically. In this program, they use the $\vec{k}.\vec{p}$ approximation for three bands (conduction band, light holes band and split-off band). In this approximation, they take into account the non parabolicity of the bands. The numerical

resolution is performed by dividing the heterostructure into several blocks with constant potential where the solution is simply a plane-wave. Considering a continuity between each blocks, the eigenenergies and wavefunctions at $k_{(x,y)} = 0$ are obtained.

1.2.3 Optical transitions

In this section, we study the light matter coupling within the QW. For that we will consider the interaction between an electromagnetic wave with a radiation frequency of ω and two ISB electronic states $\left|\Psi_{i,k}\right\rangle$ and $\left|\Psi_{f,k}\right\rangle$ with bands indices i and f. The wave vector is $\mathbf{q} = \mathbf{n}\omega/c$ and the polarization vector $\boldsymbol{\varepsilon}$. The corresponding electric field is then:

$$\mathbf{E} = E_0 cos(\mathbf{q}.\mathbf{r} - \omega t)\boldsymbol{\varepsilon} \tag{1.18}$$

Following the Fermi's golden rule [Helm, 1999], we can obtain the rate of transition from band i to band f under the perturbation of $\hat{H}_{int}$:

$$W_{if} = \frac{2\pi}{\hbar}\left|\left\langle\Psi_{i,k}\right|\hat{H}_{int}\left|\Psi_{f,k}\right\rangle\right|^2 \delta(E_f - E_i \pm \hbar\omega) \tag{1.19}$$

The *plus* and *minus* sign in the delta parameter is due to energy conservation between the level $(E_f - E_i)$ in absorption (-) or in emission (+) case.

The perturbation $\hat{H}_{int}$ corresponds to the light-matter interaction. By neglecting the second order contribution of the electric field, $\hat{H}_{int}$ is expressed in the Coulomb gauge as:

$$\hat{H}_{int} = -\frac{e}{2m^*}(\mathcal{A}.\mathbf{p} + \mathbf{p}.\mathcal{A}) \tag{1.20}$$

where $\mathcal{A}$ is the potential vector, $\mathbf{p}$ and e respectively the electron momentum and charge. The corresponding vector potential which is related to the electric field by $\mathbf{E} = \frac{\partial\mathcal{A}}{\partial t}$ is written as:

$$\mathcal{A} = \frac{iE_0\boldsymbol{\varepsilon}}{2\omega} cos(\mathbf{q}.\mathbf{r} - \omega t) + c.c. \tag{1.21}$$

Under the dipole approximation, i.e. in the case where the radiation wavelength λ is bigger than the width of the QW ($\lambda >> L$), we can neglect the wavevector of the photon in comparison to the electron momentum. Thus $\mathbf{p}$ commutes with $\mathcal{A}$ and the perturbed Hamiltonian is then equal to:

$$\hat{H}_{int} = -\frac{e}{m^*}\mathcal{A}.\mathbf{p} = \frac{ieE_0}{2m^*\omega}\boldsymbol{\varepsilon}.\mathbf{p} \tag{1.22}$$

In this approximation, the equation 1.19, in the case of an absorption, becomes:

$$W_{if} = \frac{2\pi}{\hbar}\frac{e^2E_0^2}{4m^{*2}\omega^2}\left|\left\langle\Psi_{i,k}\right|\boldsymbol{\varepsilon}.\mathbf{p}\left|\Psi_{f,k}\right\rangle\right|^2 \delta(E_f - E_i - \hbar\omega) \tag{1.23}$$

We can see from the equation 1.23 that the transition rate is proportional to the square of the matrix element of the photon absorption process. This matrix element can be separated in two independent parts thanks to the envelope function approximation:

$$\left\langle\Psi_i\right|\boldsymbol{\epsilon}.\mathbf{p}\left|\Psi_f\right\rangle = \varepsilon.(\left\langle u_v\right|\mathbf{p}\left|u'_v\right\rangle\left\langle f_n\right|f'_n\rangle + \left\langle u_v\right|u'_v\rangle\left\langle f_n\right|\mathbf{p}\left|f'_n\right\rangle) \tag{1.24}$$

where v and v' are the bands indices, n and n' are the subbands indices for respectively the initial state and the final state. The integral corresponding to the overlap of the bands $\langle u_v|u'_v\rangle$ is equal to zero when $v \neq v'$ because the Bloch's functions are orthogonal. The integral is equal to 1 when $v = v'$. Thus, in the matrix development in equation 1.24, the first term corresponds only to the interbands transitions ($v \neq v'$) and the second term only for intersubbands transitions ($v = v'$). For intersubbands transitions, the equation 1.24 is simplified as follow:

$$\left\langle f_{n,\boldsymbol{k}_{(x,y)}} \middle| \boldsymbol{\varepsilon}.\mathbf{p} \middle| f_{n',\boldsymbol{k}'_{(x,y)}} \right\rangle = \frac{1}{S} \int e^{-i\boldsymbol{k}_{(x,y)}.\boldsymbol{r}} \Phi_n(z)(\varepsilon_x.p_x + \varepsilon_y.p_y + \varepsilon_z.p_z) e^{i\boldsymbol{k}'_{(x,y)}.\boldsymbol{r}} \Phi_{n'}(z)\, \mathrm{d}^3 r \tag{1.25}$$

The terms including ε_x and ε_y are equal to zero as for $n \neq n'$ the functions f_n and f'_n are orthogonal. Thus, for an intersubband transitions, only terms proportional to ε_z contribute to the matrix element corresponding to the transitions rate. We can then simplify the expression to:

$$\langle n|p_z|n'\rangle = \int \Phi^*_n(z) p_z \Phi'_n(z)\, \mathrm{d}z \tag{1.26}$$

The optical transitions are vertical in the reciprocal space, in other words $k'_{(x,y)} = k_{(x,y)}$. Thus, the energies and rate of transition are independent of the in plane wavevector. One important aspect of this selection rule that needs to be pointed out is that it is only valid for n-type doped QWs based on intersubband transitions between Γ-valley derived states. For p-type doped QWs, there is a strong mixing among the heavy holes and light holes at non zero wavevector in the valence band that makes absorption of normal incidence IR right possible [Hoff et al., 1996]. This optical transitions selection rule for intersubbands has shown experimentally an accuracy of 0.2% for $GaAs$ and of 3% for $InGaAs$ QWs [Liu, 2000] [Liu et al., 1998].

The coupling quality between the light and the subbands can be expressed thanks to the oscillator strength $f_{nn'}$:

$$f_{nn'} = \frac{2}{m\hbar\omega_{nn'}} \left|\langle n|p_z|n'\rangle\right|^2 = \frac{2m^*\omega_{nn'}}{\hbar} \left|\langle n|z|n'\rangle\right|^2 \tag{1.27}$$

where $\omega_{nn'}$ is the frequency between the final state n' and the initial state n. The oscillator strength is an non-dimensional parameter.

In the parabolic approximation, this quantity verifies the sum rule:

$$\sum_n f_{nn'} = 1 \tag{1.28}$$

that is valid for any initial state n towards the sum of n' other possible states. Considering the even parity of the ground state, the expression for the oscillator strength of an infinite barrier QW becomes:

$$f_{nn'} = \begin{cases} \frac{64}{\pi^2} \frac{n'n'^2}{(n'^2-n'^2)^3} & for \quad odd \quad (n'-n) \\ 0 \qquad for \quad even \quad (n'-n) \end{cases} \tag{1.29}$$

Thus, $f_{nn'}$ is non-zero only for parity-changing transitions due to the inversion symmetry of the potential [Emmanuel Rosencher, 2002]. The dominant transition among the all possible ones, remains for consecutive bands.

For a finite barrier QW, the oscillator strength corresponding to a bound to bound transition or bound to continuum transition is expressed as:

$$f_{B-B} = \frac{8\hbar C_1^2 V_b^2}{m\omega(E_2 - E_1)^2} cos^2(k_1 L/2) \frac{E_2 x_2 sin^2(k_2 L/2)}{E_2 x_2 L/2 + V_b sin^2(k_2 L/2)} \tag{1.30}$$

$$f_{B-C} = \frac{8\hbar C_1^2 V_b^2}{m\omega(E - E_1)^2} cos^2(k_1 L/2) \frac{(E - V_b) tan^2(k_2 L/2)}{E + (E - V_b) sin^2(k_2 L/2)} \tag{1.31}$$

One of the main properties of intersubband transitions governing their applications in ultra fast processes is their lifetime. The relaxation processes of the electrons are either radiative or non radiative

- The radiative emission corresponds to the spontaneous emission. An electron from subband n can relax to another subband n' with lower energy level by emitting spontaneously a photon. The expression of the emission rate is [Faist, 2013]:

  $$W_{nn'}^{spont} = \frac{1}{\tau_{spont}^{nn'}} = \frac{e^2}{6\pi m_0 c^3 \epsilon_0 \hbar^2} n_r f_{nn'} E_{nn'}^2 \tag{1.32}$$

  with m_0 the electron mass, c the speed of light, ϵ_0 the vacuum permittivity and n_r the refractive index.

  The spontaneous emission lifetime is inversely proportional to the square of the photon energy. Thus, $\tau_{spont}^{nn'}$ is in the order of microseconds in THz and tens of nanoseconds in MIR.

- The non radiative process occurs when an electron leaves its subband for another one by elastic or non elastic processes (e.g. absorption or emission of optical and/or acoustical phonons, electron-electron interactions, etc.).

  The optical phonon emission is dominant when the subbands energy difference is higher than the phonon energy of the corresponding structure.

1.2.4 Comparison with interband transitions

In comparison to intersubband transitions, interband transitions involve absorption or emission of photons between the valence and conduction band. The minimum photon energy absorption and/or emission is fixed by the band gap energy (E_g) of the semiconductor material. Figure 1.15 shows comparison scheme between interband and intersubband transitions.

In intersubbands transitions, as we have seen in the previous demonstration, the energy transition varies with the width of the QW (L). For this reason, intersubband transitions can be tuned with geometrical parameters of the involved QWs.

Moreover, as shown before and can be seen in figure 1.15, in the reciprocal space, the difference in energy between two subbands is constant and does not depend on $k_{(x,y)}$. The density of states is narrow and centered around E_{12}. The gain width in the case of emission or the absorption width for a detection is due to non radiative relaxation process. On the other hand, for interband transitions, the carrier lifetime is dominated by the electron and hole recombination time, giving a typical value

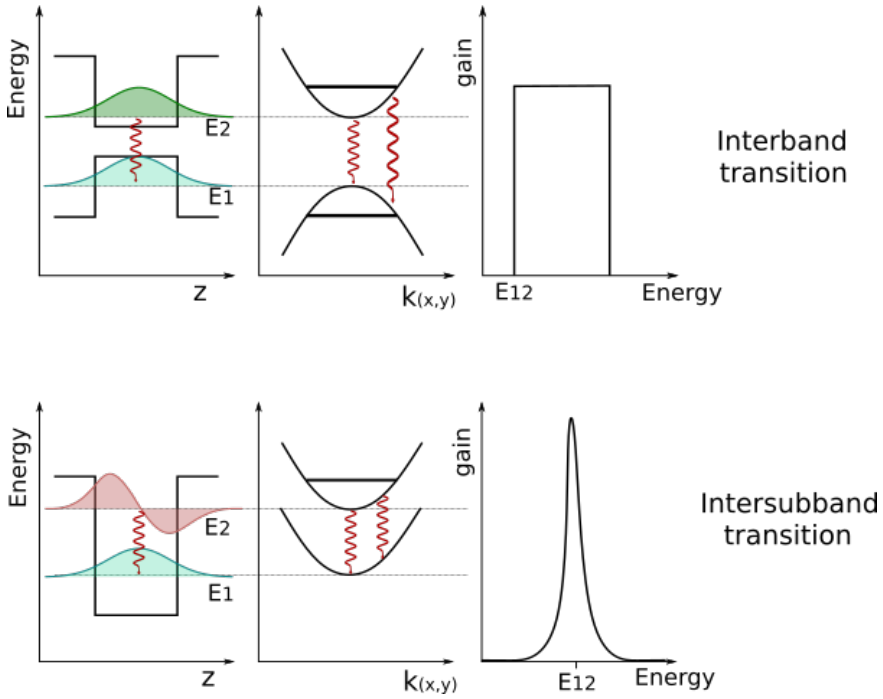

FIGURE 1.15: From left to right: energy in Z space, in k space and the density as a function of the energy for interband transitions (top) and intersubband transitions (bottom).

in the order of nanoseconds. The gain is also much larger because of the opposite curvature of the energy bands (see Figure 1.15).

Table 1.1 summarizes the comparison between different characteristics of intersubband and interband transitions.

Interband Transitions	**Intersubband Transitions**
Absorption at energy equals and above $E = h\nu$	Absorption at $E = h\nu$
Energy Gap defines the minimum transition energy	QW width (L) defines the transition energy
Long carrier lifetime ($> 1\ ns$)	Short carrier lifetime ($< 1\ ps$)
High radiative efficiency	Low radiative efficiency

TABLE 1.1: Comparison table of the different characteristics defining the intersubband and interband transitions.

1.3 Sources and detectors in the MIR

In the following, we present an overview of principal sources and detectors in MIR. Most of these devices are based on ISB transitions. We give a panorama on both kinds of devices pointing their advantages and drawbacks.

1.3.1 Sources

Figure 1.16 shows different categories of IR sources according to their spectral range.We can see from this figure that the whole range of MIR is nowadays covered by sources.

IR sources based on interband transitions like InGaAs/Sb and lead salt lasers have a really broad range of emission from 3 to 30 μm [Preier, 1990].

ISB lasers such as QCLs are now really well developed. Room temperature operation with output power of the order of hundred of mW have been demonstrated up to 23 μm wavelength. They are good candidates for high frequency measurements due to the short carrier lifetime.

The different IR sources will be developed in the following of this section.

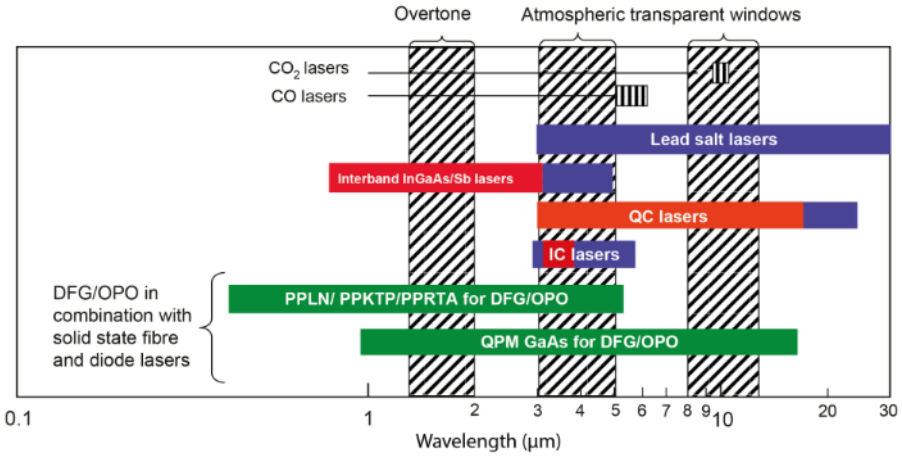

FIGURE 1.16: Overview of the state of the art of light sources in the MIR and NIR (source: http://www.qoe.ethz.ch/Tutorials.html).

Diodes

- Interband diodes

  Interband diodes are based on optical transitions between the conduction band and the valence band. Thanks to a p-n junction, the carriers are injected to the structure and are recombined by emitting a photon with the energy of the bandgap. III-V diodes were the first lasers emitting in the MIR. In 1963, p-n junctions made of InAs and InSb have been demonstrated emitting at respectively 3.1 μm and 5.3 μm [Phelan et al., 1963], [Melngailis, 1963]. For longer wavelength emission, materials such as lead telluride (PbTe) and lead sulfide (PbSe) have been introduced [Butler et al., 1964]. Later on, double heterostructure (DH) lasers based on lead compounds remained the standard for MIR lasers. Grown on PbS, PbSe or PbTe substrates, they cover the wavelength range from 3 to 30 µm, and have reached a maximum operating temperature in CW of 200K [Feit et al., 1996], [Preier, 1990].

- Interband QW diodes

  In QW diodes, MIR emission is obtained thanks to antimony (Sb) material. Multiple QW laser diodes based on the GaIn(As)Sb/AlGaAsSb system showed striking results in CW operation at high temperature [Belenky et al., 2008]. The operating wavelength can be tuned between 2 to 3 μm by varying the concentration of Indium. Heterostructures based on III-V materials have interesting properties in band gap energy and band discontinuity which allow the formation of deep QWs (for holes and electrons). Thus for higher wavelength emission, lasers based on the InAs/GaInSb system (known as type-II "W") have emerged. Pulsed wave operation at room temperature and continuous wave

operation up to 220K have been observed for this type of laser [Canedy et al., 2005].

- Interband cascade lasers

  Interband cascade lasers (ICL) also based on type II InAs/GaInSb system have been developed [Yang, 1999]. In this type of structure, the QW where the emission occurs is simply multiplied in order to increase the efficiency. Between each QW, a series of QWs ensure the injection of carriers to the next QWs. ICLs have been demonstrated characteristics such as CW operation at temperature up to $118°C$ and a maximum power of 400 mW at pulsed operation at RT and a single-mode output at 5.2 μm [Vurgaftman et al., 2015] [Bewley et al., 2013].

Optical parametric Oscillator (OPO)

In an OPO source, a pump signal is divided into two outputs; the signal and the idler. The frequencies of both photons depend on intrinsic parameters of the crystals in particular on the phase match. The crystal is placed in a cavity that is resonant with either the signal or the signal and the idler. It was first achieved in 1965 by Giordmaine and Miller [Giordmaine and Miller, 1965]. This type of source can achieve watt in the output. This technique permits also to obtain tuning ability over a larger range than the micrometers. OPOs working in CW and pulsed wave from 1.5 μm to 12 μm [Ebrahim-Zadeh, 2008]. They can also operate at or above room temperature and can be configured in a compact architecture [Devi and Ebrahim-Zadeh, 2017].

Gas lasers

The most used gas laser is based on CO_2 and was developed in 1964 [Patel, 1964]. It emits high power up to several hundreds of watt in the IR domain at 9.6 μm and 10.6 μm. Because of its high efficiency (up to 20%) it is used for metals cutting and welding in industries but also for photoacoustic spectroscopy. Among the other gas lasers operating in the MIR, we can cite the CO laser which is line-tunable in the $5 - 8$ μm region and the He-Ne laser at 3.39 μm.

QCL

Quantum cascade lasers are light sources based on electronic transitions between quantum states in the conduction band of semiconductor QWs. As they are based on ISB transitions, the separation between the confined states can be controlled by engineering the QWs widths. Emission wavelength for such sources has indeed been demonstrated from the MIR to the THz region of the electromagnetic spectrum. Moreover, the nature of these transitions makes them extremely fast typically in the sub-picosecond range. For this reason the gain dynamic of QCLs has peculiar properties compared to standard semiconductor diode lasers. Any information given to the system in terms of variation of electron population is refreshed at extremely high frequency (>100 GHz), hinting that population inversion in QCLs can be varied extremely rapidly. Predicted performances for modulated QCLs strongly exceed the one of standard laser diodes and the main limitation to the frequency band of QCL remains in the device package and chip parasitic.

First CW operation QCL above room temperature have been observed in 2002 [Beck, 2001]. Then, performances of QCL have increased rapidly. An improvement

in the output power and wallplug efficiency have been observed for QCL operating at 300K [Bai et al., 2011] [Lyakh et al., 2009]. Operating wavelength of the QCL has also been extended to the THz domain in 2002. Figure 1.17 summarizes the state of art of QCLs operating at different wavelength and temperature. We can see from this figure that QCLs are now really well developed. RT operation with high output power have been demonstrated up to 23 μm wavelength. More details about the working principles of QCL will be presented in chapter 4.

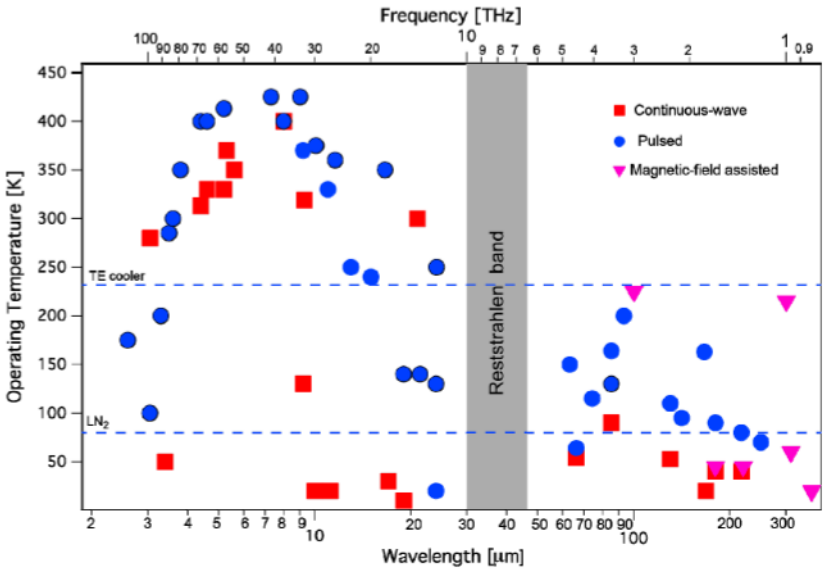

FIGURE 1.17: Operating temperature plot as a function of the emission wavelengths for QCLs [Vitiello et al., 2015].

1.3.2 Detectors

Detectors in the IR can be classified in two classes: thermal or photonic. In this section we will explain briefly the thermal detectors and go into details with the photonic detectors, as they are the ones that we will study during this thesis.

Figure 1.18 presents detectivity for different demonstrated IR detectors. Dashed lines represent the theoretical value for ideal thermal and photonic (either photovoltaic or photoconductive) detectors.

We will develop in the following paragraph the characteristics of different detectors operating in the MIR with their advantages and drawbacks.

Thermal detectors

Thermal detectors are based on measurements of thermal variation of the material due to IR radiation absorption. This temperature variation can come from different aspect.

Bolometers for example, that are the most commonly used thermal detectors, are based on resistance variation of a heat sensing material due IR absorption.

On the other hand, *pyroelectric* detectors, fabricated with different material depending on the operating wavelength (e.g. Sapphir for 0.1−7 μm; Quartz for 0.2−3.5 μm; most common material LiTaO3 and DLaTGS for MWIR and LWIR) are based on spontaneous change of the electrical polarization with temperature.

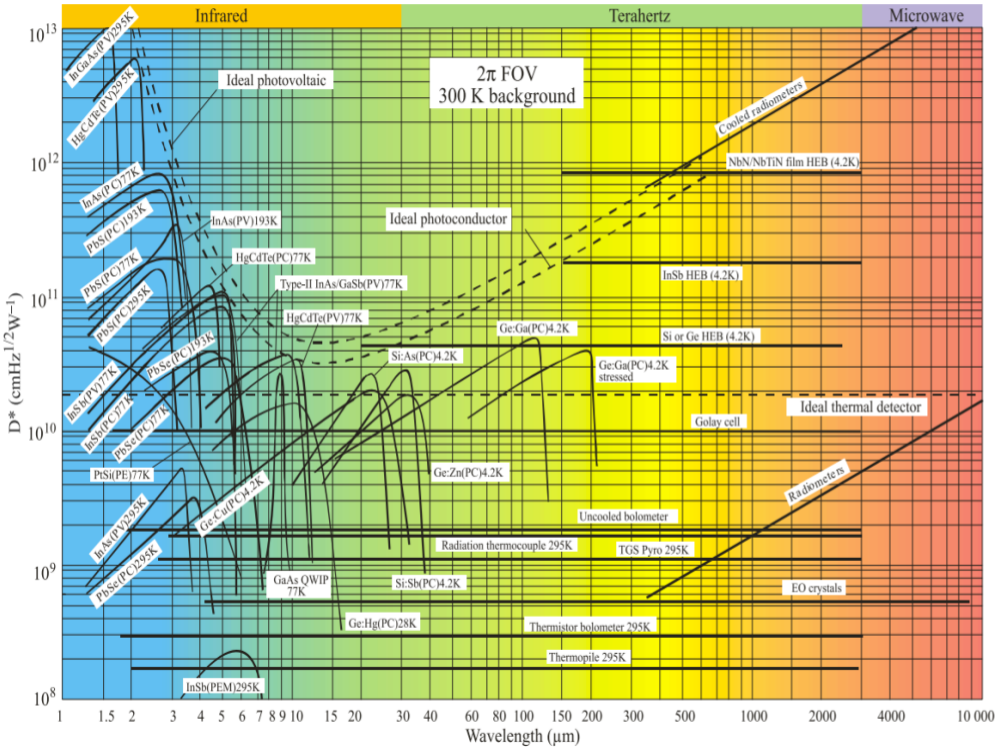

FIGURE 1.18: Comparison of specific detectivity of different IR detectors at different operating wavelength. The operating temperature for each detector is mentioned newt to the curve. The detectivity is normalized by a background of 300K (source: [Rogalski, 2012]).

Thermocouples and *thermopiles* detect the IR radiation from objects and convert the heat passively to an electrical potential. Based on Seebeck effects, a thermal diffusion current between two different metals generated an electrical voltage which is then measured.

Finally, Golay cells IR detectors are based on pressure change of a gas in a chamber due to a temperature variation.

Most of thermal detectors work at room temperature. Their performances can be improved by decreasing the operating temperature. In array technologies and for IR cameras, currently, the microbolometer detectors are produced in larger volumes than all other IR array technologies [Rogalski, 2012]. Thermal detectors have the advantage to be broadband in IR domain and they possess reasonable value of detectivity ($D^* = 10^9$ *Jones*). Their drawbacks remain their low cut-off frequency due to their long response time that is in the order of 10 *ms* to 100 *ms*[Henini and Razeghi, 2002].

Photonic detectors

Photonic detectors are based on direct creation of current due to photon absorption between two energy levels of the material that constitute the detector. Photonic detectors can be classified into two types: interband (IB) and intersubband (ISB).

At present, MCT detectors, based on IB transitions, have the best detectivity performances ($D^* = 10^{12}$ *Jones*) and they are the most widely used semiconductor

IR detectors. However, they operate at cryogenic temperature and are not suitable for fast response application [Theocharous et al., 2005]. Moreover, after Minamata convention on mercury, the uses of mercury will be forbidden in 2020 [6].

Serious competitors from alternative technologies have then merged. ISB detectors based on III-V materials have introduced a new way of detection in the MIR such as QWIPs and QCDs.

We present in the next section, these three detectors in the IR range: the MCT based on IB transitions, the QWIP and the QCD relaying on ISB transitions.

MCT

Mercury Cadmium Telluride (MCT or HgCdTe) are the most used photodetectors and they operate from 3 to 12 μm. They are based on interband transitions where electrons from the valence band are excited to the conduction band. The minimum of photon energy required is equal to the bandgap of the structure.

First IR photonic detectors were fabricated in the 1950 made of Lead Sulfide (PbS) and absorbing in the $1.3 - 3$ μm band. They have been followed by Indium Antimony (InSb) detectors working at higher wavelength ($3 - 5$ μm). MCT detectors have been developed and first fabricated in 1960 by Lawson and co-workers [Lawson et al., 1959]. The first MCT was operating in the $8-14$ μm band. However, nowadays, a variety of MCT alloy can be fabricated leading to a wide range of wavelength absorption. Since these years, MCT detectors have continue to improve in term of performances and as they have reached a high sensitivity with high performances, they have led to the development of IR imaging systems. An overview of IR detectors from that days up to 2016 can be found in the paper of Rogalski and co-workers [Rogalski et al., 2016].

Again, advance in MBE techniques for growth of HgCdTe on top of Silicon substrate has allowed to achieve cost effective MCT detector production.

QWIP

Quantum well infrared photodetectors (QWIP) are photonic detectors based on intersubband transitions. The structure is based on a main QW where the ISB absorption occurs. Then, photoelectrons are collected by applying an external bias to the device. This type of detector are called photoconductive detectors and the change of device's resistance under illumination is measured.

There are different types of QWIPs depending on the barrier structure and the position of the excited states. They can be classified as follow: bound-to-bound (B-B), bound to quasibound state (BQB), bound to continuum (B-C) and bound to miniband (B-M). Figure 1.19 presents the energy band diagram structure for these four different types of n-type QWIPs.

- **B-B**

  In bound to bound QWIP, the absorption occurs between two bound states with a lower potential than the top of the well. In this case, the electrons often escape the well by either quantum tunneling or thermionic emission. This type of QWIPs has narrow absorption spectra and large dark current.

[6] http://www.mercuryconvention.org/

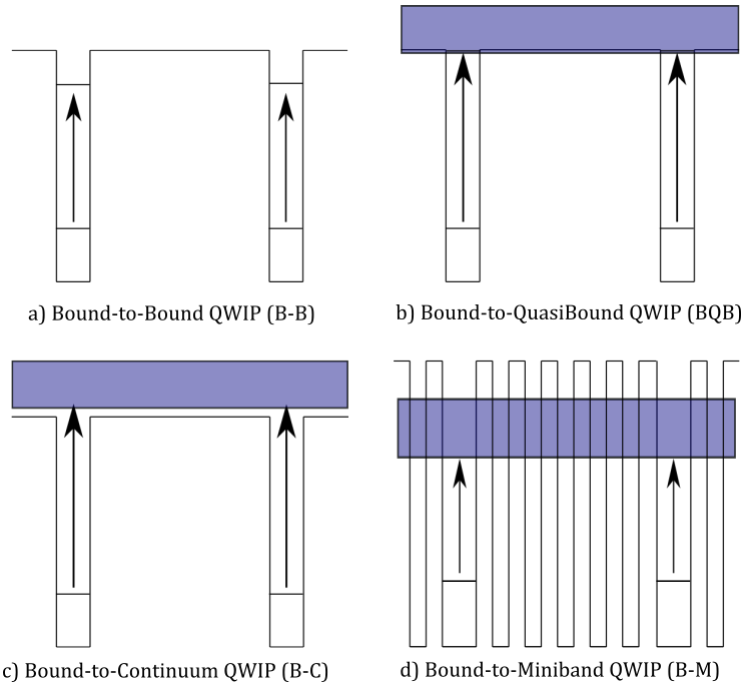

FIGURE 1.19: Schematic energy band diagram for a) B-B, b) BQB, c) B-C and d) B-M QWIPs.

- **BQB**

  In bound to quasibound QWIP the wave function of electrons in upper excited states is aligned with the top of the well. In this configuration, the barrier height limits the wavelength and a sharp cut-off is observed for this type of QWIP. For this configuration, the absorption spectrum is slightly wider but it is still considered as a narrow absorption detector.

- **B-C**

  In bound to continuum QWIP, the absorption occurs between a bound state and the continuum. In this type of QWIP the peak absorption is relatively small but the absorption spectrum is wide compare to B-B and BQB QWIP because of the broad final state (cf figure 1.20).

- **B-M**

  In bound to miniband QWIP, the transition occurs from the localized bound ground state in individual well to a resonant coupled miniband of a superlattice barrier. In this type of QWIP, there is a strong interaction between the initial and final states due to a large overlap of the wavefunctions. The maximum of bandwidth corresponds to the alignment of the final state in the middle of the miniband. B-M QWIPs, compare to other mentioned QWIPs, have another degree of freedom that offers more flexibility in tuning the detector wavelength and spectral bandwidth.

The first demonstrated QWIP was B-B QWIP with a peak wavelength at 10.9 μm and a net absorption of 5% realized by Levine in 1987 [Levine et al., 1987]. Then, one year later, Levine designed another QWIP based this time on B-C intersubband absorption. To do that, he has reduced the QW width and pushed the excited state in the continuum [Levine et al., 1988]. He has then observed the first B-C QWIP. Later

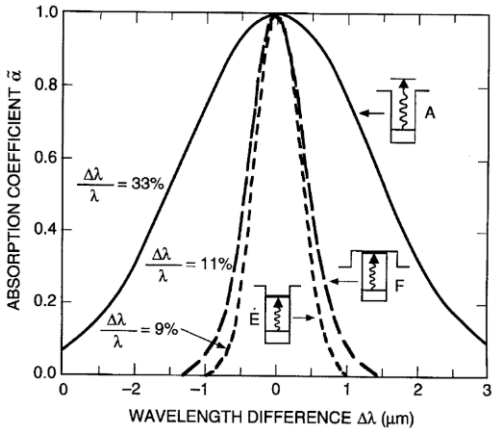

FIGURE 1.20: Normalized absorption spectra as a function of the wavelength for B-B, BQB and B-C QWIPs. (source: [Nalwa, 2002])

on, in 1995, Gunapala and Bandara [Gunapala and Bandara, 1995] have improved the performances of the QWIP by designing a BQB QWIP.

Since their invention, QWIPs have presented high performances in MIR detection, such as high detectivity [Gunapala and Bandara, 1999] and responsivity [Schneider and Liu, 2007] but also high ultra fast modulation performances [Grant et al., 2006]. Thus, QWIPs have shown a competitive detectivity ($D^* = 10^{10}$ *Jones*) in addition to high frequency response theoretically up to 100 *GHz* [Schneider and Liu, 2007]. Moreover, QWIPs focal plane arrays sensitive at wavelengths between 8 μm and 10 μm have reached commercial maturity. Gunapala et al. have presented a MIR camera based on GaAs/AlGaAs QWIP with a 1024 × 1024 pixel dual focal plane array with cutoff wavelengths of 5.1 μm and 8.4 μm [Gunapala et al., 2005].

The drawbacks of photoconductive QWIPs is the dark current flowing inside the detector that is the limiting parameter of the device. Indeed, as the dark current increases exponentially with temperature, the performances of the QWIPs degrade rapidly with temperature. Thus, most of the QWIPs have to be cooled down to cryogenic temperature in order to preserve their good performances. However, room temperature QWIPs have also been demonstrated in the MIR detection [Ravikumar et al., 2013] [Richards et al., 2003] and heterodyne measurements [Grant et al., 2006]. Recently, in our group, a 9 μm wavelength QWIP used as a patch resonator has been demonstrated working at room temperature as GHz heterodyne receiver [Palaferri et al., 2018]. A QWIP operating at 5 μm has also been demonstrated for room temperature HF measurements up to 26 *GHz* [Rodriguez et al., 2018].

In order to reduce the dark current noise, researches have turned towards photovoltaic QWIPs. They are by definition devices with a built-in inversion asymmetry acting as an internal field. Thus, no external bias voltage is needed for the devices to operate. Even though, photovoltaic QWIPs do not benefit from the large responsivity as photoconductive QWIPs do, but due to a lower dark current noise, they can partly overcome this lack. Schneider *et.al* have shown also that optimizing a photovoltaic QWIP will have better performances in terms of dynamical range and capability to work at higher photon flux than photoconductive QWIPs [Schneider, 1993]. Indeed, THz detector have been first demonstrated by a photovoltaic detector [Graf et al., 2004] before a photoconductive QWIP [Liu et al., 2008].

Different devices concepts have been introduced for photovoltaic QWIPs [Schneider and Liu, 2007]: interminiband absorption in a superlattice with an adjacent blocking barrier [Kastalsky et al., 1988], single QW with surface depletion layer [Goossen et al., 1988], ISB transition QW between an asymmetrically doped double-barrier QW [Schneider, 1993].

Later on, a new geometry for a photovoltaic QWIP has been proposed in 1997 by Schneider*et.al* named "Four-zone" QWIP [Schneider et al., 1997].

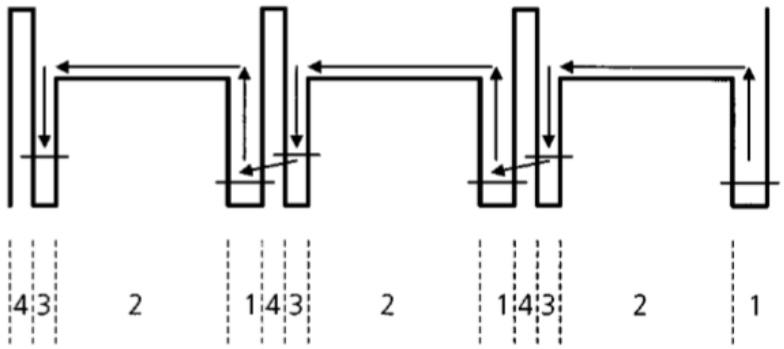

FIGURE 1.21: Band structure of a four-zone QWIP illustrated in the paper of Schneider *et.al* with the different zones [Schneider et al., 1997].

Figure 1.21 shows the band structure of a four zone QWIP. Each period of the active region in these structures consists of four zones, namely an excitation zone (zone #1), a drift zone (zone #2), a capture zone (zone #3), and a tunneling zone (zone #4). This QWIP is composed of two different QWs. One (zone #1) plays the role of the absorber which is BQB QW, and the other one (zone #3) is the captor zone, where charges are injected from its ground state to the ground state of the next QW (the absorber). This geometry allows the QWIP to work at zero-bias which reduces the the electrical noise. The photocurrent is as in standard QWIP transport and measured in the continuum states. A thermal camera based of a photovoltaic four-zone QWIP operating at 8.5 μm with 256 x 256 focal plane array has been demonstrated with very low noise equivalent temperature difference of 5.2 mK [Schneider et al., 2000].

QCD

In analogy to the photovoltaic QWIP approach, another photovoltaic detector based on QWs intersubband transitions has been demonstrated by V. Berger's group in 2004 [Gendron et al., 2004] [7]. The structure of the QCD is inspired by the QCL. A photogenerated electron from ISB transition in a QW is tunneled out from a thin barrier to a region composed of successive QWs. This region, named as cascade region, extracts the electron down to the ground state of the next QW (where the absorption occurs) thanks to an LO-phonon scattering process. The cascade region has an asymmetric potential that gives to the carriers a preferential transport direction. This ensemble of QWs represents one period in a QCD. This period can be repeated N times in order to ensure a good signal to noise ratio. Figure 1.22 shows

[7] French patent: V. Berger, "Détecteurs à cascade quantique", (2001), French national reference number 0109754.

a schematic comparison between QWIP and QCD structure. More details and band structure of QCD are developed in next chapter.

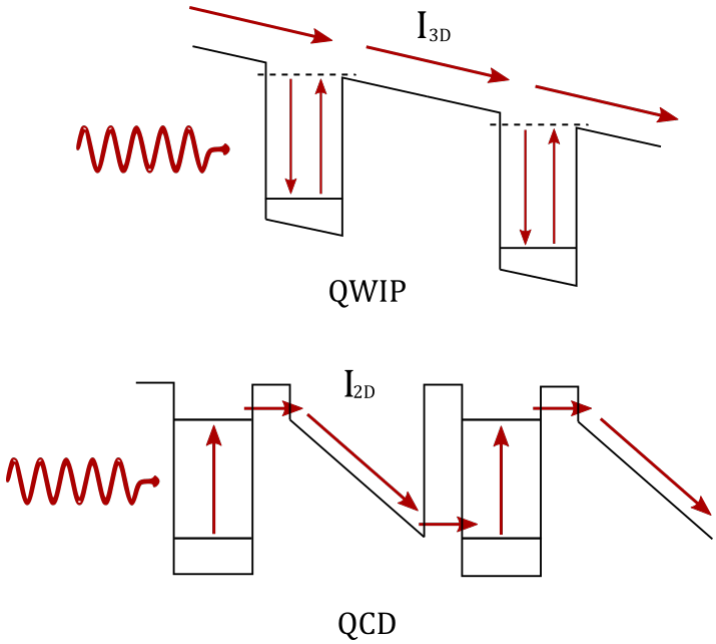

FIGURE 1.22: Schematic band structure of QWIP (top) and QCD (bottom). Red arrows correspond to the current flow. The current in the QWIP is collected in the continuum hence I_{3D} whereas in the QCD the corresponding photocurrent is collected at the end of the QWs period (I_{2D}).

Now on, QCDs have been demonstrated in the MIR [Gendron et al., 2004] and in the THz range [Graf et al., 2004]. In wavelength range between 5 and 17 μm, QCD based on InGaAs–InAlAs lattice matched to InP are used. For shorter wavelength, other materials have to be used. Indeed, due to conduction band offset (CBO), heterostructures using InGaAs can have ISB transitions above 4 μm. The CBO is limited to 520 meV. There exists two alternatives in order to overcome this: grow lattice matched InGaAs-AlAsSb or strained InGaAs-InAlAs.

The photovoltaic aspect of QCDs is responsible to the low thermal noise of the device. This advantage allows QCDs to operate at room temperature. QCDs working at wavelength between 3 to 5 μm have been demonstrated working at room temperature with comparable or higher performances than QWIP devices [Graf et al., 2006] [Giorgetta et al., 2009] [Hinds et al., 2011]. During the last few years, important step forward in terms of QCD devices performances have been demonstrated [Gendron et al., 2005]. However, improvements need still to be done in terms of detectivity performances at high temperature [Giorgetta et al., 2009].

QDIP

In both of the previous QW detectors, absorption can only occur if the electromagnetic field is along the QWs growth direction axis (cf polarization selection rule section 1.2.3). The quantum dot infrared photodetector (QDIP) permits to overcome this restriction by confining the carriers in all three spacial directions [Pan et al., 1998]. Moreover, QDIPs have the advantage of weak thermionic coupling between

the ground state and excited states that leads to lower thermal excitation thus lower dark current noise compare to QWIPs [Campbell and Madhukar, 2007]. Theoretically, an ideal QDIP is expected to be substantially superior than QWIP [Liu et al., 2001].

First photocurrent measured with a QDIP was performed by Phillips *et.al* in 1998 at 17 μm [Phillips et al., 1998]. Later on, a great progress have been made in QDIPs in terms of performance characteristics and applications such as focal plane arrays [Bhattacharya and Mi, 2007]. Also broadband QDIP from 4 to 11 μm with relatively flat detection and high responsivity has been demonstrated [Lin et al., 2010]. In order to improve absorption efficiency in QDIPs, the quantum dots can be confined in QWs known as dot in a well (or DWELL) [Le et al., 2003]. Based on this technique, 640 x 512 focal plane arrays with a noise equivalent temperature difference of 40 mK at $T = 60\ K$ have been reported around 8 μm [Krishna et al., 2007].

2 Quantum Cascade Detector

Contents

In this chapter we present the working principle of quantum cascade detector (QCD) operating in the MIR range of the electromagnetic spectrum. We introduce the electrical and optical properties of these devices, with particular interest to the dark current and resistance at zero bias (R_0) as well as to the photocurrent, responsivity and detectivity. We conclude the introductory part of this chapter with the band structure of the specific QCD studied in this thesis. This is based on III-V ternary heterostruture made of GaInAs quantum wells sandwiched between AlInAs barriers. The QCD has been designed to operate at 4.9 *µm with a maximum of response at small applied negative bias for more stable performances. As first step, we present the clean room process to fabricate electrically driven QCD. It is based on wet etching technique optimized to have an extremely careful control of the etching depth on a large surface. We perform detailed electrical and optical characterization of the QCD in a mesa geometry (of the order of* $(100\ \mu m)^2$ *surface) and results are reported in this chapter. We demonstrate a background limited infrared photodetector (BLIP) temperature of* 135 *K and a detectivity at this temperature of* 2×10^{11} *Jones. Both values are comparable with the state of the art and the detectivity at BLIP temperature is the highest reported (to our knowledge) on this material platform. In the last part of the chapter we investigate the characteristic of the QCD under reverse bias (opposite to the phonon extraction cascade). In this regime, above a certain bias, the device switches to a QWIP like operation, in a bound to continuum scheme. This specific characteristic is demonstrated by optical measurements and band structures calculations.*

2.1 Working principle of QCD

Quantum cascade detector is based on intersubband transitions in multiple quantum well. Figure 2.1 presents schematically the conduction band of one period of a QCD. Photon absorption takes place between the first two levels of a doped quantum well (red arrows in figure 2.1). Electrons pass from the fundamental to excited state of the quantum well. This state is coupled to a cascade of levels with energy separation close to phonon resonance. These levels belong to a succession of quantum wells and barriers with increasing width. A photocurrent is generated along the structure after photon absorption thanks to phonon scattering, without any applied bias. In this scheme an electron, after a photon absorption, experiences an internal potential with a preferential direction that gives rise to a photocurrent. We define the probability of tunneling from the excited state of the main QW to the adjacent cascade region as the escape probability p_e and it is defined as [H. C. Liu, 2000]:

$$p_e \equiv \frac{\tau_{relax}}{\tau_{relax} + \tau_{escape}} \tag{2.1}$$

where the electron scattering lifetime from the resonant energy level down to the ground state is τ_{relax} and towards the cascade region is τ_{escape} (see figure 2.1). For ideal QCDs, we consider no leakage current due to diagonal transitions from the main QW to the cascade region (figure 2.1). In this case the probability of escape is considered to be equal to one [Delga et al., 2013], and the electron has a zero probability to fall down to the initial state (since $\tau_{relax} \gg \tau_{escape}$). A probability of capture (p_c) is defined as the probability of the photo-electron to be captured in the ground state of the main QW.

The unit presented in Figure2.1 can be repeated N times. In this case, N photons are needed to generate a single photo-electron. This reduces the photodetector gain of a factor N but it increases the absorption quantum efficiency.

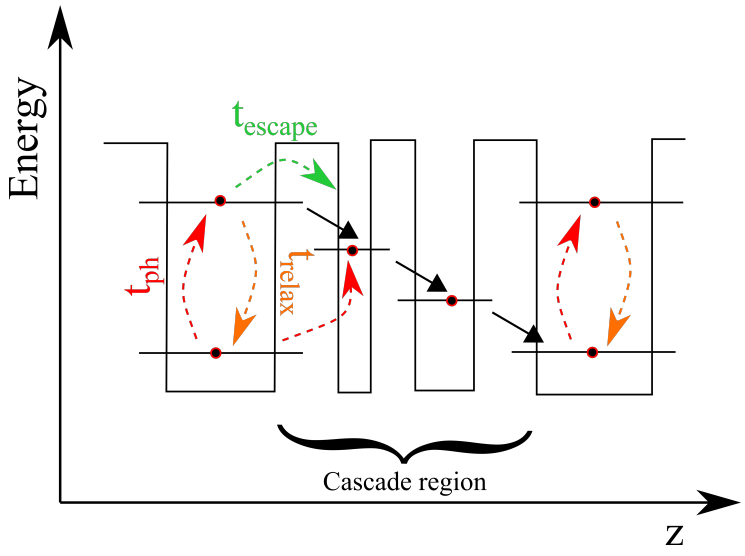

Figure 2.1: Scheme of one period of the conduction band of a QCD. Red arrows: photon absorption (vertical or diagonal). Orange arrows: Relaxation process down to the ground state of the main QW. Green arrows: tunneling to the cascade region. Black arrows: Phonons emission.

Spectral response of QCD is determined by the main quantum well characteristics. In Figure 2.2 we present a schematic view of the absorbing well and we show its energy levels. In the approximation of infinitely high barriers and parabolic bands [West and Eglash, 1985b] the energy levels are:

$$E_i = \frac{\pi^2\hbar^2}{2m_{eff}L_w^2}i^2 \qquad [eV] \tag{2.2}$$

where i is an integer, $\hbar$ the Planck's constant, L_w the width of the well and m_{eff} the effective mass of the carrier for the corresponding material compound. We can notice that the energy levels depend strongly on the well thickness ($E \propto 1/L_w^2$).

The intersubband transition energy in the quantum well between the lowest energy level and the first excited state is:

$$E_2 - E_1 = \frac{3\pi^2\hbar^2}{2m_{eff}L_w^2} \qquad [eV] \tag{2.3}$$

We define then the activation energy as the amount of energy needed for electron to pass in the higher state and tunnel out of the well at 0 bias:

$$E_a = E_2 - (E_1 + E_F) = \frac{\pi\hbar^2}{m_{eff}}\left(\frac{3\pi}{2L_w^2} - n_D L_w\right) \qquad [eV] \tag{2.4}$$

where E_F is the Fermi energy level and is defined for low temperature ($k_B T < E_F$) as [Karunasiri, 1996]:

$$E_F = \frac{n_D\pi\hbar^2 L_w}{m_{eff}} \qquad [eV] \tag{2.5}$$

where $n_D[cm^{-3}]$ is the doping concentration in the well.

From equation 2.4 we can see that E_a depends not only on the width of the well but also on the doping concentration.

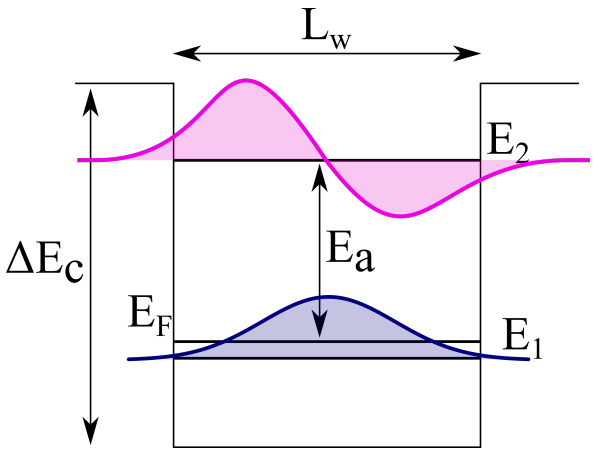

FIGURE 2.2: Simplified scheme of the different energy definition in the conduction band of the main quantum well of the QCD structure. ΔE_c is the conduction band offset and E_a is the activation energy.

2.1.1 Electrical Characterization

In the following we give a detailed presentation of the electrical and optical characterization of a QCD. We present the electron transport in the structure and the definition of resistance at zero bias. We then focus on optical and spectral performances with the presentation of the detector photocurrent and responsivity. In last place, we present noise study and definition of detectivity.

Model of electronic transport (state of art)

As the transport within the cascade region is mainly lead by phonon emission, a bias is not necessary for the photocurrent to be collected. Indeed, after photon absorption, the electron rapidly tunnels out to the cascade region and follows the cascade towards the collector. The QCD is then a photovoltaic detector. The energy levels involved in the transport of carrier in the QCD are all confined states. Thus, the transport of carrier within the QCD can be studied in two dimensions. The scattering of photo-electrons and electrons in the continuum is negligible.

A distinctive property of a QCD is its resistance in the absence of light presented in the following. In particular, dealing with a photovoltaic detector, we define the R_0 parameter, the resistance at zero bias. We present in the following two main models reported in literature (well developed in [Buffaz et al., 2010], [C. Koeniguer and Berger, 2006]) to describe transport in QCD to give a deeper insight on this mechanism. However in this thesis we will use a more simplified approach based on the analogy with interband photodiode.

Thermalized cascade model was one of the first model for the understanding of the electronic transport This model is based on two main approximations.

- First of all, the energy difference between the electronic levels in a QCD is high enough to neglect the interaction between electron and acoustical phonons. In this model, only the electron-optical phonon interaction is taken into account. Moreover, since QCDs work at high temperature (greater than 4K), this model neglects all the elastic diffusion mechanism (i.e. interface roughness, impurity scattering, etc.). Finally, the electron-electron interaction is also negligible since it is only efficient inside a subband for electron thermalization. This interaction is order of magnitude lower when the subband separation corresponds to the energy of the LO-phonon scattering.
- The second approximation is to consider each cascade as an electron reservoir at quasi thermodynamical equilibrium with a given quasi Fermi level.

As, in this model, each cascade is considered to be a perfect conductor, the resistance of the QCD is only governed by the transition between consecutive cascades. The R_0 is then expressed as follow:

$$R_0 A = \frac{k_B T}{q^2 \sum_{i \in A} \sum_{j \in B} G_{ij}(0)} \tag{2.6}$$

where k_B yields for the Boltzmann constant, q the electronic charge, and G_{ij} to the electronic transfer from a subband i of the cascade A to a subband j to the successive cascade B.

However, this model is only valid up to a certain temperature below room temperature (lower than 200 K). This is mainly due to the second assumption of the model. Indeed, the current flow is overestimated at high temperature.

There is another approach for the electronic transport in QCD that completes the previous one named **Thermalized subband model**. The difference between this model and the thermalized cascade model is that in this last model each subband within a cascade is seen as a quasithermalized one and not the whole cascade. So each energy level has its own quasi Fermi level. In this model the resistance at zero bias times the active area of the photodetector A is defined as:

$$R_0 A = \frac{k_B T}{q^2 \sum_{j=1}^{N} \eta_j \times G_{j1}(0)} \tag{2.7}$$

with η_j a value that represents the diode nonideality. The diode nonideality has a value between 1 (for diffusion current) and 2 (for recombination current).

In this formula, the resistance of the device is approximated to be only due to intercascade transitions between the ground state ($i = 1$) of the main quantum well and energy levels of the following cascade (j). The intracascade resistance is neglected. In this model, the cascade region is assumed to be an electron reservoir. For that, the capture probability (p_c) is set to be equal to one. This model has shown a fine agreement with the experiments over eight order of magnitude for temperature between 40 K and 300 K. Below this temperature, the model is no more valid because it does not take into account coherent transport [C. Koeniguer and Berger, 2006].

The transition rate G, is one of the most important parameter in the understanding of the electrical transport in the QCD. Figure 2.3 shows the possible transitions within the subband of a cascade (intracascade figure a) and between two consecutive cascades (intercascade figure b). The horizontal lines in figure 2.3 represent the QCD energy levels.

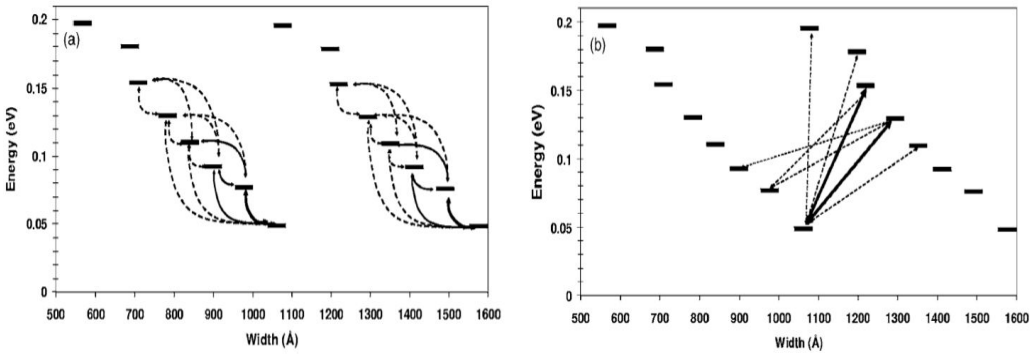

FIGURE 2.3: Schematic of possible transition rates represented with the dash line arrows for a) intracascade and b) intercascade transitions. (source: [C. Koeniguer and Berger, 2006])

The transition rate G is related to the transition time τ by the 2D carrier density n_{2D}: $G = n_{2D}/\tau$. The transition time between subbands of a cascade is lower than between cascades (respectively ten of ps and μs). Thus, the intracascade transition rate is higher compared to the intercascade transition rate. In QCD, they have typical values in the order of respectively $10^{25}\ m^{-2}s^{-1}$ at cryogenic temperature and not higher than $10^{18}\ m^{-2}s^{-1}$ [C. Koeniguer and Berger, 2006]. That's why, as said, we can consider the cascade region as an electron reservoir and neglect the intracascade resistance.

Dark current and R_0A

In order to describe the electrical properties of QCD in dark condition (without illumination from external sources or thermal background at 300 K), we model the detector as an ideal Schottky diode as referenced in [Buffaz et al., 2010], [C. Koeniguer and Berger, 2006]. Neglecting diagonal transitions, the ground state of the main QW can be considered as the metal and the thermalized cascade as the semiconductor [Delga, 2012]. Figure 2.4 a) represents schematically the analogy of a Schottky diode with one period of a QCD.

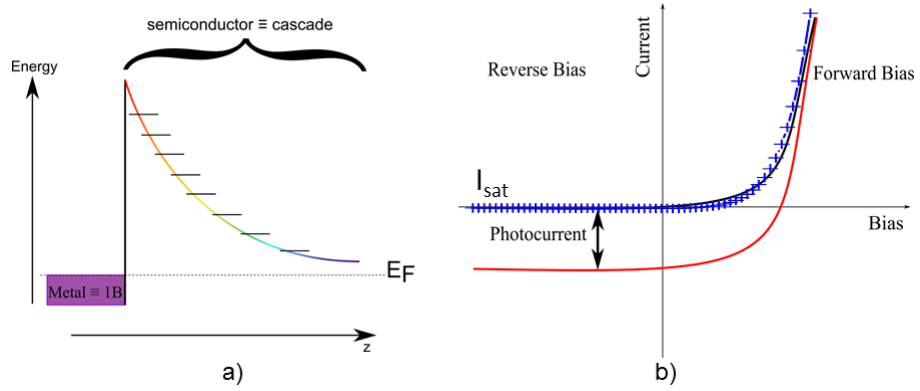

FIGURE 2.4: a) Comparison between a QCD and a Schottky diode. Energy levels at a metal semiconductor interfaces. They are overlapped with energy levels of a QCD. b)I-V characteristic of a QCD in dark (black line) and illuminated condition (red line). The blue crosses are experimental data in arbitrary units for representative comparison with Schottky theory.

In QCD, dark current (black curve in Figure 2.4 b)) is dominated by thermionic emission from the doped QW. In this approximation we can assume a Boltzmann distribution for electronic population. Dark current as a function of the temperature T and applied bias V is written as:

$$I_{Dark}(V,T) = I_{Sat}(e^{\frac{qV}{k_BT}} - 1) \qquad [A] \tag{2.8}$$

where I_{Sat} is the reverse saturation current that depends on the specific distribution of energy levels and on the doping of the structure, q the electronic charge and k_B the Boltzmann constant. Considering the approximation of a Schottky diode, the saturation current is defined as [Mahato et al., 2017]:

$$I_{sat} = AA^*T^2 exp(\frac{-E_a}{k_BT}) \qquad [A] \tag{2.9}$$

where A^* is known as the Richardson constant related to thermal emission and it is equal to:

$$A^* = \frac{4\pi q m_{eff} k_B^2}{h^3} \qquad [A.m^{-2}K^{-2}] \tag{2.10}$$

E_a is the activation energy defines in equation 2.4. The dark current density of the QCD $J_{Dark} = I_{Dark}/A$ is:

$$J_{Dark}(V,T) = J_{Sat}(e^{\frac{qV}{k_BT}} - 1) \qquad [A/cm^2] \tag{2.11}$$

From this model, we can observe that a minimum energy of $qV = E_a$ is needed in order to generated a dark current.

When the detector is illuminated, an additional contribution to the current is introduced J_{photo}(red curve in figure 2.4 b)). The total current density in the detector is then equal to:

$$J_{tot}(V,T) = J_{DK}(V) - J_{photo} = J_{sat}(e^{(\frac{qV}{k_BT})} - 1) - J_{photo} \qquad [A/cm^2] \tag{2.12}$$

In the following we present the direct estimation of the QCD activation energy from the dark current measurements.

The resistance of the device is deduced from the dark current expression (equation 2.11):

$$R(V)A = \frac{dV}{dJ_{tot}} \qquad [\Omega.cm^2] \tag{2.13}$$

$$\frac{dJ_{tot}}{dV} = J_{sat}\frac{q}{k_BT}e^{(\frac{qV}{k_BT})} \tag{2.14}$$

$$R(V)A = \frac{1}{dJ_{tot}/dV} = 1/J_{sat}\frac{k_BT}{q}e^{(\frac{-qV}{k_BT})} \qquad [\Omega.cm^2] \tag{2.15}$$

Be replacing J_{sat} using its definition 2.9 in previous equation we obtain:

$$R(V)A = \frac{k_bT}{qA^*T^2}e^{(\frac{E_a-qV}{k_BT})} \qquad [\Omega.cm^2] \tag{2.16}$$

The natural logarithm of equation 2.16 becomes:

$$ln(R(V)A) = ln(\frac{k_bT}{qA^*T^2}) + ln(e^{(\frac{E_a-qV}{k_BT})}) = ln(\frac{k_bT}{qA^*T^2}) + \frac{E_a - qV}{k_BT} \tag{2.17}$$

As the operating point for photovoltaic photodiode is at zero bias, equation 2.17 is then rewritten as:

$$ln(R_0A) = ln(\frac{k_bT}{qA^*T^2}) + \frac{E_a}{k_BT} \tag{2.18}$$

The variation of the ln(1/T) as a function of the temperature is negligible compare to the variation of (1000/T)(see figure 2.5).

Thus, equation 2.19 becomes:

$$ln(R_0A) \simeq \frac{E_a}{k_BT} \tag{2.19}$$

Plotting the natural logarithm of the resistance for a defined bias as a function of the temperature gives the value of the activation energy at this bias (up to the Boltzmann constant).

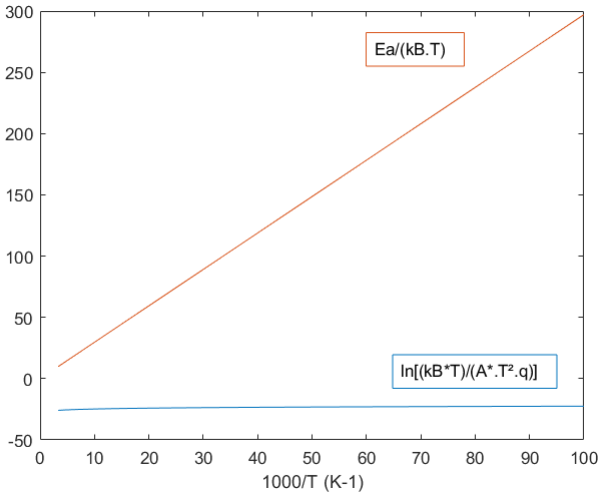

FIGURE 2.5: Numerical estimation of the two contribution in equation 2.19 as a function of 1000/T for $E_a = 250\ meV$ and $m_{eff} = 0.041 m_0$.

2.1.2 Optical Characterization

In addition to the electrical characterization of the QCD, optical characterization are introduced in this section. We will first present the photocurrent and the responsivity of the detector. Then, by giving a detailed presentation of the existing noise in the detector, we will define the detectivity.

Photocurrent and Responsivity

In order to describe the behavior of the detector under illumination, we consider energy levels of the main QW (figure 2.1, 2.2). Due to photon absorption, a photocurrent I^1_{photo} is generated that can be expressed in terms of photon flux as [H. Schneider, 2007, p. 60]:

$$I^1_{photo}(\lambda) = e\phi_\lambda \eta^1 p_e \qquad [A] \tag{2.20}$$

where p_e is the escape probability presented in section 2.1, $\phi_\lambda = \frac{P_{in,\lambda}\lambda}{hc}[s^{-1}]$ is the incident photon number per unit time, $P_{in,\lambda}[W]$ the incident power at wavelength λ. η^1 is the absorption quantum efficiency of one main quantum well. The total absorption quantum efficiency of the QCD with N periods is $\eta = N\eta^1$. It is defined as the number of photoelectrons (N_e) absorbed over the number of incident photons (N_p) [Graf, 2006, p. 14], [A. rostami, 2011, p. 102].

$$\eta = \frac{N_e}{N_p} \tag{2.21}$$

The total photocurrent of the structure is the photocurrent of one period over the capture probability;

$$I_{photo}(\lambda) = \frac{I^1_{ph}(\lambda)}{p_c} = e\phi_\lambda \eta g_{photo} \qquad [A] \tag{2.22}$$

with $g_{photo} = \frac{p_e}{N p_c}$ the photovoltaic gain of the QCD.

We then introduce the responsivity $\mathcal{R}$[A/W] that corresponds to the measured photocurrent over the incident power on the detector.

This depends upon the active area of the detector, the detection field of view (FOV) and the wavelength.

From equation 2.20 the spectral current responsivity is written as:

$$\mathcal{R}(\lambda) = \frac{I_{photo}(\lambda)}{P_{in,\lambda}} = \frac{\lambda e}{hc}\eta g_{photo} \qquad [A/W] \tag{2.23}$$

It is worth mentioning that the responsivity is independent of the detector active area. It is only related to the material composition and electronic structure of the device as reported in ref [H. Schneider, 2007]. The absorption quantum efficiency η, at first order of approximation, depends linearly on the number of periods (cf figure 2.6 top). As the gain g_{photo} is inversely proportional to N thus the responsivity is independent of the number of periods (cf figure 2.6 bottom). After a certain value of N (nearly for $N = 10$) the responsivity starts to decrease with N. This is due to the decrease of overlap of the electromagnetic field within the whole structure [A. Gomez, 2008].

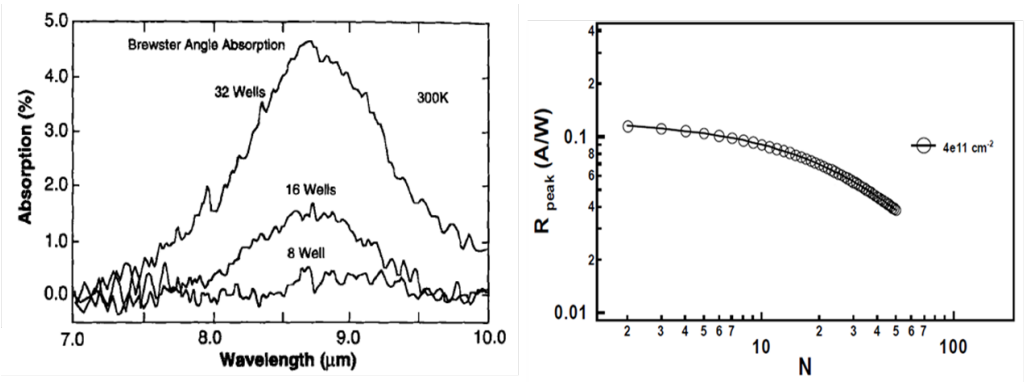

FIGURE 2.6: Absorption spectra for different number of periods N (left)(ref: [H. C. Liu, 2000, p. 156]) and responsivity as a function of N for a given doping concentration (right)(ref: [A. Gomez, 2008])

Noise current and Detectivity

The limiting factor of the performances of a photodetector is the noise contribution to measured current. QCD is submitted to three different type of noises: the $1/f$ noise, the shot noise and the Johnson-Nyquist noise.

- In electronics, "white noise" corresponds to a noise with flat response in frequency. The **1/f** noise is intrinsic to most of the electronic processes and devices and can overcome the "white noise" at low frequency.

- The **shot noise** is a quantum noise effect, related to the wave-particle duality phenomenon. It defines the generation and recombination of electrons. The spectral density associated to the current noise is written $S_{ST} = uqg_{noise}I_{tot}$ with I_{tot} the total current, $g_{noise} = \frac{1}{Np_c}$ the noise gain, q the electronic charge and u a constant value that is equal to 4 for generation and recombination noise (photodetectors). The noise spectral density is by definition the noise power per unit of bandwidth (Δf). The total shot noise current is defined as the sum of two different currents

noise: a dark current noise and a photon current noise $I_{tot} = I_{dark} + I_{photo}$. They correspond to the variation of electrons number caused by thermionic emission (I_{dark}) and photogeneration (I_{photo}) processes. In the infrared region, photodetectors always detect photons coming from the room temperature background. The photo current noise ($I_{photo} \equiv I_{300K}$) in the case of IR detector is defined as the background noise.

- The **Johnson-Nyquist noise** is also known as the thermal noise of the photodetector. The Johnson noise is the noise related to the thermal agitation of the carrier inside a device at thermodynamic equilibrium. This noise depends only on the temperature (T) and the resistance (R) of the device. It has been demonstrated in the 1928 by Johnson and Nyquist, hence the denomination. This current has it source in the transition between the ground state of the main quantum well and an energy level of the cascade. The corresponding spectral density is expressed as $S_I = 4k_BT/R$.

The total current noise of the photodetector is then expressed as:

$$i_N = \sqrt{(S_I + S_{ST})\Delta f} = \sqrt{(\frac{4k_BT}{R} + 4eg_{noise}(I_{dark} + I_{300K}))\Delta f} \qquad [A] \tag{2.24}$$

Since we are in the approximation of $p_c = 1$ and $p_e = 1$:

$$g_{photo} = \frac{p_e}{Np_c} \approx g_{noise} = \frac{1}{Np_c} \approx \frac{1}{N} = g \tag{2.25}$$

So we define a unique gain "g" for the detector.

The noise power of the photodetector, can be deduced by dividing the current noise (equation 2.24)by the detector responsivity:

$$P_N = \frac{i_N}{\mathcal{R}} \qquad [W] \tag{2.26}$$

The noise equivalent power (NEP) is by definition the power that gives a signal over noise ratio of one for a bandwidth of $1Hz$. It is equal to:

$$NEP = \frac{P_N}{\sqrt{\Delta f}} = \frac{i_N}{\mathcal{R}\sqrt{\Delta f}} \qquad [W/\sqrt{Hz}] \tag{2.27}$$

From equation 2.27 we can see that the NEP corresponds to the noise spectral density divided by the detector responsivity.

The detectivity D^* is then derived from equation 2.27 and it corresponds to the square root of the active area (A) divided by the NEP :

$$D^* = \frac{\sqrt{A}}{NEP} = \frac{\mathcal{R}\sqrt{A}\sqrt{\Delta f}}{i_N} \qquad [cm\sqrt{Hz}/W] \tag{2.28}$$

Inserting equation 2.24 into equation 2.28 we obtain:

$$D^*(T) = \frac{\mathcal{R}}{\sqrt{4k_BT/R + 4eg(I_{dark} + I_{300K})}}\sqrt{A} \qquad [cm\sqrt{Hz}/W] \tag{2.29}$$

From 2.29, the detectivity of the QCD is its responsivity divided by the noise normalized by the surface of the QCD for a bandwidth of $\Delta f = 1\ Hz$. The detectivity is expressed in $cm.\sqrt{Hz}/W$ also known as Jones.

As photovoltaic detectors work at thermodynamic equilibrium, it is interesting to introduce D_0^* that corresponds to the specific detectivity of the detector at 0 V. In that configuration, the dark current (I_{dark}) can be neglected respect to I_{photo}. Thus, R_0 will be extracted from the background current measurement only and the total photocurrent will be $I_{tot} = I_{300K}$. So, within these approximation, the detectivity is simply equal to :

$$D_0^*(T) = \frac{\mathcal{R}_0}{\sqrt{4k_BT/R_0 + 4egI_{300K}}}\sqrt{A} \qquad [cm\sqrt{Hz}/W] \tag{2.30}$$

As said before the Johnson noise is strongly temperature dependent. In a first approximation of equation 2.22, the photocurrent does not depend on the temperature. So the temperature dependency of the detectivity is mainly coming from the Johnson noise. A critical temperature is then defined where the background noise starts to overcome the thermal noise. This value of the temperature is called the **B**ackground **L**imited **I**nfrared **P**erformances (**BLIP**) temperature.

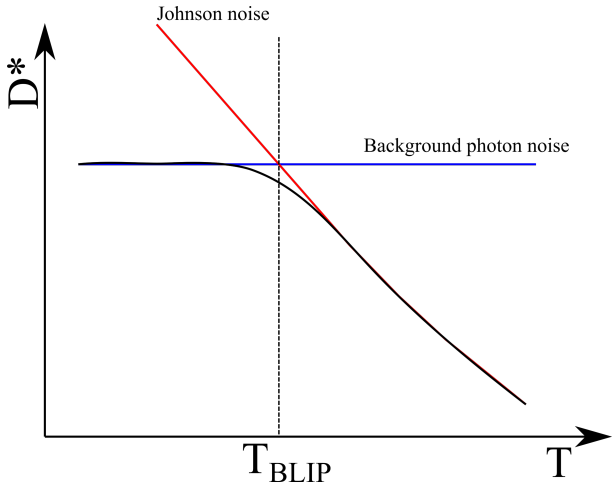

FIGURE 2.7: Specific detectivity (black), specific detectivity with the Johnson noise only (red) and specific detectivity with background noise contribution only (blue) as a function of temperature. The temperature at which the blue and the red curves cross is the BLIP temperature.

At temperature below the BLIP temperature, the detectivity is limited by the photon noise coming from the background. In other words, cooling down the detector below the BLIP value is useless as the detectivity will remain constant. In this region, the detectivity is then expressed as:

$$D_0^*(T < T_{BLIP}) = \frac{\mathcal{R}}{\sqrt{4egI_{300K}}}\sqrt{A} = \frac{\sqrt{\mathcal{R}}}{\sqrt{4eg\phi_{300K}\frac{hc}{\lambda}}} \qquad [cm\sqrt{Hz}/W] \tag{2.31}$$

with ϕ_{300K} the photon flux at 300 K (300 K background). Equation 2.31 is constant for different temperatures and is represented by the blue curve in figure 2.7.

After the BLIP, the current noise is mainly Johnson noise and hence a rapid decrease of the detectivity. In this regime, the detectivity can be written as:

$$D_0^*(T > T_{BLIP}) = \frac{\mathcal{R}}{\sqrt{4k_BT/R}}\sqrt{A} \qquad [cm\sqrt{Hz}/W] \tag{2.32}$$

represented by the red curve in the figure 2.7.

The BLIP temperature is an important parameter for photodetectors. A higher BLIP temperature reduces the use of cryogenic systems for the photodetector operation which are costly systems.

We want to point out that since the photocurrent depends on the detector field of view (FOV), the detectivity is also a function of the set up geometry. The detectivity becomes:

$$D^*(T,\theta) = \frac{D^*(T,2\pi)}{sin(\theta)} \qquad [cm\sqrt{Hz}/W] \tag{2.33}$$

where θ is the acceptance angle of the detector.

2.1.3 QCD working at 4.9 μm and RT

In the following, the heterostructure design of the sample studied during this thesis is presented. The growth sheet is presented in the appendix A.1.

In previous paragraph we identified the principle parameters governing the QCD performances. This analysis is well summarized in the detectivity formula 2.30.

To design a detector with a high detectivity we have to engineer quantum structure in order to have high quantum absorption efficiency (η) and high escape probability (p_e) to efficiently tunnel from the main well to the cascade region. At the same time this value controls the device resistance that is directly proportional to the detectivity in term of noise reduction. According to the formula 2.7, the resistance of the device is mainly due to intercascade transition rate Gij. Being able to decrease theses transitions rates, will help to increase the resistance so to reduce the noise which is important for the performances of the photodetector (section 2.1.2). However, decreasing too much the transition rate will reduce the optical response of the photodetector. A compromise between these two trends has to be found in QCD design in order to optimize its performances.

The QCD that have been studied during this PhD is a III-V ternary heterostruture made of $GaInAs$ quantum wells sandwiched between $AlInAs$ barriers. The growth has been done using molecular beam epitaxy (MBE) at III-V Lab. The design of the structure is from A.Delga and the growth has been realized by A. Evirgen. The simulated band diagram structure is shown in figure 2.8. It has been calculated using the home made software of our group presented in the introduction. Each period is named by a letter. The numbers correspond to each energy level in ascending order. The QCD studied in this work has 20 periods ($N = 20$).

The energy separations between neighbor levels in the cascade region is close to the $InGaAs$ phonon energy which is equal to 34 meV at room temperature [Yu.A. and Schmidt, 1999]. It deviates from the nominal value of ≈ 3 meV in order to have the cascade alignment under small bias. Even though QCDs are photovoltaic detectors and have this interesting property to operate at null bias, when they are inserted in an electrical circuit, they are slightly exposed to a bias. This bias is not stable and can influence the performances of the detector. Thus, it is more interesting, for an application point of view, to design the QCD in order to have a maximum photocurrent at a fixed bias that can be tuned.

From the band structure (see figure 2.8) we expect main absorption of the QCD from level 1B to 9C by an optical transition. Depending on the doping and the operating temperature, level 2B can be populated and photoelectrons can be created from 2B to 11C transition. Thanks to the designed barrier width, diagonal transitions are limited.

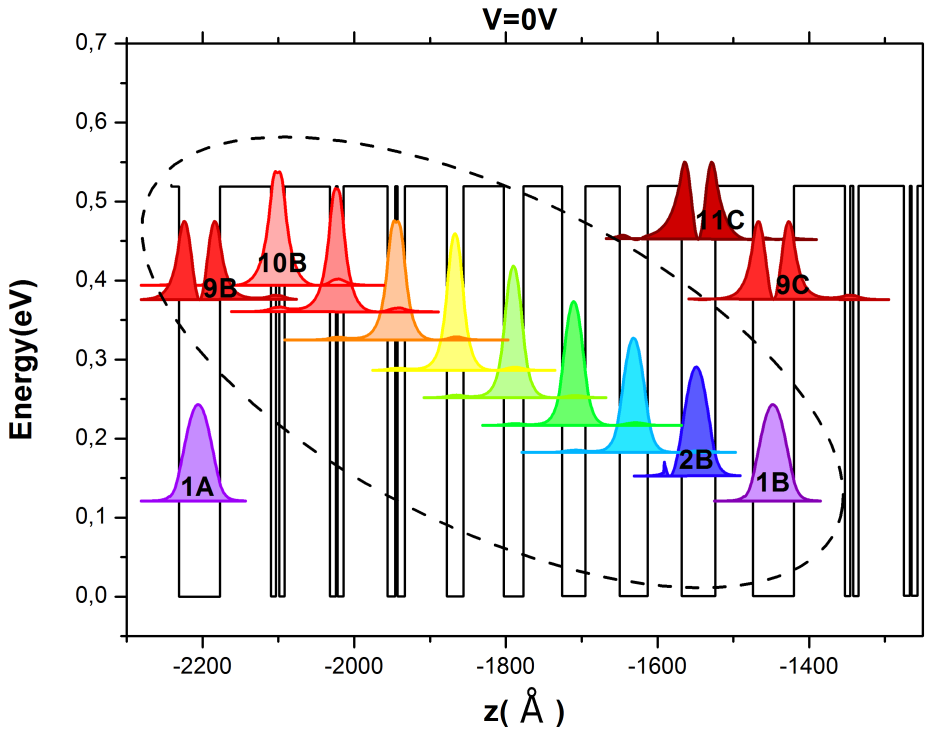

FIGURE 2.8: Simulated band diagram corresponding to the design growth (at $V = 0\ V$). The different energy levels of the conduction band are named with the letter corresponding to the cascade and the number corresponding to the energy level within the cascade with the lower number corresponding to the energy level with lower energy. The dashed circle surround one period (period B in this scheme).

From the nominal values of the QCD geometry, we can estimate the activation energy at 0 V (equation 2.4) where E_F is (equation 2.5) :

$$E_F = \frac{10^{18}\pi\hbar^2 30.10^{-10}}{0.04 * m_e}.1000 = 17.48meV \tag{2.34}$$

$$E_a = \frac{\pi\hbar^2}{0.04 * m_e}\left(\frac{3}{2(30.10^{-10})^2} - 10^{18}30.10^{-10}\right).1000 = 260meV \tag{2.35}$$

with $m_e = 0.5110\ MeV/c^2$ the electron rest mass. The well is $L_w = 30$Å wide and it is doped at $n_D = 10^{18}\ cm^{-3}$. This value is in agreement with the energy separation of E_{1A} to E_{9B} calculated in figure 2.8. The escape probability of our structure is estimated at 0.7.

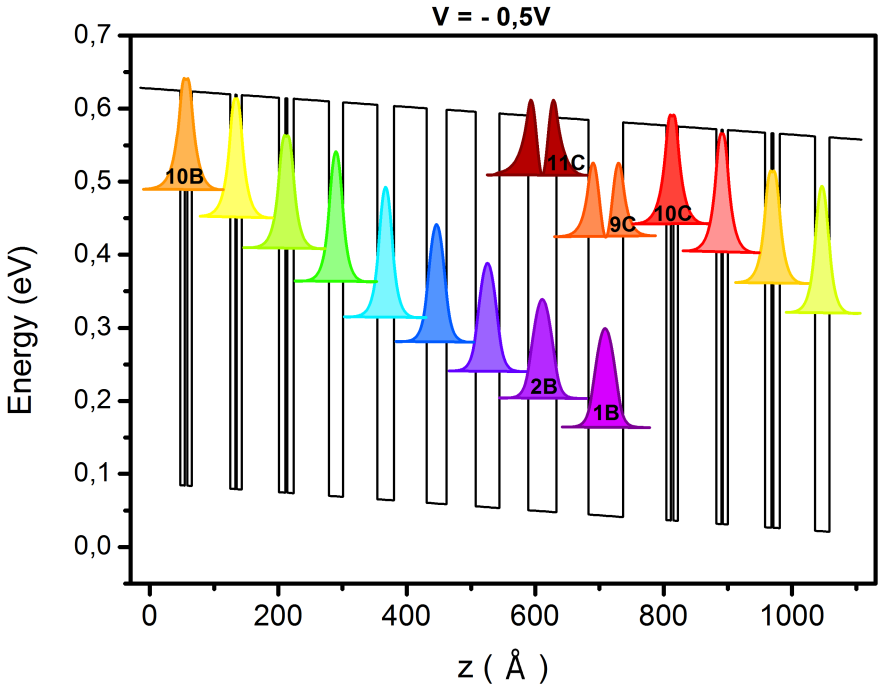

FIGURE 2.9: Band diagram of one period with an applied negative bias of -0.5V

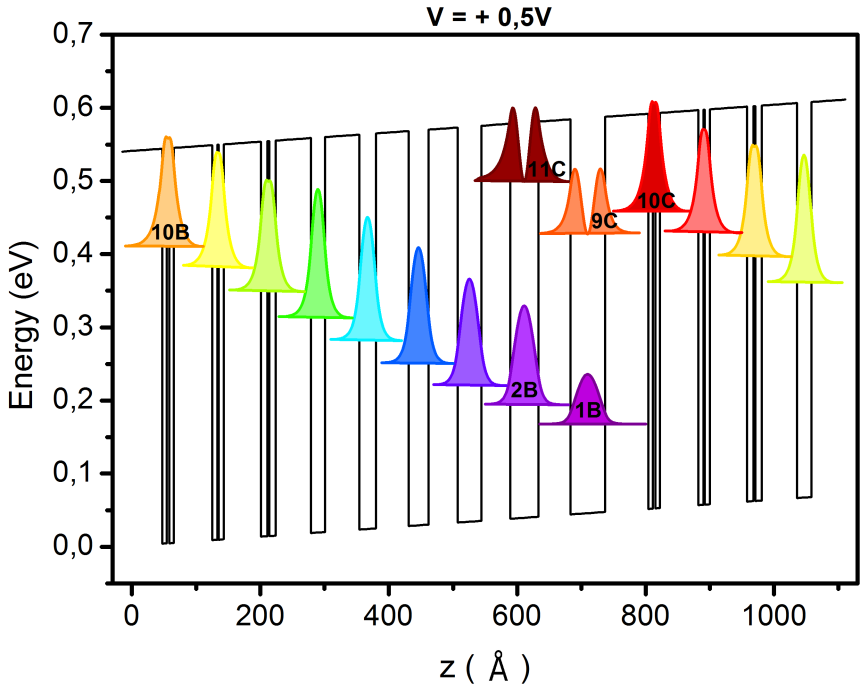

FIGURE 2.10: Band diagram of one period with an applied positive bias of +0.5V

In order to have a wider insight on the characteristics of the QCD, we study the energy levels alignments for different applied bias.

In figure 2.9 we present the band structure of a nominal negative bias of $-0.5\ V$.

The applied field drives electrons through the cascade structure and it facilitates the photocurrent collection. In this case the energy difference between the levels of the cascade region increases proportionally to the applied field. The optical transition in the main QW stays confined and does not suffer from the appearance of leakage channels to the continuum. At negative bias, the population of 2B level decreases and as a consequence the optical transition 2B-11C is less favorable compared to the 0 bias operation.

On the other side when a positive bias is applied on the structure (figure 2.10) the cascade levels approach and they can eventually merge in a sort of energy miniband. Electrons ascend the cascade under the influence of the field independently of the incident photons. The photocurrent coming from the absorption in the main well and electronic transition in the cascade is opposite to the thermal generated current. At strong positive field a parallel channel for photon detection can be observed. 11C level starts to leak in the continuum and photocurrent can be generated by 2B-11C absorption without any interaction with the cascade.

2.2 Experimental characterization of QCD

In this paragraph we present electrical and optical study of the QCD design developed in this thesis. We will first explain in details the fabrication process of the sample, needed to perform the characterizations. We then present the measurement setups and discuss the experimental results for electrical and optical measurements respectively in paragraph 2.2.2 and 2.2.3.

2.2.1 Fabrication Process

In this paragraph we present the main steps of the fabrication process of the QCD devices. The QCD has been completely processed in the clean room of MPQ Laboratory at Paris Diderot University.

Figure 2.11 shows the step by step clean room fabrication process of the sample:

- **Top ohmic contact**
  - *Lithography* First of all, S1805 resist is spin coated on the surface of the growth after the surface being cleaned by acetone followed by isopropanol. S1805 is a positive photoresist and has a thickness of 500 nm at standard spin speed (5000 RPM). We use a mask in order to illuminate the surface that we want to be exposed to the ultra violet (UV) light. Indeed, as the photoresist is positive, an exposition to UV light will wipe away the resist at the development step. The remaining part of the photoresist that has not been exposed will stay on the surface. The behavior will be reversed if the photoresist is negative. The mask is designed using L-Edit software. Its pattern includes circles with varying diameter from 40 μm to 190 μm. After the development with MF-319 solution, the sample is put inside a high vacuum chamber for metal evaporation.

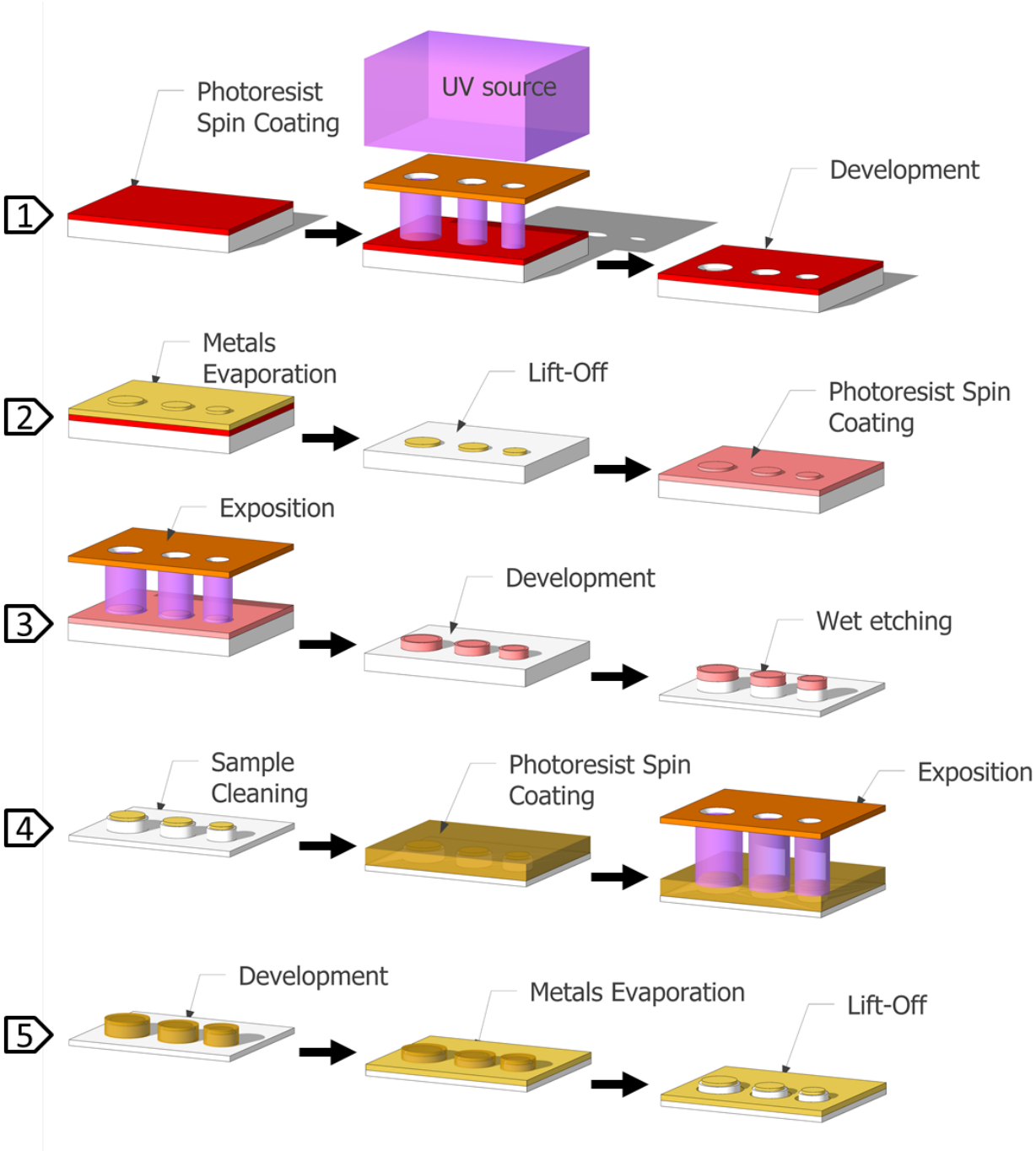

Figure 2.11: Steps of clean room fabrication of the sample.

- *Metal evaporation* High vacuum evaporator Plassys (MEB550S model) based on electron gun for the metal evaporation has been used. Metals evaporated for the top ohmic contact are Ge/Au/Ni/Au with thickness of respectively 15/50/20/200 nm.
- *Lift-off* After the evaporation, a lift-off process is done in order to remove the metals where there is resist remaining underneath. This process is done by dipping the sample into heated acetone (50°C). After few minutes the resist peel off from the surface, removing with it the metals.

- **Mesa wet etching** Wet etching process is performed in order to etch the whole active region down to the bottom contact. S1805 photoresist is spin coated on the surface. The mask pattern is a series of circles with diameter of 10 μm larger than the top contact. After the development, the sample is dipped into a solution for the wet etching.

  At this step we study three different solutions.

  - **$HBr/HNO_3/H_2O$ − 1 : 1 : 10** : As our contacts are composed of aluminum and indium, we have first made an etching solution using HBr and HNO_3 as they are good etchant for these elements [Perrin Walker, 1991]. To do that we have used two different approach for the wet etching: fixing the sample and using a magnetic rotator in the solution or moving the sample gently by hand in the solution without using a magnetic rotator.

    With the magnetic rotator we should obtain an homogeneous etching over the whole surface of the sample. We have performed two different rotations. One with the rotator turning in one direction only and the other one alternating the rotation direction.
    Using the rotation for one minute in only one direction, removes the photoresist in one side of the sample even though this is supposed to be resistant to these etching acids.
    Alternate rotation in clockwise and anticlockwise direction (with 10sec of rotation in each direction) is performed for an even more homogeneous etching. After one minute, the photoresist is also disappearing, this time, in both side of the sample.
    The etching process using the magnetic rotator is not adapted to our etching conditions. Indeed, regarding the thickness of the photoresist that we use and the amount of materials that we want to etch, the photoresist is etched more rapidly than the growth compounds.

    For the other solution, we use an adapted tweezers to hold the sample which is then dipped into the solution. Using tweezers, the sample is moved gently backward and forward in order to expose continuously the surface to fresh etching. After two minutes and a half of etching, by measuring every 30 s the etching depth with Dektak, the structure is etched down to the bottom contact. Figure 2.12:left shows SEM image of the sample. We can see that the etching is not homogeneous. Indeed, the etch depth is different near the mesa or far from the mesa. We measure a ditch all around the mesa that has a depth of ≈ 500 nm. Unfortunately, with this approach and by etching the sample down to the bottom contact layer all over the surface, we will completely etch the bottom contact layer near the mesa.

– **$HBr/HAce/K_2Cr_2O_7$ $-1:1:1$** : This solution is composed of hydrobromic acid, acetic acid and potassium dichromate in equal proportion. It is named *BCK* and is not selective. The etching was done in the previous configuration using tweezers. This solution has also exhibit a non homogeneous etching. Figure 2.12:right shows cross section of the mesa where we can see the difference in etching depth.

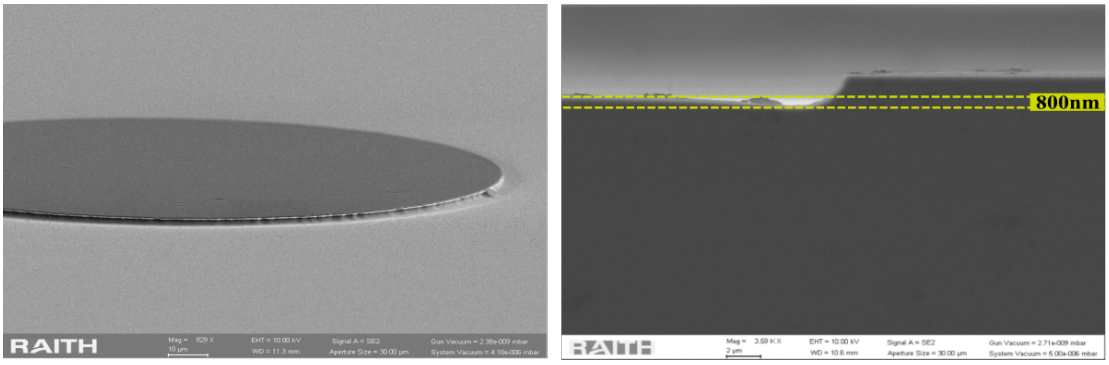

FIGURE 2.12: SEM images of mesa after wet etching using $HBr/HNO_3/H_2O$ as chemical solution on left and $HBr/HAce/K_2Cr_2O_7$ on right. We can see from both image the ditch around the mesa. A ditch with 800 *nm* deep, which is higher than the bottom contact layer thickness is observed.

– **$H_3PO_4/H_2O_2/H_2O$ $-1:1:5$** : The other chemical solution used is composed of $H_3PO_4 : H_2O_2 : H_2O$ with $1:1:5$ proportion. This solution etches non selectively AlInAs and InGaAs. The solution was prepared 4 hours before the etching in order to reach the equilibrium. The sample was hold using an adapted tweezers and moved as explained before in the previous solution. A first 35 *sec* of etching was realized followed by another 45 *sec* where the etching rate was measured by Dektak. A 1500 *nm* depth has been etched. SEM image of the sample shows a flat surface and no ditch is observed near the mesa. Figure 2.13 shows SEM image of the wet etched sample.

After the wet etching, the sample is cleaned with acetone and isopropanol to remove the photoresist.

- **Bottom ohmic contact** Last step is to evaporate the ohmic contact for the bottom electrode. For that we do again the steps for photoresist coating, but this time we use a thicker resist in order to completely cover the mesa that we have just etched. The photoresist used for this part is $S1828$ with 2.8 μm thick at 5000 RPM. The mask used for the lithography includes circles with diameter of 60 μm to 210 μm, 10 μm larger than mesa's diameter in order to avoid short circuit between top and bottom contact. We evaporate Ge/Au/Ni/Au as for the top contact.

- **Top and bottom contact annealing** In order to reduce the contact resistance we perform thermal annealing. The used oven for the annealing is a rapid thermal annealing (RTA) oven from SSI (SOLARIS 75 model) that is efficient at reaching rapidly the wanted temperature and being a good temperature

FIGURE 2.13: SEM image of the QCD after wet etching with H_3PO_4 : H_2O_2 : H_2O.

stabilizer during the annealing process. Our sample is annealed at 420°C for one minute (*ICOM 2012*).

- **Electrical contacts** For electrical measurements, after the annealing, the sample is taken out from the clean room and both top and bottom contacts are connected to adjacent conductive pads through gold wires (25 μm thick). We connect then the different power supply and measurements instruments to the pads via standard cables.

- **Mounting for optical measurements** For optical measurements, before bonding the sample to gold wires, we need to ensure the light matter coupling within the mesas. As seen in section 1.2.3 in Introduction, the optical intersubband transition is induced only by light polarized in the direction of quantum wells growth. In order to satisfy this selection rule, we mechanically polish one side of the sample at 45°. Photons come from the mirror polished 45° facet to the mesa. Figure 2.14 presents a sketch of the geometry of the sample used for the optical measurements.

2.2.2 Electrical characterization

Current-voltage (I-V) measurements are key measurements of a photodetector. In this section, we performed I-V measurements in two different conditions: without any illumination (dark current) or with background illumination (background current). We used the generator in bias mode and measured flowing current. From these results, we can study the detector noise and responsivity, and estimate the activation energy and the R_0 of the device.

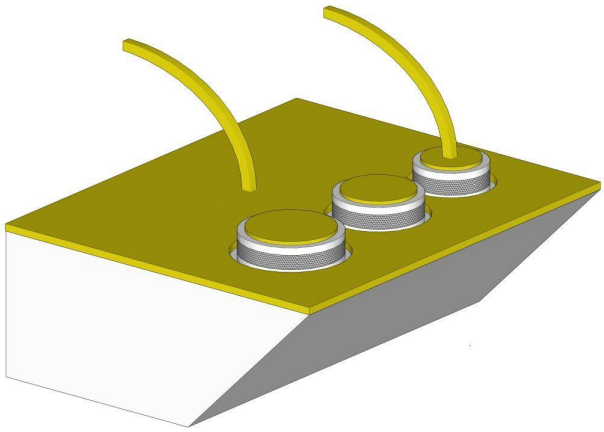

FIGURE 2.14: Geometry of the sample for optical measurements with a mechanical 45° mirror polishing. The darker part in the mesa represents the active region of the structure. The yellow arcs represent the gold wires bounded to both the top and bottom ohmic contacts.

Dark and background current

In order to measure the dark current, the sample is mounted on a copper submount using indium paste (99% of Indium). The submount is connected to a cold finger of a cryostat in order to perform temperature sweeps. The cryostat model used for all the temperature measurements is Janis ST-300. An additional chamber is added to the cryostat called cryo-shield where a temperature sensor is placed. This shield screens the environment background radiation and its temperature can be the same as the one of the sample.

Figure 2.15 shows the dark current of a 200 μm diameter square mesa as a function of the applied external bias for different values of the temperature.

The dark current increases exponentially with temperature following the equation 2.11 (see inset of figure 2.15)

A quasi constant current flows in the QCD at negative bias whereas at positive bias, the current increases rapidly corresponding to the forward bias regime (see figure 2.15). The asymmetric behavior of I-V curve is related to the electronic band structure as discussed in section 2.1.3.

In real application, a blackbody radiation is incident on the detector and the current flowing is higher than in dark condition. The signal represents the background current, one of the principle noise source in detection (as explained in paragraph 2.1.2). For background characterization, the current as a function of the applied bias is measured without the cryo-shield. The QCD is detecting the room temperature background radiation. The field of view in this setup is equal to 70°. Figure 2.16 shows the current density of a 200 μm diameter mesa measured as a function of the external applied bias for different temperatures.

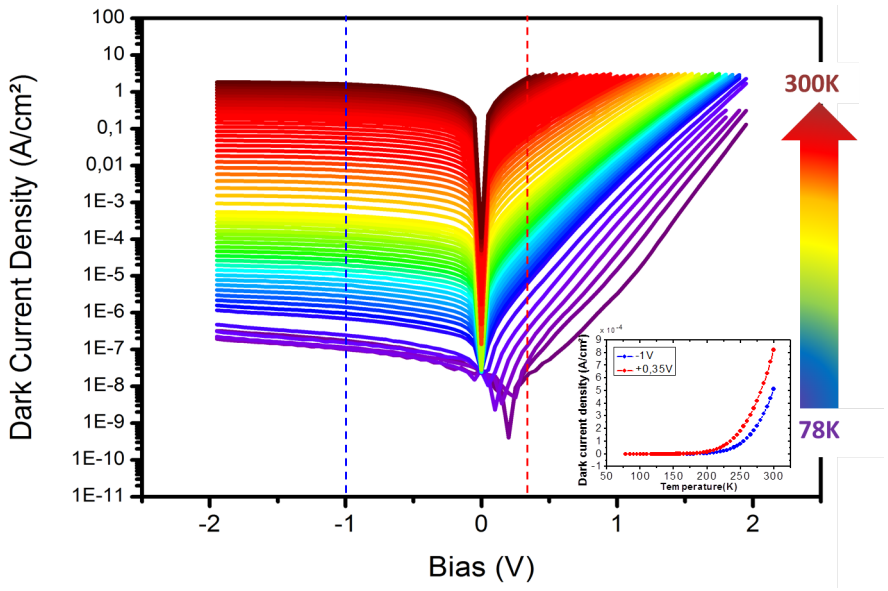

FIGURE 2.15: Measured dark current density of a circular mesa of 200 μm diameter as a function of the bias for temperature from 78 K to 300 K. inset: Dark current density as a function of temperature at -1 V and $+0.35$ V respectively in blue and red.

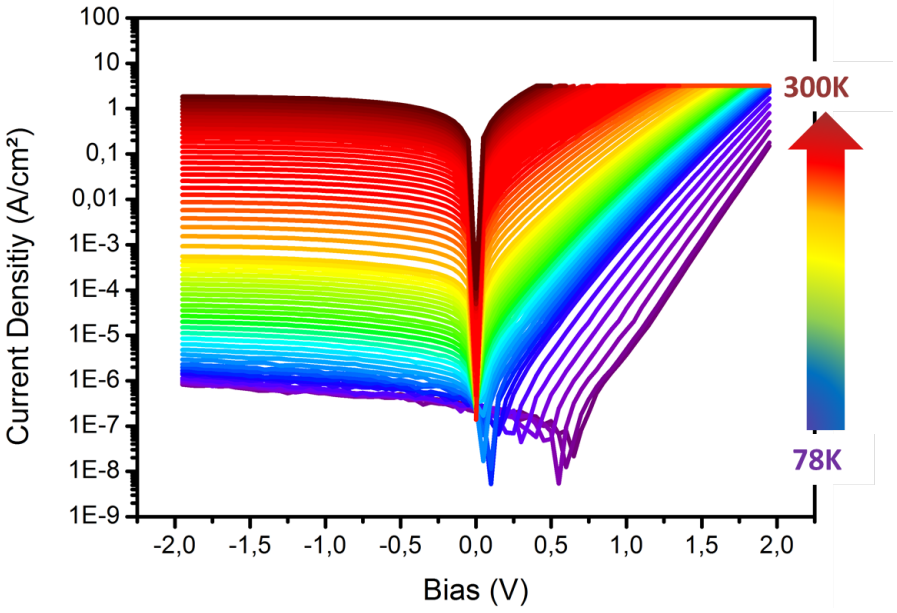

FIGURE 2.16: Background (room temperature) current density of a 200 μm diameter mesa as a function of the applied bias for temperature from 78 K up to room temperature with a $FOV = 70°$.

Compared to dark current measurements (figure 2.15), the values of the current flowing inside the detector is much higher in background conditions. This effect comes from the contribution on the photocurrent of background photons (see figure 2.4b) and equation 2.12).

In figure 2.17, we present comparison of the background performances of different sizes of QCD. We report current density of 3 different devices for 78 K, 100 K,

150 K, 200 K and 300 K. As expected similar characteristics are reported for the the 3 devices demonstrating the quality of fabrication process and epitaxial growth of the QCD. Small fluctuations in the current density values are inferred to the error bar in measuring geometrical dimensions of the detector.

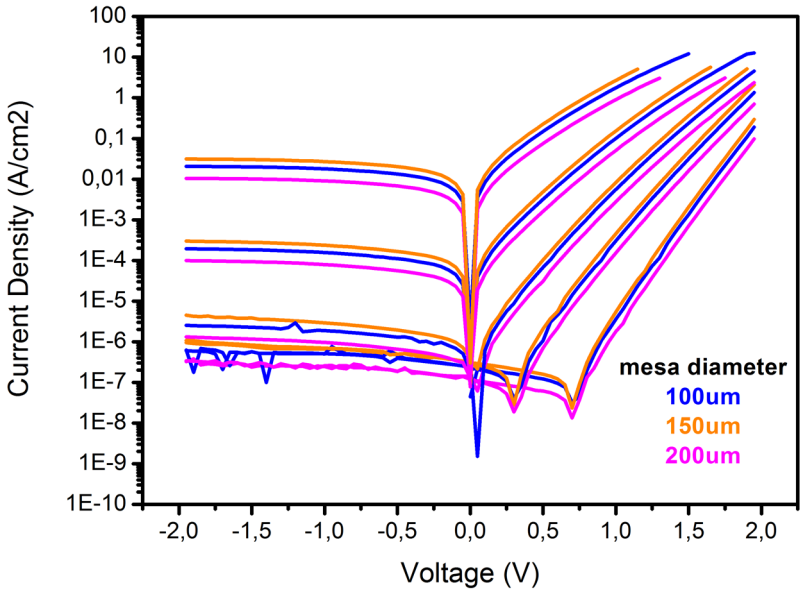

FIGURE 2.17: Measured background (room temperature) current density of samples with mesa diameter of 100 μm, 150 μm and 200 μm as a function of the applied bias for temperature from different temperatures with a $FOV = 70°$.

For the three devices we notice that the transition from positive to negative photocurrent does not occur at zero bias but at an operating voltage known as the open circuit bias (V_{OC})

If we look at figures 2.16 and 2.17, we see that V_{OC} changes with temperature. Figure 2.18 presents this shift as a function of the temperature for different size of mesa.

In analogy with the photodiode model of the QCD, we can express the V_{OC} voltage (equation 2.12 when $I_{tot} = 0$) as:

$$V_{OC} = \frac{k_B T}{q} ln(1 + \frac{I_{photo}}{AA^* T^2} exp(\frac{E_a}{k_B T})) \tag{2.36}$$

From equation 2.36, we can report a strong influence of the incident power on the V_{oc} value. This is well known in solar cells study [Garcia-Belmonte, 2010].

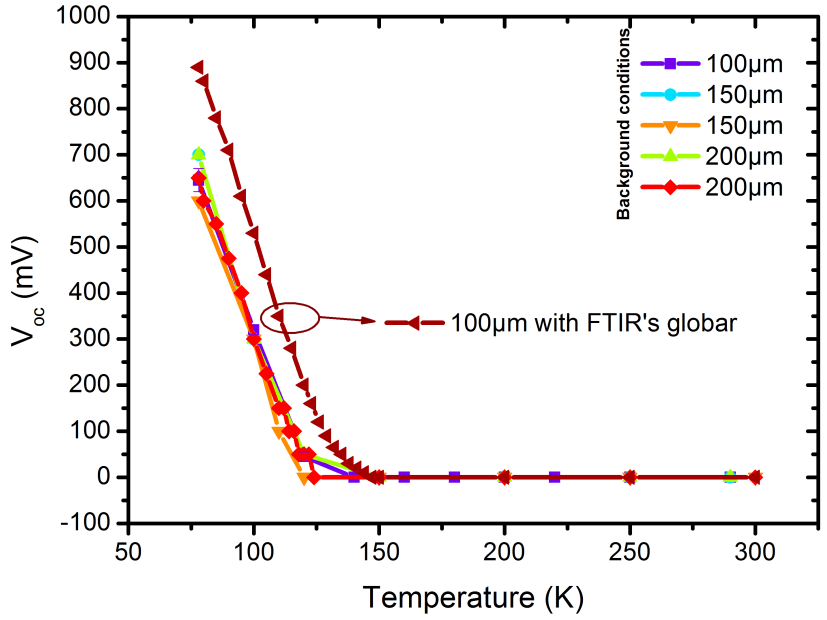

FIGURE 2.18: Estimated V_{OC} as a function of the temperature for different mesa sizes in background condition.The graph with triangles is for a QCD with 100 μm illuminated by the globar source of a FTIR.

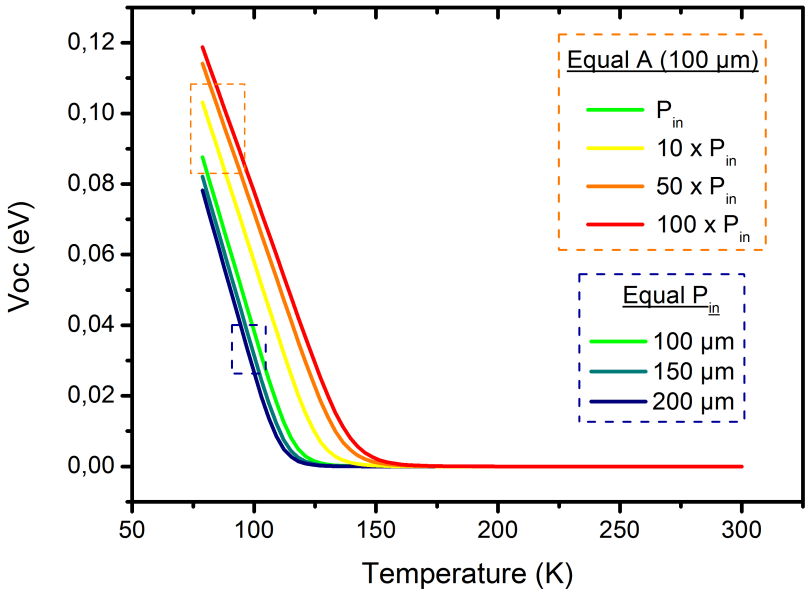

FIGURE 2.19: Estimated V_{OC} as a function of the temperature for different size of mesa in background condition and different incident power (respectively 10, 50 and 100 times the initial incident power (background)).

From equation 2.36 and Figure 2.19, we identify two different regimes.

- The first regime corresponds to temperatures above a certain $\tilde{T}$, where $\frac{I_{photo}}{AA^*T^2} exp(\frac{E_a}{q}) \ll 1$ or in other word when $I_{photo} \ll I_{sat}$ (I_{sat} in equation 2.9). In this case, where

$I_{photo} = I_{300K}$, the estimated V_{OC} is equal to zero since the 300 K background induced photocurrent is less than dark current (I_{sat}).

- In the second regime, where $T \ll \tilde{T}$, V_{OC} can be simplified as:

$$V_{OC} = \frac{k_B T}{q}(ln(\frac{I_{photo}}{AA^* T^2}) + \frac{E_a}{k_B T}) \tag{2.37}$$

We notice by our V_{OC} estimation in graph 2.19 a linear dependency of the bias with temperature as it is also measured experimentally (see figure 2.18). In the same regime, for increasing incident power, so increasing photocurrent (see equation 2.20) V_{OC} varies as a logarithm, $V_{OC} \approx log(I_{photo})$. Indeed, in figure 2.18 we can see an increase of V_{OC} by illuminating the detector using the FTIR globar (a source at a temperature around 1300K) instead of a 300 K background. We present in figure 2.19 the calculated variation of V_{OC} for different amount of incident power.

The $\tilde{T}$ temperature, with 300 K background illumination, corresponds to the condition where the background photocurrent is equal to the limiting dark current ($I_{300K} = I_{sat}$). In this approach, we can then identify $\tilde{T}$ as the T_{BLIP} of the detector (presented in section 2.1.2). Since the V_{OC} estimated for different device overlap we deduce that, as expected, the T_{BLIP} is not dependent on the geometrical structure of the QCD but only on the band structure and background conditions. From the graph 2.18, we can estimate from all the different mesa size an average temperature equal to $\tilde{T} = (130 \pm 5)\ K$.

Device resistance and activation energy

From experimental measurements we estimate the differential resistance of the device and its activation energy. In order to study noise performances of the detector, we exploit background current measurements (equation 2.30).

Figure 2.20 shows the differential resistance of the 200 μm QCD in log scale at different temperatures extracted from background current measurements (figure 2.16).

Figure 2.21 shows R_0A as a function of $1000/T$ extracted from figure 2.15 at $V = 0$.

From this curve and using equation 2.19 the activation energy of the structure can be deduced: $E_a = 243\ meV$. It corresponds to the lowest energy separation necessary to generate a thermal current through the detector. In figure 2.8, it coincides with the difference in energy between the Fermi level E_F and level E_{9B}, the main optical transition.

As we are interested into the evolution of the activation energy with the bias, we use the same approach at different operating voltage and results are reported in Figure 2.22.

The peak value of 262 meV in the activation energy is reached at $-0.4\ V$. This value corresponds to the transition between E_{1B} and E_{9C} at a bias where our extraction levels are resonant with phonon energy.

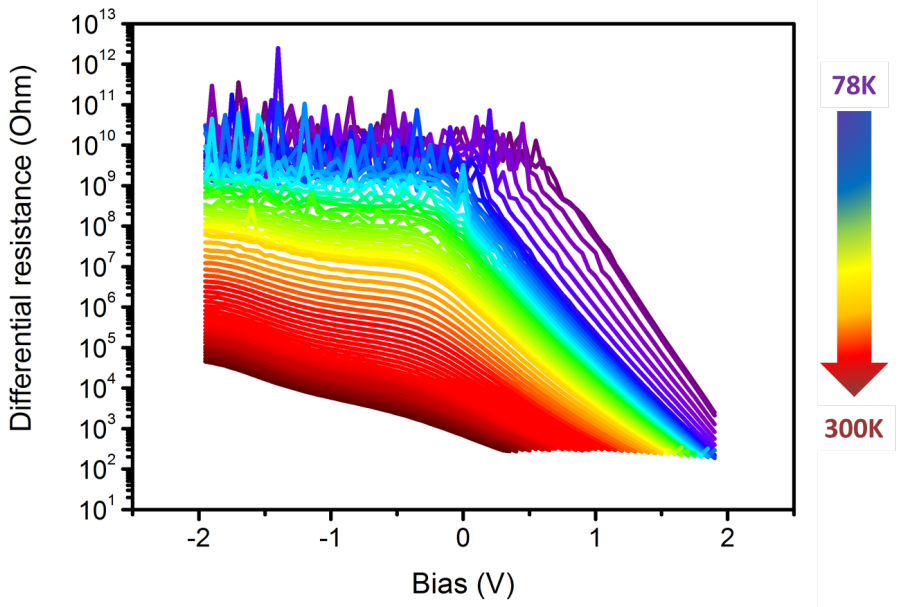

FIGURE 2.20: Measured differential resistance as a function of the bias for temperatures from 78K up up to 300K

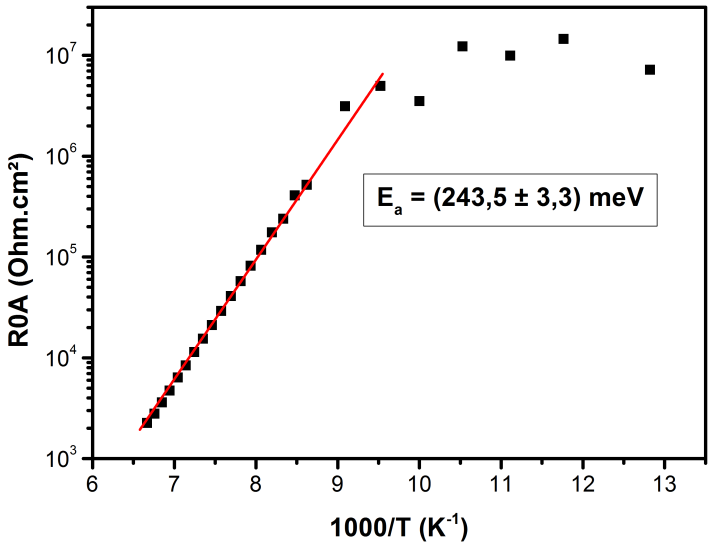

FIGURE 2.21: Resistance at 0 applied bias times the mesa surface as a function of 1000/T. Linear fit in red

This value stays almost constant at negative applied bias reaching a minimum value of 256 meV at -2 V. As presented in section 2.1.3 at negative voltage, the distance between the cascade levels increases and the lowest energy needed for the electron transition is the main well optical transition and it stays almost constant. Figure 2.23a) shows schematically the value of the activation energy when a negative bias is applied to the structure. For stronger applied field the probability of diagonal transitions can increase and as consequence reduce slightly the expected value of the activation energy.

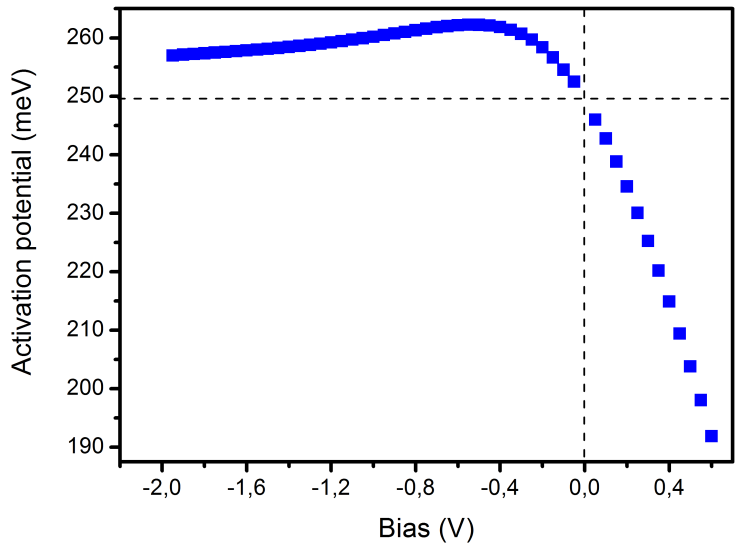

FIGURE 2.22: Estimated activation energy of QCD as a function of different applied bias extracted from dark current I-V curves (Figure 2.15).

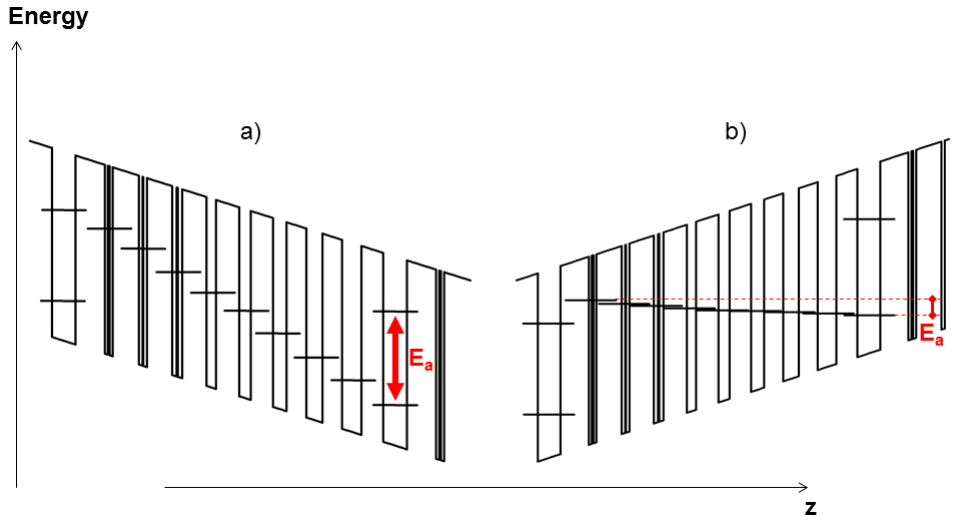

FIGURE 2.23: Band diagram of one period of a QCD with an applied bias of a)$-0.3\ V$ and b)$+0.3\ V$. The horizontal lines correspond to the energy levels. The activation energy is represented in red.

On the contrary, for a positive applied bias, data of figure 2.22 show that the activation energy decreases rapidly with bias reaching the value of 190 meV at 0.5 V. This is in agreement with the band structure presented in figure 2.10. A positive field reduces the distance between the cascade levels so that electrons can generate a current at energies below the main well transitions value. Figure 2.23b) shows schematically the value of the activation energy when a positive bias is applied to the structure.

2.2.3 Optical measurements

In this paragraph we present the response of QCD under illumination. We perform two parallel studies: the first is based on the measurement of the spectral component of the signal with a FTIR setup and the second is the characterization of the photo current under calibrated blackbody illumination.

Spectral study of QCL photocurrent

In order to study spectral properties of QCD we carried photocurrent and absorption measurement. The experimental setup for the spectral measurements is presented in figure 2.24. The QCD is mounted inside an under vacuum cryostat with the 45° facet perpendicular to the incoming radiation. The electrical connection are done with gold wires bonded to the structure (as shown in figure 2.14) and electrical cables soldered in the cryostat. The bias is applied to the QCD thanks to a transimpedance DLPCA-200. The transimpedance amplifier converts the incoming current to voltage with user defined amplification gain. The output bias of the amplifier is connected to the analogical to digital converter (ADC) of the FTIR. By realizing scans in rapid modes, we obtain photocurrent spectra of the device.

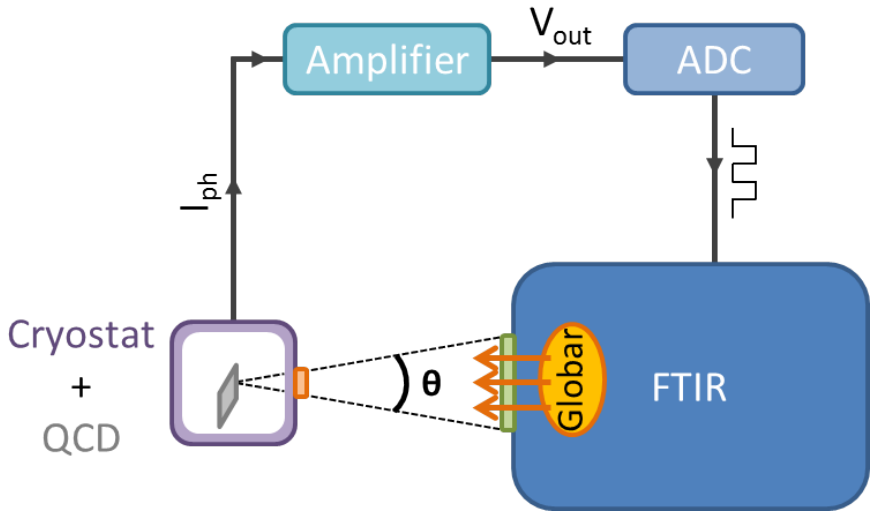

FIGURE 2.24: Experimental setup for the photocurrent measurement using the FTIR rapid scan mode and the transimpedance amplifier. The light coming from the FTIR is focused on the QCD facet thanks to a germanium coated lens. A zinc selenium (Zn:Se) window is fixed in front of the cryostat. θ determines the field of view angle.

Schematically, the equivalent circuit of the setup is shown in figure 2.25 with more details on the transimpedance amplifier.

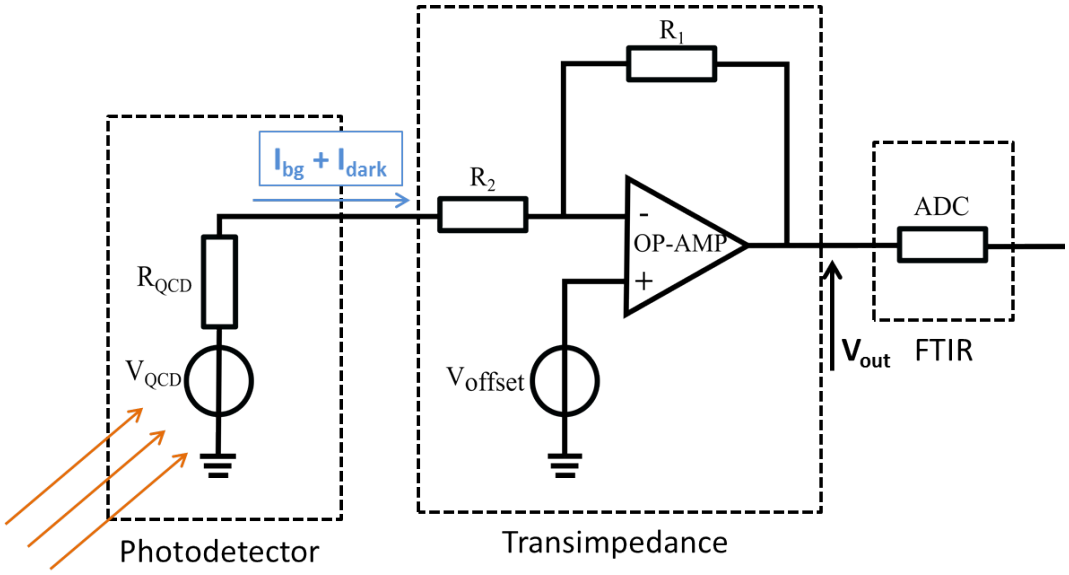

FIGURE 2.25: Scheme of an equivalent circuit of the photocurrent measurement setup with the amplifier.

The bias measured at the output of the transimpedance amplifier (V_{out}) is expressed as:

$$V_{out} = V_{offset} + \frac{V_{offset} - V_{QCD}}{R_2 + R_{QCD}} R_1 \tag{2.38}$$

with R_1 the gain resistance (e.g. $R_1 = 10^5\ \Omega$ for $gain \equiv 5$) and R_2 the input impedance which is equal to 50 Ω for $R_1 = 10^5\Omega$. V_{offset} of the transimpedance amplifier is set manually to a value near 0 V by connecting it with a high input resistance.

At low temperature, the resistance of our device is in the order of $G\Omega$ that is much higher than R_2 ($R_{QCD} \gg R_2$). In this case, the equation 2.38 is rewritten as:

$$V_{out} = V_{offset} + \frac{V_{offset}}{R_{QCD}} R_1 - \frac{V_{QCD}}{R_{QCD}} R_1 \tag{2.39}$$

where $\frac{V_{QCD}}{R_{QCD}}$ is the current flowing inside the QCD I_{QCD} which is amplified by $R1$.

V_{offset} is amplified by R_1 / R_{QCD}. In this configuration, the amplification is really small and negligible (e.g. for $R_{QCD} = 10^9\ \Omega$ and $R_2 = 10^5\ \Omega$, the gain is in the order to 10^{-4}). Thus, the output bias is equal to:

$$V_{out} = V_{offset} - \frac{V_{QCD}}{R_{QCD}} R_1 \tag{2.40}$$

For high temperature measurements, where the resistance of the device starts to decrease and to approach a value close to the resistance R_2, the change of V_{offset} starts to be non negligible. According to the equation 2.38, the amplification factor is $\frac{R_1}{R_2 + R_{QCD}}$.

In our case, at room temperature, the QCD has a typical resistance value of $R_{QCD} = 3\ k\Omega$. Taking the example of a gain of 5, we find that V_{offset} is now multiply by a factor of 34.

These variations have to be taken into account when measuring photocurrent with the transimpedance amplifier.

Figure 2.26 shows the spectra of a 200 μm diameter QCD at 0 V for temperatures in the range between 78 K and 300 K. The spectra were taken in rapid scans, with a resolution of 20 cm^{-1}, and averaged over 1000 scans.

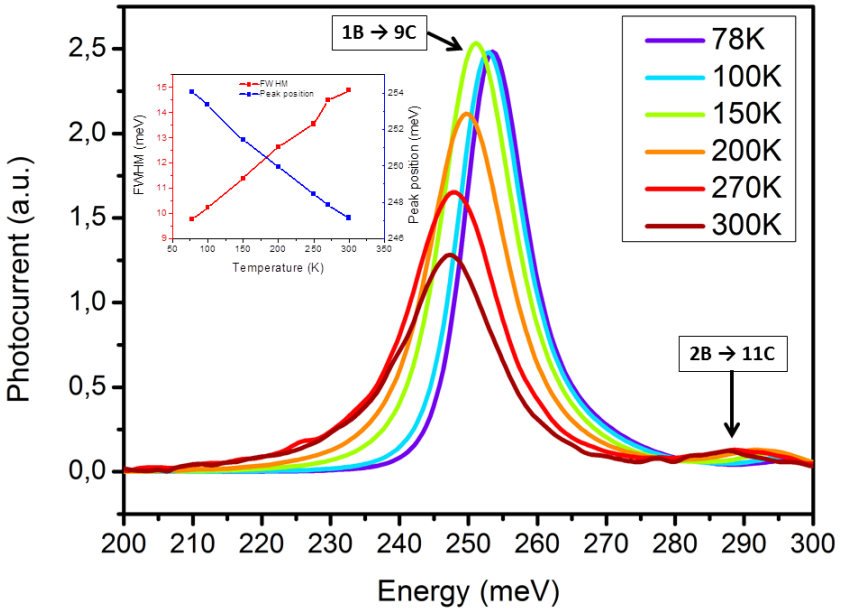

FIGURE 2.26: Measured spectra of a 200 μm diameter circular mesa as a function of the temperature at 0 V. inset: Variation of the peak position (blue) and the broadening (red) of the peaks as a function of the temperature.

The photocurrent peak shifts from 254 meV to 247 meV with temperature going from 77 K to 300 K (see inset Figure 2.26). The full width at half maximum (FWHM) increases with temperature from 9.5 meV to 15 meV in agreement with homogeneous broadening. Values have been obtained by numerical lorentzian fit of the spectra. As presented in the band structure (figure 2.8), at 0 V photocurrent peak corresponds to the energy transition from level $1A \rightarrow 9B$. A second peak is observed at higher energy (290 meV at 300 K) corresponding to vertical transition from level $2B \rightarrow 11C$. The photocurrent corresponding to this second peak is less strong than the main photocurrent peak because the $2B$ level has lower electron density compare to $1B$ energy level. Moreover, the photoelectron at $9C$ is better coupled with energy levels in the cascade region than photoelectron at level $11C$.

In order to have insight in the performances of the device, spectra as function of the bias are measured. To do that, the mounted QCD in the cryostat has been cooled down to cryogenic temperature and stabilized at around 78 K. Figure 2.27 shows the photocurrent spectra, in log scale, at 78 K for a sweep of applied bias from -2.5 V to $+1.3$ V. Each spectrum is normalized by its corresponding amplifying gain.

We focus on the evolution of the main peak intensity as function of the bias (figure 2.28), spanning from -2.5 V to 1.2 V at 78 K. Photocurrent decreases with increasing voltage. Two resonances are measured at around -0.5 V and -1.6 V, that corresponds to alignments of the extraction levels with the upper state of the main well.

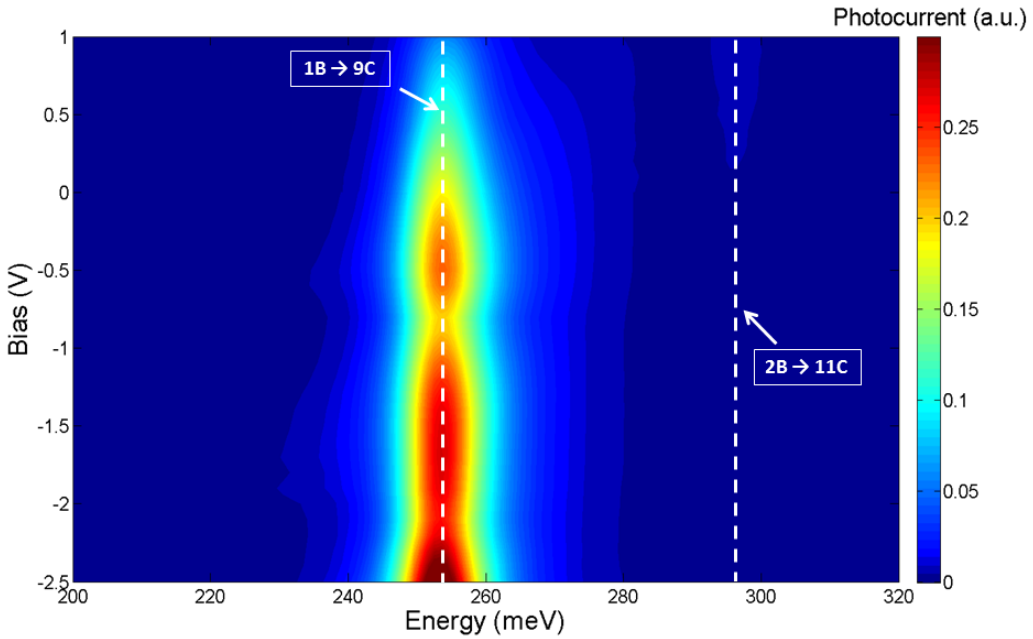

FIGURE 2.27: Photocurrent spectra of a 200 μm diameter mesa at 78 K for negative and positive bias. The color map corresponds to the photocurrent intensity.

In order to explore the performance of the QCD we worked on the reduction of the noise level of our experimental setup. With this aim, we removed the transimpedance and we measured directly the photocurrent spectrum at 0 V. Figure 2.29 shows the resulting spectrum after an average over 10000 scans measured at room temperature.

From Figure 2.29, a sharp inversion of the spectrum at around 350 meV is measured. This radical inversion is compatible with an inversion in the measured photocurrent sign.

In order to be able to explore more precisely this peak at different applied bias and to keep a significant signal to noise ratio, the bias is applied directly to the QCD thanks to a low noise power supply (2450 Source meter Keithley, with tens of pA of current noise level). The gain resistance in the transimpedance is replaced by a shunt resistance (R_{shunt}) which is in series with the QCD. The bias corresponding to the photocurrent flowing through the R_{shunt} is then read by the ADC. As the resistance is put in series with the QCD, the bias applied to the QCD differs from the output of the power supply. Knowing that, the choice for a correct value for the R_{shunt} is the most important part of this setup.

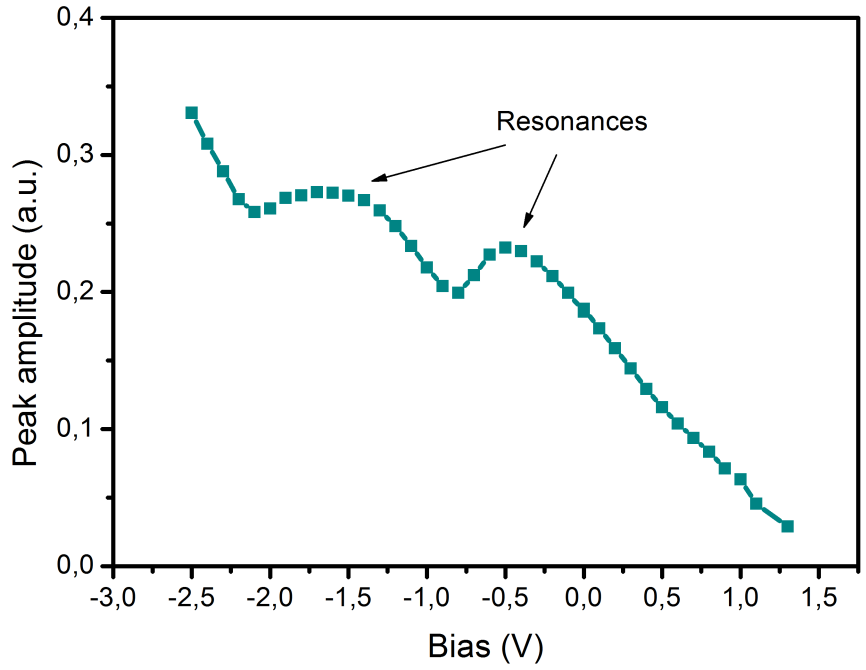

FIGURE 2.28: Amplitude of the photocurrent peak at 78K as a function of the applied bias. Values are extracted from spectra of figure 2.27 centered at energy of 254 *meV* by a lorentzian fit.

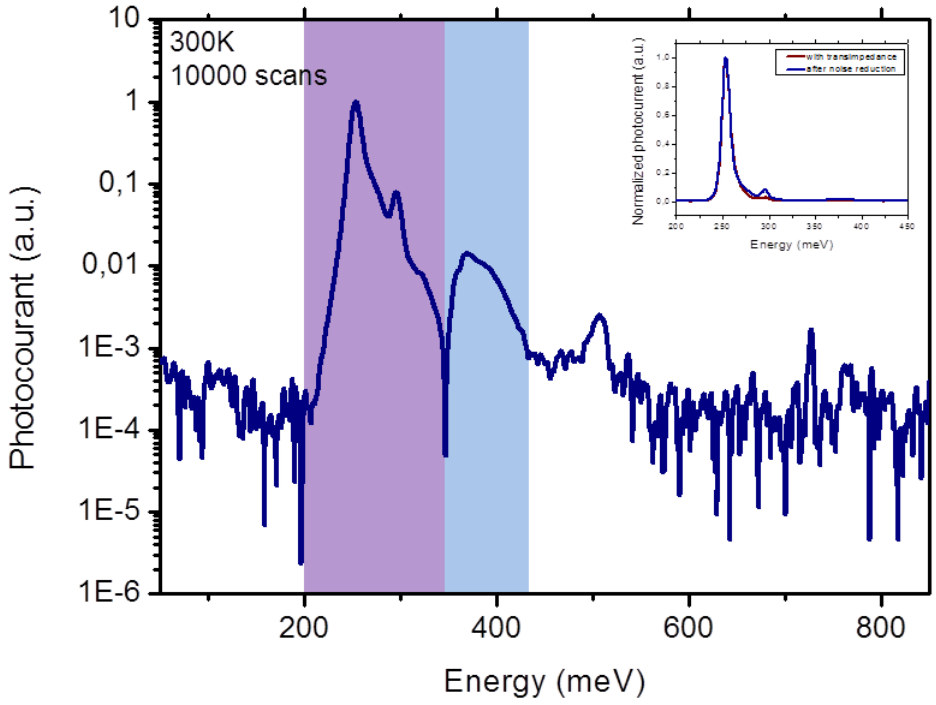

FIGURE 2.29: Photocurrent spectrum of a 200 μm diameter QCD at 300 K without applying any external bias (logarithm scale). inset: same spectrum in linear scale. The purple zone represents the negative bias and the blue zone the positive bias.

In this setup, the voltage applied to the QCD V_{QCD} is equal to:

$$V_{QCD} = V_{outputKeithley} - R_{shunt} * I_{photo} \tag{2.41}$$

with I_{photo} the photocurrent of the QCD.

Indeed, if the R_{shunt} is higher than the differential resistance of the device($R_{QCD} = \frac{dV_{QCD}}{dI_{photo}}$), most of the output voltage from the source meter will be applied to the resistance and not the QCD. On the other hand, if the resistance is really low compared to the R_{QCD}, the photocurrent will mostly flow within this resistance so we will not obtain a measurable signal. Therefore, the R_{shunt} should have a value lower than the differential resistance of the QCD but in the same order of magnitude of this.

Positively biased spectra

Thanks to noise reduction, we push the measurements to higher applied positive voltage up to 3.5 V. Figure 2.30 shows photocurrent spectra of a 200 μm diameter QCD obtained at 78 K averaged over 5000 rapid scans. The shunt resistance used is at 1 $M\Omega$ as the differential resistance of the device at 78 K is around hundreds of $M\Omega$.

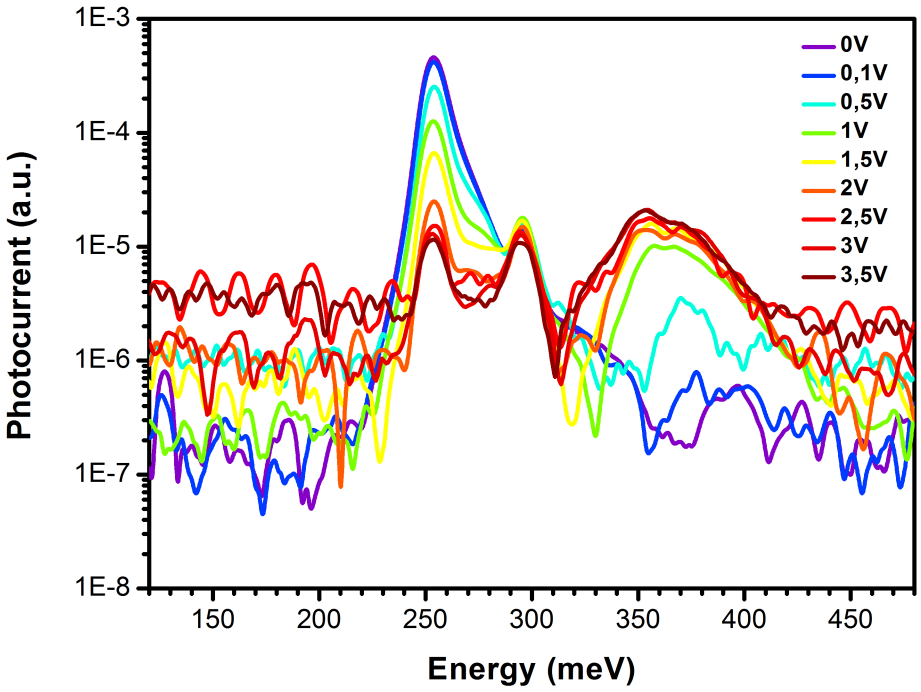

FIGURE 2.30: Photocurrent spectra of a 200 μm diameter QCD at 78 K for positive bias up to +3.5 V (curves have been smoothed (Savitzky-Golay method).

Starting from 1 V, the high energy resonance increases in intensity. As this peak is broader compared to the other two peaks, we assume it to correspond to a transition to the continuum. We observe also a shift of this peak as the bias is increased. Indeed, by increasing the applied bias, the transition energy between the energy level E_{2B} and the continuum decreases until a value where this difference in energy remains constant. This corresponds to a voltage when the upper states passes in the continuum.

In order to summarize spectral performance we present the integral over the spectra for different bias. We distinguish two different contributions to the photocurrent. One corresponding to the photocurrent due to optical intersubband absorption representing by peaks 1 and 2 (that we name the negative bias). The other one, the photocurrent flowing in the reverse direction to the previous photocurrent which corresponds to the optical transition to the continuum represented by peak 3 (name positive bias). The "negative" and the "positive" part of the photocurrent are separately plotted as a function of the bias in figure 2.31.

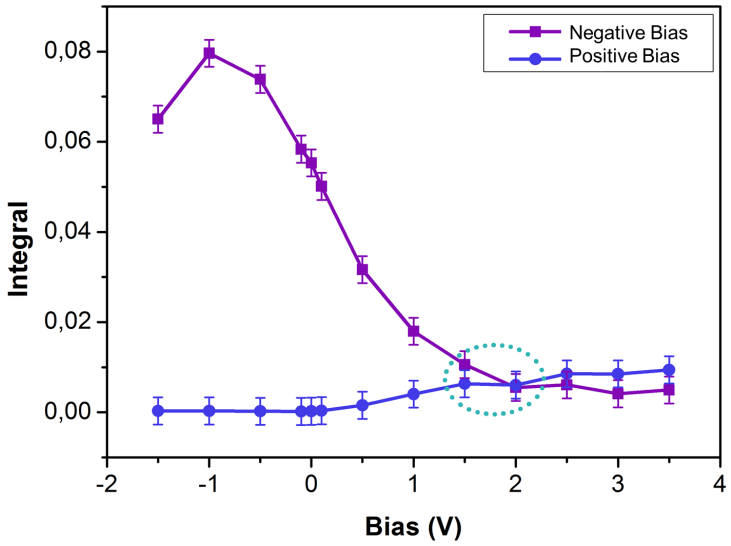

FIGURE 2.31: Integral over the peaks contributing to the photocurrent at negative bias and at positive bias respectively in purple and in blue. The dashed cyan lines indicates the cross area of the two curves.

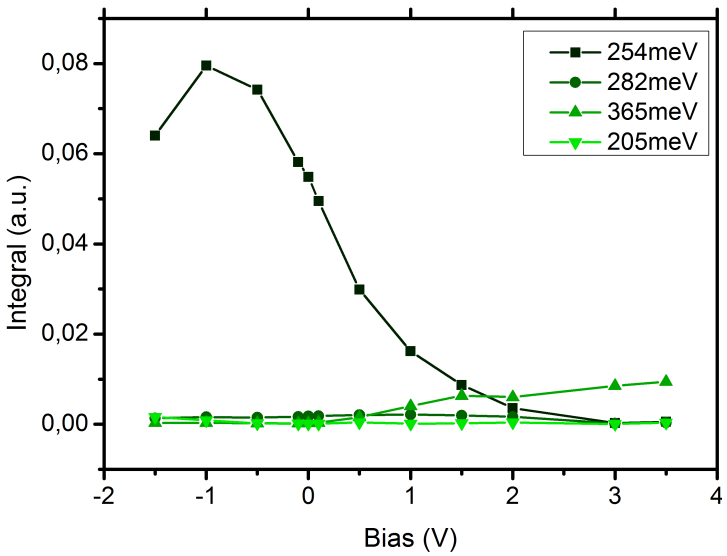

FIGURE 2.32: Integral over the different photocurrent peaks for different applied bias.The peaks at 205 *meV*, 254 *meV* and 282 *meV* contribute to the photocurrent whereas peak at 365 *meV* contributes to the photocurrent in the reverse direction.

From 1.5 V the photodetector behaves as a QWIP where the photocurrent comes from transitions in the continuum.

Figure 2.32 shows individual integral for all different peaks. From this figure, we see that the main contribution for the photocurrent is the intersubband absorption at 254 meV which is the main optical transition. All the other peaks contribute slightly to the photocurrent. Moreover we can see a net increase of the photocurrent corresponding to the third peak at 365 meV when the photocurrent at 254 meV tends to zero.

Photocurrent with calibrated blackbody

In order to be able to estimate the detectivity of the QCD, calibrated measurements have to be performed. In this section we will present the calibration measurement setup, then the results for the photocurrent and detectivity of our QCD.

For the photocurrent measurement we have used an external blackbody source with tunable operating temperature. This setup allows to control the source characteristic properties in order to calibrate the QCD response thanks to a commercial MCT calibrated detector.

Figure 2.33 shows the photocurrent measurement setups with the blackbody.

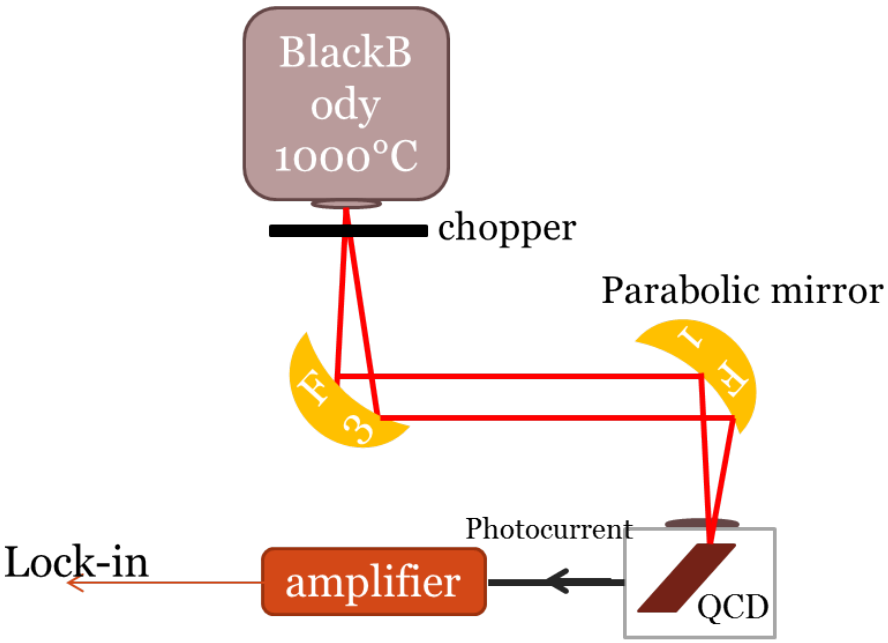

FIGURE 2.33: Setup for the photocurrent measurement using a blackbody source at 1000°C .

The blackbody source of Goosh & Housego Instruments (model OL 480) was used for this measurements. The temperature of the blackbody is set to 1000°C. Thanks to a rotating disk with different size of aperture, we have chosen the source size of the emitted thermal radiation to be 0.2 $inch$ ($\approx 5mm$). The output beam is then chopped at $f_{chopper}$ before being focused on the detector thanks to two parabolic mirrors. A F3 parabolic mirror put in front of the source collimates the radiation and a second F1 mirror put in front the detector, focuses the radiation on the active area of the detector. The QCD is screwed on a copper submount inside an under

vacuum cryostat with the 45° facet perpendicular to the incoming radiation. The electrical connections are done with gold wires bonded to the structure, as shown in Figure 2.14, and electrical cables soldered in the cryostat. The bias is applied to the QCD thanks to 2450 Source Meter Keithley power supply. The photocurrent is collected with the DLPCA-200 transimpedance which is then amplified and measured on a lock-in amplifier. We use Stanford Research SR830 as a lock-in amplifier and the chopper frequency is sent as a reference to the instrument. The offset bias of the transimpedance is set to zero when the QCD is at room temperature so lowest value of R_{QCD}.

The photocurrent signal from the device is the voltage read on the lock-in amplifier divided by the gain of the transimpedance amplifier.

$$I_{photo} = \frac{V_{lock-in}}{g_{ampl}} \frac{\pi}{\sqrt{2}} \tag{2.42}$$

$\frac{\pi}{\sqrt{2}}$ corresponds to the calibration factor of the lock-in amplifier. As the lock-in amplifier detects only the root-mean-square (RMS) signal of the frequency, there is a $\frac{\pi}{\sqrt{2}}$ factor between the output of the lock-in amplifier and the peak amplitude of the signal which is a square wave signal. As the input resistance of the transimpedance amplifier is $R_2 = 50\ \Omega$ (in equation 2.38), the applied bias to the QCD is equal to the output of the power supply. Moreover, the input resistance of the lock-in amplifier which is $R_{Li} = 10\ M\Omega$ can be neglected. The electrical setup is similar to the figure 2.25 with the lock-in amplifier added at the output of the transimpedance with an input resistance of R_{Li}.

Figure 2.34 presents the lock-in signal measured as a function of the applied bias for temperatures going from 78 K up to room temperature. The chopper frequency is set to $f_{chopper} = 130\ Hz$. The amplifier gain was changed during the measurements as the transimpedance was overloaded with current while increasing the temperature.

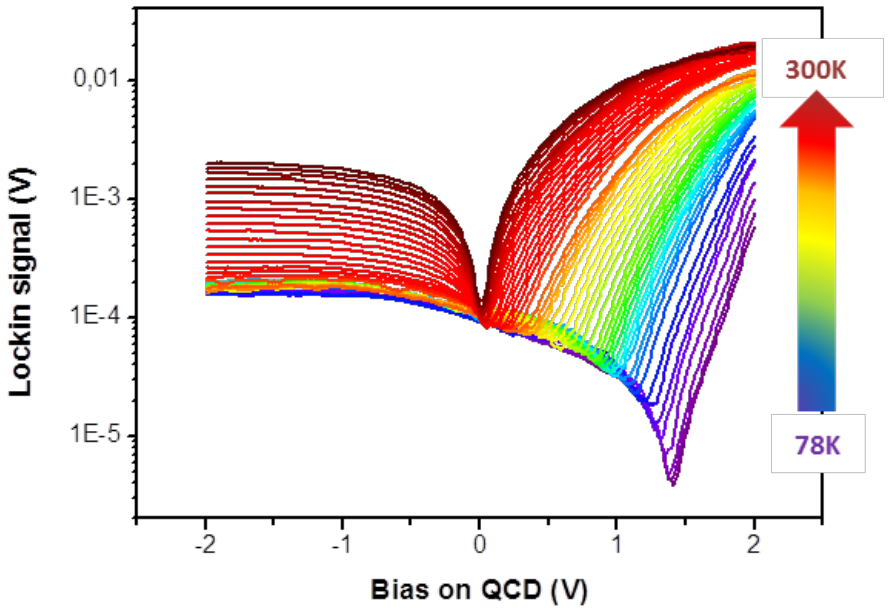

Figure 2.34: Lock-in signal read using the photocurrent setup measurement as a function of applied bias on a QCD of diameter 100 μm.

This signal represents only the photocurrent contribution of the current flowing in the device. In Figure 2.35 we report the representative photocurrent at a fix temperature compared with the total current measured with a Keithley in the same conditions.

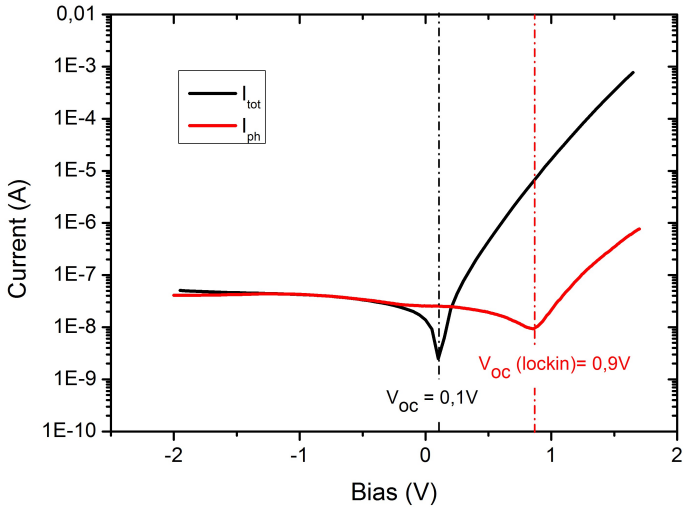

FIGURE 2.35: Photocurrent as a function of applied bias in black and its corresponding I-V curve in red obtained at 144 K.

As we can see, we are able to separate the dark contribution in the current measurements. In addition, we notice that at a fixed temperature, $V_{OC}(lockin) > V_{OC}(keithley)$. We remind that V_{OC} is the voltage where $I_{tot} = 0 \rightarrow I_{photo} = I_{dark}$. Since in the photocurrent measurements we get rid of the I_{dark} contribution, the I_{photo} measurement depends on QCD band structures and on the alignment of electronic levels with voltage. In this case, $V_{OC}(lockin)$ corresponds to the transition from the QCD to QWIP operation in agreement with spectral measurements (e.g. at 78 K, $V_{OC}(lockin) \approx 1.42$ V: see Figure 2.30 and integrals in Figure 2.31).

In Figure 2.36 we compare the measured resistance as a function of the inverse of the temperature for a fixed bias of -0.5 V in different conditions: dark (in black), background (in brown) and with FTIR globar (in red) and 1000°C blackbody (in orange) illumination. The data are extracted from I-V curves obtained thanks to a cw Keithley generator. As expected, all these measurements overlap in the high temperature region with the same slope proportional to the activation energy E_a (see section 2.1.1). At the same time, the operating temperature at which each curve starts to overlap with the one measured at dark condition, varies according to the incident power in agreement with equation 2.12.

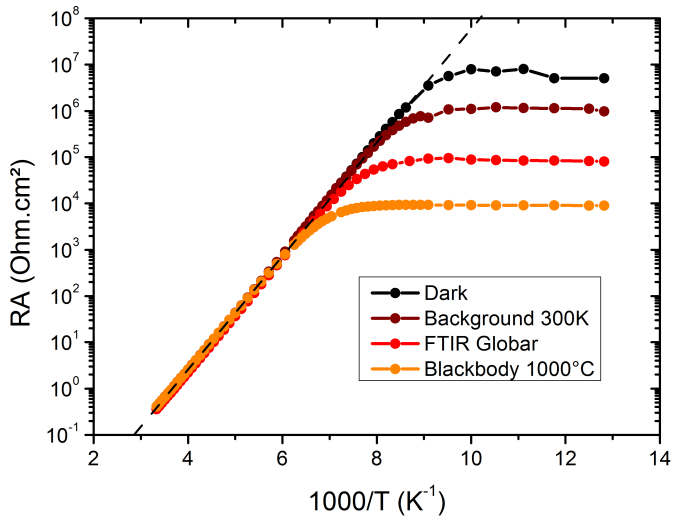

FIGURE 2.36: Logarithm of the resistance of the device times the surface area as a function of the inverse of the temperature for different measurements conditions: dark (in black), background 300K (in brown) and with FTIR globar (in red) and 1000°C blackbody (in orange) illumination. The black dashed line corresponds to the linear fit of the curves at higher temperature representative of the activation energy.

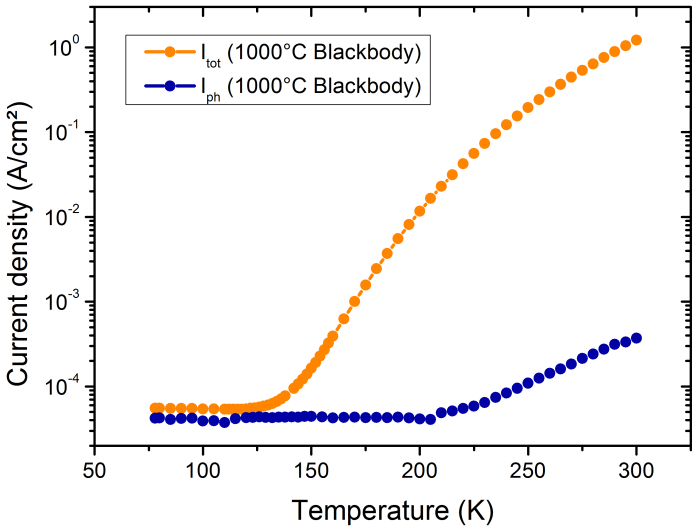

FIGURE 2.37: Total current density in log scale as a function of the temperature at −0.5 V in orange, and the photocurrent in blue measured at the same time using the setup shown in Figure 2.33.

In Figure 2.37, we study the influence of the operating temperature on the photocurrent under blackbody illumination (1000°C) with set up reported in Figure

2.33. These measurements were performed at the same time of corresponding I-V curves (orange data) and both are reported in Figure 2.37.

In the low temperature regime, the two curves almost overlap in agreement with assumption of a signal dominated by the photocurrent; small residual difference comes from the dark current contribution. In the high temperature region, the photocurrent stays almost constant up to $\bar{T} = 210\ K$, where it starts to grow exponentially. From these data, we notice that, with increasing temperature, dark current actives photocurrent parasitic channels and, following the same analysis of equations 2.8 and 2.19, we estimate the corresponding activation energy to approximately 145 meV.

Looking at the calculated band structure in figure 2.9, we see that electrons in the state $2B$ can transit to level $9C$ or $11C$ and generate a parasitic photocurrent toward the continuum by gain of an energy close to the estimated activation.

In order to get only the contributions of the main optical transition (i.e. the intersubband transition in the main quantum well) to the photocurrent at high temperature, we have to exploit spectral characteristic of the QCD. Figure 2.38 presents the integral over the whole spectra and the integral only under the main absorption peak (between 200 meV and 350 meV) taken at 0 V as a function of the temperature respectively in blue and black. In this figure we notice that the background contribution is negligible and that both integrals remain nearly constant as temperature increases. This is agreement with a constant responsivity (photocurrent) of the device with the temperature.

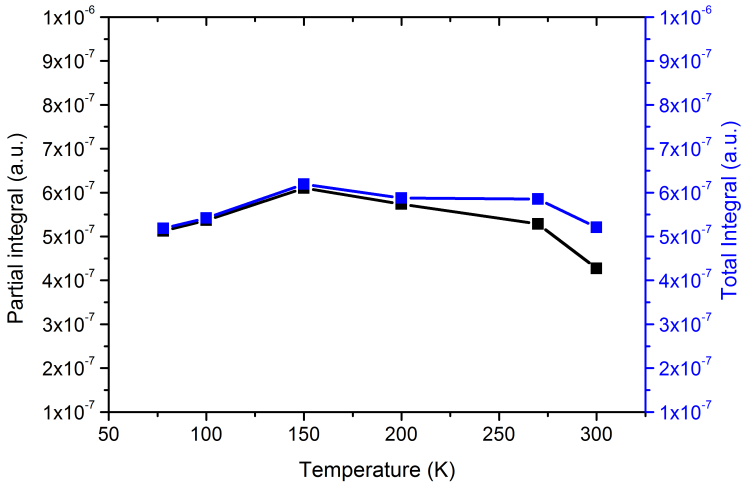

FIGURE 2.38: Integral over the whole spectra in blue and only under the absorption peak (between 200 meV and 350 meV) in black, at 0V bias

Figure 2.39 shows the same spectral integral as previous but at an applied bias of $-0.1\ V$.

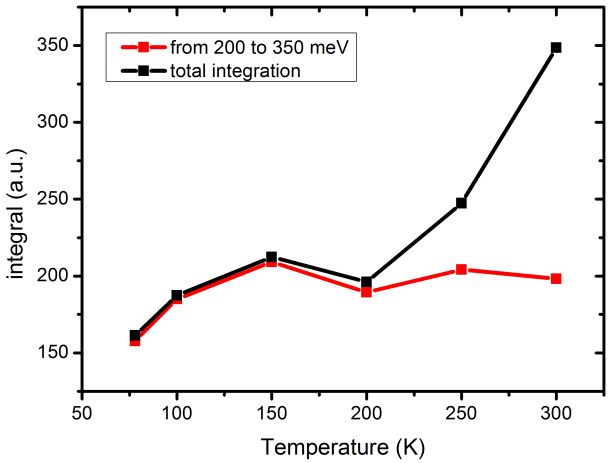

FIGURE 2.39: Integral over the main transition peak and the whole spectra taken at $-0.1\ V$ respectively in red and black

We can see that the integral under the main transition peak remains roughly constant with temperature. On the contrary at this bias the integral over the whole spectra increases with temperature starting from the transition temperature ($\bar{T}$) estimated in photocurrent measurements (Figure 2.37).

Consequently, in our experiment with the blackbody, we have decided to complete our measurements beyond the transition temperature $\bar{T}$ by taking into account the optical spectra of the device.

Responsivity and detectivity

In order to calculate the responsivity, the incident power to the detector needs to be estimated (see equation 2.23). To do that we use the same setup as figure 2.33 but this time we replace the QCD by a calibrated photodetector and in particular a calibrated MCT.

The alignment of the setup remains the same as with what we have done the photocurrent measurement. Only the MCT is aligned to the beam after the F1 parabolic mirror. The output signal of the MCT is amplified by $Gain_{MCT}$ that is equal to 100 in our case. As the MCT has a high detectivity the output signal overload the lock-in amplifier. The lock-in amplifier that we use has a limited input bias of $1\ V$. In order to avoid the overload, we perform a voltage divider circuit. A resistance $R_1 = 86.6$ $k\Omega$ is put in series and a lower resistance $R_2 = 0.986\ k\Omega$ is put parallel to the lock-in amplifier. Thus the output bias of the MCT is equal to

$$V_{MCT} = \frac{V_{Lockin}}{Gain_{MCT}} \frac{\pi}{\sqrt{2}} \frac{R_1 + R_2}{R_2} \tag{2.43}$$

In addition to the electrical circuit, we need to consider the spectral bandwidth of the photodetector. Indeed, as the blackbody is a broad source of photons, the input power to our detector has to be estimated by taking into account the ratio between the spectral bandwidth of the two detectors. Thus, in spectral approach, the output bias of the MCT can be rewritten as:

$$V_{MCT} = A_{MCT} \mathcal{R}^{peak}_{MCT} \Phi_{MCT} E \tag{2.44}$$

where A_{MCT} is the active surface area of the MCT and $\mathcal{R}_{MCT}^{peak}$ its peak responsivity (in V/W). The MCT detector that we used has its active area in square shape with 0.025 *cm* edge.

Φ_{MCT} is the integral of the normalized blackbody radiation (Φ_{BB}^{norm}) with the normalized responsivity of the MCT($\mathcal{R}_{MCT}^{norm}$) corresponding to the purple strip in figure 2.40. It represents the number of incident photons per unit surface per second. E is the energy of the peak photon flux of the blackbody at a defined temperature. The incident power on MCT is simply equal to $P_{MCT} = \frac{V_{MCT}}{\mathcal{R}_{MCT}^{peak}}$

The integral Φ_{MCT} is expressed as:

$$\Phi_{MCT} = \int \frac{d\Phi_{BB}^{norm}}{dE} \mathcal{R}_{MCT}^{norm}(E) dE \tag{2.45}$$

The responsivity of the MCT is obtained through provided data sheet from the supplier.

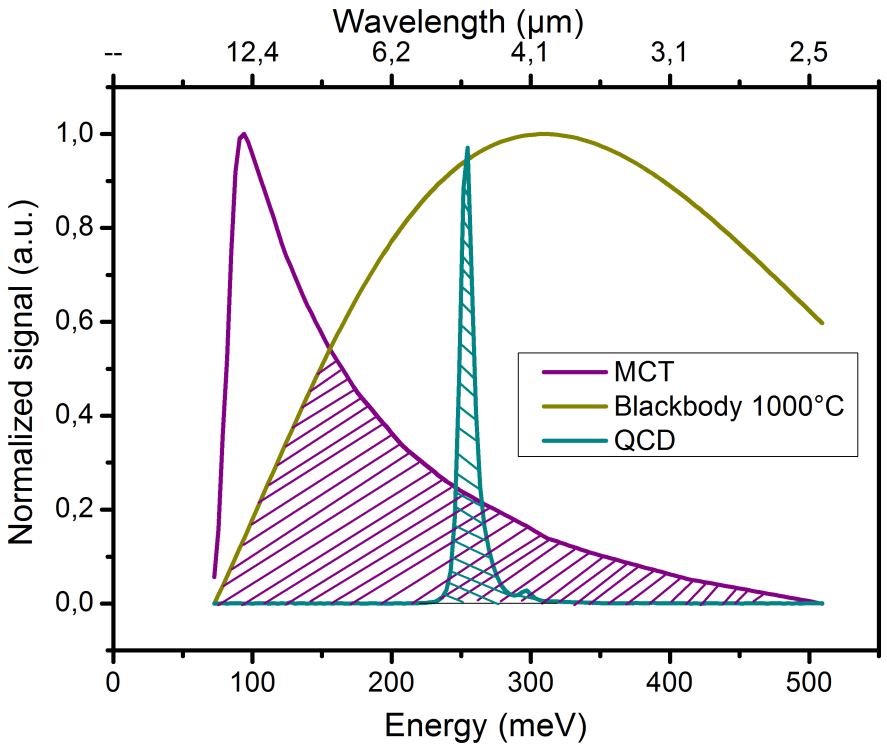

FIGURE 2.40: Normalized response of the QCD and the MCT as a function of energy respectively in blue and purple plot together with the normalized signal for the blackbody radiance at 1000°C in green. The stripes represent the calculated Φ for each photodetector.

We do the same spectral approach for the QCD detector. Using equations 2.20 and 2.23 the photocurrent is written as

$$I_{QCD} = A_{QCD} \mathcal{R}_{QCD}^{peak} \Phi_{QCD} E \tag{2.46}$$

where A_{QCD} is the active surface of the QCD and Φ_{QCD} the number of incident photons per unit time per unit surface of the QCD. The integral Φ_{QCD} corresponding to the blue stripes in figure 2.40 is expressed as:

$$\Phi_{QCD} = \int \frac{d\Phi_{BB}^{norm}}{dE} \mathcal{R}_{QCD}^{norm}(E) dE \tag{2.47}$$

The optical input power is then equal to

$$P_{QCD} = A_{QCD} \Phi_{QCD} E \tag{2.48}$$

If we replace E by its definition with the MCT (equation 2.44) we have

$$P_{QCD} = \frac{P_{MCT} A_{QCD} \Phi_{QCD}}{A_{MCT} \Phi_{MCT}} \tag{2.49}$$

With this calibration setup, we have been able to estimate the incident optical power to the QCD knowing the incident power to the MCT $P_{QCD} = 3.4\ \mu W$. Knowing this parameter, we can estimate the responsivity of the QCD for different measurement parameters.

Figure 2.41 shows the responsivity of the detector at $V = 0\ V$ for different temperature.

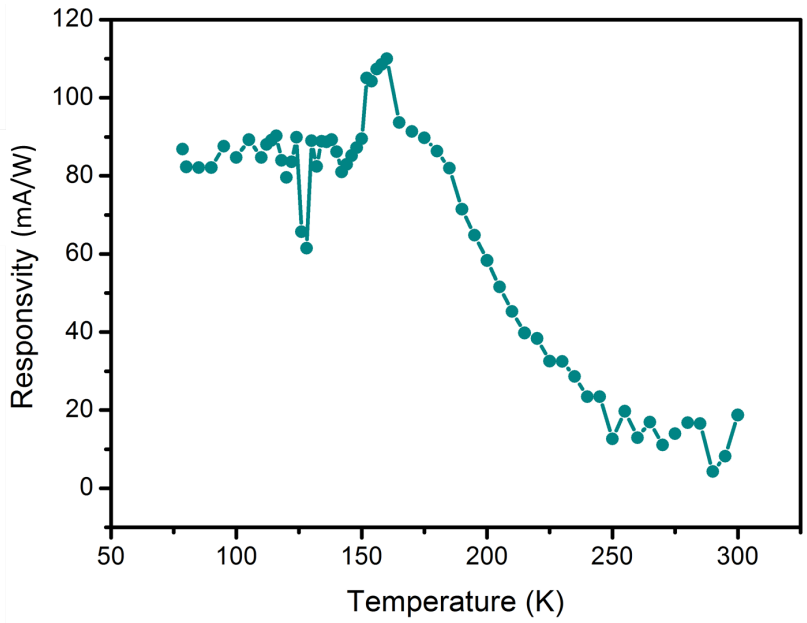

FIGURE 2.41: The responsivity(mA/W) of the QCD at 0 applied bias as a function of the temperature.

The responsivity has a constant value up to around 185 K and starts to decrease. The responsivity of our device at 0 V goes from 86 mA/W at 78 K to 19 mA/W at room temperature. The responsivity for a specific wavelength λ remains constant as function of the temperature as what have been observed with the integrals in figures 2.38 and 2.39.

The detectivity is then obtained following the equation 2.30. Figure 2.42 shows the detectivity of the detector at $V = 0\ V$. The R_0 parameter of the noise from the equation 2.30 is taken from the background current of the detector measured in parallel with the photocurrent. The specific detectivity of our QCD at 0 V is equal to 2.9×10^{11} *Jones* at 78 K and 7.2×10^{7} *Jones* at room temperature. From Figure

Temperature [K]	Responsivity(0V) [mA/W]	Detectivity*(0V) [Jones]
78	86	2.9×10^{11}
300	19	7.2×10^{7}
$T_{BLIP}=135$	90	2×10^{11}

Table 2.1: Summary of the QCD performances

2.42 we obtain a BLIP temperature of 135 K with a detectivity at this temperature equal to 2×10^{11} $Jones$.

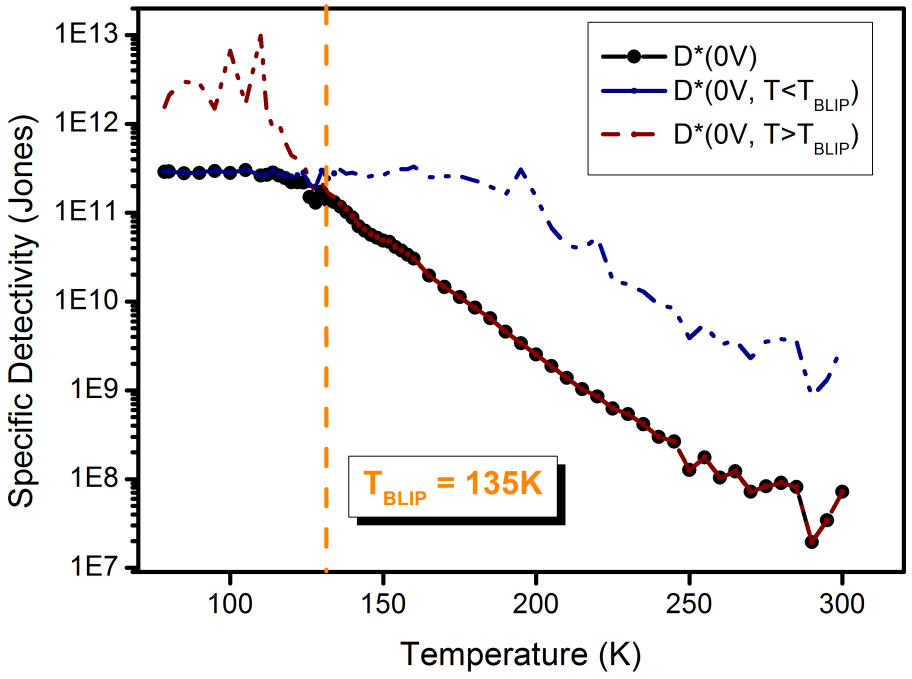

Figure 2.42: The detectivity(Jones) of the QCD at 0 applied bias as a function of the temperature in black dots ans line. The dashed lines correspond to the detectivity with the contribution of only one of the noise (in blue the background noise and in red the Johnson noise).

Table 2.1 summarizes the performances of our detector.

The detectivity obtained together with the BLIP temperature are higher than already existing QCD using the same heterostructure. Table 2.2 presents the state of the art of InP-based QCDs operating around 5 μm.

QCL optical detection

Using our QCD photodetector and a QCL as a source, we have performed optical spectra and L-I-V curves.

Results are reported in Figure 2.43. QCD is placed as a detector at the output of an FTIR and QCL a source at the input. Similar spectra have been obtained using the QCD and the MCT as detector.

Characteristic	InGaAs/AlGaAs [Hofstetter et al., 2010]	InGaAs/InAlAs [Graf et al., 2006]	InGaAs/InAlAs [Schwarz et al., 2017]
BLIP	108 K	150 K	124 K
Detectivity at BLIP (Jones)	2×10^{11}	2×10^{8}	2.1×10^{11}
RT spectrum	?	OK	OK

Table 2.2: State of the art of QCD

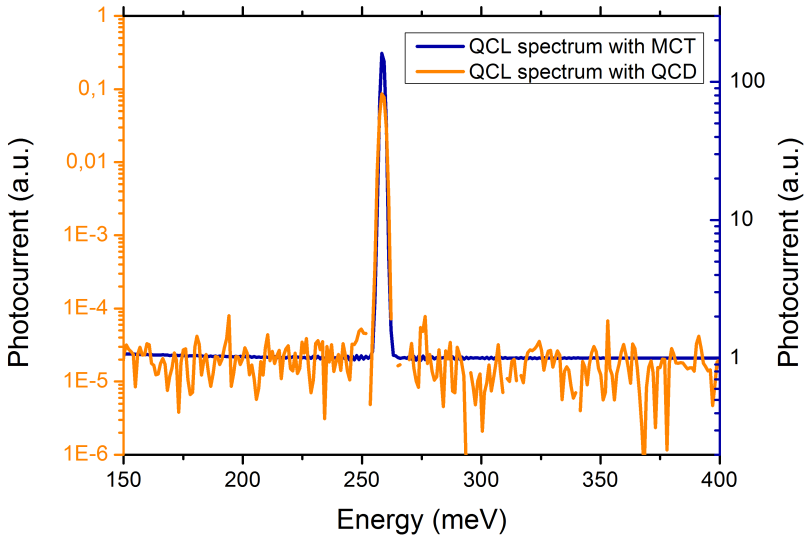

Figure 2.43: Spectra of the QCL with an MCT in blue and with the QCD in orange.

In Figure 2.44, we show light-current-voltage (L-I-V) measurement of the QCL using the QCD as a photodetector. The QCL beam was focused on the QCD active area using two lenses. For a fixed temperature of the QCL and the QCD, we have measured the photocurrent flowing in the QCD while sweeping the bias of the QCL. Figure 2.44 shows L-I-V measurement of the QCL using the QCD with an active area of 50×50 μm^2 at room temperature. The current threshold of the QCL is nearly equal to 280 mA.

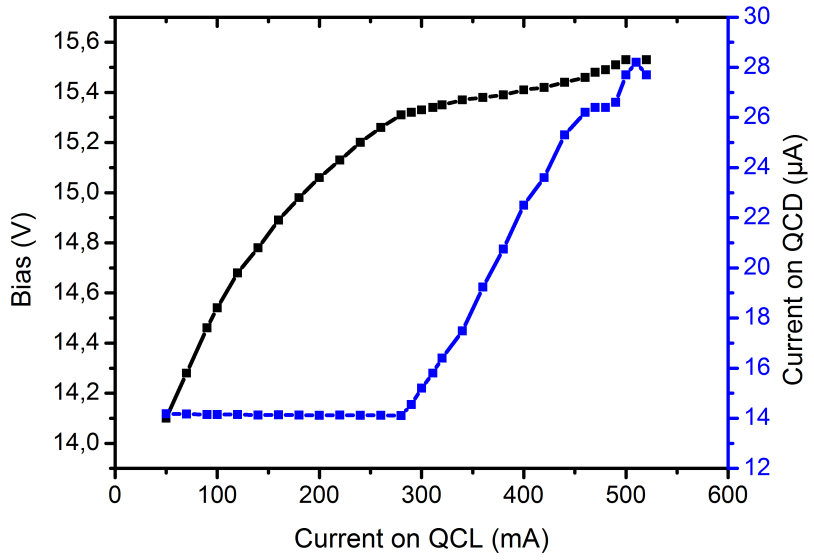

FIGURE 2.44: L-I-V measurement of the QCL with the QCD. The current voltage (I-V) corresponds to the laser and the "light" is the measured current on the QCD.

3 High Frequency QCD

Contents

In the first part of this chapter we present the design of a QCD integrated in a coplanar waveguide adapted to $50\,\Omega$ *impedance. In order to reduce the parasitic inductance of wire bonds the electrical connection between the coplanar line and the QCD mesa is done via a gold air bridge. Details of the fabrication process are presented with the related strategies to overcome the sample contamination and low reproducibility of the dry etching procedure. In the second part we perform the experimental measurements of the high frequency response of QCD in coplanar geometry using the rectification technique: the device itself is used as a rectifier element in order to convert the fast modulation in a low frequency signal. In order to attend the expected band pass of the detector governed by electronic transport, we carry out a complementary work on the optimization of the measurement electronic circuit with target bandpass of* $40\ GHz$*. Frequency response as function of the mesa size shows that one order of magnitude of signal is lost at around* $3\ GHz$ *for the* $50\ \mu m$ *size mesa, whereas this value reaches* $11\ GHz$ *for the* $10\ \mu m$ *one. Thanks to an equivalence to a RLC circuit, we estimate the capacitance for different mesa sizes. The obtained values are two orders of magnitude higher than the expected ones, in the approximation of the QCD as a parallel plate capacitor of given permittivity. The quadratic dependence on the mesa size witnesses that the main influence to the estimated capacitance, comes from the QCD itself rather than the electronic circuit. In order to take into account for the estimated value, we report a detailed study of the electronic structure of the QCD. Electrons populate mainly the ground level of largest quantum well of the detector. However depending on the applied bias and operating temperature the population of adjacent quantum well can increase and this charge distribution can act as parasitic capacitance. Indeed in this work we point out that the ultimate limit in high frequency performance of QCD is not simply the intersubband lifetime but it is governed by the specific band structure and its charge distribution. In the last part of the chapter we study the actual high frequency (HF) characteristics of QCD detectors exploiting as sources QCL with bandpass in order of ten GHz. Indeed rectification measurements are only a first step toward a realistic estimation of the QCD as HF optical detector. We report first demonstration of high frequency optical measurements based on a QCD detectors up to* $5\ GHz$*, limited by the parasitic capacitance related to the band structure, as reported for rectification measurements.*

QCD are promising devices for applications that need fast detectors. In order to study high frequency response of MIR detectors, it is commonly used a method based on the measurement of a rectified voltage. The device itself is used as a rectifier elements in order to convert the fast modulation in a low frequency signal. Best performances have been demonstrated for a QCD geometry with 20 μm square side [Yuhong Zhou and Wang, 2016]. State of the art of QCD HF characteristics is summarized in Table 3.1. However rectification measurements are only a first step toward a realistic estimation of the QCD as HF optical detector. With this aim in this thesis we study the actual HF characteristics of QCD detectors exploiting as sources QCL with bandpass in order of ten GHz.

In order to attend the expected band pass of the detector governed by electronic transport it is important to design an electronic circuit optimized for HF measurements. In this thesis we worked on the design of a MIR detector optimized for HF. We design a QCD embedded in a coplanar waveguide (CPW) to ensure efficient HF signal injection. At the same time, we worked on the optimization of the frequency response of the modulation circuit with target bandpass of 40 GHz.

In the following, we present the design of the HF setup, then the fabrication process of the device with its coplanar structure and finally the high frequency measurements results.

Detection wavelength [μm]	Mesa size [μm^2]	Band pass (-3dB) [GHz]	Reference
4.35	20×20	9	[Yuhong Zhou and Wang, 2016]
4.35	50×50	4	[Yuhong Zhou and Wang, 2016]
5.3	100×100	4	[D. Hofstetter and Blaser, 2006]

Table 3.1: State of art of high frequency band pass measured in rectification technique

3.1 High Frequency Setup

In this section we first present the different electrical elements of the HF setup, their characteristics and then the design of the CPW.

Figure 3.1 presents a simplified scheme of the circuit for HF QCD characterization. From the radio frequency (RF) generator to the QCD, the modulation signal is first transferred through different electrical circuit elements, to then reach the QCD via a CPW. Both of these parts are schematically presented in figure 3.1 with black dash lines. In order to reduce as much as possible the RF reflections, both of these parts have to be adapted with the impedance output of the RF generator that is equal to 50 Ω, as most of RF and microwave electronics.

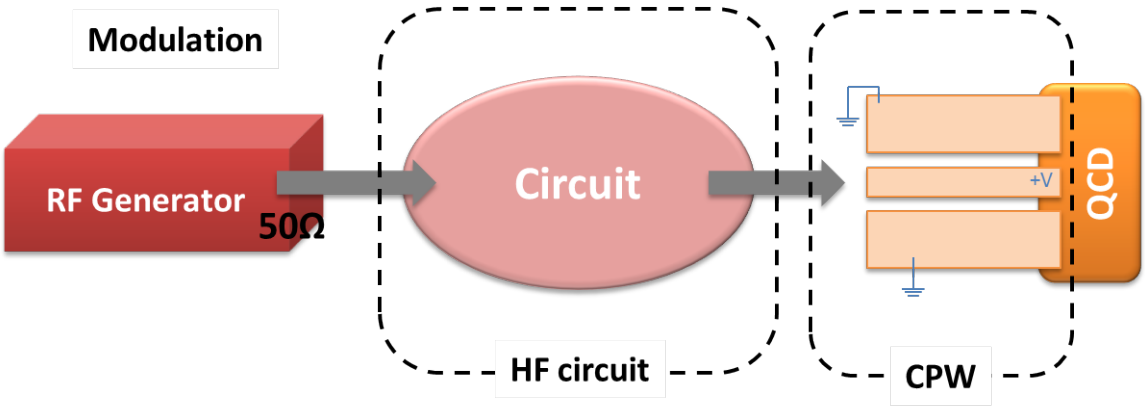

FIGURE 3.1: Simplified diagram of RF measurement. The RF generator has a 50 Ω impedance output. The whole system is designed in order to match the impedance. In one part the electrical circuit elements and in other part the design and fabrication of the coplanar waveguide (CPW).

3.1.1 HF circuit

We have performed three different experimental setups for the high frequency characteristics measurement of the QCD. Two of them are adapted for temperature measurements, so the QCD is mounted in a cryostat, and one of them is realized for room temperature measurements. For the three solutions we used commercial RF components specified in the following.

The RF signal generator used is `Anritsu MG3693B` that generates an AC signal up to 30 *GHz*. For the RF signal measurement, we used a spectrum analyzer `Agilent E4407B` with a frequency band pass of 26.5 *GHz*.

We have gathered the frequency cutoff of all the different electrical components and measurement instruments used for the RF setup in table 3.2.

Electrical components and instruments	Frequency Band-Pass (GHz)
RF pulse generator	30
Spectrum Analyzer	28.5
Bias-Tee	45
Molex connector	40
SMP cables	12
Launcher	110
Type-K cables and connectors	40
Probe (GSG)	67
Type-V cables and connectors	67
SMA cables and connectors	26.5

TABLE 3.2: Maximum frequency response of the different elements for the RF frequency measurement setup

- **Cryostat setup**

We have adapted the whole cryostat band pass at 40 GHz using cables and connectors adapted to this frequency cutoff known as Type-K or 2.92mm connectors. The connectors and cables have an impedance of 50 Ω. They are from Fairview Microwave company.

As last element of the RF circuit with the cryostat setup, we explored two different solutions. The first one (MOLEX) for easy mounting but with bandpass limited to 12 GHz, and the second one (SOUTHWEST MICROWAVE) with higher frequency response (40 GHz) but extremely sensitive to sample mounting.

FIGURE 3.2: Images of connectors used for high frequency measurements. Left: MOLEX connector; Center: SOUTHWEST MICROWAVE launcher; Right: MICROWORLD RF probe.

I) The MOLEX connector (setup bandwidth of 12 GHz) is chosen to have a simple plug and play system for our measurement setup. Leftest picture in figure 3.2 shows the connector. It has a central pin that is soldered to the CPW. The corresponding RF cable is then simply plugged to the connector. Each QCD has its own integrated connector that can not be removed otherwise the QCD is damaged.

Eventhough the MOLEX connector has a frequency bandpass of 40 GHz, the cable that we plug to the connector is limited up to 12 GHz. The benefit of this setup remains its simplicity of use.

II) The other connector (middle picture of figure 3.2) that we use when the sample is mounted in the cryostat is a RF launcher from SOUTHWEST MICROWAVE (setup bandwidth of 40 GHz). Figure 3.3 is a photo of a QCD mounted in a cryostat and connected with a launcher. The launcher is made of a pin that we bring close to the CPW of the detector by screwing gently until having an electrical connection. The launcher has a cut off frequency of 110 GHz and the cables connected have $Type-K$ ends (so cut off frequency of 40 GHz). This system is less handy than the previous one, as we need to screw and unscrew the pin every time we want to change the detector. This can also damage the metal contact since the pin is not completely fixed to the sample, we have to be careful when mounting the detector to avoid scratching the contact surface. This is the price to pay for higher frequency bandpass.

- **Room temperature setup**

III) To perform QCD characterization at room temperature we used a connector that is a RF probe from MICROWORLD company (setup bandwidth of 40 GHz)that is made of three separated pins in a ground-signal-ground

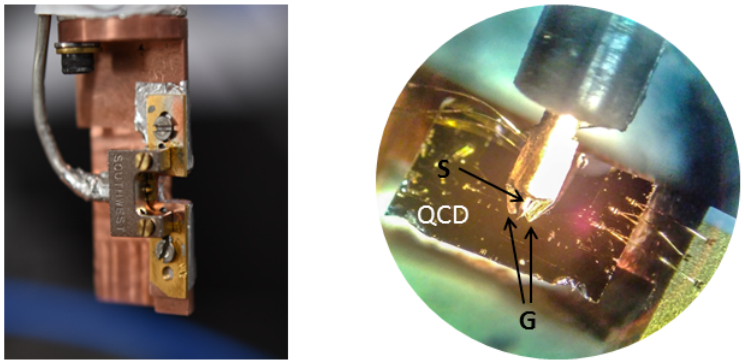

FIGURE 3.3: left: Photograph of a QCD mounted on a cryostat and connected with a launcher and adapted RF cable. The indium foil is used for a better thermal contact between the QCD ans the cryostat. right: photograph of a QCD mounted on a horizontal support and connected with a 3 pins probe. S and G stand respectively for signal and ground.

(GSG) configuration (cf picture on right in Figure 3.2). The connector used is a Type-V (or 1.85mm) connector that has a cutoff frequency up to 67 GHz. The probe is also adapted for 50 Ω impedance. The two pins on the side of the probe are positioned on the ground contact of the device and the one in the middle is positioned on the signal contact. For this setup, the probe is approached to the sample thanks to a specific micrometric screws. In order to ensure a proper electrical contact between the probe and the sample, QCD has to be mounted horizontally parallel to the optical bench.

For the optical characterization of QCD it is important to take into account the polarization of the incident optical signal (c.f section 1.2.3). Since we measure the modulated light emitted by a QCL, we have to be careful to design an optical setup where the growth direction of the two devices are parallel. In this thesis, we use a QCL mounted in a cryostat. For setup I and II the detector and the source are mounted in the same configuration, so polarization matching is preserved.

On the other hand, for the setup at room temperature (setup III) as the QCD is mounted horizontally for the probe to approach correctly the contacts of the detector, we used a system with two mirrors to change the incoming light polarization. The two mirrors were positioned like in a periscope but with one of the mirror rotated at 90° with respect to the other one. This will change the polarization for 90° following Malus law. Figure 3.4 shows the experimental setup and how the polarization is changed using the mirrors.

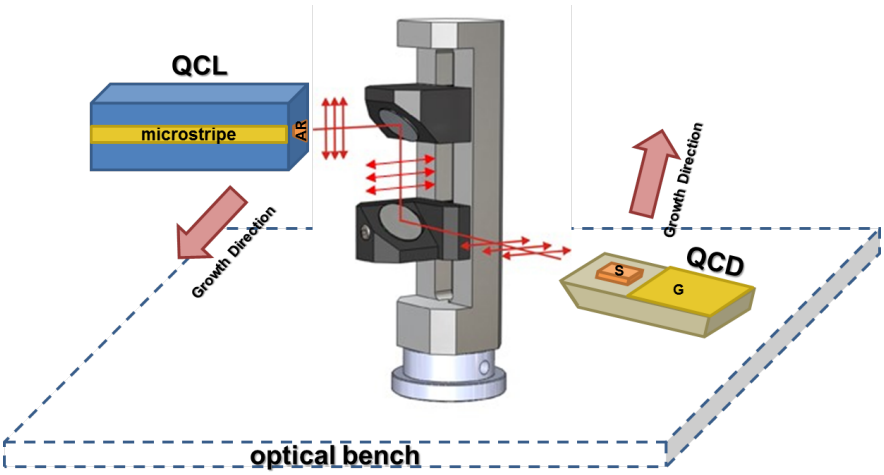

FIGURE 3.4: Scheme of the optical bench when the laser is mounted on a cryostat and the QCD mounted horizontally. The set of mirrors is used for the polarization change.

3.1.2 Coplanar waveguide design

The mesa design, presented in the previous chapter is limited for high frequency applications by the resistance and the capacitance due to its size. As the injection is done via a gold wire, the inductance related to the length and diameter of the wire limits also the HF performances. So we design a coplanar waveguide for 50 Ω impedance match over the whole structure and small inductance L. A schematic of the coplanar waveguide (CPW)'s geometry for the QCD is presented in figure 3.5.

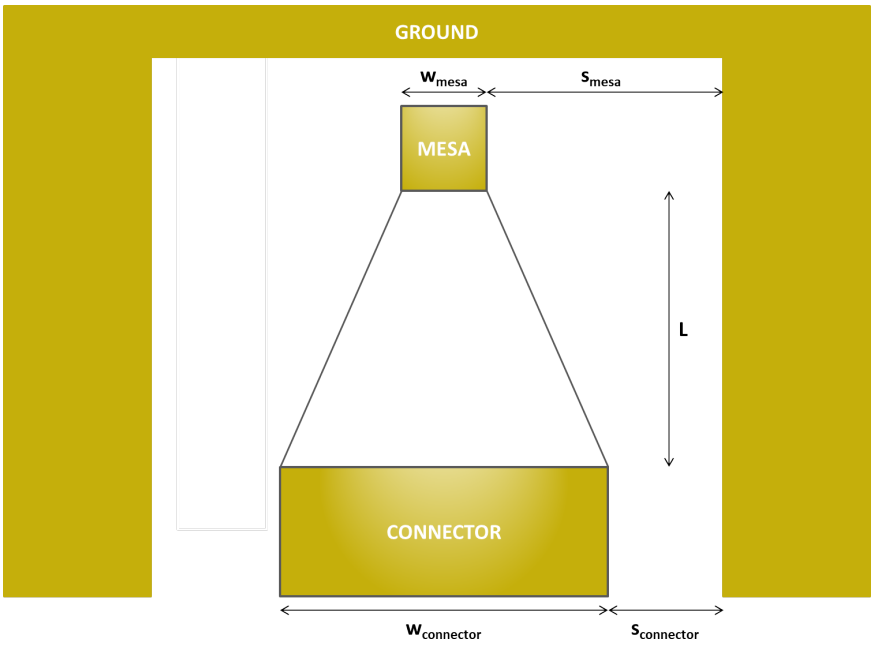

FIGURE 3.5: Top view sketch of the CPW and its horn shape with the different variables.

For the CPW design, we used two different software available online. One from Janilab[1] and the other one from Sourceforge[2]. The final design has been chosen by an average among the two different results that have been verified to be close, respect to the expected fabrication tolerance. Figure 3.6 presents a simplified cross section of the CPW at the connector side and the mesa side. The gold parts represent the CPW contacts on top of our material.

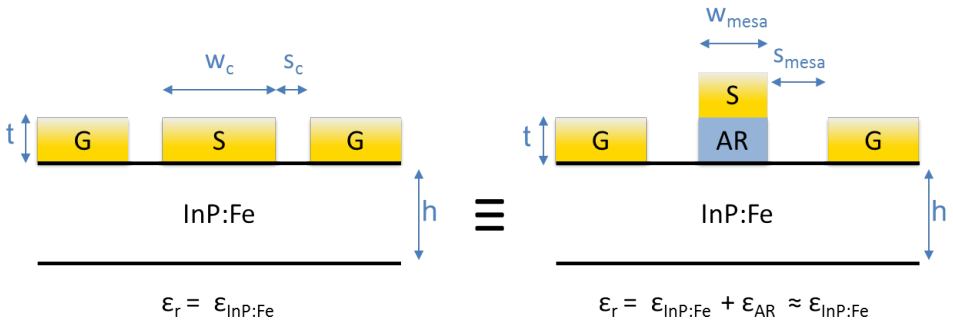

FIGURE 3.6: Simplified scheme of the geometry of the CPW at the connector side (left) and the mesa side (right).

Input parameters are ϵ_r and h respectively the substrate dielectric constant and thickness. For our sample, the dielectric constant of the InP is $\epsilon_r = 12.5$ with a thickness of $h = 350\ \mu m$. The permittivity for the mesa is taken equal to the permittivity of InP, we have thus made an approximation for the mesa contribution to the permittivity value. The metal contact on top has a thickness of $t = 300\ nm$ and a width represented by the parameter w. The width depends naturally on the size of the mesa and also on the connector that we use.

For the setup **I**, the metal width needed to solder the Molex connector was around $w_c = 400\ \mu m$. Concerning setups **II** or **III**, the launcher and/or the probe width needed is $w_c = 100\ \mu m$. In the design, we targeted a band pass of 40 GHz and and impedance of 50 Ω.

Regarding different mesa size (w), we calculated the corresponding gap (s) and the length of the coplanar (L) needed to conserve an impedance of 50 Ω. Figure 3.7 summarizes the simulation for our structure.

A linear fit of the curve of the gap (s) as a function of the mesa size (ω), represented by a red line in figure 3.7, gives the following function that is used for all the different gap calculations.

$$s = 0.65w + 11.7\mu m \qquad [\mu m] \tag{3.1}$$

Fixing the mesa sizes and choosing one of the connectors (Molex, launcher or GSG probe) we had to calculate the length of the coplanar (L) that gave us a horn shape of the CPW (Figure 3.5).

As the substrate of our structure is not doped (InP:Fe), the CPW is evaporated directly on the top of the substrate. Indeed, the epitaxial growth is etched down to the bottom contact layer. this latter is left only in the region close to the detector. The signal follows the ground on the substrate until it reaches the QCD via a metallic bridge. (See Figure 3.8).

[1] http://janielectronics.com/szamitasok/Transmission%20Line/Coplanar%20Waveguide%20Calculator/janilab.php
[2] http://wcalc.sourceforge.net/cgi-bin/coplanar.cgi

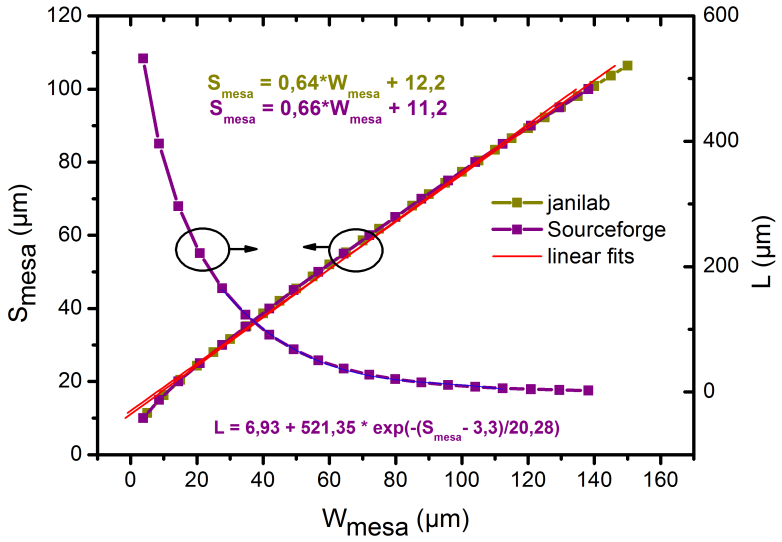

FIGURE 3.7: Simulated values for the gap (s_{mesa}) and the waveguide length (L) as a function of the mesa size (w_{mesa}) for a matching impedance of 50 Ω. The red lines correspond to the linear fits.

For our experiments, we have fabricated lithography masks for mesa size going from 5 μm to 50 μm and adapted this geometry to all the connectors. Details of the fabrication process are presented in the following paragraph.

In figure 3.9 we show electromagnetic simulation with commercial available software COMSOL. We use the "Mode Analysis" to study the light propagation inside the mesa. The simulation is a $2D$ simulation perpendicular to the propagation axis in order to model a facet of the QCD. In this $2D$ simulation, the length of the mesa in considered to be semi-infinite.

The color bar in figure 3.9 represents the magnitude of the normalized electric field in the propagation direction y. We can see from the simulation that with this configuration the electromagnetic field is well confined within the active region of the structure.

In order to predict the HF performances of CPW for HF modulation we study the equivalent circuit. Considering the QCD as a current source, we draw an equivalent circuit of our system presented in figure 3.10.

In this scheme, C_d is the device capacitance, R_c is the access resistance determined by the coplanar metal contacts and the resistivity of the contact layer of the heterostructure, $R_L = 50\ \Omega$ is the transmission line impedance and L_p the parasitic inductance. The parasitic impedance comes from the wire bonding and it depends on the length of the wire [Lundin, 1985]. Thus, by replacing the wire bond by the air bridge we reduce the parasitic inductance L_p. The QCD capacitance is expected to be the main contribution to C_d. Considering the QCD as a parallel plate capacitor :

$$C_d = \frac{\epsilon_0 \epsilon_r A_{QCD}}{d_{AR}} \tag{3.2}$$

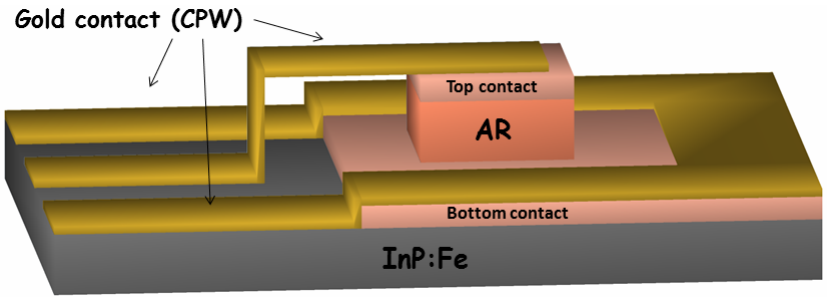

FIGURE 3.8: Scheme of the CPW on top of the mesa structure of our QCD. The gold colors represent the metallic deposition. The pink is for the top and bottom contact layer. The orange art represents the active region of our QCD

with $\epsilon_0 = 8.8510^{-12}\ F.m^{-1}$ the vacuum permittivity, $\epsilon_r = 15$ the dielectric function of InGaAs/InAlAs [D. Hofstetter and Blaser, 2006]. A_{QCD} the detection area of the QCD and $d_{AR} = 757\ nm$ the thickness of the active region of our device. The values for the capacitance for different mesa size is presented in figure 3.11. As L_p is neglected and if we consider that our QCD is ideal (i.e we neglect R_c respect to R_L by assuming the metal contact of the coplanar and the top contact layer as a perfect conductor), the circuit becomes a simple RC circuit. Thus, the -3dB cutoff frequency is equal to:

$$\omega_{cutoff} = \frac{1}{R_L C_d} \tag{3.3}$$

In this case, the cutoff frequency depends only on the capacitance of the device. Figure 3.11 shows the variation of both C_d and ω_{cutoff} as a function of the size of a square mesa of QCD.

This estimation of the capacitance value takes into account only the active region contribution. However, in our structure composed of N uncorrelated successive periods, a higher value of capacitance comes from a charge conservation in each period. We will see this aspect further on this chapter in section 3.3.1.

3.2 Fabrication Process

In this section, we present in details the fabrication process of the device for the HF measurement setup. Since the mesa sizes are of the order of few microns, in order to have straight sidewalls, we explored dry etch process. However, we saw that with this etching technique, we have faced some contamination and non reproducibility problem that lead us to fabricate the devices with the wet etching introduced in chapter 2.

For the dry etching process we have used an inductively coupled plasma (ICP) machine. In ICP technique both chemical and physical processes are involved. The etching is a combination between the different gases in the chamber, the power of the radio frequency generator and the temperature of operation. A compromise between the different parameters has to be found in order to obtain straight edges mesas with small roughness. The indium component presents in the substrate and in the heterostructure produces a radical during the etching which is less volatile than radicals of other components such as gallium or arsenic which makes this dry

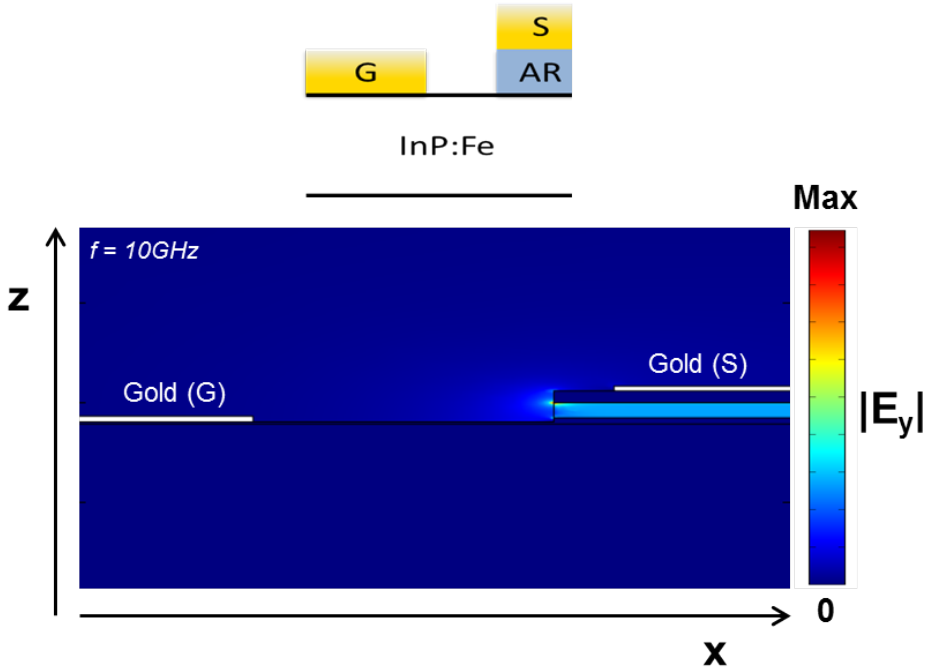

FIGURE 3.9: 2D simulation of the electromagnetic field coupled in the active region at frequency of 10 GHz.

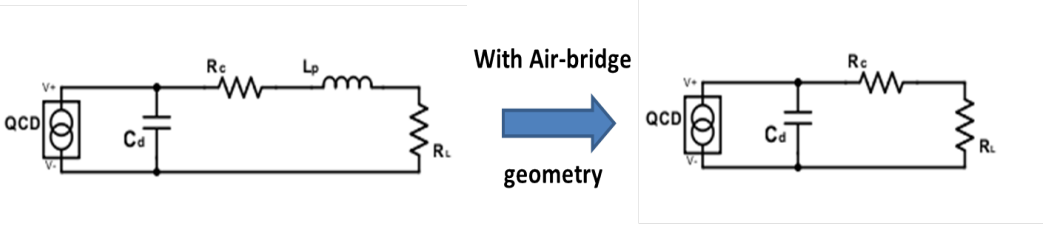

FIGURE 3.10: Equivalent electrical circuit with (left) or without the air-bridge (right). (inspired by: [Yuhong Zhou and Wang, 2016])

etching more complex [Deng, 2012]. Details of influence of different parameters of the dry etching procedure of the mesas are described in the following. The mask used for all the ICP etching is $2\mu\ m$ of SiN_4 deposited at $120°C$ with RF generator PECVD (Plasma-Enhanced Chemical Vapor Deposition).

- Influence of RF power and substrate temperature on the plasma etching

  The gases used for this recipe are $Ar/H_2/SiCl_4$ with respectively $2/7/13$ $sccm$. The RF power on surface is 350 W and the etching temperature is equal to $200°C$. The etching had a proper rate of $\approx 2.3\ nm/s$. A controllable etching process with a quite slow etching rate is an important results since the bottom contact of our structure is only 300 nm thick. Results of 10 minutes etching are presented in figure 3.12a). As we can see, the SiN_4 mask is damaged during processing, since the semiconductor is etched in the opening.

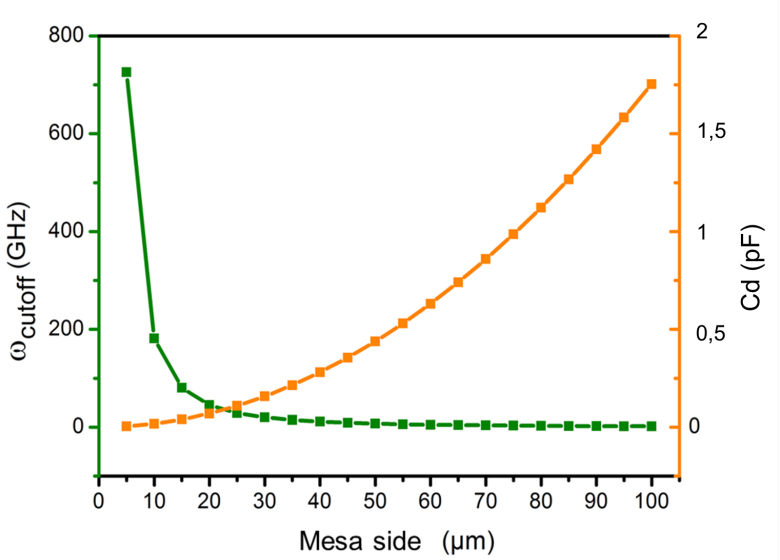

FIGURE 3.11: Variation of the capacitance of the device in orange and cutoff frequency (-3dB) in green as a function of the size of the square mesa for an ideal QCD.

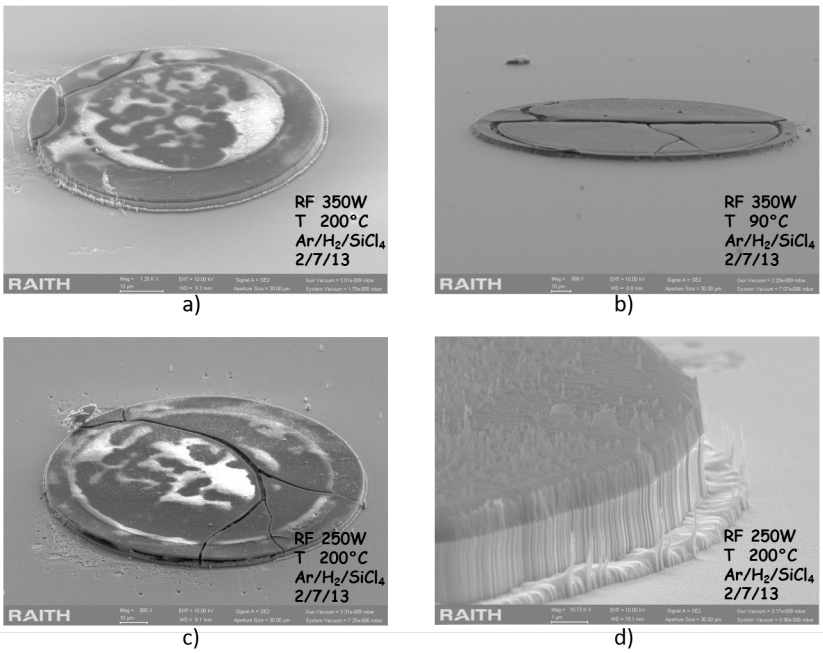

FIGURE 3.12: SEM images for high temperature and high RF power of ICP recipe.

Cooling down sample's temperature in plasma etching leads to a more uniform etch [Giapis et al., 1990]. Moreover, a reduced RF plasma power permits to have a more controllable etching rate as the RF power determines the ion bombardment energy [Ayon, 1999].

Figures 3.12b) and 3.12c) show the SEM images of the QCD after ICP etching respectively with a temperature of 90°C instead of 200°C and a power of 250 W instead of 350 W. We can see for both of the experiments that the silicon nitride is still damaged. On the other side, underetch of the structure is improved.

The etching recipe preserving SiN mask integrity is presented in the following.

- RF power: 140 W and Substrate temperature: 60°C

  For a fixed value of low enough temperature and RF power where the SiN mask does not break, we have studied the influence of H_2 and $SiCl_4$ gases.

  – Study of H_2 influence

    The plasma is made of $Ar/SiCl_4$ with respectively 5/10 $sccm$. The RF power is equal to 140 W and the temperature at the sample is 60°C. Figure 3.13a) presents the SEM image of the QCD after fifteen minutes of etching using this recipe. We can see that the silicon nitride mask is not damaged. However, the edges are not straight and we can notice a trenching effect. This effect is generally due to high bombardment plasma regime [Combrie et al., 2005]. An origin can be the reflection of ions on the sidewalls that combine with ions coming straight from the plasma, generate stronger etching reactions at the bottom of the sidewalls. This trenching effect is really an issue for our case as it has been mentioned in the wet etching part. Thus, if we want to use dry etching process, this trenching effect needs to be removed.

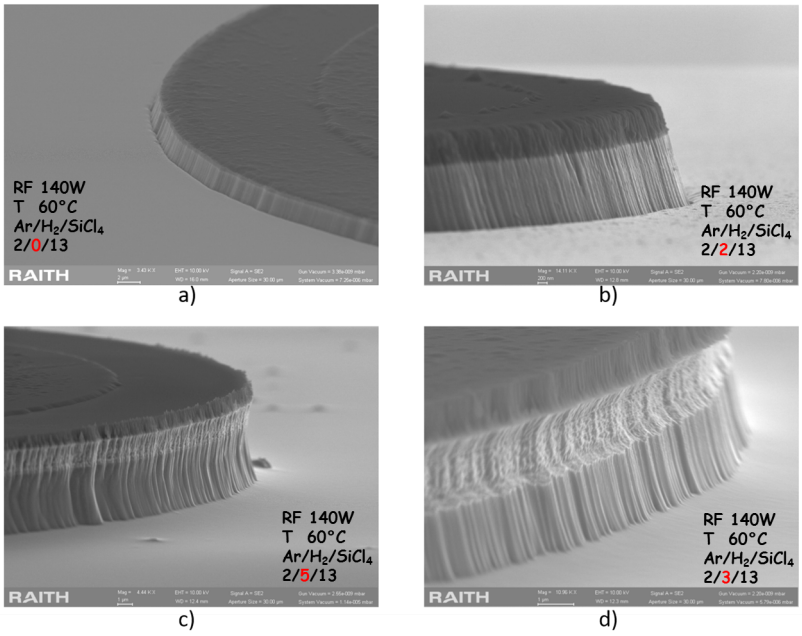

FIGURE 3.13: SEM images for ICP etching at 60°C and RF power of 140 W with fixed amount of $Ar/SiCl_4$ gases (5/10 $sccm$) and for varying value of H_2 gas a) 0 $sccm$, b) 2 $sccm$, c) 5 $sccm$ and d) 3 $sccm$.

H_2 gas can control the etching rate and the consequent shape of the sidewall and related underetch [Rommel et al., 2002]. Figure 3.13b) shows

SEM image of the QCD after five minutes of etching with 2 *sccm* of H_2 (etching rate $\approx 5\ nm/s$). We do not notice a drastic change in the geometry of the sidewalls. The trenching effect is still present.

What is a key parameter is the ratio between the H_2 gas and all the other gases present in the plasma [Rommel et al., 2002]. Figure 3.13c) shows SEM image of an ICP etching by increasing the amount of H_2 gas from 2 *sccm* to 5 *sccm*. In this configuration the etching was faster compared to lower amount of H_2 (etching rate $\approx 25\ nm/s$) . We were not able to stop at the bottom contact layer. However, the edges are more straight and the trenching has also disappeared (Figure 3.13c)). After this fast etching, the active region is partially etched leaving a rough surface.

Decreasing the amount of H_2 gas down to a value between 2 *sccm* and 5 *sccm* is done in order to keep the performances obtained with higher amount of H_2 but having a lower etching rate as in 2 *sccm* case. The same behavior as for 5 *sccm* of H_2 is also observed for 3 *sccm* of H_2 (Figure 3.13d)).

– Study of $SiCl_4$ influence

Fixing the value of H_2 gas at 2 *sccm* we study the influence of $SiCl_4$ gas. Figure 3.14a) presents the SEM image of QCD etched with $Ar/H_2/SiCl_4$ respectively $5/2/11$ *sccm* and RF power of 140 W and a temperature of $60°C$.

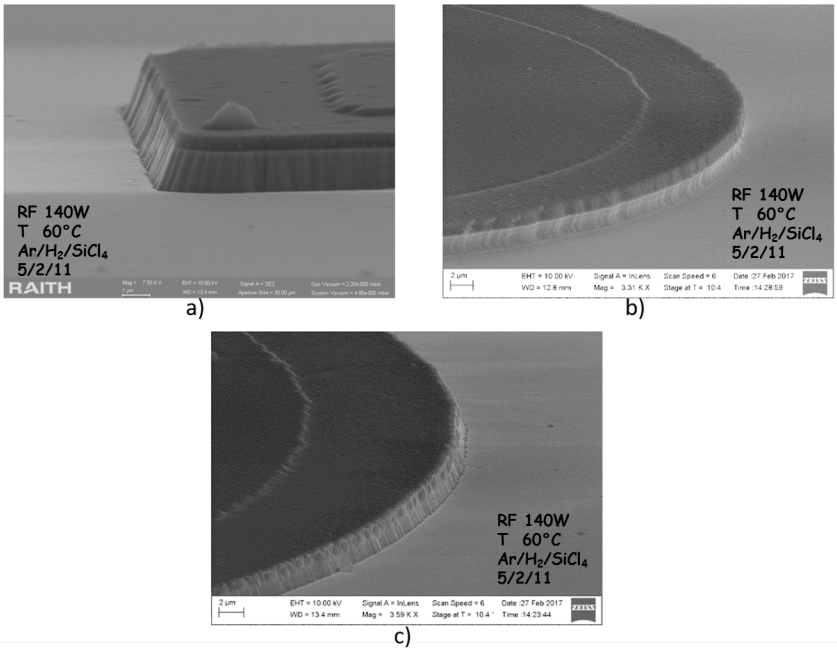

FIGURE 3.14: SEM images of successive ICP etching using the same recipe ($Ar/H_2/SiCl_4$ respectively $5/2/11$ *sccm* and RF power of 140 W and a temperature of $60°C$) that gives different shapes for different etching rate.

Increasing the amount of $SiCl_4$ from 10 *sccm* to 11 *sccm* gives straighter edges than before but still not vertical. The trenching has also been reduced. The etching rate is sufficiently low ($\approx 7.6\ nm/s$) to be able to stop at the bottom layer contact.

However, repeating the same recipe does not give the same etching rate. Figure 3.14b) shows SEM image for an etching rate of around $\approx 27\ nm/s$ and figure 3.14c) $\approx 5.4\ nm/s$.

Having a non reproducible ICP recipe is not ideal. Different aspect can explain this behavior.

As our samples are small (squares of 3x3mm), we assume that they were not touching equally the sample holder. Thus a variation in the temperature of the sample from one to another run could explain the etching rate variation. On the other hand, the ICP chamber conditions differ from one run to another run. The chamber has to be completely cleaned in order to not be influenced by previous etching and prevent any byproduct re-deposition. The ideal case would have been to clean between each new run. But this is not something that can be achieved easily. First, only the clean room staff can do the clean of the chamber. Secondly, in addition to the security problem with the toxic gas for the clean room staff (they use adapted gas masks) it is also dangerous for all the clean room users. In order to perform the cleaning the whole clean room has to be evacuated.

Thus, because of these main reasons, we were not able to achieve a reproducible recipe for our QCD dry etch.

- Removing of SiN mask

  Figures 3.15a) and b) show SEM images of QCD in a square geometry after 140 seconds of ICP etching. The recipe used is $Ar/H_2/SiCl_4$ respectively 5/2/11 *sccm* and RF power of 140 W and a temperature of 60°C. We can observe the vertical sidewalls of the mesas and the lack of trenching. The etching rate was high, so it has been stopped just after the bottom layer contact (Figure 3.15c)).

  The next step in the dry etching process is to remove the silicon nitride mask. The mask is removed using a reactive ion etching (RIE) machine. The RIE recipe is a plasma made of CHF_3 and O_2 (respectively 50 and 5 *sccm*) gases used for 40 minutes. After the mask removal residual materials are remaining on top of the mesa. Figure 3.17a) shows a zoom in one edge of the mesa after the RIE process where we can see also residual material deposit on the sidewalls.

  An X-Ray Diffraction (XRD) measurement is done in order to determine the composition of this material. Figure 3.16 shows the X-Ray spectra at the edge of the sample before RIE process (top) and after RIE process (bottom).

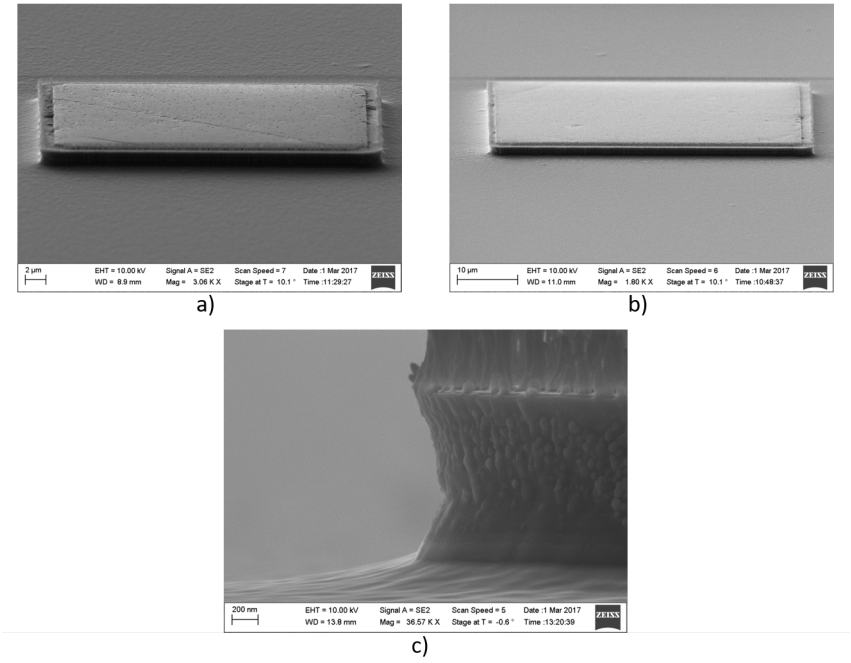

FIGURE 3.15: SEM images of square QCDs after ICP etching and RIE mask removal. Figure a) and b) are QCDs with respectively 30 and 50 μm side. Figure c) is a zoom on one sidewalls.

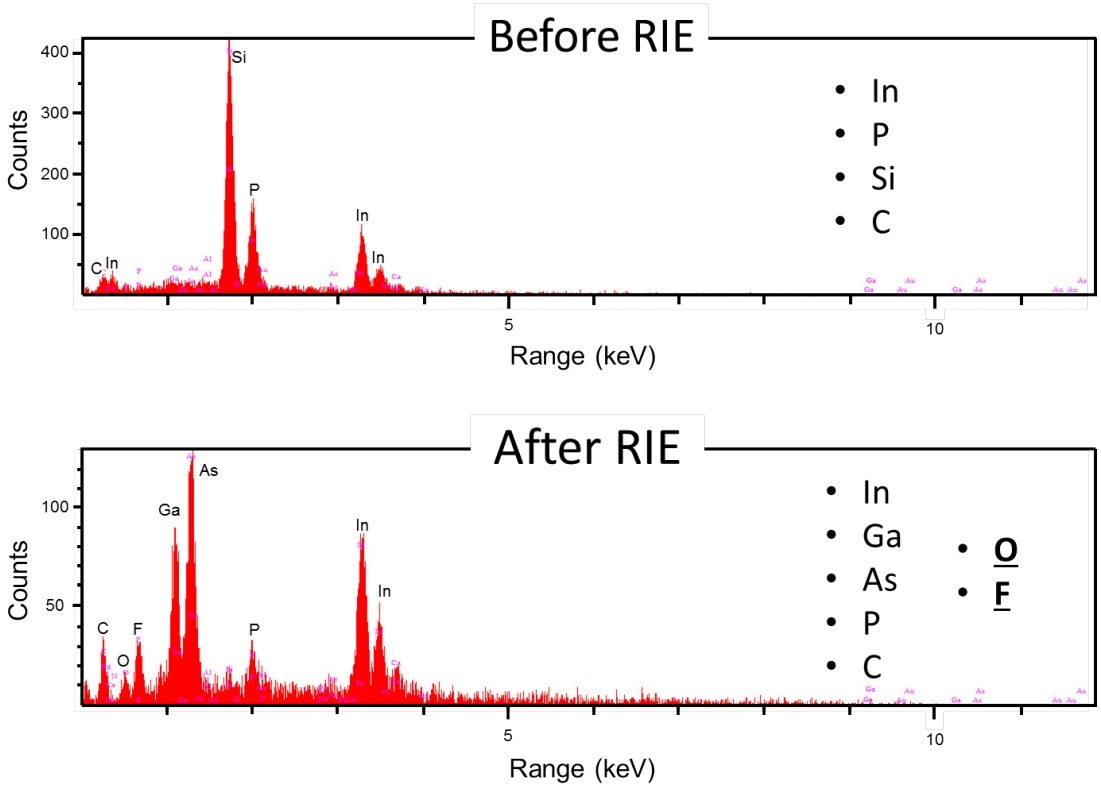

FIGURE 3.16: X-Ray spectra of a mesa with incident beam on the mesa sidewall with the silicon nitride mask, before RIE process on top, and after mask removal on bottom.

From these graphs we can see that after the RIE, we have additional oxygen and fluorine components. These two components are introduced only at the RIE step when we remove the silicon nitride mask. With CHF_3 plasma, polymer radicals in the form of CF_x are created [Kastenmeier et al., 1996], [Mele, 1984]. These polymers are responsible of the silicon nitride etching. However, sometimes, secondary reactions between these fluorocarbon radicals can form a blocking layer that slows down the etching rate. According to what we observed in the the XRD study and what have been previously studied, we can assumed that this "nanopillars" are fluorocarbon radicals.

Increasing the amount of oxygen will decrease the formation of these radicals by creating volatile compounds as CO and CO_2 [Kastenmeier et al., 1996]. However we didn't see an improve when increasing the oxygen from 5 *sccm* to 10 *sccm* (figure 3.17b)).

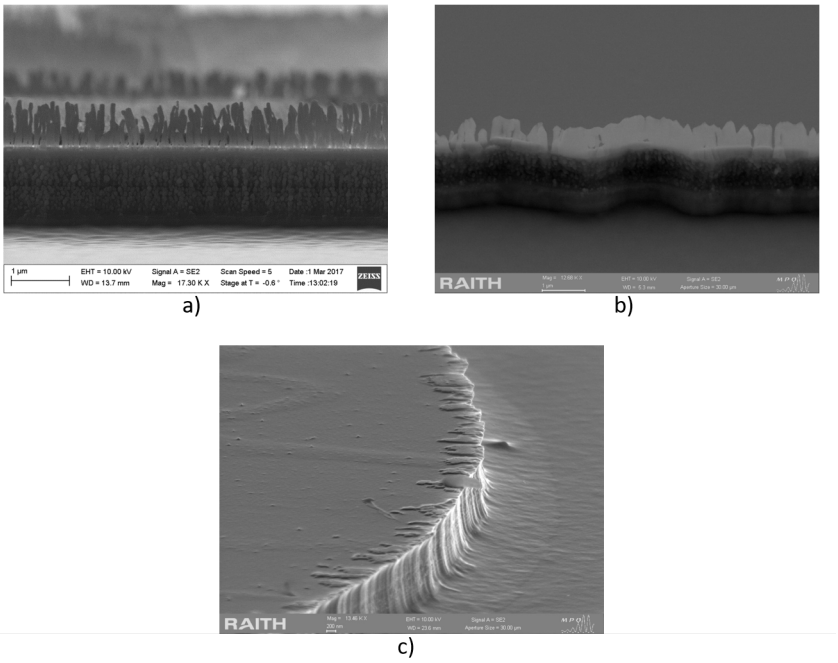

FIGURE 3.17: SEM images of QCDs side after RIE (a)), after another RIE with more oxygen flow (b)) and after 2 seconds of HF (c)).

The pillars have started to melt with each other and form a "wall" on top of the mesa.

We have decided to use a hydrofluoric acid (HF) to try to remove the pillars. Figure 3.17c) shows SEM image of our sample after 2 seconds of HF etching. we can see that the pillars are still there but have fallen down.

As we were not really sure about this pillars and how they could affect our measurements, we have decided to not pursue with this sample.

We have decided to fabricate the devices using the same wet etching process as previously explained (Chapter 2 section 2.2.1). Square mesas with sizes from 5 μm to 50 μm were realized. Then, in order to ensure an adapted RF injection to the mesa, we have processed a coplanar waveguide followed by an "air-bridge" that make a connection between the top of the mesa and the input RF source as showed in figure 3.8.

3.2.1 Air-bridge fabrication process

- Optical lithography for air bridge

  First, we realized an optical lithography with a positive photoresist. The mask corresponds to rectangles that are placed between the mesa and the CPW. These rectangles will play the role of pillows that will support the bridge.

- Baking of the photoresist

  The baking is important in this part, because it will determine the adhesion of this positive photoresist. Thus, additional to standard baking for photolitography, we did five baking of five minutes from $110°C$ to $150°C$ each $10°C$. Moreover, to give to the bridge a more spherical shape, the bake is done in an oven were the sample is put under a cup made of aluminum.

- Second optical lithography for CPW

  Then, it is followed by another optical lithography, this time with a negative photoresist. This step defines the design of the CPW. The mask is the structure of the CPW designed for each of the different mesa size.

- Lift-off

  After the development the sample is put on the evaporator to deposit gold ($300\ nm$) for the CPW. In order to homogeneously deposit the contact all over the bridge, we do the evaporation at three different angles: $-30°$; $0°$; $30°$ following the direction of the CPW. We finally do a lift-off. Figure 3.18 shown an SEM image of the final structure with the coplanar waveguide and a the air-bridge.

FIGURE 3.18: SEM image of the QCD at 10 μm mesa size with the air-bridge and the gold coplanar waveguide.

In order to make a more robust, we have decided also to grow gold on top of the bridge with gold electrolysis process. But we have seen that, as the gold is deposit all over the bridge, we make short-circuit between the bridge and the bottom contact with a consequent low yield for this process. So we decided to keep the thickness of gold around 300 *nm* that corresponds only to the evaporation part.

3.3 High Frequency Characterization

In order to characterize the HF performance of the QCD we carried out two kinds of experimental measurements. On one side we used the device itself as a rectifier element in order to convert the high frequency response in a measurable DC signal (rectification). In this scheme the intrinsic response of the detector can be studied with HF bandpass limited only by the electrical circuit. However rectification measurements are only a first step toward a realistic estimation of the QCD as HF optical detector. With this aim we performed optical measurement where an input HF modulated optical signal is incident on the detector. As a source, we used a QCL biased using a HF adapted circuit. In this case the frequency response is governed by the interplay of both contributions coming from the source as well as from the detector.

3.3.1 Rectification

Theory

The microwave rectification measurement relies on the inherent non linear I-V characteristic of the QCD. This technique is based on measuring the change in the voltage (measuring current) while applying an external microwave signal to the device. It was first introduced by H.C. Liu [Liu et al., 1996] for QWIP devices and have been used later on as a high frequency QCL characterization measurements [Stefano Barbieri and Sirtori, 2007]. The setup is illustrated in figure 3.19.

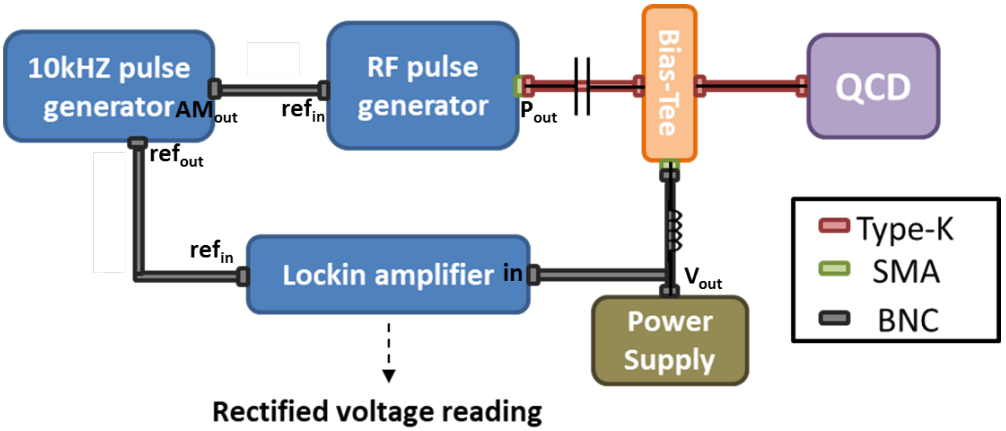

FIGURE 3.19: Rectification setup for the QCD.

The RF signal is amplitude modulated (AM) at 10 kHz thanks to a pulse generator with 50% of duty cycle. The modulated signal is injected through a bias tee into the QCD. The rectified DC voltage is collected through the DC port of the bias tee

where we bias also the QCD. The rectified voltage is measured thanks to a lockin amplifier synchronized with the pulse generator.

In the small signal regime, the current measured at a fixed bias V_0 can be expressed as:

$$I(V_0+\delta V) = I(V_0) + \frac{\partial I}{\partial V}(V_0)\delta V + \frac{1}{2}\frac{\partial^2 I}{\partial V^2}(V_0)\delta V^2 + o(\delta V^2) \tag{3.4}$$

where $\frac{\partial I}{\partial V}(V_0)$ stands for the derivative of the I-V curve calculated at V_0.

A modulated bias at frequency ω is $\delta V = V_\omega cos(\omega t)$ with V_ω the amplitude of the modulation. With this expression of the voltage, the current averaged in time becomes:

$$< I >= I(V_0) + \frac{1}{4}\frac{\partial^2 I}{\partial V^2}(V_0)V_\omega^2 \tag{3.5}$$

From the previous expression (equation 3.5) we can see that the average in time of the current corresponds to the current at the measured bias plus an additional current that varies with the voltage and depends on the frequency of modulation. This additional expression is the rectified current:

$$I_{rect} = \frac{1}{4}\frac{\partial^2 I}{\partial V^2}(V_0)V_\omega^2 \tag{3.6}$$

This equation (equation 3.6) can be rewritten as :

$$I_{rect} = \frac{1}{4}\frac{\partial^2 I}{\partial V^2}(V_0)\alpha(\omega)V_{\omega 0}^2\beta(\omega) \tag{3.7}$$

where $\frac{\partial^2 I}{\partial V^2}(V_0)|_0$ and $V_{\omega 0}$ are the low frequency limit of respectively $\frac{\partial^2 I}{\partial V^2}(V_0)$ and V_ω. We separate the frequency dependency of the rectified current in two contribution named $\alpha(\omega)$ and $\beta(\omega)$. The first term represents the intrinsic-transport mechanism and is dependent on the lifetime of the carrier. The β takes into account the circuit dependence in the form of an RLC circuit.

The frequency behavior of the the intrinsic transport mechanism is expressed as a low pass filter where the cut-off frequency is set by the lifetime of the photoelectron:

$$\alpha(\omega) = \frac{1}{1+(\omega\tau)^2} \tag{3.8}$$

τ corresponds to the lifetime of the photoelectron.

$V_{\omega 0}^2$ is expressed as follows (ref: p.177 [H. C. Liu, 2000]):

$$V_{\omega 0}^2 = 8R_L P_{out}\beta(\omega) \tag{3.9}$$

with P_{out} the output power from the microwave source in watt.

In order to study the high frequency response in QCD detector, we replace the ideal current generator circuit of fig 3.10 with an equivalent RLC circuit presented in figure 3.20

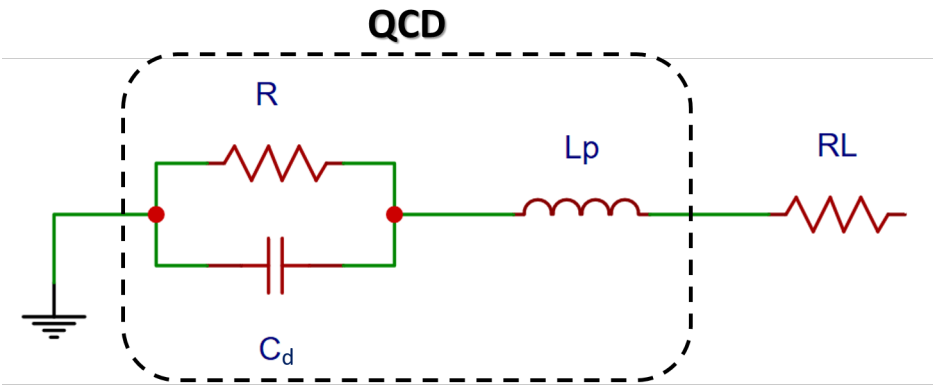

FIGURE 3.20: Equivalent circuit of the QCD schematized as an RLC circuit. L_p being the parasitic inductance is mainly eliminated thanks to the airbridge geometry.

In this configuration, $\beta(\omega)$ is defined as (ref: [H. C. Liu, 2000]):

$$\beta(\omega) = \frac{1}{(1-\omega^2 L_p C_d)^2 + \omega^2 (R_L C_d + \frac{L_p}{R})^2} \tag{3.10}$$

With R the differential resistance. For QCD we have usually $R >> R_L$, $R + R_L \approx R$. If we are in the low frequency regime, $\omega \to 0$,$\beta(\omega)$ tends to zero and $V_{\omega 0}$ is simply equal to $8 R_L P_{out}$. For $L_p \to 0$ (see figure 3.10), we find the usual RC roll-off : $\beta(\omega) = \frac{1}{(1+(\omega R_L C_d)^2)}$. (with the cutoff frequency at equation 3.3).

Experimental Results

In figure 3.21 we present the DC characterization of the coplanar QCD (figure 3.8). The measurements are done for a QCD with 10 μm mesa side from 155 K up to room temperature.

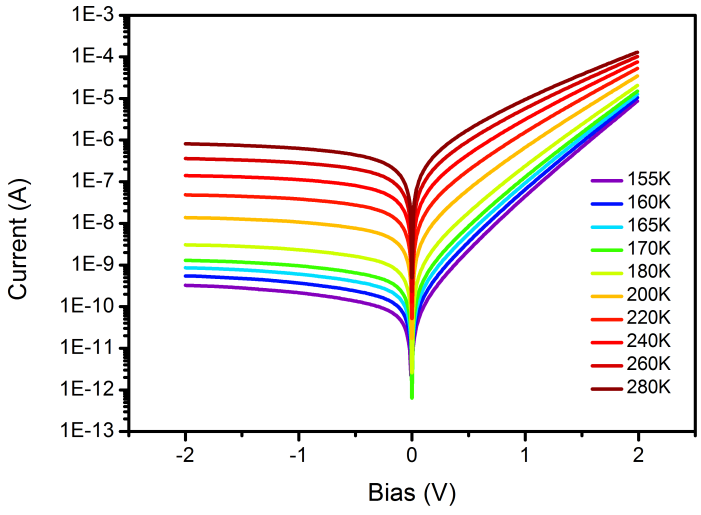

FIGURE 3.21: I-V characteristic of a square mesa of 10 μm with the CPW and the air bridge geometry.

In first approximation, the current density is equivalent to that of the circular mesas presented previously and residual deviations can come from depletion effects of small devices as well as from estimation of geometrical size. Figure 3.22 shows J-V curves measured for 4 different size of mesa at two temperatures (200 K and 300 K).

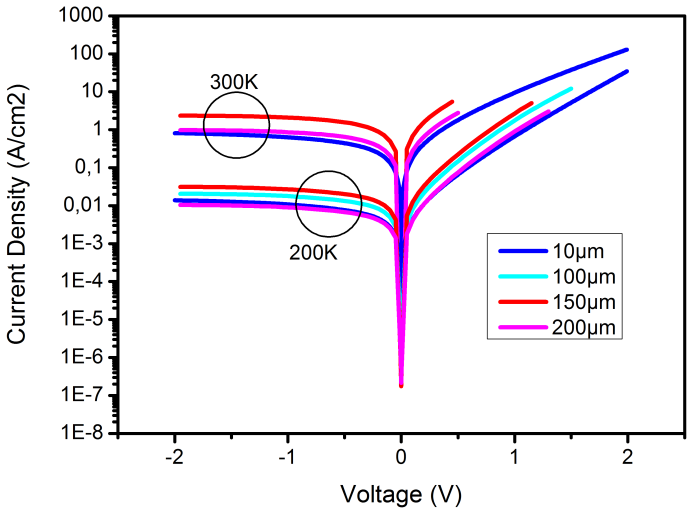

FIGURE 3.22: J-V characteristic of square mesas of different sizes with the CPW and the air bridge geometry.

In figure 3.23 we present rectification measurements realized on different mesa sizes using the setup II with the launcher connector. The measurements are done at room temperature with an applied bias of $-220\ mV$ for mesas of size 10 μm, 20 μm, 30 μm and 50 μm. The RF power was set to 0 dBm in order to respect the small signal approximation.

As it can be seen from this graph and according to the equation 3.3, the cut off frequency increases with a reduce mesa size. One order of magnitude of signal is lost at around 3 GHz for the 50 μm size mesa whereas this value has increased up to 11 GHz for the 10 μm one.

Using the rectification equation (equation 3.7) and the circuit equation (equation 3.10), we fit the experimental data and deduce a value for the capacitance of the device. Figure 3.23 shows the fit obtain for each of the rectification for the different mesa size.

The inductance value used in the fitting formula is obtained theoretically using the general equation for flat wire inductance calculation [Wadell, 1991].

$$Lp = 2.10^{-7} L(ln(\frac{2L}{w+h}) + 0.5 + 0.2235(\frac{w+h}{L})) \qquad [\mu H] \tag{3.11}$$

The corresponding inductance value for each mesa side (w) is given in table 3.3. The differential resistance is deduced from the I-V curves. The load resistance is set to 50 Ω and the time τ equal to 1 ps (see table 3.3). Figure 3.24 shows the device capacitance obtained thanks to the fitting for different mesa size.

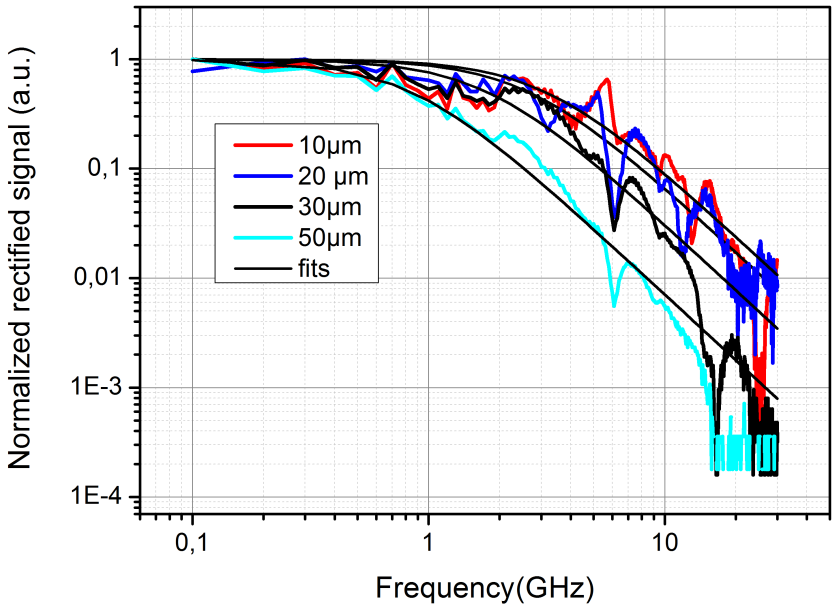

FIGURE 3.23: RF rectification measurements of mesa with 10 μm, 20 μm, 30 μm and 50 μm at room temperature. All the measurements have been done with an external applied bias to the QCD of -220 mV and an RF input power of 0 dBm. The black lines represent fitting following rectification equation 3.10.

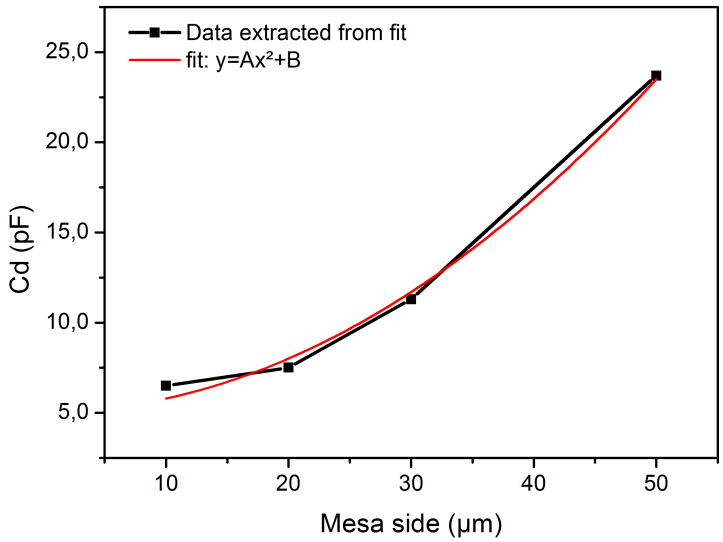

FIGURE 3.24: Capacitance of the different mesa side extracted from the fitting. Red curve corresponds to a fit with $y = A*x^2 + B$ function.

From this graph we observe a quadratic behavior of the capacitance with the surface of the detector in agreement with expected parallel plane approximation (c.f. formula 3.2). However, the values of the capacitance derived from the fit have two orders of magnitude of difference with the ones estimated from the geometrical

factors.

Mesa size (μm)	**Lp (H)**	**Cd (F)** (fitted)	**Cd (F)** (estimated)	**R (kOhm)**
10	3.5E-12	6.44E-12	1.7E-14	1184
20	1.9E-12	7.57E-12	6.8E-14	296
30	1.6E-12	1.13E-11	1.5E-13	131
50	1.4E-12	2.37E-11	4.2E-13	47

TABLE 3.3: RLC parameter for different mesa size of the QCD

It is important to add, as we are in the small signal approximation, we are able to observe and measure the rectification signal only after a certain temperature of the device. Indeed, for lower temperature, the current is below nA and the rectified signal is drowned under the noise level.

In order to understand results in table 3.3, additional studies need to be done in order to determine the origin of the capacitance in a QCD. Indeed, this cannot be considered simply as a dielectric of permittivity ε but the fine structure of electronic distribution in the different periods has to be taken into account.

3.3.2 Optical high frequency measurement

In an optical high frequency measurement, a RF signal is carried by an emitting light and it is detected by a photodetector. The measured light generates a microwave signal on the photodetector which is then observed on a spectrum analyzer. This measurement setup completes the rectification as, in this configuration, the QCD detects optically the microwave signal. The setup for optical characteristics is presented in figure 3.25.

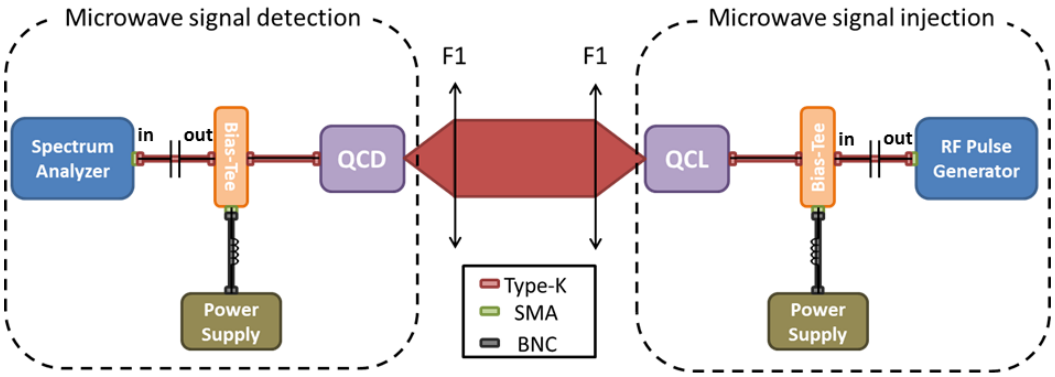

FIGURE 3.25: High frequency optical measurement setup with a QCL as an RF source and QCD for the detection.

Light from a QCL is modulated by a RF source through a bias tee. The laser beam is collected from the QCL and focused on the active area of the detector thanks to two F1 lenses. The total electrical output signal of the QCD goes through a second bias tee where the RF signal is measured thanks to a spectrum analyzer.

The QCL as well as the QCD is in a cryostat and it is biased through a launcher (setup **II**). The electrical circuit including cables and connectors is the same for the laser and the detector. Figure 3.26 shows a photo of the measurements setup with the two cryostat for the QCL and the QCD.

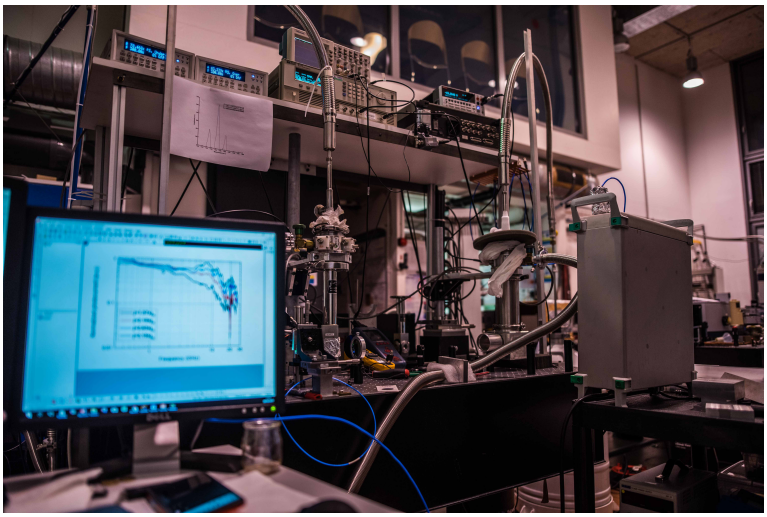

FIGURE 3.26: Photo of the measurements setup for optical high frequency detection with QCD (credit: Etienne Rodriguez).

In order to measure the frequency response of the QCD we sweep the modulation frequency of the laser bias. Using a spectrum analyzer we measure the intensity of the detected signal on the QCD at the modulation frequency. As background reference, we perform the same experience and we hide the optical signal with a MIR absorbing material.

Figure 3.27 shows three typical measured spectra at 3 GHz, 8 GHz and 9 GHz. Black curves correspond to the signal and red curves to the background.

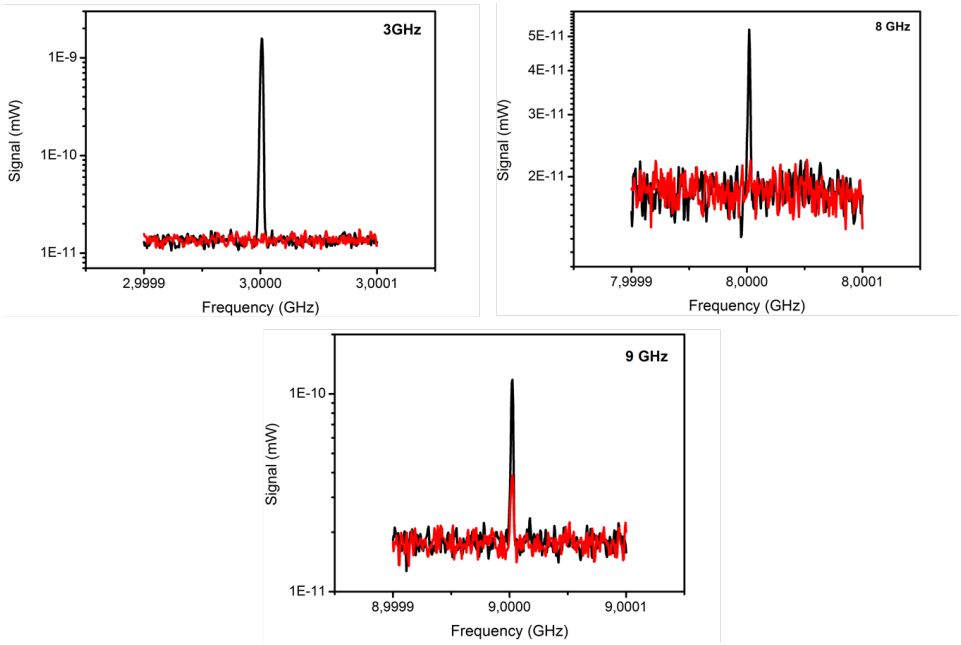

FIGURE 3.27: Spectra of high frequency optical measurements at frequencies of 3 GHz, 8 GHz and 9 GHz using the QCL as a RF source and a QCD with 50 μm mesa size as a detector. The QCL was at 78 K and the QCD at room temperature. Black color spectrum represents the signal and red the background.

We can see from figure 3.27 that at 3 GHz the ratio of signal over the noise is 100. This ratio decreases as we increase the frequency. At 9 GHz we can see that even by hiding the laser beam, we can see a signal at the injected frequency. This peak is not due to optical transfer of the RF signal but is due to RF pick-up noise.

By performing a sweep of the laser frequency and extracting the value of the signal and the noise at the injected frequency, we obtain the results of figure 3.28 that represents the signal minus the noise value for each injected frequency. The values presented in figure 3.28 are for a mesa size of 50 μm biased at -0.22 mV. The RF power injected to the QCL was equal to -5 dBm.

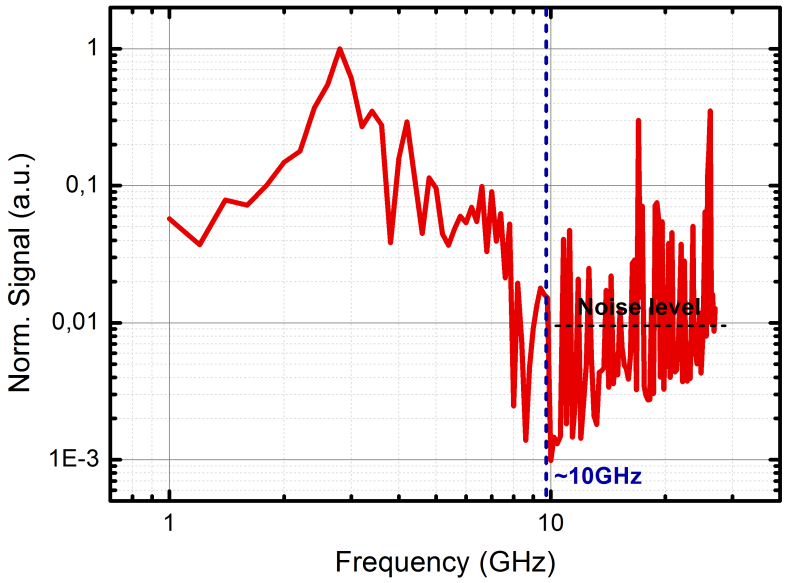

FIGURE 3.28: Modulated signal as function of the modulation frequency for a QCD size of 50 μm at 78K obtained using the optical measurement setup with RF power of -5 dBm injected to the QCL.

A signal is observed up to 10 GHz with the 50 μm mesa. At higher frequencies, the noise level is too high to measure the modulated signal.

We then perform an analysis of the influence of QCD dimension on the optical high frequency response. For this study we had to replace the laser source. The high frequency performances of this source are lower than the one of the laser used in the previous experiments. Indeed in this case the frequency response of a 50 μm mesa is limited at 5.4 GHz (figure 3.29 a)) despite of results presented in figure 3.28. We perform same measurements for a 10 μm mesa and we see a flat frequency response up to around 4 GHz (figure 3.29 b)).

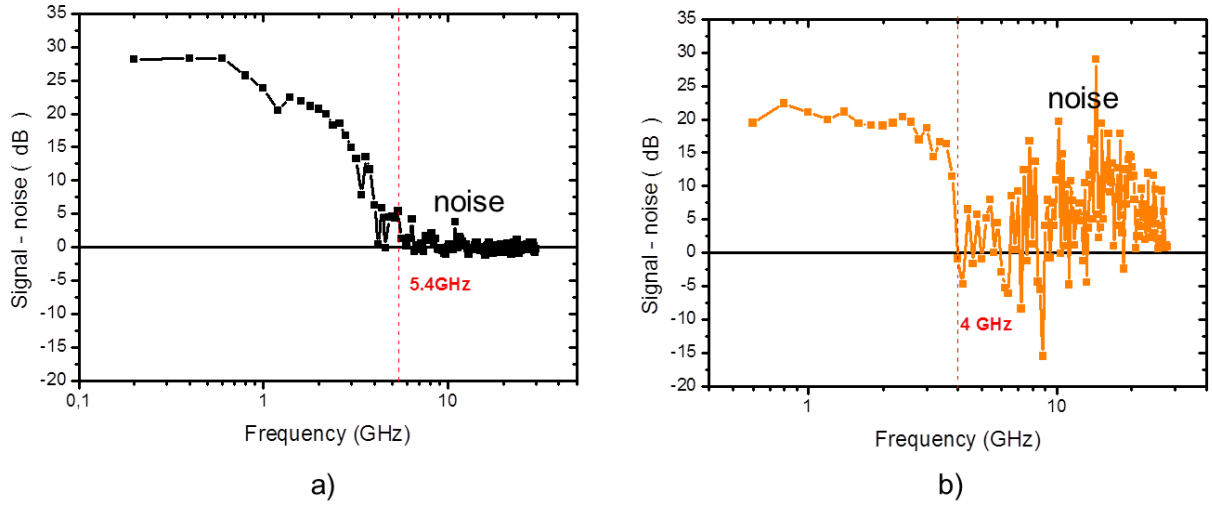

FIGURE 3.29: Modulated signal as a function of the frequency for the QCD of size a)50 μm and b)10 μm. The photocurrent measured for this experiment for the 50 μm QCD was more than the double of the one for the 10 μm.

In Figure 3.30 we compare the performances of the two mesas. We present the maximum of the normalized signal (solid line) and noise (dashed line) as a function of the injection frequency for 50 μm (black) and 10 μm (orange) mesa size. From this graph, we can see that for both of the QCDs, the noise level is low at lower frequency up to 4 GHz. After 4 GHz, a drastic increase in the noise level is observed. This increase prevents the measurement at higher frequency (figure 3.29).

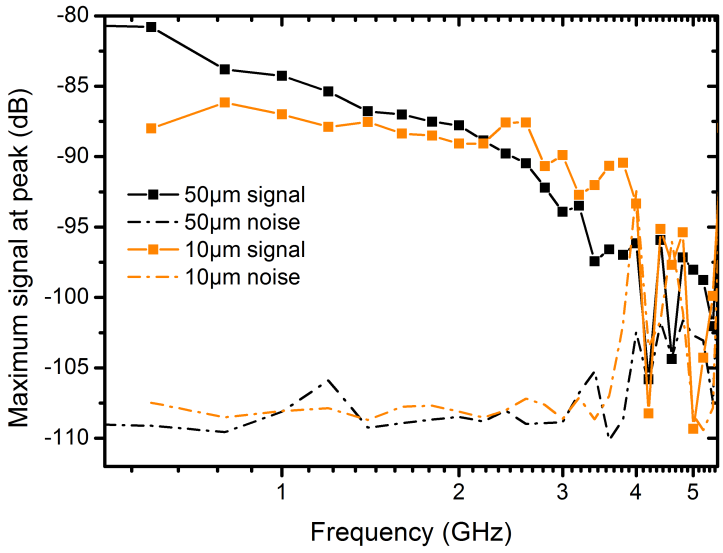

FIGURE 3.30: Signal and noise as a function of the frequency for the QCD of size a)10 μm and b)50 μm.

Figure 3.31 compares the rectification measurements of the two mesa sizes 10 μm and 50 μm presented in figure 3.23 with the HF signal measured and presented in Figure 3.29.

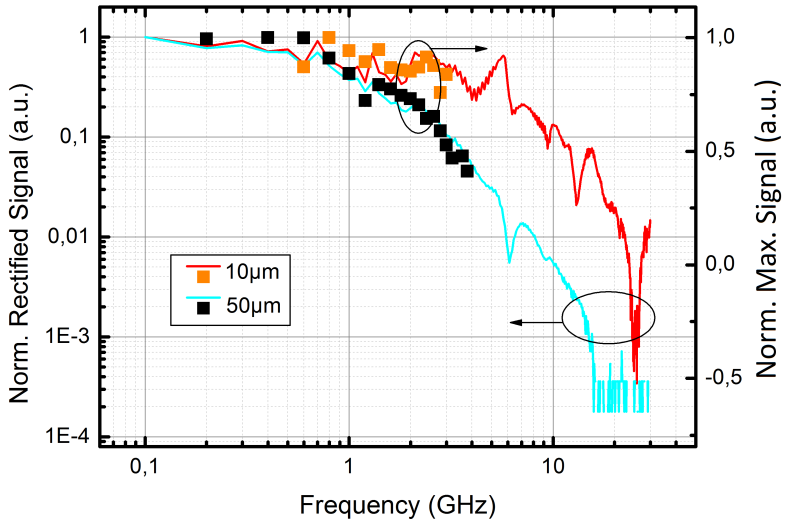

FIGURE 3.31: Rectification measurements in solid line compared to HF optical signal for the 10 μm and 50 μm mesa sizes.

From this figure, we can notice that the intrinsic HF response of each QCD follows very well the optical response measured with the QWIP.

Our optical measurements are limited in one side by the QCD itself which we assume that comes from the capacitance that we have developed in section 3.3.1, and on the other side by the noise level of the QCL at higher frequency.

4 High frequency QCL

Contents

In this chapter we explore two of the main applications of fast amplitude modulations of laser emitting in the MIR: frequency comb and free space optical communication. After an introductory part on quantum cascade lasers and their operation under high frequency modulation, we present two new high frequency designs for these sources. High frequency modulation experiments have already been demonstrated in the group using a microstrip geometry. Laser was embedded between two metallic plates as in microwave lines. Cutoff frequency of 15 *GHz at* 9 *µm and injection locking over MHz range has been demonstrated. Despite of state of art results, the drawback of this solution was an extremely low yield in the fabrication process. In this chapter we present the integration of buried heterostructure laser in a plug and play mounting, commercially available. We perform high frequency characterization using an ultrafast QWIP provided by an external laboratory (laboratory of Key Laboratory of Artificial Structures and Quantum Control). We report for this design high frequency modulation up to around* 5 *GHz. In order to improve this result we explore the influence of the metal contact size on the high frequency modulation and we combined it with the plug and play mounting. We perform numerical simulation to careful design the high frequency devices. We demonstrate the improvement of optical high frequency modulation with a cut off frequency of around* 10 *GHz. In addition, we present the generation of a comb in the mid-infrared for a plug and play mounted laser and locking of its inter-mode frequency over* 2.5 *MHz, a higher range compare to the micro strip laser (*1.5 *MHz) in the same conditions. In the last part of the chapter we study the laser performances in communication experiments with eye diagram characterization using a ultrafast oscilloscope. In addition we demonstrate free space optical communication at* 4 *Gbit/s in collaboration with J. Sarrazin of the University Pierre et Marie Curie. The transmitted signal is modulated using a Binary Phase-Shift Keying (BPSK), therefore each symbol codes one bit of information. The effective occupied bandwidth of the signal is* 7.8 *GHz thanks to a raised-cosine filter with a roll-off factor of* 0.95*, centered about a carrier frequency of* 3.95 *GHz. A bit error rate of nearly* 10^{-5} *is reached for an optical power of about* 20 *dBm. This value is a promising result for QCL based free space optical communication.*

4.1 QCL

Quantum cascade lasers (QCL) are semiconductor light sources based on intersubband electron transitions in coupled QW systems [Faist et al., 1994].

Figure 4.1 presents schematically the band structure of a typical QCL. It represents two periods of a QCL where each of them is divided into two different zones: emission and injection/extraction zone.

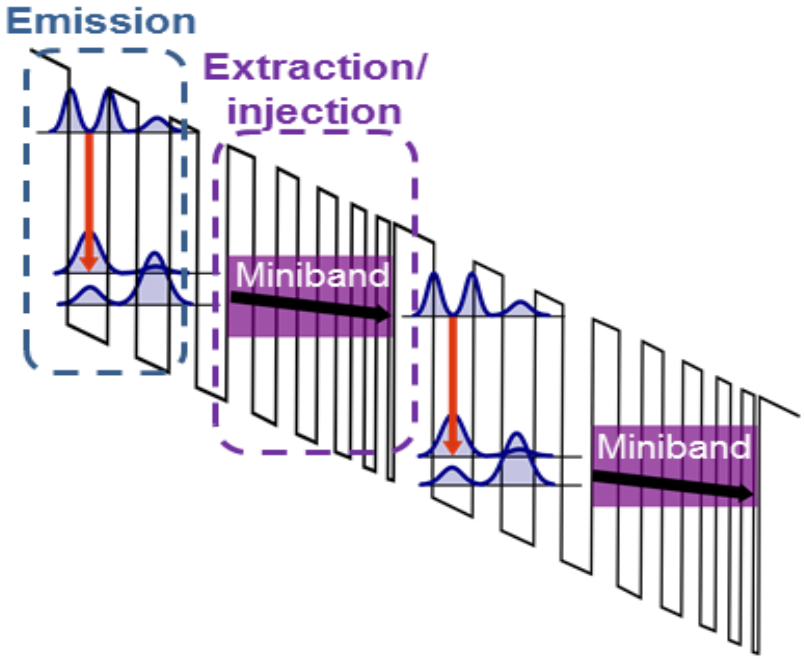

Figure 4.1: Band structure of a quantum cascade laser under an applied bias.

Population inversion takes place in the emission region and electrons transit from one period to the following through the extraction region. ISB transitions lifetime in the QCL are in the order of *ps*. QCL amplitude modulation can then attend high frequency values in the tens of *GHz* range.

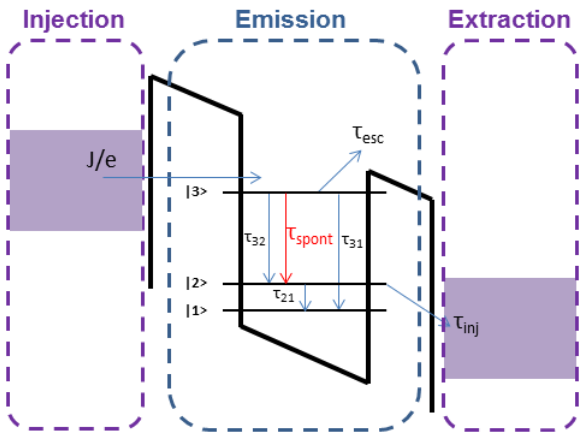

Figure 4.2: Scheme of the working principle of the emission zone of the QCL with the three-level system.

In more details, the emission zone can be represented by a three levels system (see figure 4.2). Electrons are injected in level 3. Radiative transition takes place between levels 3 and 2 and lower lasing state is depleted via 2-1 transition. Population inversion is attended if $\tau_{32} > \tau_2$. The injection/extraction zone is the bridge between the level 1 of one period and level 3 of the following one. At the same time, it prevents leakage current to the continuum and it favors electronic transport through the emission zone. In the approximation of perfect injection efficiency, the total non radiative carrier lifetime of level 3 (τ_3) is related to the optical phonons diffusion between level 3 and 2 (τ_{32}), level 3 and 1 (τ_{31}), from level 3 to the continuum of the injection zone (τ_{esc}) and spontaneous emission (τ_{spont}).

$$\tau_3^{-1} = \tau_{32}^{-1} + \tau_{31}^{-1} + \tau_{esc}^{-1} + \tau_{spont}^{-1} \qquad [s^{-1}] \tag{4.1}$$

The total non radiative carrier lifetime at level 2 (τ_2) is related to the optical phonons diffusion between level 2 and 1 (τ_{21}) and between level 2 and the miniband of the adjacent injection zone (τ_{inj}).

$$\tau_2^{-1} = \tau_{21}^{-1} + \tau_{inj}^{-1} \qquad [s^{-1}] \tag{4.2}$$

In this approximation, laser rate equations are:

$$\begin{cases} \frac{dn_3}{dt} = \frac{J}{e} - \frac{n_3}{\tau_3} - \sigma S(n_3 - n_2) \\ \frac{dn_2}{dt} = \frac{n_3}{\tau_{32}} + \sigma S(n_3 - n_2) - \frac{n_2 - n_2^{th}}{\tau_2} \\ \frac{dS}{dt} = (\sigma(n_3 - n_2) - \frac{c}{n_{eff}}\alpha)S + \beta\frac{n_3}{\tau_{spont}} \end{cases} \tag{4.3}$$

where n_{eff} is the effective refractive index of the QCL cavity and n_i the electron density per period on states i. n_2^{th} corresponds to addition of electrons from the injection zone to the level 2 due to temperature[1]. J is the current surface density and σ the optical cross section. $\alpha = \alpha_m + \alpha_c$ corresponds to the optical losses per unit length of the system with $\alpha_m = \frac{1}{2L} ln(\frac{1}{r_1 + R_2})$ the distributed losses due to the mirror facets (with L the cavity length and R_1 and R_2 the reflectivity of the two mirrors of the cavity) and α_c the cavity losses. β is related to the amount of spontaneous emission coupled with the mode. This coupling factor is really small ($\beta \approx 0.001$) and $\tau_{spont} \gg \tau_3$, so we can neglect the spontaneous emission in our equations above threshold. In these approximations and by assuming $n_2 = 0$ equation 4.3 becomes:

$$\begin{cases} \frac{dn_3}{dt} = \frac{J}{e} - \frac{n_3}{\tau_3} - \sigma S n_3 \\ \frac{dS}{dt} = (\sigma n_3 - \frac{1}{\tau_{phot}})S \end{cases} \tag{4.4}$$

with $\tau_{phot} = \frac{n_{eff}}{c\alpha}$ the photon lifetime in the cavity.

From rate equations we can model the response of QCL to HF modulation. If we consider a current modulation at pulsation ω, the current surface density J is equal to:

$$J = J^0 + \tilde{J} exp(i\omega t) \tag{4.5}$$

We assume low signal approximation so $\tilde{J}/J^0 \ll 1$ around the stationary solution J^0.

[1] $n_2^{th} = n_{inj} exp(-\frac{\Delta_{inj}}{k_B T})$

The current modulation changes the electronic surface density in level 3 (n_3) and the photon surface density (S). In the low signal regime (i.e. $\tilde{n}_3/n_3^0 \ll 1$ and $\tilde{S}/S^0 \ll 1$):

$$\begin{cases} n_3 = n_3^0 + \tilde{n}_3 exp(i\omega t) \\ S = S^0 + \tilde{S} exp(i\omega t) \end{cases} \tag{4.6}$$

with n_3^0 and S^0 the stationary values for the surface density of respectively electrons and photons. By deriving the equations 4.6 and using the expression of equation 4.5 in equations 4.4, we obtain the frequency response of the photon density as function of the injected current density:

$$\tilde{S} = h(\omega)\frac{S^0}{J^0}\tilde{J} \tag{4.7}$$

with $h(\omega)$ the transfer function where its modulus is equal to:

$$|h(\omega)| = \sqrt{\frac{1}{1+\omega^4\tau_{phot}^2\tau_{stim}^2 + \omega^2\tau_{phot}\tau_{stim}(\frac{\tau_{phot}\tau_{stim}}{\tau_3^2} + \frac{\tau_{phot}}{\tau_{stim}} + 2\frac{\tau_{phot}}{\tau_3} - 2)}} \tag{4.8}$$

We see from equation 4.8 that the frequency response of the QCL depends on: the photon lifetime in the cavity (τ_{phot}), the carrier lifetime of the level 3 (τ_3) and the stimulated emission time (τ_{stim}) defines as:

$$\tau_{stim}^{-1} = (\frac{J}{J_{th}} - 1)\tau_3^{-1} \tag{4.9}$$

With representative values of $\tau_3 = 0.6\ ps$, $\tau_{phot} = 11\ ps$ and $n_{eff} = 3.2$ we model the QCL frequency response in the low signal approximation. In figure 4.3 we present the response as a function of the operating current.

An increase of the frequency cutoff is reported in the inset of the figure 4.3. We show that the expected response can attend tens of GHz thanks to ultrafast dynamics of ISB transitions. This result is superior to expected performances of interband devices such as laser diode. Due to longer lifetime in interband devices, relaxation oscillations dynamics can take place, limiting their HF performances.

4.2 QCL for HF modulation

There are two main applications of fast amplitude modulations of laser emitting in the MIR: Frequency comb generations ans FSO. In this work we explore both of them and main results are reported in the following.

HF modulation experiments have already been demonstrated in the group with cutoff frequency of 15 GHz at 9 μm with QCL using a microstrip geometry. Injection locking over MHz range has also been reported. Laser was embedded between two metallic plates as in microwave lines. Despite of state of art results, the draw back of this solution was an extremely low yield in the fabrication process. In this work we explored two novel solutions compatible with the state of the art of buried heterostructure process.

In the first, we integrate buried heterostructure laser in a plug and play mounting. We demonstrate optical HF modulations up to 4 – 5 GHz. In the second one, we explore the influence of the metal contact size on the high frequency modulation and

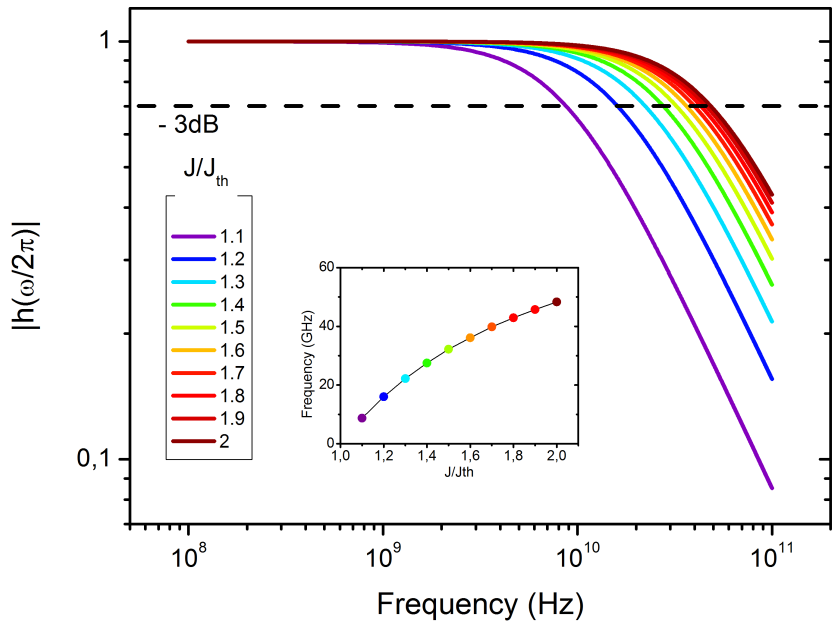

FIGURE 4.3: Frequency response of the MIR QCL for different values of current density.

we combine it with the plug and play mounting to demonstrate FSO communication at 4 $Gbit/s$.

In this thesis, we study buried heterostructure based on InGaAs/InAlAs quantum wells grown on InP substrate by MBE [Calvar et al., 2013]. An SEM image of the facet of the QCL is shown in figure 4.4. After etching of the waveguide (the active region), the sample is planarized by regrowth of Fe-doped InP on the side walls of the etched laser ridges. n-doped InP is also grown on top of all the structure to ensure the top contact.

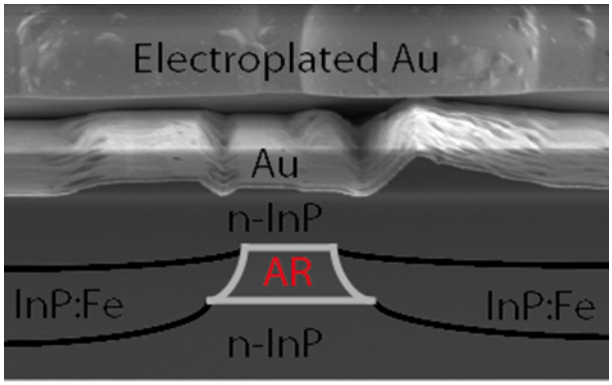

FIGURE 4.4: SEM image of the facet of a buried heterostructure QCL with the different layers. AR is the active region of the QCL.

This is made of evaporated Ti/Au with a thickness of 10/200 nm. Subsequent

electrolytic plating of a thick gold layer (4 μm) on the top contact concludes the device fabrication. The devices were cut at different lengths (corresponding to different Fabry-Perot cavity lengths) and Indium soldered to Copper holders for optimal heat dissipation. The Copper holder is screwed in a cryostat with an Indium paste again to ensure an optimal heat dissipation. Device temperature was monitored by a temperature sensor installed close to the device.

The heat dissipation is an important aspect for the experimental measurement since operating temperature of the QCL has to be stabilized in order to perform HF experiments. For this reason, we chose to use a constant nitrogen flux to keep stable the temperature of the emitting QCL.

4.2.1 Plug and Play system

In this scheme, a HF connector is directly soldered on the QCL. This mounting is compatible with plug and play operation. We used MOLEX with similar performances as explained in chapter 3.

Figure 4.5 presents a photo of the QCL with the MOLEX connector soldered on the top contact.

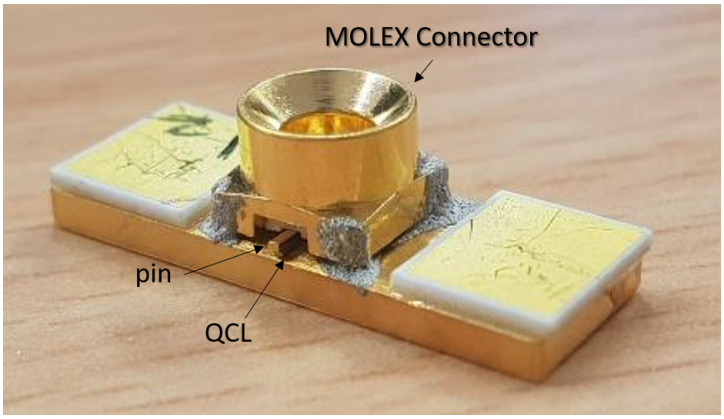

FIGURE 4.5: Photograph of a QCL mounted in the plug and play system with the MOLEX soldered to the gold coated submount.

Using this configuration, light-current-voltage (L-I-V) characteristic of the QCL are obtained and presented in figure 4.6. 2450 Source meter Keithley is used in current source and measuring bias. To collect the emitting light from the QCL, a lens is positioned in front of the window of the cryostat and focused the beam on a power meter. The power meter that we use is a thermal power meter from OPHIR.

Figure 4.6 presents the L-I-V characteristic of a laser with an active region width of 14 μm and a cavity length of 3.2 mm. The measurement is done in CW operation and at an operating temperature of 180 K.

The current threshold is equal to $I_{th} = 225\ mA$ that corresponds to an applied bias of 10.1 V. Hundreds of mW of output power have been measured. This result shows that plug and play mounting of the sample keeps good performances compatible with HF experiments.

Following the rectification setup measurement explained in chapter 3 section 3.19, we have measured the frequency response of the QCL.

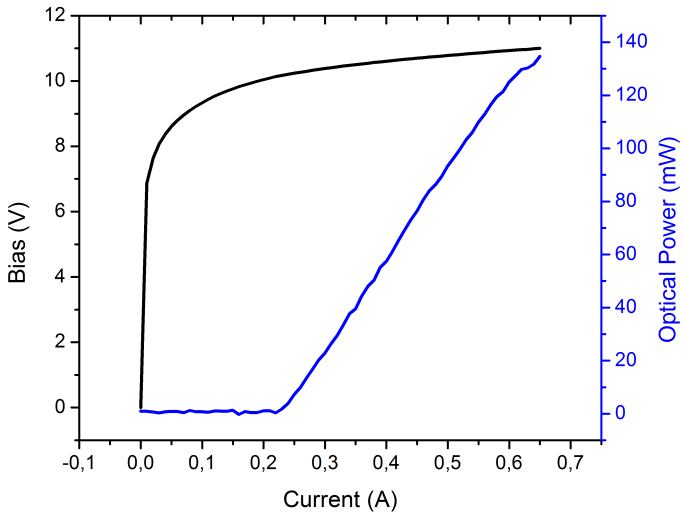

FIGURE 4.6: L-I-V measurement of QCL operating in CW at 180 K at $\lambda = 5\ \mu m$.

Figure 4.7 presents the rectified signal of the QCL at 180 K with an RF power of 10 dBm for different operating current.

We can see from figure 4.7 a frequency response at $-3\ dB$ around 1 GHz. The rectification signal is the same if the QCL operates (above threshold) or not (below threshold). However, around the threshold, where the laser starts to work, we can see an increase in the frequency response around 14 GHz (see inset of figure 4.7). The frequency of this peak response corresponds to the round-trip frequency within the Fabry Perot cavity of our QCL.

Indeed successive modes in a Fabry Perot laser are separated by the round-trip frequency of the cavity. This frequency gives important insight on the noise of the laser modes.

In more details, the total electric field E(t) of N modes propagating in the laser cavity is written as:

$$E(t) = \sum_{k=0}^{N-1} E_0 cos(\omega_0 t + k\Delta\omega t + \phi_k(t)) \tag{4.10}$$

with E_0 the amplitude of the longitudinal modes, ω_0 the smallest angular frequency, ϕ the phase of the mode and $\Delta\omega$ the angular round trip (beta note) frequency of the cavity that is equal to:

$$\Delta\omega = 2\pi\Delta\nu = 2\pi\frac{c}{2n_g L} \tag{4.11}$$

with c the speed of light, L the cavity length and n_g the group index.

In our case, for 3.2 mm cavity length, we expect a beat note of

$$\Delta\nu = \frac{c}{2nL} = 13.8Ghz \tag{4.12}$$

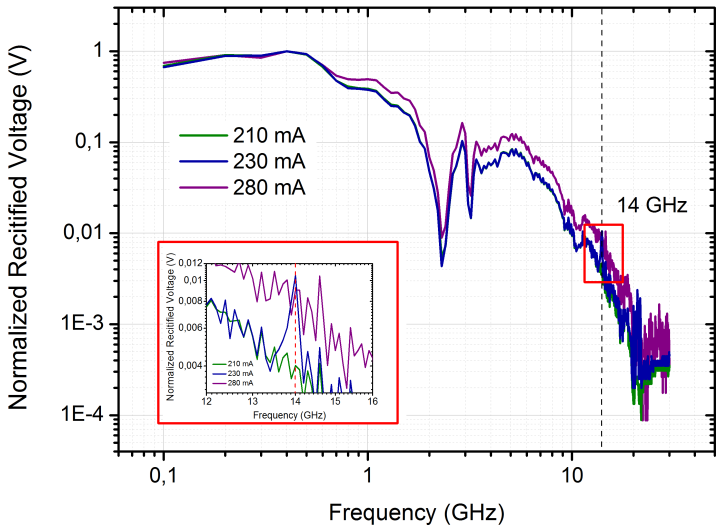

FIGURE 4.7: Frequency response of a QCL with 3 mm long and 14 μm active region width. The RF input power is equal to 10 dBm and the measurements are done at 180 K for different QCL current.

with $n = 3.4$ the refractive index of the AR (InGaAs) and $L = 3.2$ mm the Fabry-Pérot cavity length.

A microwave field at $\Delta\omega$ frequency rises from the beating of the different optical modes in the cavity and it is named the beat note. This peak in the frequency response at the beat note has never been observed in rectification measurements. In our plug and play setup, this characteristic might has been favored by non-linearities of the QCL [Saint-Jean, 2015].

In order to measure the HF optical signal emitted by the laser we used a QWIP developed by H.C Liu of the laboratory of *Key Laboratory of Artificial Structures and Quantum Control* [Liu et al., 2001]. The surface area of the QWIP is 120 $\mu m \times 170$ μm and it has an estimated cutoff frequency of 65 GHz [Grant et al., 2006]. Figure 4.8 presents the spectral response of the QWIP that is around 10 μm with a FWHM of 260 cm^{-1}. In this measurement, the QWIP is biased at $+4$ V for a signal detection without a significant electrical dissipation in the detector. All the different components of the experimental setup are similar to the ones of Figure 3.25.

Using the QWIP with a doping of $1{\times}10^{12}$ cm^{-2}, and the same setup for optical HF modulation explained in section 3.3.2 in chapter 3, we measured the modulation of the QCL output power with the QWIP. We vary the modulation frequency from 0.1 GHz to 26.5 GHz by steps of 300 MHz. Figure 4.9 presents the frequency response optically detected with the QWIP for an operating current of 350 mA of the QCL.

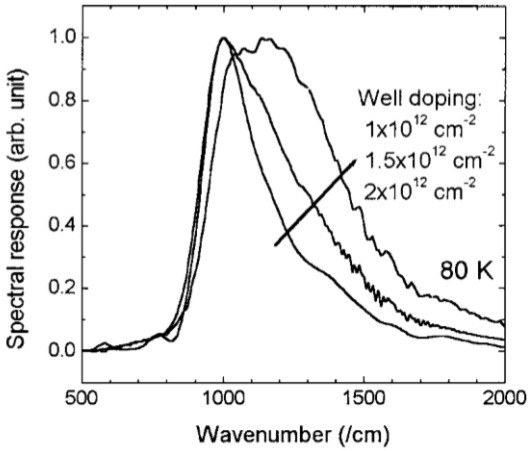

FIGURE 4.8: Spectral response QWIPs developed by H.C Liu for different doping [Liu et al., 2001]. The one used in this work for high frequency measurements is doped at $1 \times 10^{12}\ cm^{-2}$.

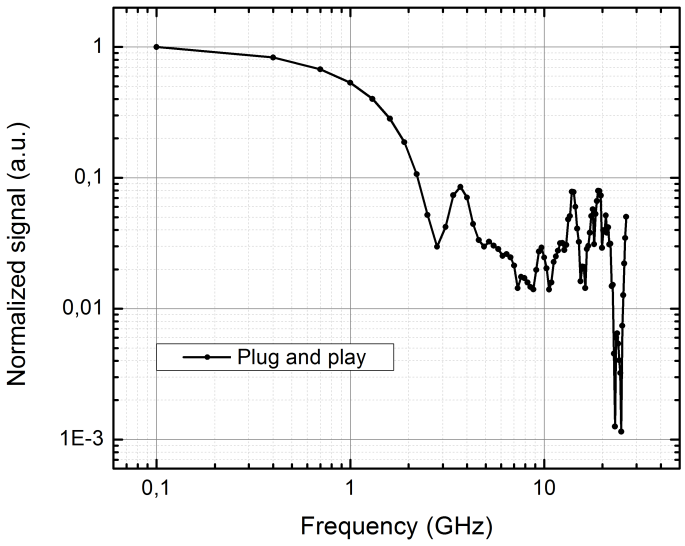

FIGURE 4.9: Normalized optical high frequency response of the QCL at 350 mA.

We observe $-3\ dB$ signal before 1 Ghz, and one order of magnitude loss at around 2 GHz. An absorption at 3 GHz is also observe which is probably due to an electrical component. From 3 GHz up to higher frequency the signal remains constant.

4.2.2 Narrow stripe

In order to further improve the performances, we have studied the influence of the top contact width in high frequency measurements.

The propagation of the microwave field in the laser cavity has been studied using commercially available finite-element software. By simulating an infinite long device we calculate the eigenmodes for a given frequency. The complex permittivities for the different semiconductor layers have been evaluated from their mobilities and the Drude model. We estimate the propagation losses in the structures from the obtained values of the complex refractive indexes and we calculate the effective figure of merit, defined as the ratio of the overlap of the microwave field with the active region over the propagation losses in the cavity. Simulations of the laser device for different widths of the top contact for a fixed waveguide width of 400 μm have been performed and results are presented in figure 4.10.

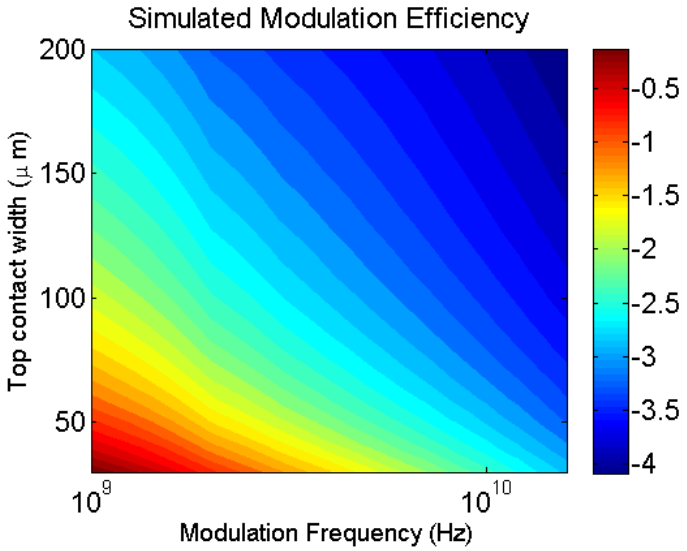

FIGURE 4.10: Figure of merit of the QCL for a varying top contact width. The X-axis is the width of the top contact. The Y-axis is the studied frequency. The color scale represents the figure of merit which is the ratio of the electric field within the AR over the propagation losses in the laser. So higher this value, better the confinement of the modes in the AR.

The figure of merit is reported in color scale as function of the top contact width and of the microwave frequency. As we observe, for a given frequency the maximum of the figure of merit is obtained for narrow top contact.

Following the experimental setup shown in figure 3.25 we measured the frequency response of the QCL with a narrow stripe in a plug and play configuration. We vary the modulation frequency from 0.1 GHz to 20 GHz by steps of 50 MHz and we measure the spectra of the photo current with the spectrum analyzer at the QCL modulation frequency. Figure 4.11 shows a comparison between the high frequency response with the plug and play system (in black) and with the narrow stripe laser (in blue). As expected improved performances are demonstrated. The frequency response of the narrow strip laser remains flat up to $5-6$ GHz where we have -3 dB cutoff frequency.

In order to understand the rapid decrease in response after 6 GHz, we have performed rectification and heterodyne measurements of the QWIP.

Figure 4.12 presents the rectification of the QWIP measured at an RF power of -10 dBm (green curve).

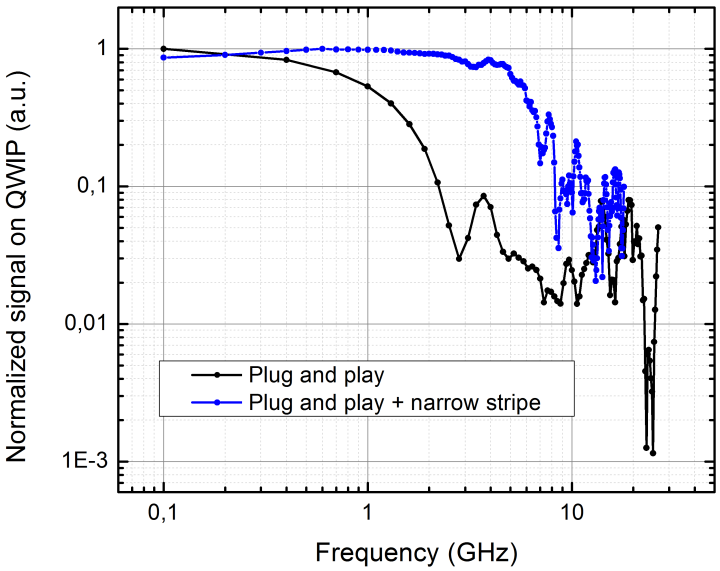

FIGURE 4.11: High frequency response of the QCL at $J/J_{th} \approx 1.3$ for the plug and play configuration (in black) and the narrow stripe geometry (in blue).

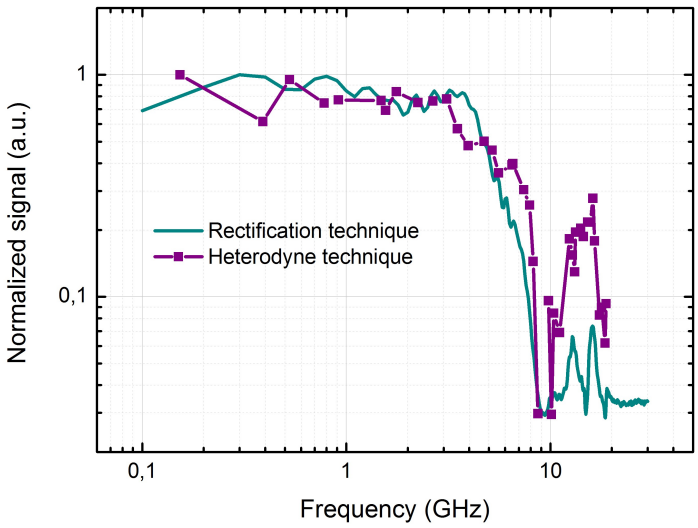

FIGURE 4.12: Frequency response of the QWIP using rectification technique at RF power of $-10\ dBm$ in blue and heterodyne technique in purple.

The optical detection of a high frequency signal using an heterodyne measurement setup is presented in Figure 4.12 in purple. This heterodyne measurement has been done using two QCLs at around 9 μm operating at room temperature stabilized with Peltiers. The result has been obtained in our group thanks to D. Gacemi and A. Bigioli.

We can notice an agreement in data, comparing the rectification measurement

of the QWIP and its high frequency response with the heterodyne setup. In Figure 4.12, we can see a flat response up to 4 GHz then a rapid decrease in the signal where one order of magnitude of signal is lost at around 8 GHz. Theses performances are inferior to the 65 GHz band-pass and we believe that this is due to possible damage of the chip.

Figure 4.13 presents the frequency response of the narrow stripe QCL presented in Figure 4.11 (blue curve) normalized by the frequency response of the QWIP presented in Figure 4.12. We observe a flat response of the QCL up to the noise level at higher frequencies.

The corresponding I-V curve of the laser operating at 77 K in CW mode is presented in the inset of figure 4.13. We would like to mention that this operating temperature is only limited by the specific performance of the available laser and not by the high frequency packaging used in this work.

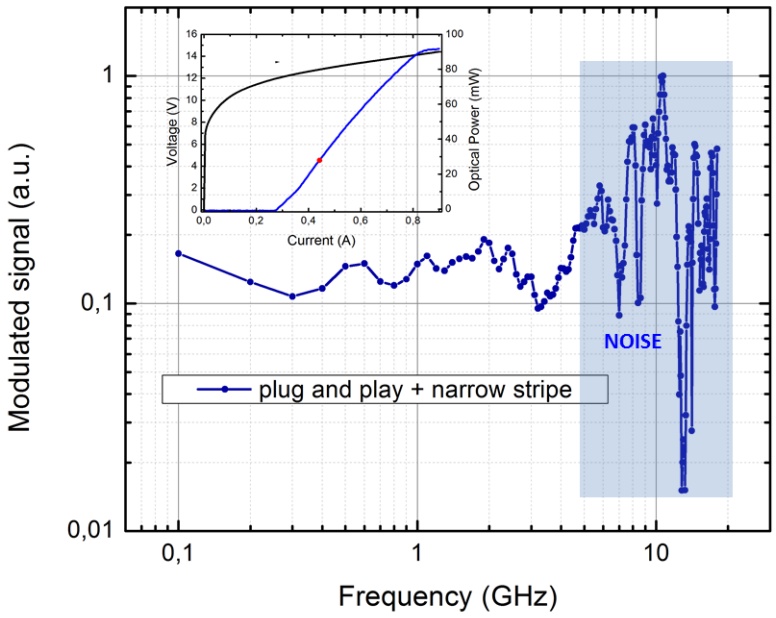

FIGURE 4.13: High frequency response of the QCL at 440 mA measured on a fast QWIP and normalized by the frequency response of the QWIP. The blue zone corresponds to the noise (inset: I-V curve of the QCL).

4.3 Applications of HF modulations

4.3.1 Frequency Comb

One of the main applications of MIR HF modulation is the comb generation. In this paragraph we present the generation of a comb at around 9 μm for a plug and play mounted laser and locking of its intermode frequency over 2.5 MHz, a higher range compared to the microstrip laser (1.5 MHz) in the same conditions [Saint-Jean, 2015].

An optical frequency comb is a coherent light source emitting a broad spectrum consisting of a set of equidistant modes in frequency space (see Figure 4.14).

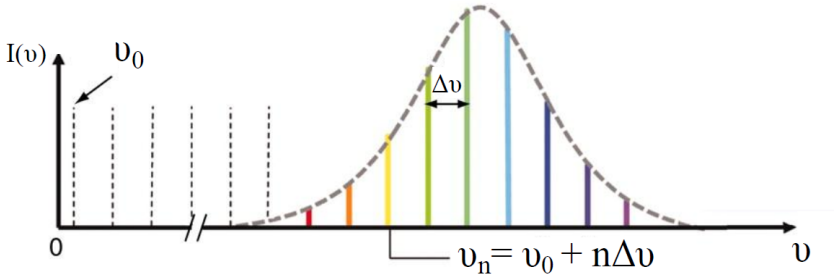

FIGURE 4.14: Optical spectrum of a frequency comb (ref: [Saint-Jean, 2015]).

In a frequency comb, the position of the n^{th} longitudinal mode (ν_n) in the optical spectrum is known exactly:

$$\nu_n = \nu_0 + n\Delta\nu \tag{4.13}$$

with ν_0 the frequency shift of the comb and n a natural number. In 2005, the physics Nobel prize was awarded to John L. Hall and Theodor W. Hänsch "for their contributions to the development of laser-based precision spectroscopy, including the optical frequency comb technique."[2]

Nowadays, frequency combs in the MIR have a broad spectral range (in the order few hundreds of cm^{-1}) with narrow beat note spectral linewidth (some Hz) and a total output power in the order of hundreds of mW [Wu et al., 2018].

One of the most interesting applications of frequency combs is the Fourier transform infrared spectroscopy. In this wavelength, instead of using a globar the frequency comb has the advantage of a faster spectrum acquisition with higher resolution [Adler et al., 2010]. Another application is the dual comb spectroscopy. Two frequency combs in the infrared with a slightly different operating wavelength can be used to generate a signal in the radio frequency domain using a heterodyne method [Villares et al., 2014].

In a more classical multimode laser, due to material dispersion and frequency broadening of the modes, the difference between the optical modes is not homogeneous limiting the generation of frequency combs. For QCL, the material dispersion can be engineered to be negligible and an optical spectrum where the modes are considered as equidistant can be obtained. However, because of cavity noise, the different modes oscillate around their frequency. In order to obtain a frequency comb, the different modes need to be fixed at their corresponding frequency.

A method to stabilize the modes in a QCL is to inject a stable hyperfrequency signal to modulate the amplitude of the signal. The modes can then be "locked" to the injected signal.

The injected signal modulates the amplitude of the electromagnetic field with a frequency of $\nu_m = \omega_m/(2\pi)$.

The electric field in the cavity is then expressed as:

[2] https://www.nobelprize.org/prizes/physics/2005/summary/

$$E(t) = (1 + mcos(\omega_m t)) \sum_{k=0}^{N-1} E_0 cos(\omega_0 t + k\Delta\omega t) \tag{4.14}$$

with m the modulation depth expressed between 0 and 1. In this equation we have neglected the noise in the resonator and we have fixed the phase to zero.

By developing the equation 4.14 we obtain:

$$E(t) = \sum_{k=0}^{N-1} [E_0 cos(\omega_0 t + k\Delta\omega t) + mE_0 cos(\omega_0 t + k\Delta\omega t) cos(\omega_m t)] \tag{4.15}$$

$$= \sum_{k=0}^{N-1} [E_0 cos(\omega_0 t + k\Delta\omega t) + \frac{1}{2} mE_0 [cos(\omega_0 t + k\Delta\omega t - \omega_m t) + cos(\omega_0 t + k\Delta\omega t + \omega_m t)]] \tag{4.16}$$

From the equation 4.16 we can see that when the signal is modulated, sidebands appear around the cavity modes spaced by a frequency of ω_m. Now, if the injection frequency is equal to the difference between two consecutive modes of the cavity, the generated sidebands are injected to the adjacent modes which are consequently coupled. This phenomenon is known as injection locking technique (see Figure 4.15).

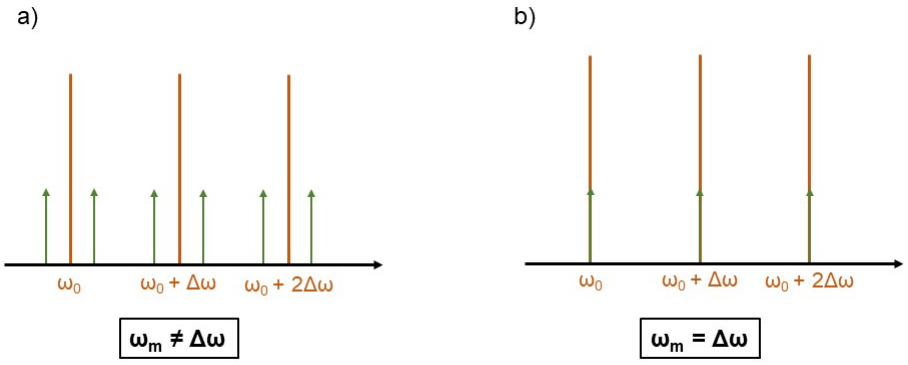

FIGURE 4.15: Amplitude modulation when the modulation frequency is a) different from the free spectral range or b) equal to the free spectral range ($\Delta\omega$).

If the coupling is strong enough, the injection locking has a given range over which the system is still locked . Thus $\Delta\omega$ is not only due to the cavity properties but it can be controlled directly with the external source all over the locking range.

It has been demonstrated that the locking range $\Delta\omega_{lock}$ is equal to:

$$\Delta\omega_{lock} = \frac{2\omega_0}{Q} \sqrt{\frac{I_1}{I_0}} \tag{4.17}$$

with I_1 and I_0 the intensity of the amplitude of the electromagnetic field of respectively the injected signal and the QCL outside the cavity. Q is the quality factor of the QCL [Saint-Jean, 2015], [Stefano Barbieri and Sirtori, 2007].

In the intermediate case, where the laser is not locked but has interaction with the injection, the oscillation frequency between the beat frequency and the injection frequency (ω_1) is equal to:

$$\omega_{osc} = \omega_0 + \frac{\omega_0^2}{Q^2}\frac{I_1}{I_0}\frac{1}{2(\omega_1 - \omega_0)} \tag{4.18}$$

As a result, the free running oscillation will not be located at ω_0 but at a slightly shifted frequency ω_{osc}. This phenomenon is known as the pulling effect, where the injected signal pulls the free running oscillation away from ω_0 and toward the injected signal frequency ω_1.

From equation 4.18 we can see that the pulling effect increases linearly with the intensity of the injected signal, and decreases with the distance between laser beatnote and modulation frequencies ($\omega_1 - \omega_0$). This phenomenon is well schematized and explained by Siegman in his book [Siegman, 1986] and adapted to laser RF modulation during M.Renaudat St-Jean's thesis [Saint-Jean, 2015].

In this work we report experimental demonstration of frequency comb generation in a plug and play scheme and locking of the intermode beat note over a range of 2.5 MHz.

Experimental setup for the beatnote characterization

For the beatnote injection characterization, we use an experimental setup based on the electrical characterization of the beatnote. The mid-infrared intracavity field is indeed considered as a modulation source that is detected as an electrical signal in the radio frequencies thanks to the intrinsic non-linearity of the laser I-V curve. Figure 4.16 shows the experimental setup for this measurement. This technique has been used for THz QCL by Gellie [Gellie et al., 2010] and for MIR QCL by Calvar and R.St Jean during their thesis [Calvar, 2013] [Saint-Jean, 2015].

The RF synthesizer is connected through a circulator to a bias-tee to perform amplitude modulation on the laser, with the latter being DC biased using a standard power supply. For the detection of the microwave signals, we use a spectrum analyzer. For this experiment we use a cavity laser with $L = 3\ mm$ and $w = 12\ \mu m$.

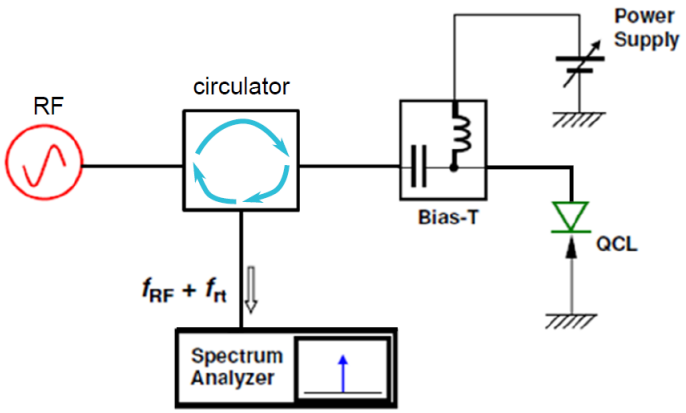

FIGURE 4.16: Setup for the characterization of the beatnote (ref: [Calvar, 2013]).

The injected frequency is varied and the RF signal is measured for each modulation frequency value. Typical results are presented in figure 4.17. In this scheme

we can measure the locking range for a given injected power. Measurements are normalized respect to the QCL beat note frequency and they start when the injected signal is 5 MHz apart from this. By approaching the injection frequency to the beat note, a pulling effect is clearly visible up to the moment where a single peak is measured and laser is locked to the RF source. Locking spans a 2.5 MHz range after which the free running beat note appears back.

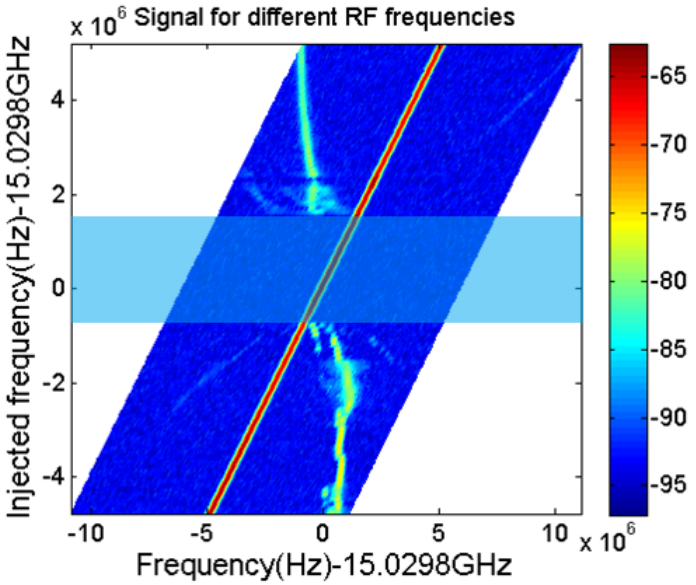

FIGURE 4.17: Measurements of the RF spectra from the QCL in plug and play configuration at a power of 10 dBm for different injected signal frequencies. The X-axis is the frequency of the signal measured on the spectrum analyzer. The Y-axis corresponds to the modulation frequency. In color scale is the intensity of the measured RF signal (dBm).

4.3.2 FSO Communication

In this work we report the experimental demonstration of FSO up to 4 $GBit/s$ using a narrow stripe laser. In order to evaluate the quality of free space communication two main characterizations have been performed: eye diagram and constellation measurements.

Eye-diagram

In high frequency communication, an eye diagram is a good indicator of the quality of the signal transmission. An eye diagram can rapidly be obtained thanks to oscilloscopes.

In order to obtain an eye diagram, a long data signal (bits) is divided into different segments by the oscilloscope. The time domain signal is driven by a clock from the oscilloscope triggered by a reference clock on the bit generator. Overlapping the traces of many bits produces an eye diagram, so called because the resulting image looks like the opening of an eye. Figure 4.18 shows a typical eye diagram presenting the different measuring parameters:

An eye diagram summarizes different important information about the quality of the signal transfer.

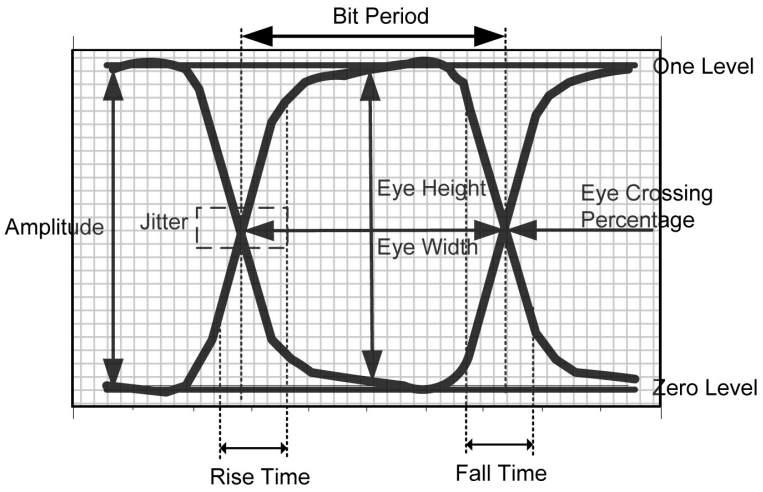

FIGURE 4.18: Scheme of an eye diagram (source: https://www.onsemi.com/pub/Collateral/AND9075-D.PDF).

- The eye's width defines the time interval over which the received signal can be sampled without error due to interference from adjacent pulses. Higher error make a thicker eye line so a shorter eye width (a more closed eye).
- The slope of the eye pattern determines the sensitivity of the system to timing errors, lower is the slope, higher are the possible timing errors.
- Jitter is defined as the noise in the photodetector and the pulse distortion during the transfer path.
- The symmetry of the eye pattern gives information about any non linearity of the channel transfer.

Having these information, we can choose the best point for communication protocol, where we have the best signal to noise ratio knowing the mount of Jitter.

In free space optical communication, data transmission at a rate of 2.5 $Gbit/s$ has been demonstrated using a QCL emitting at 8 μm at a temperature of 85 K [Capasso et al., 2002]. A QWIP has been used for the detection. Figure 4.19 shows the eye diagram obtained for this measurement.

Constellation Diagram

Constellation diagram completes the eye diagram for data transfer quality characterization. Indeed, with this technique we can estimate the error rate for a given configuration. Figure 4.20 represents a typical constellation diagram. This is a 2D graph where the x axis is called the "in-phase" axis and the y axis the "quadrature" axis. Each different symbol in the constellation diagram represents a piece of information depending on the encoding at the beginning. Each symbol is defined by a specific phase (ϕ) and amplitude (a). In figure 4.20 we have taken the example of a constant amplitude but with two carrier phases represented then by two distinct symbols in the constellation diagram. This is called a *Binary Phase Shift Keying* (BPSK) modulation. In that specific modulation, we can modulate one single bit per symbol. BPSK is the simplest way of phase shift keying modulation where the two symbols are separated by a phase of π.

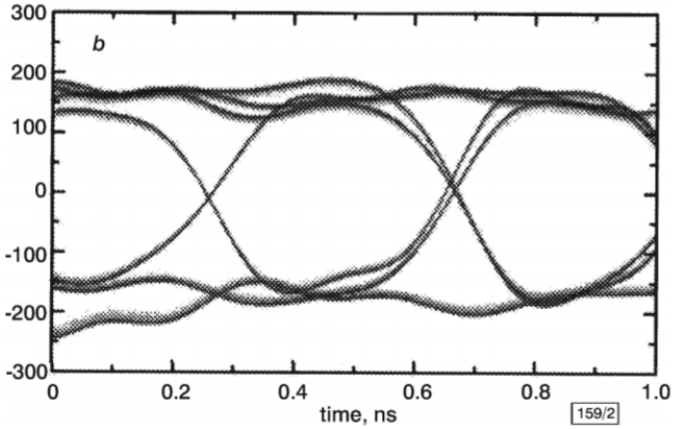

FIGURE 4.19: Eye diagram transmitter of a QCL at 85 K at a wavelength of 8 μm.

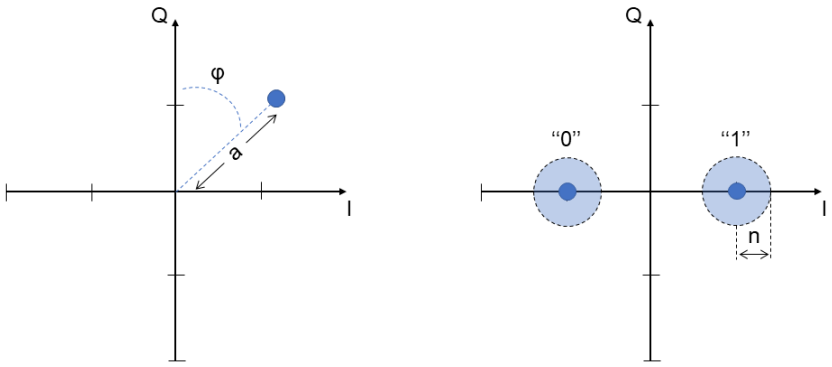

FIGURE 4.20: Scheme of a constellation diagram with symbol and their corresponding amplitude(a), phase (ϕ) and noise (n).

The noise accumulated from the transmission line and the decoder itself makes the symbol wider. The whole circle (represented in blue in Figure 4.20) represents where a received symbol is likely to appear as a result of being affected by a random noise. Thus, when symbols with their corresponding noise interfere, we will know the exact amount of signal to noise ratio, or in other words the bit error rate (BER) needed to decode correctly the information.

Results

In this paragraph, we present eye diagram measured for plug and play laser at 4 μm.

The experimental setup is similar to the setup at figure 3.25 except that the RF generator is replaced by a pulse pattern generator (Anritsu MP1763B) and the spectrum analyzer at the output of the QWIP is replaced by an oscilloscope (Teledyne Lecroy WaveRunner 6 Zi, band-pass of 4 GHz).

Using the pulse pattern generator we can either define the bit pattern directly on the generator or use the pseudo random mode with a defined frequency. We can also set the peak to peak bias value (maximum of 2 V).

Figure 4.21 shows an eye diagram for a pattern transfer of 1-0 using the oscilloscope at a frequency of 1 GHz per bits.

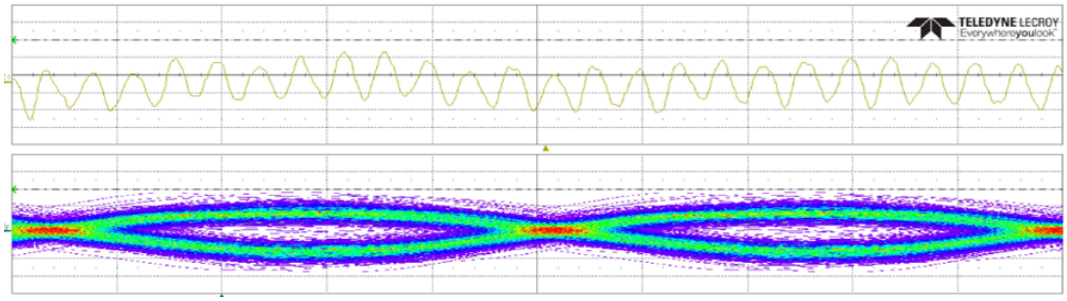

FIGURE 4.21: Top: Output signal of the QWIP (x-axis: 5ns/div; y-axis: 2mV/div). Bottom: Eye diagram obtained with the oscilloscope. The pattern injected to obtain the eye diagram is 1-0 at a frequency of 1 GHz and a peak to peak amplitude of 2 V (x-axis: 209ps/div; y-axis: 2mV/div).

We can not see in Figure 4.21 the one and zero levels. The eye width is equal to 980 ps (209 ps/div). The eye cross is at around 50%.

Figure 4.22 shows the output signal of the QWIP and its corresponding eye diagram for a pattern of 1-1-0-0-0 at 1 GHz. We can see the 0 and 1 level.

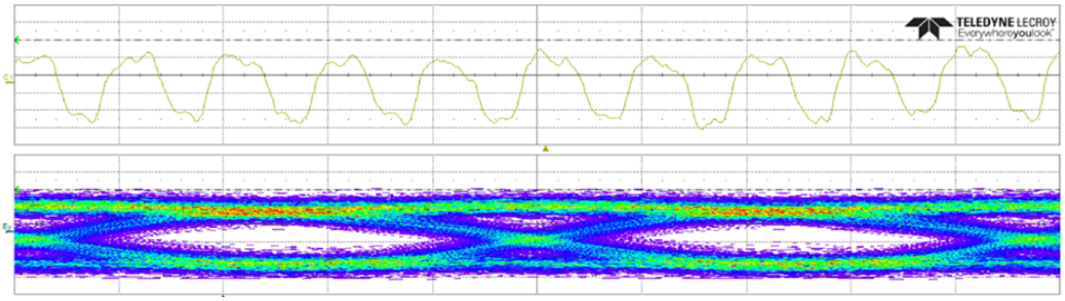

FIGURE 4.22: Top: Output signal of the QWIP (x-axis: 5ns/div; y-axis: 2mV/div). Bottom: Eye diagram obtained with the oscilloscope. The pattern injected to obtain the eye diagram is 1-1-0-0-0 at a frequency of 1 GHz and a peak to peak amplitude of 2 V (x-axis: 209ps/div; y-axis: 2mV/div).

Signal at higher frequency have been measured with averaging of the signal as function of the laser operating current. This measurement have been done using a similar QCL that emits also at around 9 μm. Figure 4.23 shows the different eye diagrams obtained with the oscilloscope. The peak to peak amplitude of the bit signal is set to 2 V and the frequency is 2.4 GHz with a succession of bit of 1-1-0.

We study the influence of the laser operating currents and results are reported in table 4.1.

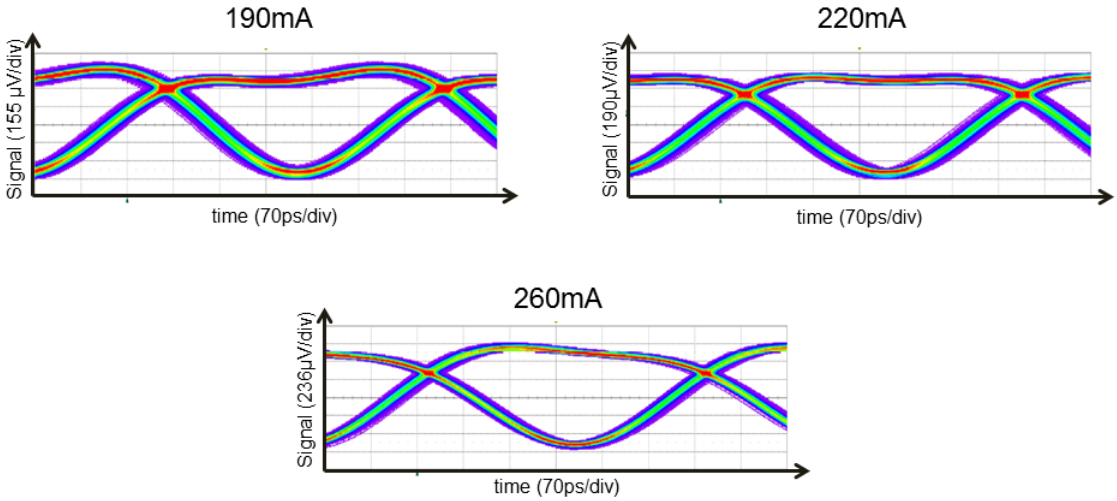

FIGURE 4.23: Eye diagram images obtained with the oscilloscope for different laser threshold. The pattern injected to obtain the eye diagram is 1-1-0 at a frequency of 2.4 GHz and a peak to peak amplitude of 2 V. In x axis the scale is 70 $ps/division$.

Current (mA)	Eye Height (μV)	Eye Amplitude (mV)	Eye Width (ps)	Eye Cross (%)
180	493	0.707	322	78
190	611	0.783	336	77
200	657	0.817	348	80
210	723	0.865	352	78
220	798	0.948	356	75
230	949	1.11	364	72
240	992	1.14	368	70
250	973	1.16	364	68
260	1002	1.19	374	67
270	947	1.14	370	64
280	955	1.13	376	64

TABLE 4.1: Table of the different parameters of the eye diagrams presented in figure 4.23

We can see that the eye diagram becomes wider as the QCL current increases, i.e. the eye height increases and it approaches the eye amplitude. In other terms, the eye is more "open" at higher operating currents. The bit pattern defined is 1-1-0, we expect then an eye cross of 66%. As the current increases, we see that this percentage is getting closer to the expected value.

Both results are in agreements with expected HF improvement of laser performances with higher operating current.

FSO at 4Gbit/s

In collaboration with Julien Sarrazin from Sorbonne Université, we have performed FSO experiments using a narrow stripe plug and play QCL emitting at 4 μm and an ultra fast QWIP. HF performances of both devices are reported in Figures 4.10 and

4.12 respectively. The transmission set-up is similar to the one depicted in Figure 3.25 except that the RF source has been replaced by a Tektronix Arbitrary Waveform Generator (AWG 7122B) and the spectrum analyzer by an Agilent 40 GSa/s real-time digital oscilloscope (DSO 91204A). The AWG is used to generate a signal occupying a bandwidth of 4 GHz using a raised-cosine filter with a roll-off factor of 0.95 (which leads to an effective occupied bandwidth of 7.8 GHz) centered about a carrier frequency of 3.95 GHz. After transmission by the QCL, the signal received by the QWIP is directly sampled and recorded by the scope. Figure 4.24 shows the spectrum of the theoretical transmitted signal (in red) as well as of the measured received signal (in black) for an optical power of 13.5 dBm. In the highest part of the spectrum, an attenuation is clearly observed which is due to the low-pass behavior of the RF components in the set-up between the AWG and the laser and between the QWIP and the scope (a strong attenuation is faced after 6 GHz).

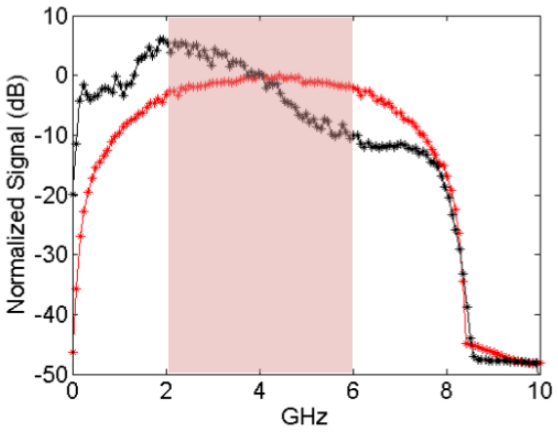

FIGURE 4.24: Spectrum of transmitted data in red and received data in black

The transmitted signal is flat from 2 Ghz to 6 GHz (4 GHz bandwidth). The received signal has an oscillating behavior in this frequency range respect to the measurements presented in Figure 4.10. This is probably related to the specific circuit used in this experiment.

The transmitted signal is modulated using a Binary Phase-Shift Keying (BPSK) modulation and therefore each symbol codes one bit of information. 10 frames of 10200 bits are sent 50 times each, which leads to a total of 5.1 millions of bits processed. A preamble mixing rate of 100 is used to compensate for the channel dispersive behavior. The demodulation is performed off-line in Matlab and the uncoded Bit Error Rate (BER) is plotted in Figure 4.25 for different optical powers that have been obtained by varying the current. As expected, the BER drops as the optical power gets higher. It can be observed that the 4 $Gbit/s$ transmission is effectively achieved with a reasonable BER using a modulation as simple as BPSK. Indeed, a BER of nearly 10^{-5} is reached for an optical power of 20 dBm. The BER obtained through this transmission technique is a promising value for QCL/QWIP free space optical communication.

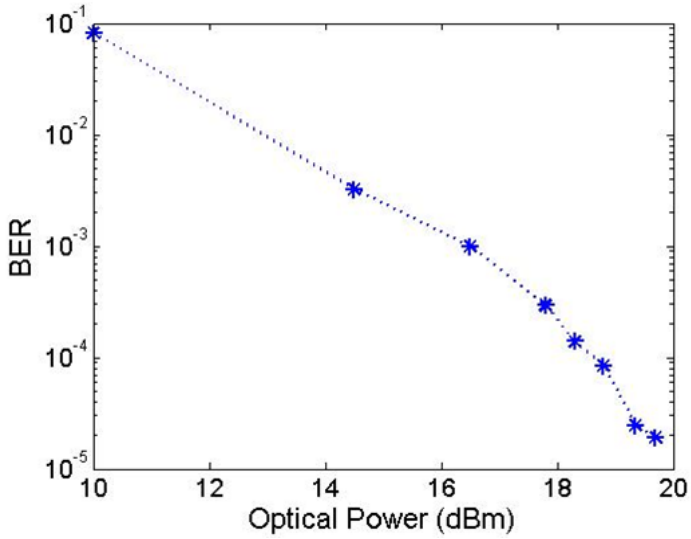

FIGURE 4.25: Bit error rate BER

The constellation diagram of the communication is presented in figure 4.26. In this constellation diagram we can clearly identify two symbols corresponding to two distinct bits.

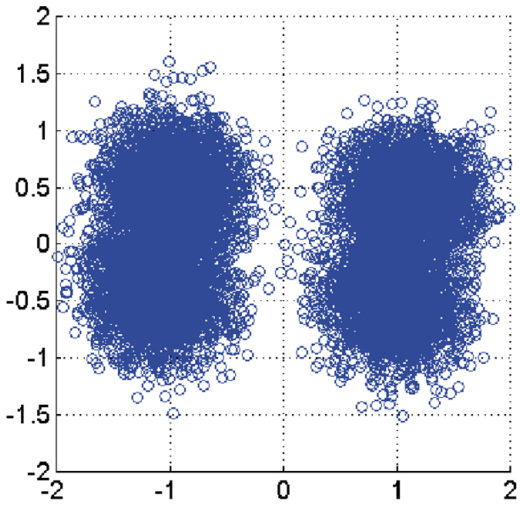

FIGURE 4.26: Constellation

We furthermore emphasized that the transmission achieved here uses a band-pass signal. So, taking into account the high modulation frequency of the QCL, using such a well-defined bandwidth is promising for enabling frequency multiplexing to transmit different channels over the same link in order to increase the overall throughput while limiting the hardware complexity. We have done these measurements for three different QCLs and the results shown here are for the best one that we have obtained.

5 Conclusion

Contents

5.1 Conclusion

The main goal of this thesis was to achieve a room temperature, high frequency, plug and play system to be exploited in MIR free space optical communication. We demonstrated high frequency characterization employing quantum cascade devices as lasers (QCL) and detectors (QCD).

In the first part, thanks to detailed study of the electrical and optical characteristics of the QCD, we explored and investigated novel operating regimes of such devices, an important step in the field of intersubband detectors. We have shown that QCD can operate at the same time in a cascade like regime or in a bound to continuum one according to the applied bias. It can indeed act as photovoltaic detector as well as photoconductive one. Photocurrent measurements under bias operation presented an increasing value above a given temperature. Spectral characterization of this signal revealed that this result comes from dark activated parasitic channels and not from the main optical transition at 5 μm. We have measured a BLIP temperature of 135 K with a competitive detectivity of 2.9×10^{11} $Jones$.

In the second part, we focused on the high frequency performances of QCD. We designed and realized square mesa shape devices with small surface (tens of micrometer side) to reduce parasitic capacitance. Thanks to an air-bridge technology, it has been integrated in a 50 Ω matched circuit, optimized for 40 GHz band pass. Performing rectification measurements we attended frequency band pass (frequency corresponding to a factor ten reduction) of 15.5 GHz, the highest reported for such devices. At the same time, using a QCL as sources, we were able to measure directly on the QCD at room temperature an optical signal modulated up to 5 GHz, limited by the available lasers. Thanks to a careful study of the high frequency performances of QCD measured by rectification as function of their geometrical size, we identified its capacitance as the limiting element, to attend the ultimate bandpass set by the electronic lifetime (of the order of tens of GHz). We showed that the parallel plate approximation, conventionally used to estimate device capacitance, fails for room temperature devices. Thermally activated levels induce a charge redistribution in the detector acting as an additional capacitance dominating over the parallel plate like contribution. Thanks to this work we established that a careful engineering of the electronic band structure of the detector is required in order to attend high frequency performances for room temperature detectors.

Toward the final goal of realizing an optical communication experiment we carried out an optimization work on the QCL sources. By reducing the surface area of the injection contact we attended flat frequency response to direct modulation up to 4.5 GHz and injection locking of the inter mode frequency and frequency comb generation over a 2.5 MHz range.

In the last part of our work, we have performed free space optical communication using an externally provided QWIP as a photodetector. We have measured binary signal transfer from the QCL to the QWIP by using an oscilloscope triggered with the pattern generator. We have then obtained eye diagrams for different optical output power and demonstrated improved performances with increasing laser operating current. Moreover, thanks to a collaboration with the laboratory L2E of the Sorbonne Université, we have transferred signals at 4 $GBps$ in the free space, which is, to our knowledge, the highest frequency for FSO communication using a QCL and a QWIP in the MIR. We have also performed constellation diagram using

binary phase shift keying modulation. The results are really promising as we were able to distinguish bit 0 from bit 1 over a large number of signal transfer.

5.2 Perspectives

In this part, we present different perspectives of this thesis.

5.2.1 Deign of the QCD

In the chapter 3, we have seen an important difference between the estimated capacitance of the QCD and the experimental one. This variation is due to a parasitic capacitance of the QCD. A parametric study needs to be done in order to understand the source of this additional capacitance that affects the high frequency performances of the device operating close to room temperature and under applied bias. The theory about the estimation of the capacitance has to be reviewed for QCDs regarding the different sub energy levels in quantum wells and the overlaping of them with temperature and bias variation.

5.2.2 Patch antenna geometry

In the mesa geometry with the 45° facet, the light passes through the substrate before reaching the active region. This has two consequences: there is a transmission coefficient that lowers the signal and only one polarization of the incident light is effectively coupled with the ISB transition, obeying the polarization selection rule.(see section 1.2.3 in the Introduction).

The geometry of the detector can be adapted for more efficient light coupling. Interesting results have been demonstrated for a device consisting of an array of square shaped microcavities with a bottom metallic ground and a top pattern layer. These photonic resonators are able to support guided transversemagnetic TM modes as standing waves at a resonant wavelength $\lambda = 2n_{eff}S$ where S is the size of the patch and n_{eff} is the effective index of the microcavity [Todorov et al., 2010]. The semiconductor layer sandwiched between the two metals has a thickness L (between few hundreds of nm up to few mum) much smaller than the wavelength of the confined electromagnetic field.

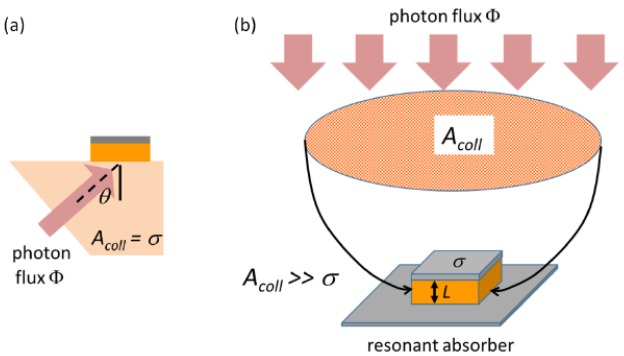

FIGURE 5.1: Mesa and patch antenna geometry [Palaferri et al., 2018].

The antenna changes the polarization of the incident light, allowing to store z-oriented electromagnetic field in the active region (so respecting the ISB selection rule).

The photon collection efficiency is increased, as the photocurrent is proportional to the collection-area A_{coll}, which in the antenna is much bigger than its geometrical cross section. A strong confinement of electromagnetic energy density in the sub-wavelength semiconductor layer is observed. The semiconductor surface can be scaled in order to reduce the detector pixel size and achieve high frequency modulation.

In our group, D. Palaferri has shown during his thesis a room temperature operating QWIP at 9 μm using the patch antenna geometry [Palaferri et al., 2018]. He has studied also its high frequency performances using the heterodyne technique.

In parallel, he has designed a QCD operating at 9 μm to study the influence of the patch antenna geometry on the performances of this detector. Figure 5.2 presents the comparison between the responsivity of the QCD as a function of the temperature in a mesa (green data) and patch antenna (red data) geometry. The measurements was done together with A. Bigioli.

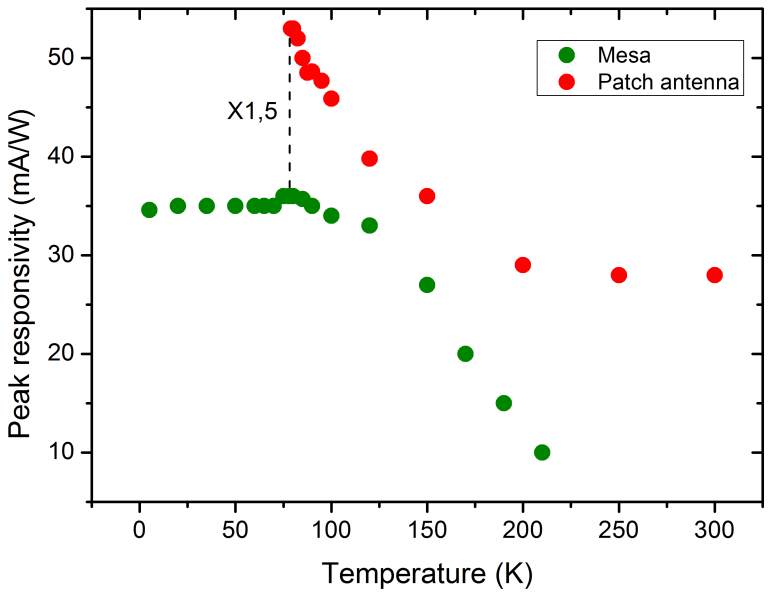

Figure 5.2: Responsivity of a QCD in mesa (green) and patch antenna (red) geometry.

From Figure 5.2, we can see an improvement in the performances of the QCD with higher measured responsivity thanks to the patch antenna geometry.

5.2.3 Heterodyne measurements

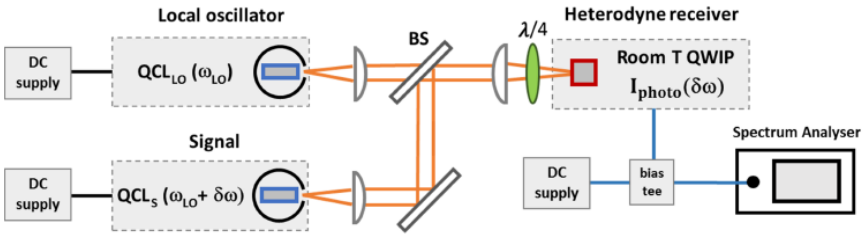

FIGURE 5.3: Setup of the heterodyne measurements technique [Palaferri et al., 2018].

The optical heterodyne technique is an example of coherent detection. Figure 5.3 shows the setup of measurement of this technique. Two electromagnetic beams with frequencies $\omega_s = hc/\lambda_s$ for the Signal and $\omega_{LO} = hc/\lambda_{LO}$ for the Local Oscillator (LO), which we assume to be in the infrared region, can be mixed into a photodetector generating a beating signal at the frequency $\omega_{het} = \omega_s - \omega_{LO}$. This conversion to a RF or microwave frequency can occur only if the detector has a frequency cut-off higher than the beating signal. We are assuming, for simplicity, that both signal and LO are single mode emitters. The measured heterodyne current is expressed as:

$$I_{het} = 2R\sqrt{P_{LO}P_S}cos(\omega_s - \omega_{LO})t \tag{5.1}$$

with P_{LO} the local oscillator output power and P_S the source power. The heterodyne signal is proportional to the square root of the incident power and therefore by using a very strong oscillator it is possible to measure very low power of the signal source. QCD are promising candidate as high frequency detectors to be used in heterodyne measurements. Indeed there are work in progress on the set up of these measurements based on QCL emitting at 4 μm.

5.2.4 FSO communication

After improving the design of the QCD for even better optical performances but also higher frequency modulation, free space optical communication could be performed. We could thus observe high enough signal to noise ratio in order to be able to perform an eye diagram (as done with the QCL and the QWIP in chapter 4). Constellation diagrams for the QCD as well as the QWIP, can be obtained with higher bit transfer per symbol, for example quaternary phase shift keying instead of binary phase shift keying.

5.2.5 Optical high frequency with launcher

During this thesis work, one of our objective was to have a plug and play system together with HF modulation for optical communication. Another connector introduced in chapter 3 was also used in our group in order to improve the HF modulation. This part of the work was mostly performed by A. Mottaghaghizadeh. Using the launcher as a connector for the QCL and the ultra fast QWIP, we have performed optical high frequency modulation and injection locking at the beat note frequency.

An optical high frequency modulation was observed up to the limit of the RF generator, i.e. 26.5 GHz. Figure 5.4 presents the frequency response of the QCL

measured with the QWIP for different operating current of the QCL (different optical output power). The I-V curve charactreistic to the QCL is presented in the inset of figure 5.4.

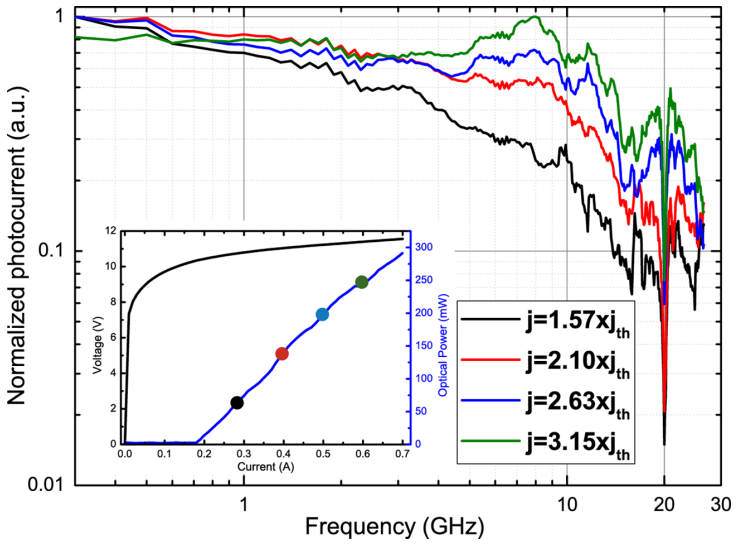

FIGURE 5.4: High frequency optical modulation with QCL and detection with QWIP. inset: I-V curve of the QCL.

Figure 5.5 shows the injection locking at the beat note frequency equal to 23 GHz at RF power of 10 dBm.

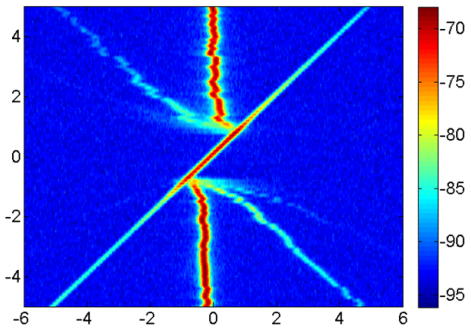

FIGURE 5.5: Injection lockin at 23 GHz at RF power of 10 dBm. Locking range of 1.8 MHz is obtained.

Appendix

A Appendix

A.1 Growth sheet of QCD

	x 10		GaInAs	12Å
		1e18cm-3	GaInAs:Si	30Å
			GaInAs	12Å
			AlInAs	67Å
			GaInAs	7Å
			AlInAs	4Å
			GaInAs	7Å
			AlInAs	60Å
			GaInAs	8Å
			AlInAs	2Å
			GaInAs	8Å
			AlInAs	58Å
			GaInAs	10Å
			AlInAs	3Å
			GaInAs	10Å
			AlInAs	55Å
			GaInAs	22Å
			AlInAs	53Å
			GaInAs	26Å
			AlInAs	51Å
			GaInAs	31Å
			AlInAs	45Å
			GaInAs	37Å
			AlInAs	45Å
			GaInAs	44Å
			AlInAs	50Å

FIGURE A.1: Growth sheet of the QCD studied in this thesis made of GaInAs/AlInAs. It has 10 periods.

A.2 Participated conference and journal papers

Ultra-fast modulation of mid infrared buried heterostructure quantum cascade lasers

A. Mottaghizadeh, Z. Asghari, M. Amanti, D. Gacemi, A. Vasanelli and C. Sirtori
Laboratoire MPQ, Université Paris Diderot- Paris 7, 10 rue A. Domon et L. Duquet, 75013 Paris France

***Abstract*- We present the first direct observation of 26.5 GHz direct modulation of mid infrared buried heterostructure quantum cascade laser (QCL) emitting at 9 µm. For these measurements we have used an ultra-fast QWIP detector with 65 GHz bandwidth. As expected the modulation frequency bandwidth increases by increasing the laser driving DC current. Finally, we demonstrate that the laser cavity round trip frequency, f_{rt}, can be injection locked by direct modulation of laser driving current hinting to mode-locked operation.**

I. INTRODUCTION

Quantum cascade lasers are semiconductor light sources, which covers from THz up to mid infrared frequency ranges [1]. They are characterized by the ultrafast upper state carrier lifetime, few picosecond, allowing the high frequency modulation up to hundreds of GHz [2]. The search for the solutions on the fast-growing demand for the higher rate data transmission became an unavoidable challenge in our time. Laser based systems for free space optical (FSO) communication is a promising alternative to accomplish the requirements for high data rate transmission particularly in hard-access rural area where the deployment of heavy infrastructures is quasi-impossible or very expensive [3]. Furthermore, the emission wavelength of mid infrared QCLs falls in the so-called transparency window (3-5 µm and 8-12 µm) in which the signal can be transmitted without a significant attenuation over km-distances.

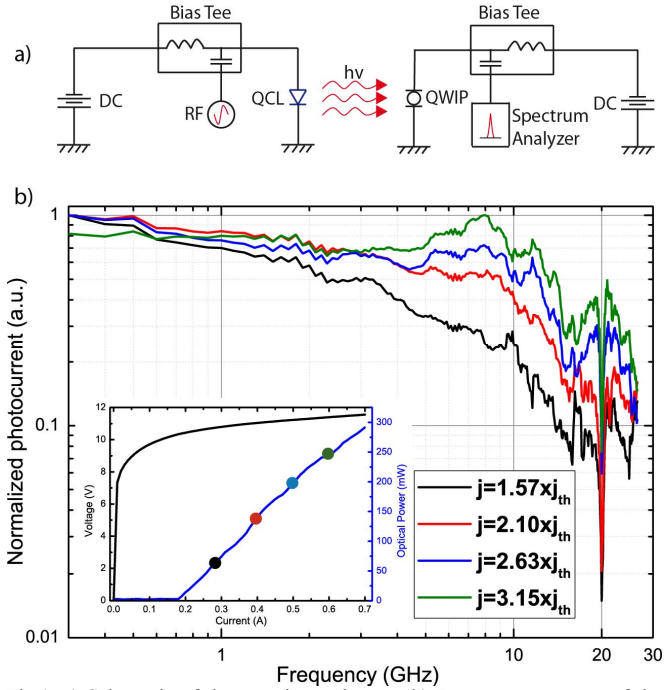

Fig.1. a) Schematic of the experimental setup. b) Frequency response of the QCL to RF modulation up to 26.5 GHz for different laser DC driving currents. Inset: LIV characterization.

II. RESULTS

Figure 1.a illustrates the high frequency characterization experimental setup schematically. The QCL is mounted on a cold finger of continuous-flow liquid nitrogen cryostat. A DC bias and microwave signal is applied through a 45 GHz bandwidth bias-tee (SHF BT 45). The modulated mid-infrared light is guided through lenses and is detected by an ultrafast QWIP [4] and is measured on a spectrum analyzer.
Figure 1.b presents the frequency response of the QCL device measured on the QWIP at different laser DC driving current. We observe a net increase of the device frequency bandwidth by increasing the laser DC current. The -3dB cutoff frequency is at 21 GHz at $j = 3.15xj_{th}$. At 26.5 GHz, which is the circuit cut-off frequency, the signal is decreased by -8dB only. The observed resonances (15GHz, 16.3GHz and 20GHz) are due to the electrical circuit. Inset of fig.2b is the laser LIV characterization at liquid nitrogen temperature. The dots corresponds to the QCL driving currents in which the frequency responses have obtained (main panel).

In figure 2 we show the RF spectra measurement of the QCL for different RF injected frequencies, f_{inj}. This measurement is obtained by changing the f_{inj} between f_{rt}-*5MHz* and f_{rt}+*5MHz*. At the beginning, the f_{inj} signal is far ftom f_{rt} and has no effects on the beat note that arises from the beating of the longitudinal modes. Note that in this case the intrinsic width of the beat note is only 40 kHz. By approaching the f_{inj} frequency to the f_{rt}, the latest moves toward the f_{inj} until when the whole f_{rt} intensity is concentrated in a single peak, in which the locking is reached and the spectra are controlled by the external injected signal. As we continue to increase the f_{inj}, the single peak splits into two separate peaks and come back to the same position as the beginning of the measurements. This measurement has been done for different RF signal power, 5dBm, 10dBm and 15 dBm.

As we observe, the locking range increases as the injected RF power increased. These results are in agreement with the previously announced measurements [5] and the classical theory of laser injection locking [6]. In figure 3 we plot the locking range as a function of microwave injected power. As predicted from equation $\Delta\omega_{lock}=2\omega_0/Q\ (I_{inj}/I_0)^{1/2}$, where ω_0/Q is the cold cavity bandwidth, I_{inj} is the injected external RF signal and I_0 is the intensity of cavity signal, the locking range follows a power law as the injected microwave power increased.

978-1-5090-6050-4/17/$31.00 ©2017 IEEE

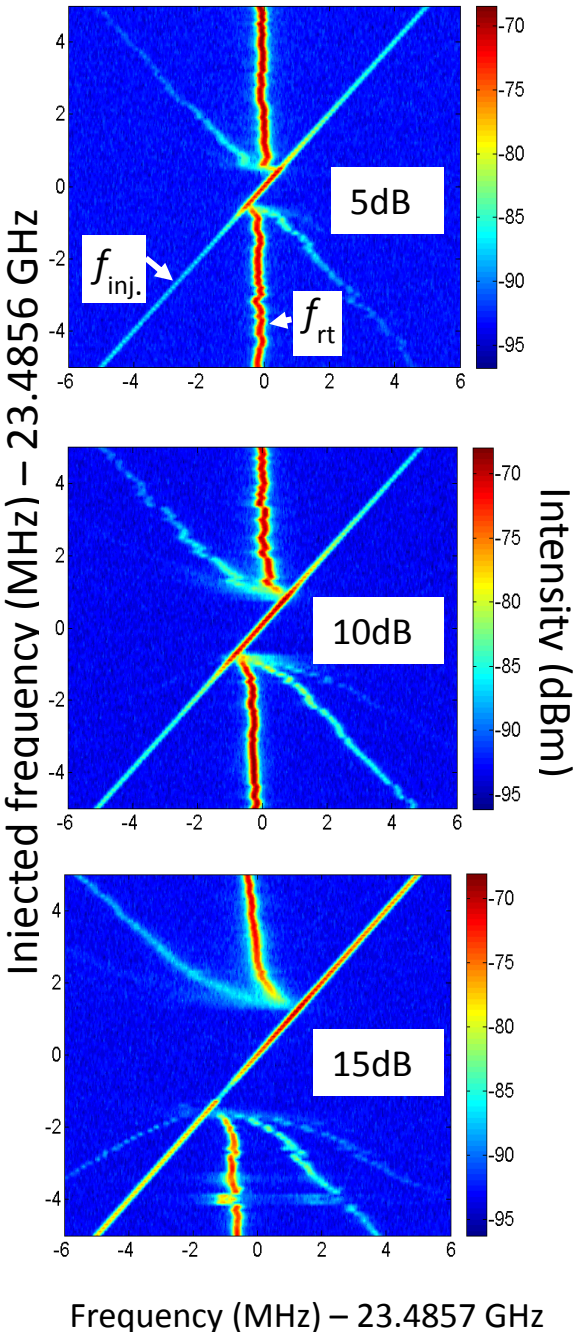

Fig.2. Measurement of the RF spectra of the QCL for different RF injected frequencies around the f_{rt} and for three different injected power, 5dBm, 10dBm and 15dBm. The laser is operating at j=2.8x j_{th}. The external RF injected frequency (f_{inj}) sweep is reported on Y-axis while the X-axis is the frequency of the signal measured on the spectrum analyzer. The color scale is the measured RF signal intensity on dBm. f_{rt} is the RF spectra of the laser at the laser cavity round trip frequency. Each graph corresponds to 200 frequency-sweep scan (10MHz span, step of 50 KHz) and each scan is an average of 100 measurements. The resolution bandwidth is set to 10 KHz.

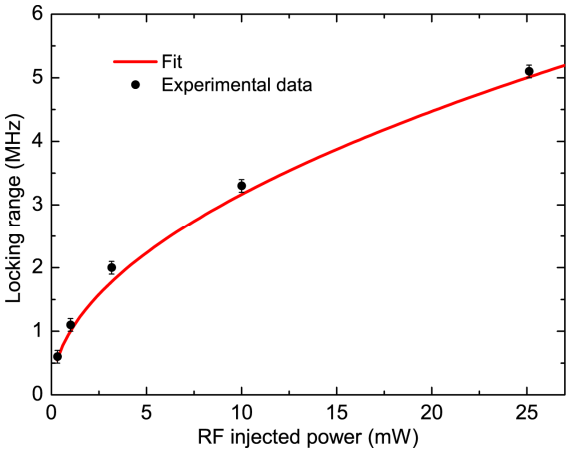

Fig.3. Locking range measured for different RF injected power. These values obtained from curves of figure 3. The red line corresponds to a square root fit of the experimental data.

III. SUMMARY

In summary, we report the first *optical* characterization of the ultra-fast modulation of mid-infrared QCL emitting at 9µm up to 26.5 GHz. Furthermore, we present a laser injection locking at 23.5 GHz and a locking range of 5 MHz. These results are a first step toward the high data rate (> 20 Gbps) transmission using a mid-infrared QCL.

REFERENCES

[1]. J. Faist, F. Capasso, D. L. Sivco, C. Sirtori, A. L. Hutchinson, and A. Y. Cho, "Quantum Cascade Laser," Science 264, 553–556 (1994).
[2]. J. Faist, "Quantum cascade lasers", Oxford University Press (2013).
[3]. H. Henniger, O. Wilfert "An Introduction to Free-space Optical Communications Radio Engineering", 19, 203 (2010).
[4] H. C. Liu, R. Dudek, T. Oogarah, P. D. Grant, Z. R. Wasilewski, H. Schneider, S. Steinkogler, M. Walther, and P. Koidl, Circuits and Devices Magazine, IEEE 19, 9–16, (2003).
[5] St-Jean, M. R., Amanti, M. I., Bernard, A., Calvar, A., Bismuto, A., Gini, E., Beck, M., Faist, J., Liu, H. C. and Sirtori, C. (2014), Injection locking of mid-infrared quantum cascade laser at 14 GHz, by direct microwave modulation. Laser & Photonics Reviews, 8: 443–449.
[6] A. E. Siegman, Lasers (University Science Books, 1986).

Article

Room temperature, wide-band Quantum Well Infrared Photodetector for microwave optical links at 4.9 μm wavelength

Etienne Rodriguez, Alireza Mottaghizadeh, Djamal Gacemi, Daniele Palaferri, Zahra Asghari, Mathieu Jeannin, Angela Vasanelli, Azzurra Bigioli, Yanko Todorov, Mattias Beck, Jerome Faist, Qi Jie Wang, and Carlo Sirtori

ACS Photonics, **Just Accepted Manuscript** • DOI: 10.1021/acsphotonics.8b00704 • Publication Date (Web): 30 Jul 2018

Room temperature, wide-band Quantum Well Infrared Photodetector for microwave optical links at 4.9 μm wavelength

Etienne Rodriguez,[1,2*] Alireza Mottaghizadeh,[3] Djamal Gacemi,[3] Daniele Palaferri,[3] Zahra Asghari,[3] Mathieu Jeannin,[3] Angela Vasanelli,[3] Azzurra Bigioli,[3] Yanko Todorov,[3] Mattias Beck,[4] Jerome Faist,[4] Qi Jie Wang,[1,2*] and Carlo Sirtori[1,3*]

[1]School of Electrical and Electronic Engineering, Nanyang Technological University, 639798, SINGAPORE

[2]CINTRA CNRS/NTU/THALES, UMI 3288, Research Techno Plaza, 50 Nanyang Drive, Border Block, Level 6, 637553, SINGAPORE

[3]Université Paris Diderot, Sorbonne Paris Cité, Laboratoire Matériaux et Phénomènes Quantiques, UMR7162, 75013 Paris, France

[4]ETH Zurich, Institute of Quantum Electronics, Auguste-Piccard-Hof 1, Zurich 8093, Switzerland

**Email:* etienne.rodriguez@gmail.com, qjwang@ntu.edu.sg and carlo.sirtori@univ-paris-diderot.fr

High-speed room temperature quantum well infrared photodetectors (QWIPs) at λ ~ 4.9 μm have been realised in a strain compensated $In_{0.1}Ga_{0.9}As/Al_{0.4}Ga_{0.6}As$ heterostructure grown on a GaAs substrate. The high-speed properties at room temperature have been optimised by using a specifically designed air-bridge structure which greatly reduces the time constant of the effective RC circuit, thus allowing transmission and detection of high-frequency signals. By modulating a high-speed quantum cascade laser (QCL) centred at λ ~ 4.7 μm we were able to record a modulation of the photocurrent up to ~26 GHz, which is limited by our setup. At 300 K and under a bias voltage of –5 V our device shows high responsivity and detectivity of 100 mA/W and 1 x 10^7 Jones, respectively. The developed high-performance QWIPs at this wavelength are highly promising for optical heterodyne measurement, high-speed free space communications in microwave optical links and frequency comb QCLs characterisations.

Keywords: Quantum devices, Mid-infrared, Photodetectors, Ultrafast devices.

Recent developments in high-speed mid-infrared (mid-IR) photonics such as free-space optical communications and frequency combs laser characterization, have placed a high demand on high performance high-speed mid-IR photodetectors. Technologies based on HgCdTe and InSb have made good progress in achieving high-responsivity and high-sensitivity photodetectors [1,2].

However, they often operate at low operating temperatures and possess a relatively low-frequency bandwidth which makes them not suitable for high-speed applications.[3] Photodetectors based on intersubband transitions, i.e. quantum well infrared photodetector (QWIP) and quantum cascade detectors (QCDs), have also shown remarkable performance in both mid-wavelength infrared (MWIR) (~3-7 μm) and long-wave infrared (LWIR) (~7-14 μm). Due to their high photoconductive gain and high-speed operation, QWIPs have attracted significant attention.[4] This photodetector technology has the advantages of high absorption,[5] wide tunability of the detection wavelength based on band-structure engineering of the quantum structures,[6] and high-speed behaviour due to their intrinsic short carrier lifetime.[7,8] This physical parameter is an inherent characteristic of the intersubband transitions which leads to high-frequency response exceeding 100 GHz[8] and a very high saturation intensity[9] allowing a wide range of applications including heterodyne detection,[8,10,11] characterisation of ultrafast laser pulses[12] and wideband free space communications.[13]

The development of QWIP has been successful in both the MWIR and LWIR bands.[2,14] Great efforts have been devoted to the development of LWIR QWIPs. It was used to detect the beating signals between two CO_2 lasers at a frequency starting from 35 GHz up to 110 GHz at 10 μm.[8] Recently, ultrahigh-sensitivity heterodyne measurements in QWIP at room temperature have been demonstrated using metamaterials to enhance light-matter interactions and significantly increase signal-to-noise ratio.[11] On the other hand, in the MWIR region, high responsivity of 1 A/W[15] and background-limited detectivity of 2×10^{11} Jones[16] have been demonstrated but only at cryogenic temperatures. As far as we know no prior work has been devoted to high-speed and high performance QWIPs in the MWIR region at room temperature.

In this work, we have demonstrated a direct modulation of high-speed QWIP up to 26 GHz at room temperature. The active region of the QWIP is made of 40 periods of strain-compensated $In_{0.1}Ga_{0.9}As/Al_{0.4}Ga_{0.6}As$ alloy grown on GaAs substrate and operate at 4.9 μm. We designed a 25 μm square MESA where the top contact is realised with an air-bridge structure for high-frequency modulations. A high-speed QCL[17] that can be modulated up to 26 GHz was used to measure the frequency response of our QWIP device and to detect the beatnote signals at 11.5 and 23.1 GHz. Moreover, we also used rectification techniques to measure the frequency response of the QWIP up to 30 GHz, where the signal is attenuated by approximately 10 dBm. The rectified response is consistent with the direct-modulated QCL measurement.

STRUCTURE, SAMPLE DESCRIPTION AND TEMPERATURE CHARACTERISTICS

The QWIP wafer was grown by molecular beam epitaxy on a GaAs substrate. The active layers are composed of 40 periods of the following sequence: 5 Å $In_{0.1}Ga_{0.9}As$, 25 Å $In_{0.1}Ga_{0.9}As$ (doped: 5×10^{11} cm^{-2}), and 5 Å $In_{0.1}Ga_{0.9}As$ separated by a 400 Å $Al_{0.4}Ga_{0.6}As$ barrier. The active region is sandwiched between two highly-doped GaAs contact layers as it is drawn in Fig. 1.

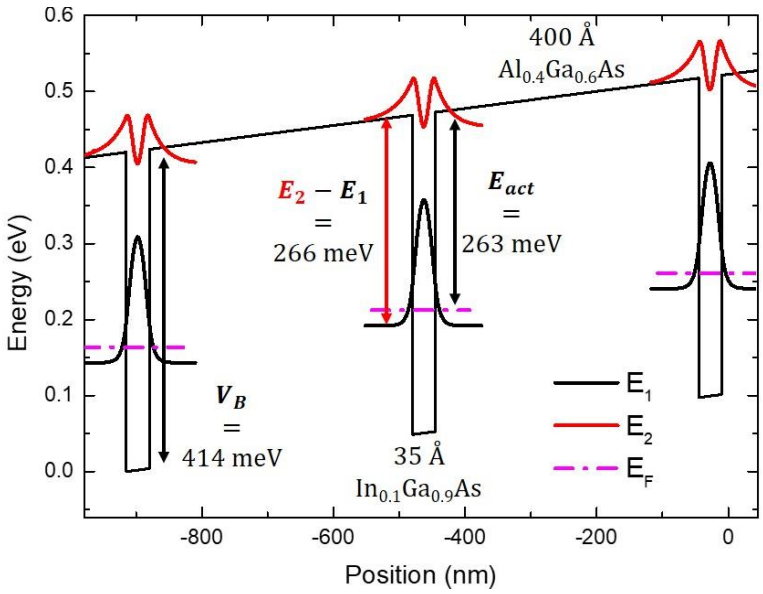

Fig. 1. *Band-structure of the developed qauntum well infrared photodetector (QWIP) with 3 quantum wells (QWs) active regions at a bias voltage of 2 V. The most relavant physical parameters of the sructure are indicated in the figure.*

The bandstructure and relevant energy levels of the detector are displayed in Fig. 1 with E_1 the lower energy state, E_2 the upper energy state and E_F, E_{act} and V_B are respectively the Fermi level, the activation energy of the QW and the total barrier height. The upper energy level is in resonance with the top of the barrier, as in the typical bound-to-quasicontinuum design.

The fabrication of the devices has been conceived to achieve high-speed performances. Square mesas were defined using Inductively Coupled Plasma (ICP) etching system on an annealed Ge/Au/Ni/Au top contact up to the bottom contact. Then, we protected the mesas using a thick photoresist before removing the bottom contact where the coplanar waveguide will take place by wet-etching. The air-bridge metal structure is realised by using two different photoresists, one positive photoresist used as a pillow to support the ridge in front of the mesa, and the negative photoresist for the lift-off process, after the Ti/Au deposition by e-beam evaporation technique. The additional bakes of the positives photoresist are essential to soften the angles and to support the development of the negative photoresist. Moreover, the e-beam deposition must be done with three different angles (+30, 0 and -30 °) following the direction of the coplanar waveguide to ensure good adhesion between the bridge and the substrate. The air-bridge between the top of the mesa and the microstrip ensures a low time constant of the effective RLC circuit. The microstrip is widened to a width fitted to the high-frequency launcher. The top view of the device is shown Fig. 2 (a), where the inset shows clearly the squared mesa and the gold air-bridge. Finally, we polished the facet of the device at 45° to efficiently couple the light into the active region.

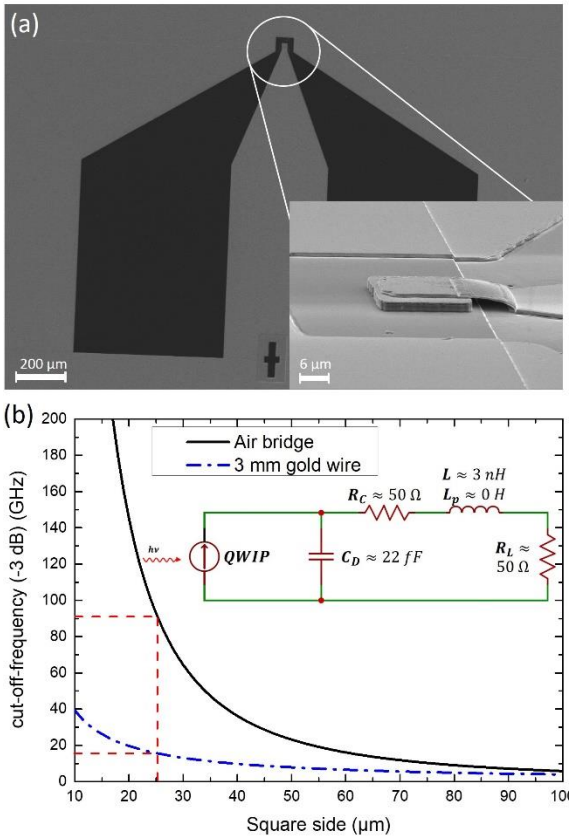

Fig. 2. *(a) The top view of the QWIP (The inset: zoom-in of the active region with the air bridge); (b) Cut-off frequency at –3 dB as a function of the MESA dimensions for the conventional wire bonding (dashed line) and the proposed air-bridge (solid line) devices (The inset: electrical circuit of the device).*

In order to optimise the electrical circuit for high speed operation, the wire inductance is suppressed by realising a contact with a small air-bridge connected to a 50 Ω microstrip line. The capacitance of the device is directly linked to the size of the mesa. Considering practical implementations, we designed a relatively small square mesa of 25 x 25 μm^2. This dimension corresponds to an electrical cut-off frequency of 92 GHz calculated using the equivalent electrical circuit model. Fig. 2 (b) illustrates the electrical cut-off frequency at –3 dB for 40 periods with wire bonding (dashed line) and with air-bridge (solid line) waveguides. The inset of Fig. 2 (b) shows the equivalent circuit where the QWIP is considered as a current generator. C_D represents the device capacitance, R_C is the access resistance of the coplanar line which is designed to be 50 Ohm to match the impedance of the system load R_L, and L is the inductance of the wire bonding (in the case of air-bridge the parasite inductance L_p is negligible).

The fabricated QWIP device is mounted on a cryostat and then cooled down at cryogenic temperatures. Photocurrents at different temperatures and bias voltages are measured by 1:1 imaging of the 0.2 inch aperture blackbody at 1000° C. In order to remove the dark current, the photon flux is chopped at 500 Hz, and the measurements are performed using a lock-in amplifier (Stanford Research SR830). The photocurrent amplitude is measured through a shunt resistance in series with the QWIP without the use of any pre-amplifier. We extracted the power on the

QWIP by using a calibrated MCT detector in the exact same configuration. Taking into account the dimensions and the spectral responses of the different photodetectors, the impinging power is 160 nW on the 25 µm square QWIP. The spectra are measured using a Bruker Fourier-transform infrared (FTIR) spectrometer with step scan technique. The signal from the detector is pre-amplified by a low-noise current amplifier (DLPCA-200) and sent to the lock-in amplifier.

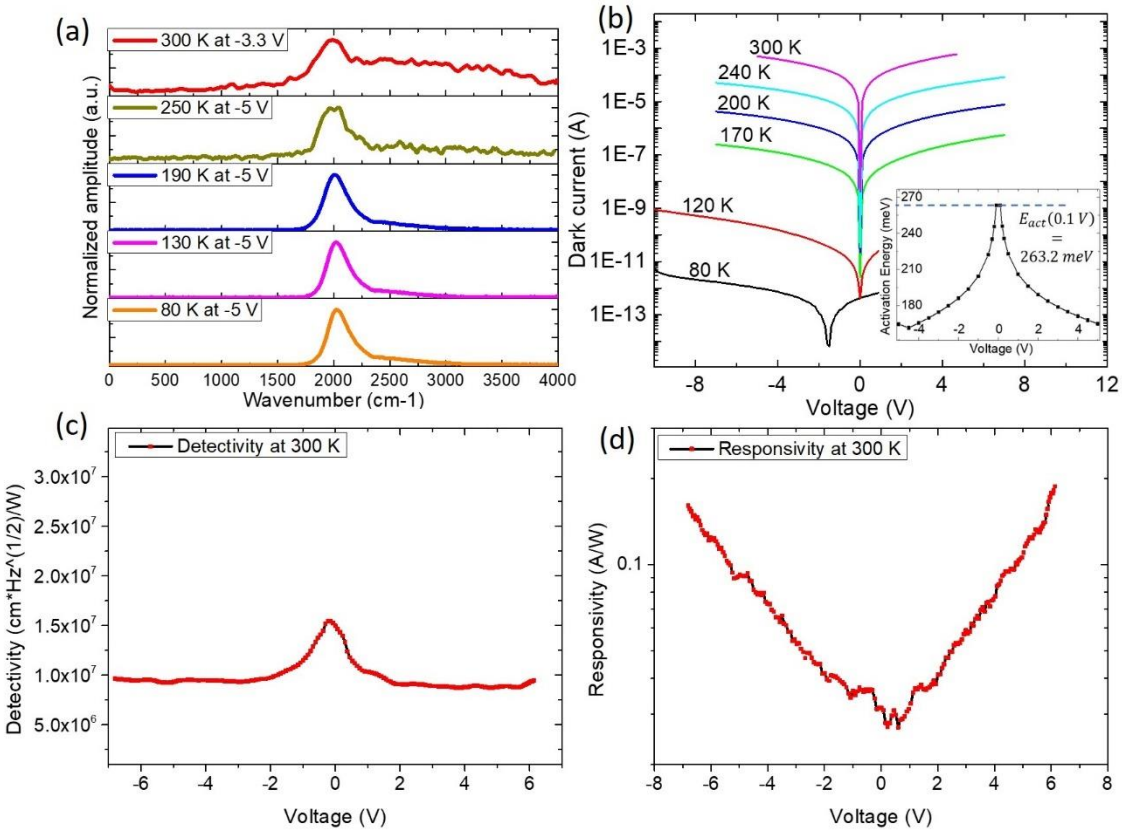

Fig. 3. *(a) Spectra of the QWIP at several different temperatures up to 300 K; (b) Current-voltage (IV) characteristics in background condition for different temperature, inset: activation energy as a function of the bias voltage; background-limited detectivity (c) and responsivity (d) of the QWIP device at 300 K as a function of the bias voltage.*

The internal IR source of the FTIR emit about 52 nW only, despite the low input optical power we were able to measure the response spectra at up to 300 K as shown in Fig. 3. (a). The spectra present an asymmetry, which corresponds to the intrinsic characteristic of the bound-to-quasicontinuum design.[18] With the increase of the temperature, the central wavelength of the QWIP slightly shifts towards the lower energy (from 2050 cm^{-1} at 80 K to 2010 cm^{-1} at 250 K due to the depolarization effect. The linewidth starts to increase from 130 K (from 27.03 meV up to 130 K to 33.48 meV at 250 K) due to the electron-phonon interactions. Fig. 3. (b) shows the evolution of the background current as a function of the voltage up to room temperature. The exponential fits of the evolution of the dark current with the temperature allowed the

calculation of the activation energy of the system which corresponds to 263.2 meV at low bias voltages. This energy is the thermal energy required to excite electrons from the Fermi energy to the continuum and is in a very good agreement with the activation energy simulated in Fig. 1.

The background-limited detectivity and the responsivity at 300 K as a function of the bias voltage are, respectively, shown in Figs. 3 (c) and (d). They exhibit a value of 100 mA/W and 1 x 10^7 Jones for a bias voltage of −5 V.

HIGH-SPEED BEHAVIOUR

The first high-speed characterizations of our QWIPs have been done by direct modulation of a QCL. The measurement setup is shown in Fig. 4 (a). A high-speed current modulated QCL at a wavelength of 4.7 µm is mounted in a high-speed cryostat and operates at cryogenic temperatures. A bias-T is used which allows the injection of the DC and the microwave currents simultaneously. The radiation from the laser is collected and then focused on the QWIP using two convex lenses. The output power of the laser corresponds to 110 mW, however, due to the small size of the detector, only a small fraction of the power is coupled with the QWIP. It results with a photocurrent of about 600 µA at room temperature. The QWIP is also connected through a bias-T in order to measure the modulated photocurrent of the QWIP at high-frequency using a spectrum analyser (Agilent E4407B) limited to 26.5 GHz. The injection is tuned from 100 MHz to 26.5 GHz using a signal generator (Anritsu MG3693B) with a step of 300 MHz at a RF power of –10 dBm.

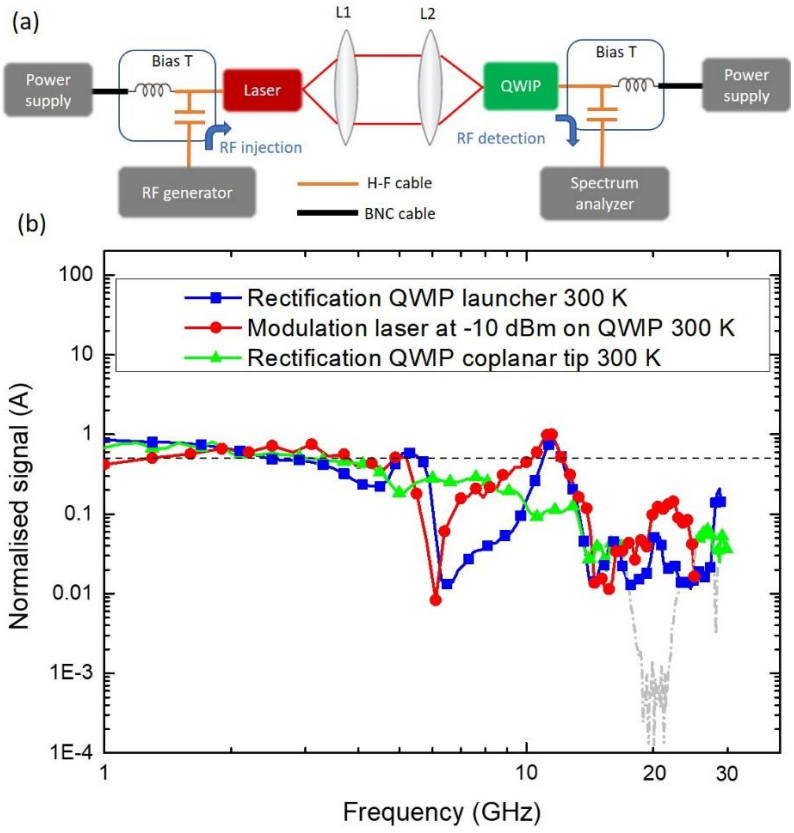

Fig. 4. *(a) The schematic illustration of the setup used to investigate the high-speed modulation of the QWIP. A high-speed direct-modulated quantum cascade laser (QCL) is used in the experiment; (b) Photoresponse of the QWIP with the QCL modulated at –10 dBm at 300 K (red line + symbol) at a bias voltage of –4 V. The rectification measurements of QWIP using the cryostat setup (blue line + symbol) and using the coplanar tip configuration (green line + symbol) with in dashed grey line the resonances due to parasitic effects of its electrical circuit. The black dashed line represents the value at -3 dB.*

To avoid microwave pick-ups, we separated the emitter and detector by more than a meter, and the power of the injected microwaves remains as low as possible. Furthermore, to remove the remaining antenna effects, we have detected the background by carrying out the same measurements but with laser beam blocked. All these measurements were realised at room temperature with a bias voltage on the QWIP at –4 V, while the laser operate at low temperature with a radio frequency (RF) injection power of –10 dBm as shown in Fig. 4 (b).

This approach is complementary with the detection of the beating signal shown in Fig. 5. In the direct modulation approach, the RF signal injected in the laser will modulate the IV curve of the laser according to the injected power. It is translated by an amplitude modulation of the laser intensity, which is then transmitted to the photodetector. Therefore, the amplitude modulation detected by the QWIP will also be dependent on the quality of the injection of the laser.

We also verified the high speed measurements by microwave rectification techniques utilising an RF launcher for the QWIP characterizations in the cryostat at 300 K. Due to the inherent non-linear I-V characteristics of QWIPs, microwave rectification technique is a way to study the roll-off behaviour of the QWIP by applying an RF signal to the photodetector and measuring the variation of its DC biasing current. This value reflects the frequency roll-off response of the device limited by the intrinsic-transport and the electrical parameters of the circuit.[5] Using this method, high speed characterizations of photodetectors are no longer limited by the spectrum analyser, but only by the synthesiser RF generator. With this, we can extend the high-speed measurement up to 30 GHz. This measurement has also been carried out by operating a lock-in amplifier technique with an electrical modulation of the RF signal using a signal generator. As a result, the RF injection is over modulated by a 10 kHz rectangular square wave with a duty cycle of 50% and sent to the QWIP though the bias-T with the bias voltage of the QWIP applied. The variation of the bias voltage is directly recovered at the terminal of the generator using a BNC-T and sent to the AC input of the lock-in amplifier synchronised with the signal generator.

The rectification measurements, displayed in Fig. 4 (b), exhibit good agreement with the direct modulation using the QCL modulated at –10 dBm, and show a frequency response up to 30 GHz. At 22 GHz the signal of the direct modulation is attenuated by approximately 8 dBm while at 30 GHz the rectification signal shows a diminution by approximately 10 dBm. We do not identify a clear change of the slope in the bode diagram of the rectification measurements or direct modulations which would correspond to the cut-off frequency. The resonances of our

system around 10 GHz are due to some parasitic effects in the electrical circuit using the launcher in the cryostat. We conducted the same measurements using a simpler electrical circuit composed of an RF coplanar tip, where these resonances were not shown as seen in green in Fig. 4 (b). However, this setup suffers from another resonance at higher frequencies represented in grey dashed line, also visible in the transmission line of the electrical circuit not displayed here.

APPLICATION ON FERQUENCY COMB QCL AND OPTICAL LINKS

The optical frequency combs have the potential to revolutionise the communication and especially the free-space communication in the atmospheric windows in the mid-IR where, recently, Joerg Pfeifle et al. has achieved a data transfer rate of 1.44 Tbit s^{-1} over up to 300 km by using frequency combs sources.[19] Our wide-band photodetector is designed to work up to RT in the MWIR. Therefore, it can be used in high-speed MWIR communication data and the characterisation of frequency comb laser by analysing the beatnote signal. The detection of the beating signal of the multimode laser is done by mixing the multiple modes in a high-speed mixer, i.e. QWIP. The frequency of this signal is directly related to the length of the cavity but also to the dispersion which makes it a powerful tool to study frequency combs lasers.

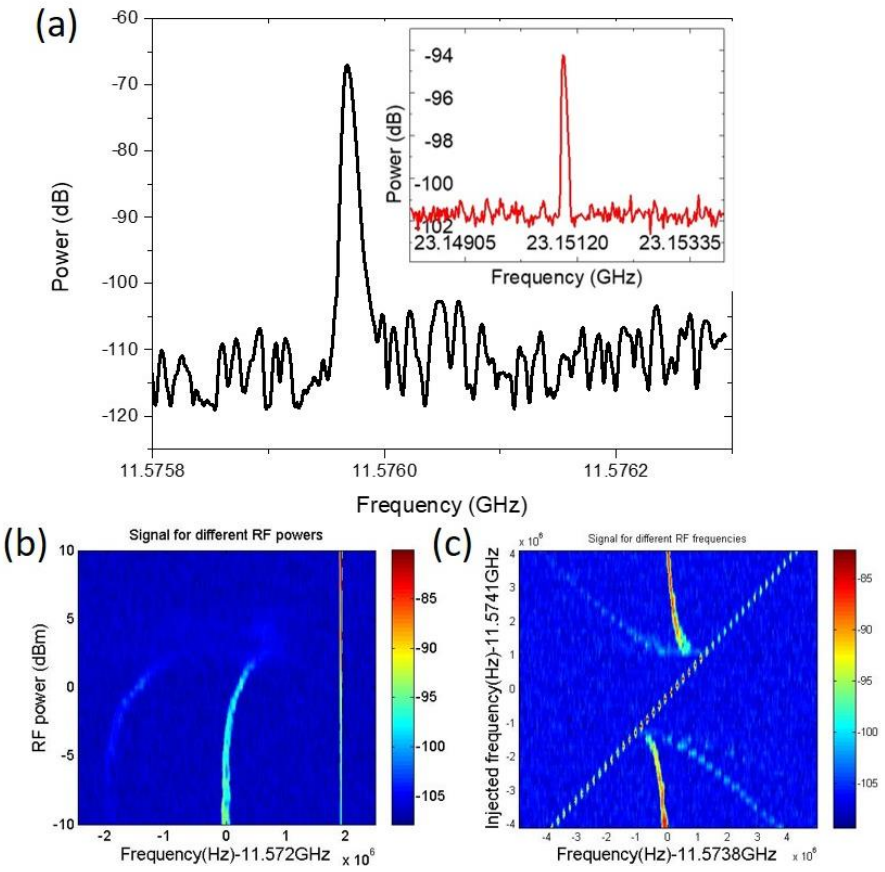

Fig. 5. *(a) The first harmonic of the beatnote, corresponding to the 3 mm laser, is collected on the QWIP at 300 K. The inset: the second harmonic of the beatnote at 23.15 GHz;*

injection-locking observed on the QWIP at 300 K by (b) increasing the injected power and (c) tuning the injection frequency on a 3 mm laser.

Moreover, as one of the important applications of mid-IR photonics, photodetectors could be used to characterise frequency comb lasers. We also detected the beatnote arising from the frequency mixing of longitudinal modes of our multimode laser. Fig. 5 (a) and the inset show the detection on the QWIP at 300 K of the first and second harmonic of the beatnote of a 3 mm laser corresponding respectively to a frequency of 11.58 and 23.15 GHz (the width at -3 dBm of the first harmonic of the beatnote is about 4 kHz). We also performed the injection-locking by increasing the injected power and the injected frequency on the laser as respectively displayed in Fig. 5 (b) and (c). We realised these measurements using a coplanar tip at room temperature. The RF signal injected near the round-trip frequency of the laser will act as a master oscillator and pull or inject the beating signal and therefore, impose the intermode frequency. The injection-locking is a power tool to achieve active mode-locking which stabilise the comb emission of the laser and can significantly broaden the emission spectrum by the generation and proliferation of sidebands in the optical range.[20,21] This method exhibits another direct method of high-frequency detection, same measurements were realised using the launcher configuration at low, and room temperature not shown here.

CONCLUSION

In conclusion, we have demonstrated that high speed QWIP at 4.9 µm with a modulation that goes up to 30 GHz at room temperature. Our high-speed QWIPs have a specific design for very high frequency based on small surface detector and air-bridges which enables the propagation and injection of high-frequency RF signals. It has been tested, up to room temperature, by direct and indirect method up to, respectively, 26 and 30 GHz both limited by the electrical systems. We also observed on the QWIP at room temperature the two first harmonics of the beating signal and the injection-locking of 3 mm lasers, which correspond to the beating signals at the frequency of 11.57 and 23.15 GHz, respectively. Beyond the high-speed behaviour of our devices, the intrinsic properties of intersubband transitions and their high responsivity at room temperature make them very promising for many applications in the 3 – 5 µm atmospheric window in the MWIR, especially in heterodyne detection, free-space communication and frequency comb QCLs characterisations.

Funding. Singapore National Research Foundation, Competitive Research Program (NRF-CRP18-2017-02) and Singapore Ministry of Education Tier 2 Program (MOE2016-T2-2-159).

Acknowledgement. We would like to thank Maria Amanti her useful discussions and suggestions on this work.

REFERENCES

(1) Norton, P. HgCdTe Infrared Detectors. *Opto-Electronics Rev.* **2002**, *10* (3), 159–174.

(2) Rogalski, A. Infrared Detectors: Status and Trends. *Prog. Quantum Electron.* **2003**, *27* (2–3), 59–210.

(3) Varesi, J. B.; Bornfreund, R. E.; Childs, A. C.; Radford, W. A.; Maranowski, K. D.; Peterson, J. M.; Johnson, S. M.; Giegerich, L. M.; De Lyon, T. J.; Jensen, J. E. Fabrication of High-Performance Large-Format MWIR Focal Plane Arrays from MBE-Grown HgCdTe on 4" Silicon Substrates. *J. Electron. Mater.* **2001**, *30* (6), 566–573.

(4) Liu, H. C. Photoconductive Gain Mechanism of Quantum-Well Intersubband Infrared Detectors. *Appl. Phys. Lett.* **1992**, *60* (12), 1507–1509.

(5) H. Schneider and H. C. Liu. Quantum Well Infrared Photodetectors. In *Springer Series in Optical Sciences*; 2007.

(6) Capasso, F. Band-Gap Engineering: From Physics and Materials to New Semiconductor Devices. *Science (80-.).* **1987**, *235* (4785), 172–176.

(7) Liu, H. C.; Li, J.; Buchanan, M.; Wasilewski, Z. R. High-Frequency Quantum-Well Infrared Photodetectors Measured by Microwave-Rectification Technique. *IEEE J. Quantum Electron.* **1996**, *32* (6), 1024–1028.

(8) Grant, P. D.; Dudek, R.; Buchanan, M.; Liu, H. C. Room-Temperature Heterodyne Detection up to 110 GHz with a Quantum-Well Infrared Photodetector. *IEEE Photonics Technol. Lett.* **2006**, *18* (21), 2218–2220.

(9) Vodopyanov, K. L.; Chazapis, V.; Phillips, C. C.; Sung, B.; Harris, J. S. Intersubband Absorption Saturation Study of Narrow III - V Multiple Quantum Wells in the Spectral Range. *Semicond. Sci. Technol.* **1997**, *12* (6), 708–714.

(10) Hofstetter, D.; Graf, M.; Aellen, T.; Faist, J.; Hvozdara, L.; Blaser, S. 23 GHz Operation of a Room Temperature Photovoltaic Quantum Cascade Detector at 5.35 Mm. *Appl. Phys. Lett.* **2006**, *89* (6), 2004–2007.

(11) Palaferri, D.; Todorov, Y.; Bigioli, A.; Mottaghizadeh, A.; Gacemi, D.; Calabrese, A.; Vasanelli, A.; Li, L.; Davies, A. G.; Linfield, E. H.; et al. Room-Temperature Nine-Mm-Wavelength Photodetectors and GHz-Frequency Heterodyne Receivers. *Nat. Publ. Gr.* **2018**, *556* (7699), 85–88.

(12) Hugi, A.; Villares, G.; Blaser, S.; Liu, H. C.; Faist, J. Mid-Infrared Frequency Comb Based on a Quantum Cascade Laser. *Nature* **2012**, *492* (7428), 229–233.

(13) R. Martini, R. Paiella, C. Gmachl, F. Capasso, E.A. Whittaker, H.C. Liu, H.Y. Hwang, D.L. Sivco, J. N. B. and A. Y. C. High-Speed Digital Data Transmission Using Mid-Infrared Quantum Cascade Lasers. *Electron. Lett.* **2001**, *37* (21).

(14) Schneider, H.; Maier, T.; Fleissner, J.; Walther, M.; Koidl, P.; Weimann, G.; Cabanski, W.; Finck, M.; Menger, P.; Rode, W.; et al. Dual-Band QWIP Focal Plane Array for the Second and Third Atmospheric Windows. *Infrared Phys. Technol.* **2005**, *47* (1–2), 53–58.

(15) Costard, E.; Bois, P.; Marcadet, X.; Nedelcu, A. QWIP Products and Building Blocks for High Performance Systems. *Infrared Phys. Technol.* **2005**, *47* (1–2), 59–66.

(16) Guériaux, V.; Nedelcu, A.; Bois, P. Double Barrier Strained Quantum Well Infrared Photodetectors for the 3–5 Mm Atmospheric Window. *J. Appl. Phys.* **2009**, *105* (11), 114515.

(17) Calvar, A.; Amanti, M. I.; Renaudat St-Jean, M.; Barbieri, S.; Bismuto, A.; Gini, E.; Beck, M.; Faist, J.; Sirtori, C. High Frequency Modulation of Mid-Infrared Quantum Cascade Lasers Embedded into Microstrip Line. *Appl. Phys. Lett.* **2013**, *102* (18), 1–4.

(18) Palaferri, D. Antenna Resonators for Quantum Infrared Detectors and Fast Heterodyne Receivers, University Paris Diderot - Paris 7, Laboratoire Matériaux et Phénomènes Quantique (MPQ), 2018.

(19) Pfeifle, J.; Brasch, V.; Lauermann, M.; Yu, Y.; Wegner, D.; Herr, T.; Hartinger, K.; Schindler, P.; Li, J.; Hillerkuss, D.; et al. Coherent Terabit Communications with Microresonator Kerr Frequency Combs. *Nat. Photonics* **2014**, *8* (5), 375–380.

(20) St-Jean, M. R.; Amanti, M. I.; Bernard, A.; Calvar, A.; Bismuto, A.; Gini, E.; Beck, M.; Faist, J.; Liu, H. C.; Sirtori, C. Injection Locking of Mid-Infrared Quantum Cascade Laser at 14 GHz, by Direct Microwave Modulation. *Laser Photonics Rev.* **2014**, *8* (3), 443–449.

(21) Li, H.; Laffaille, P.; Gacemi, D.; Apfel, M.; Sirtori, C.; Leonardon, J.; Santarelli, G.; Rösch, M.; Scalari, G.; Beck, M.; et al. Dynamics of Ultra-Broadband Terahertz Quantum Cascade Lasers for Comb Operation. *Opt. Express* **2015**, *23* (26), 33270.

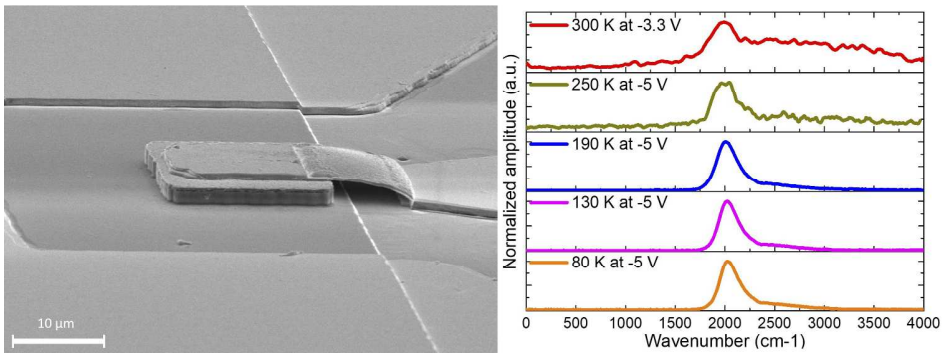

239x85mm (300 x 300 DPI)

LASER & PHOTONICS REVIEWS

www.lpr-journal.org

Tunability of the Free-Spectral Range by Microwave Injection into a Mid-Infrared Quantum Cascade Laser

Etienne Rodriguez, Alireza Mottaghizadeh, Djamal Gacemi, Mathieu Jeannin, Zahra Asghari, Angela Vasanelli, Yanko Todorov, Qi Jie Wang,* and Carlo Sirtori**

The free-spectral range (FSR) of quantum cascade lasers (QCLs) emitting at 4.7 μm can be tuned through direct microwave modulation. The intrinsic short carrier lifetime of inter-subband transitions, along with impedance matched electrical packaging, allows a high-speed modulation up to more than 30 GHz. A significant broadening and flattening of the lasing spectrum is observed under radio frequency (RF) injection with frequencies close to the round-trip cavity. An accurate analysis of the high resolution spectra of the laser shows a comb-like regime for both free-running and RF modulated QCLs, if the modulation frequency is within the locking-range of the device. One of the main advantages of collecting high-resolution mid-infrared spectra, over the plain investigation of the beatnote in the microwave region, is the access to all the longitudinal modes and thus the accurate measure of the FSR over the whole optical spectrum. The use of high-resolution spectroscopy provides an in-depth and comprehensive analysis of lasing spectra under microwave modulations.

1. Introduction

The development of quantum devices based on inter-subband transitions (ISBT), especially since the invention of quantum cascade lasers (QCLs), has revealed significant advantages in the mid-infrared (MIR) domain. In addition to their compactness and electrical pumping, the unique properties of QCLs offer a remarkable degree of freedom for the choice of the wavelength emission and, contrary to conventional laser, are suitable for high-speed applications due to their ultrashort carrier lifetime. Recently, the comprehension of the intrinsic nonlinear mechanism responsible for the self-comb formation in QCLs has becoming a promising research topic in this field.[1,2] New techniques have been developed to study the phase and the stabilities of frequency comb QCL. The shifted-wave interference Fourier-transform spectroscopy (SWIFTS) measures the intermodal phase relation of the QCL comb using a coherent beatnote spectroscopy[3] and the Fourier-transform analysis of comb emission (FACE) study of the dual-comb multi-heterodyne detection and Fourier-transform analysis.[4] Both cases are consistent and show a nontrivial phase relation among the modes translating the complex mode-locking mechanism. Indeed, the strong dipole matrix elements of ISBT allow giant second and third order susceptibilities responsible for the generation of four-wave mixing (FWM) in QCLs.[5–9]

FWM is a powerful mechanism for generating a stable frequency comb regime in the MIR region owing to its extremely broad bandwidth resulted from the ultrashort intrinsic lifetime of these quantum structures.[8,10]

In the case of low-dispersion spectra, the common beating signal of the optical modes in the radio frequency (RF) domain induces a modulation of the population inversion which is converted into a resonance in the current through the structure. Conversely, an external direct microwave modulation at the round-trip frequency of the QCL can enhance this process and generates sidebands of the free-running modes. In the case of low-dispersion regions, it is known that active mode-locking through RF modulation can be achieved.[10–12] Moreover, electrical injection-locking of MIR QCLs has been shown to be a powerful technique that enables the generation of coherent frequency combs along with the ability to mitigate the downside of the

Dr. E. Rodriguez, Prof. Q. J. Wang, Prof. C. Sirtori
School of Electrical and Electronic Engineering
Nanyang Technological University
Singapore 639798, Singapore
E-mail: etienne.rodriguez@phys.ens.fr; qjwang@ntu.edu.sg; carlo.sirtori@ens.fr

Dr. E. Rodriguez, Prof. Q. J. Wang
CINTRA CNRS/NTU/THALES
UMI 3288
Research Techno Plaza
50 Nanyang Drive, Border Block, Level 6 Singapore 637553, Singapore

Dr. A. Mottaghizadeh, Dr. Z. Asghari
Laboratoire Matériaux et Phénomènes Quantiques
UMR7162
Université de Paris
Paris 75013, France

Dr. D. Gacemi, Dr. M. Jeannin, Prof. A. Vasanelli, Dr. Y. Todorov, Prof. C. Sirtori
Laboratoire de Physique de l'Ecole Normale Supérieure
ENS
Université PSL
CNRS
Sorbonne Université
Université de Paris
24 rue Lhomond, Paris 75005, France

The ORCID identification number(s) for the author(s) of this article can be found under https://doi.org/10.1002/lpor.201900389

DOI: 10.1002/lpor.201900389

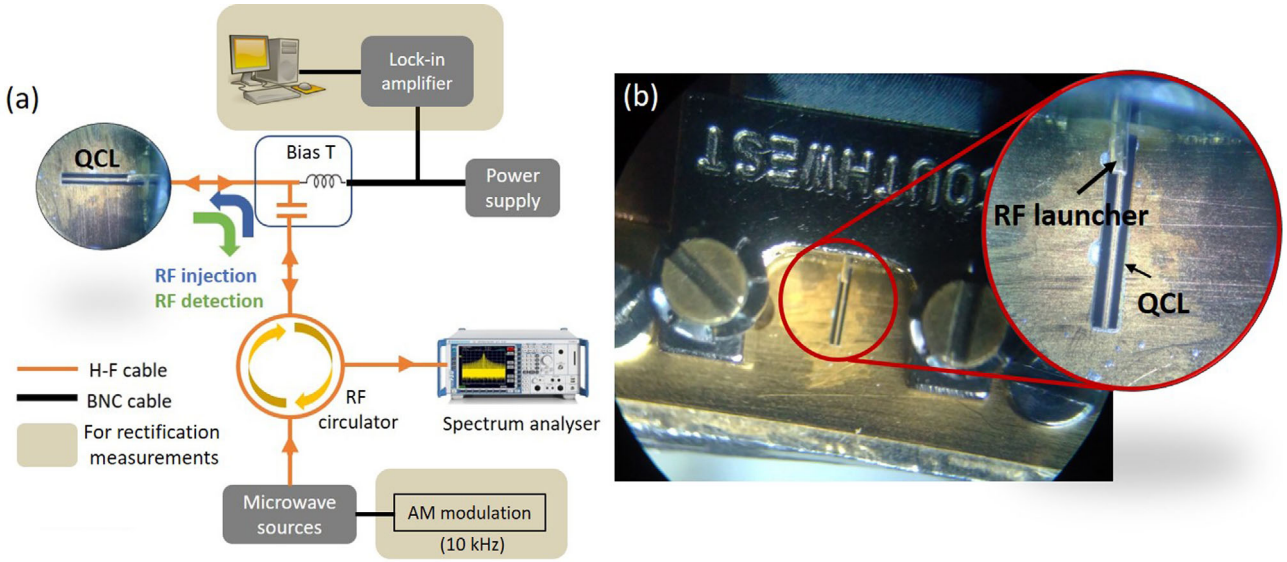

Figure 1. a) Setup used to inject and analyze the beating signal. The circulator and bias-T ensure the detection of the beatnote by the spectrum analyzer, and the injection of the microwave modulation in the device. The colored boxes represent the add-ons for the rectification measurements. b) Picture of the high-speed adaptation in the cryostat, the RF launcher is used to inject both AC and DC current in the QCL.

optical feedback which is an important obstacle to dual-comb spectroscopy based on QCLs.[13,14] The abilities of operating QCLs at frequency comb regimes offer an opportunity for many breakthroughs in various areas. Coupled with the newly developed wide-band quantum well infrared photodetectors (QWIPs), they pave the way toward microwave optical links in the atmospheric window.[15] For instance, recently, Pfeifle et al. have achieved a data transfer rate of 1.44 Tbit s^{-1} over up to 300 km by using near-infrared frequency comb sources,[16] demonstrating the capability of frequency comb in free-space communication applications. Besides, one of the great advances on dual-comb spectroscopy relies on their ability to tune the FSR to match narrow molecules absorption. Until now, this is mainly achieved by tuning the temperature or current of the QCL. The microwave injection permits an instantaneous shift of the FSR along with being a powerful tool for all-electrical frequency stabilization which would greatly benefit dual-comb multi-heterodyne experiments.[13,17,18]

In this paper, we demonstrate high-speed modulation of QCLs emitting at 4.7 µm up to 30 GHz, the speed of which is limited by our RF generator. This high-speed behavior enables the amplitude modulation (AM) at the round-trip frequency of our QCLs. This external oscillator can interact with the beating signal, which corresponds to the free-spectral range (FSR) of the cavity, and allows injection pulling and injection-locking mechanisms. This interaction has been studied through the evolution of the high-resolution spectra for free-running and injection-locked QCLs. The free-running lasers display a multimode operation with a narrow inter-mode beating signal. The external microwave modulation is injected at the same or a frequency close to the one of the beating signals, and we observe the injection-locking mechanism for a frequency placed at the locking-range of the beating signal. For both configurations, the high-resolution measurements show a constant FSR, corresponding to no observable dispersion beyond 10 MHz over the entire spectra. We also observed a noticeable generation of optical modes in the injection-locked spectra corresponding to side-band generation. Furthermore, these measurements allow us to observe clearly the change of the FSR following the frequency injected.

2. Sample Description and High-Speed Behavior

Recently, significant progress has been reported in the high-speed behavior of quantum devices based on ISBT, for instance, advanced design based on QCL embedded into microstrip line showed direct modulation up to 14 GHz.[19] The lasers used in this article are standard buried-heterostructures of about 3 µm thick InGaAs/InAlAs active region grown on InP substrate by molecular-beam epitaxy at a emitting wavelength of 4.7 µm. Ridge lasers are processed with a width between 4 and 10 µm. The length of the cavity is of 2, 3, and 4 mm, which is directly related to the beating frequency. In order to improve the external modulation performance in the GHz range, the active region is embedded in a 70 µm thick, 50 Ω impedance matched microstrip waveguide as represented in the picture **Figure 1**b and illustrated in the inset of **Figure 2**a.

The high-speed behavior of continuous wave (CW) operated QCLs requires a specific configuration, for which the cryostat must be adapted for high-speed transmission. The analog current (AC) and direct current (DC) injection is done using an RF launcher that we carefully place on the ridge as seen in the inset of Figure 1b. The packaging designed here would not be ideal in an environment with strong vibrations. To overcome this limitation an external coplanar waveguide can be attached to the ridge as a platform to weld the launcher. The electrical setup is shown in Figure 1a, where the RF circulator allows the injection and detection of the RF signal. We used a 45 GHz bias-T to ensure the DC and AC injection to the laser properly. The measurements of the current–voltage (IV) curves along with the RF injection

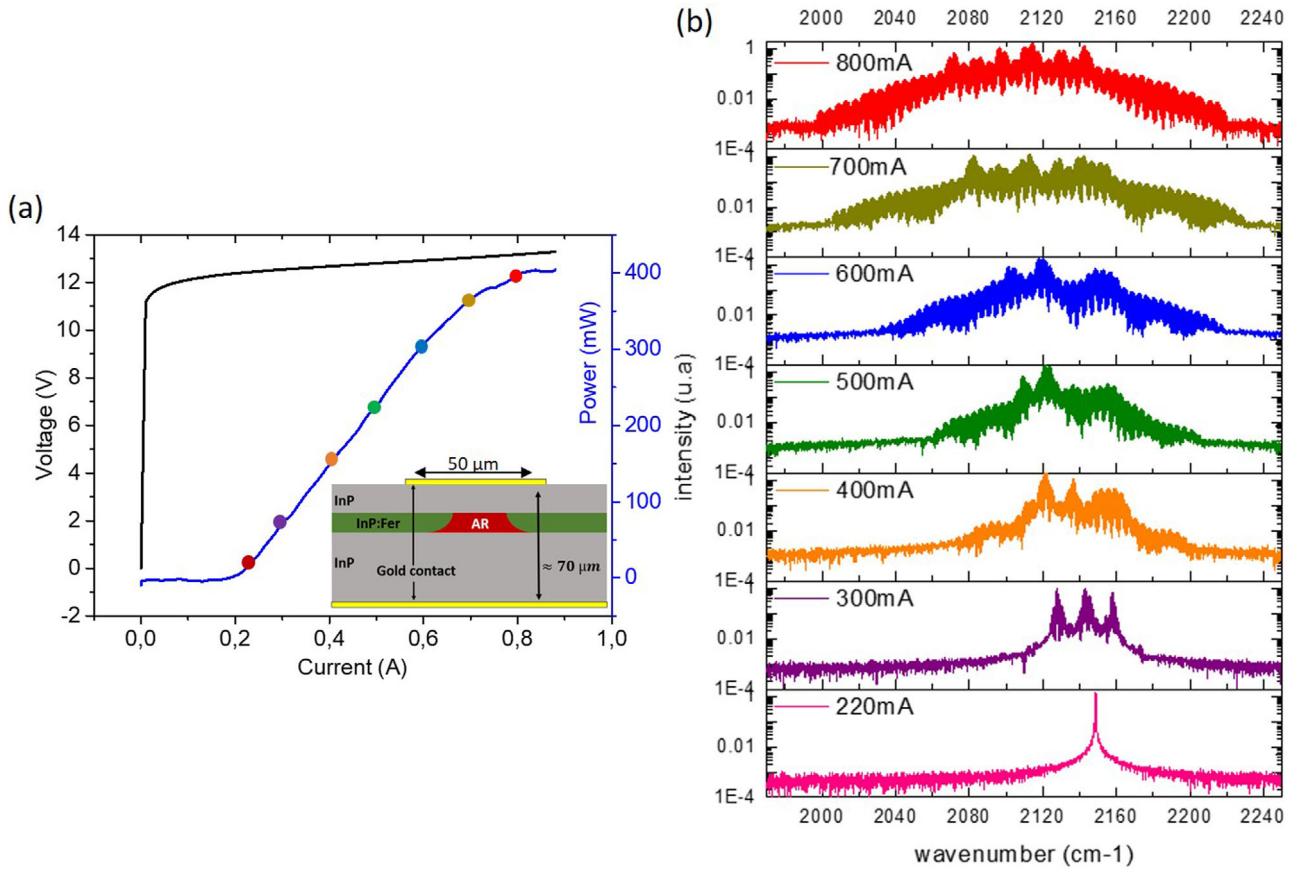

Figure 2. Characterization of the QCL used at CW operation at 80 K. a) current–voltage curves. The inset: diagram of the waveguide and b) spectra as a function of the current following the colored dots on the IV curve.

and the detection of the modulated signal is ensured respectively by a source meter (KEITHLEY 2400), a signal generator (Anritsu MG3693B) and a spectrum analyzer (Agilent E4407B). The high-resolution spectrum was recorded using a Bruker IFS 125 HR Fourier transform infrared spectrometer (FTIR) at the AILES beamline of SOLEIL with an absolute resolution of 60 MHz. The more important parameters are the relative precision of the optical mode position, the implementation of zero-padding, and cubic spline interpolation which largely increase the peak precision and allow us to record spectra with a peak precision of about 6 MHz.

Figure 2a shows the IV characteristic of a 3 mm long and 10 µm wide QCL emitting at 4.7 µm and operating in CW at 80 K. Emission spectra are recorded at various pumping currents (at each dot along the IV curve) and reported in Figure 2b. The laser operates in single-mode near the threshold, and then a multimode behavior with the increase of the current with broadened emission spectra spreading over more than 200 cm^{-1} near the roll-over.

The frequency response of the QCL is the product of the intrinsic transfer function of the laser, $h(\omega)$, and the transfer function of the electrical packaging.[10] QCLs can be modeled as equivalent lumped element circuits acting as a low-pass filter. In standard designs, the inductance introduced by the wire bonding dominates the circuit response and decreases drastically the cut-off frequency of the circuit. **Figure 3**a shows the simulation for a gold wire bonding connecting the laser to a lossless RF injection line. The deep and light blue curves represent respectively the cut-off frequency for a single 3 and 1 mm gold wire. Therefore, to ensure high-frequency propagation, the wire bonding connection is replaced by the RF launcher placed on the top contact. As a consequence, the inductance can be neglected, and the electrical circuit becomes a simple RC circuit. The cut-off frequency of the packaging circuit only depends on the differential resistance and the equivalent capacitance of the active region and the insulator layer. The differential resistance depends on the injected current and the capacitance can be calculated using the parallel plate capacitor approximation. The black curve in Figure 3a displays the cut-off frequency of our device with a differential resistance of 2 Ω while the red curve corresponds to the capacitance introduced by the active region as a function of the surface of the active region for the different widths.

The transient behavior and the theoretical frequency response of our quantum devices to a small modulation of the driving current can be expressed as[10]

$$|h(\omega)| = \frac{1}{\sqrt{1+\omega^4\tau_{\text{phot}}^2\tau_{\text{stim}}^2+\omega^2\tau_{\text{phot}}\tau_{\text{stim}}\left(\frac{\tau_{\text{phot}}\tau_{\text{stim}}}{\tau_3^2}+\frac{\tau_{\text{phot}}}{\tau_{\text{stim}}}+2\frac{\tau_{\text{phot}}}{\tau_3}-2\right)}}$$

$$\text{with } \tau_{\text{phot}} = \frac{n_{\text{eff}}}{c\alpha_{\text{tot}}} \text{ and } \tau_{\text{stim}}^{-1} = \left(\frac{J}{J_{\text{th}}}-1\right)\tau_3^{-1} \quad (1)$$

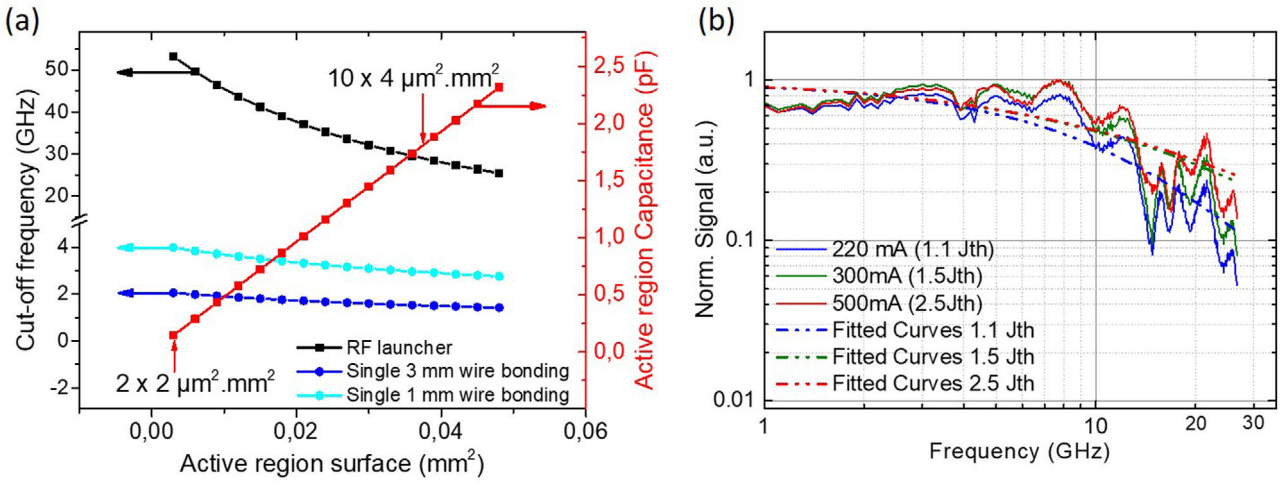

Figure 3. High-speed characterization of the QCL used at CW operation at 80 K. a) Capacitance of the active region of our laser (solid red line) and cut-off frequency for RF launcher (solid black line), single 3 and 1 mm wire bonding configurations (respectively solid deep and light blue line) as a function of the surface for a differential resistance of 2 Ω, and b) normalized rectification curves (solid line) and simulated curves (dashed line) for different J/J_{th} ratio up to 27 GHz.

τ_{phot} represents the lifetime of the photon in the cavity which is inversely proportional to the total loss in the cavity, τ_{stim} the lifetime of the stimulated emission directly linked to the structure alignment before the gain saturation and τ_3 the upper state lifetime. For a QCL in the MIR region, the typical value of the upper state lifetime at low temperature is about one to few picoseconds.

The high-speed behavior of our devices is measured by the microwave rectification technique at 80 K. This technique exploits the inherent nonlinear IV characteristics of QCLs to investigate their frequency response by applying an RF signal to the QCL and measuring the variation of its DC biasing current. The rectification methods reflect the frequency roll-off behavior of the intrinsic transfer function and the electrical circuit, along with other parasitic effects.[20,21] As shown in the colored boxes of Figure 1a, we applied an AM low-frequency modulation (10 kHz) to the RF generator and measure the DC rectification-voltage by the lock-in amplifier triggered at the frequency of the AM modulation. The variation of the current is then normalized and plotted on a log-scale graph for different driving currents. We used a RF injection power of 10 dBm with a step frequency of 100 MHz. The noise of the measurements was reduced by using a lock-in amplifier. Figure 3b exhibits the normalized rectification measurements performed at several J/J_{th} ratios in solid line limited by the RF generator which has a bandwidth of 30 GHz. The dashed line represents the simulation of the theoretical frequency response of the QCLs at the different currents considering the electrical circuit and the different lifetimes. After the threshold, the differential resistance drops to about 2 Ω and the capacitance of the device calculated is ≈2 pF. The lifetime of the stimulated emission represents, for a current of 1.1, 2, and 2.5 J_{th}, a value of 10, 1, and 0.67 ps, while the photon lifetime is set at $\tau_{phot} = 6.6$ ps which corresponds to a loss of about 15 cm^{-1}. As described by the theory, before gain saturation the cut-off frequency increases with the J/J_{th} ratio, as it can be observed in Figure 3b. The electrical resonances observed around 15 GHz, corresponding to a centimeter scale, are not inherent to the devices and are due to the reflections in the electrical circuit, these artifacts are often experimentally observed.[22,23]

The unique properties of ISBT, along with an impedance matched electrical circuit allow reaching a frequency modulation higher than 30 GHz. Therefore, this system unlocks all the benefits of an external modulation of the laser at the beating signal and opens the door to investigate the effect of an injection at the higher harmonics of the beating signal.

The high-speed behavior of our devices allows us to inject efficiently an external modulation at the FSR of our laser and generate new optical modes in the spectrum. The injection-locking mechanism of the beating signal is ease in low-dispersive regimes. However, in QCLs zero dispersion is not always required. The FWM process taking place in the active region is sensitive to the frequency and the relative phases of the optical modes. In low dispersion regime, it has the abilities to correct the dispersion by fixing the intermodal spacing and, therefore, facilitate the creation of frequency comb spectra. The material dispersion introduced by the InP and other materials constituting the waveguide is very low in the MIR (from 3.3 to 10 µm).[24] The evolution of the electric field of the fundamental mode with the frequency, seen in the inset of **Figure 4**, introduces a change of the confinement factor which translates in a variation of the group refractive index of the longitudinal modes over the spectrum. Thus, as shown in Figure 4, the group velocity dispersion (GVD) decreases rapidly with the width of the ridge. Nevertheless, the expansion of the active region will lead to the appearance of higher-order transverse modes oscillating in the Fabry–Perot (FP) cavity. As it is essential to maintain a low-dispersion regime to ensure frequency combs operation, a trade-off must be found between the dispersion management and the number of transverse modes lasing in the cavity.

To limit the waveguide dispersion of our devices, we will favor the use of wider active regions. For instance, for a waveguide of about 10 µm width without considering the

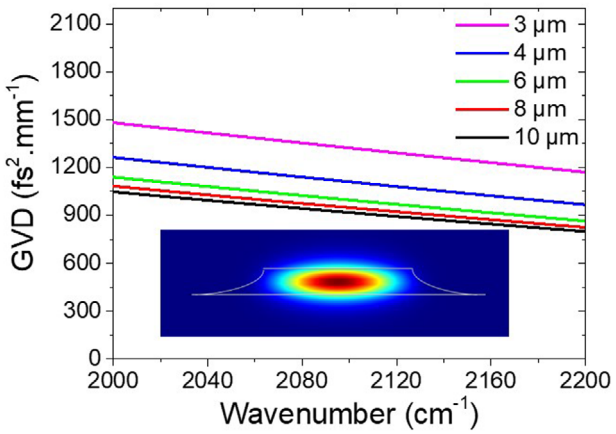

Figure 4. Waveguide dispersion for different widths of the ridges as a function of the wavenumber. Inset: simulation of the electric field of the fundamental mode in the waveguide.

contribution from the active region gain, the sum of the waveguide and material dispersion remains relatively low for a QCL in the MWIR.[24] However, such large waveguide sustains higher-order transverse modes that may oscillate in the cavity and can perturb the high-resolution spectra analysis as observed in the measurements.

3. Injection-Locking and Results on the Optical Spectrum

The phenomenon of injection-locking is well described by Adler's equation on coupled oscillators.[25] Indeed, this phenomenon can be related to the locking injection between a master oscillator (here the microwave modulation) and the slave oscillator (here beating signal of the Fabry–Perot modes) such as

$$\Delta\omega_{\text{lock}} = \frac{2\omega_0}{Q}\sqrt{\frac{I_0}{I_1}} \tag{2}$$

Where ω_0 and I_0 represent respectively, the frequency and intensity of the microwave modulation, I_1 the intensity of the beating signal and Q the quality factor of the slave laser resonator. For an injected frequency highly detuned from the cavity frequency, the beating signal is unperturbed by the RF injection. When the RF frequency approached the round-trip frequency of the cavity, we observe the generation of RF sidebands and the pulling effect of the beatnote toward the injected frequency. While further increasing the frequency of the master oscillator, the beating signal gets fully injected and follows the frequency of the external microwave modulation within the locking-range. These observations are directly accessible in the RF domain. However, it is the same mechanism governing the injection locking in the spectral domain. The external modulation applied to the laser will create sideband separated by the injection frequency next to the Fabry–Perot cavity modes. When the sidebands are close enough to the next optical modes, the Fabry–Perot modes become locked to the master oscillator.[19] As mentioned earlier, for free-running QCLs, the FWM is a passive mechanism. Nevertheless, it can be enhanced by an external microwave modulation at the same frequency than the beating signal. Thus, it can significantly broaden the spectrum by generating sidebands spaced by the injection frequency. On the other hand, for an injection out of the locking-range, the creation of the sidebands in the optical spectrum is too distant from the corresponding FP modes; they cannot be amplified by the gain and does not contribute to the evolution of the optical spectrum. Therefore, in the low-dispersion regions, the external microwave modulation at the round-trip frequency will not only generate new frequencies but also create a comb-like regime with a fixed spacing between the modes. **Figure 5**a shows the evolution of the spectrum with the power of the microwave modulation at the round-trip cavity of 4 mm emitting at 4.7 µm. We observed the generation of a large number of optical modes and a new distribution of the energy among them over the spectra. The sidebands generated are locked at the frequency of the RF generator which is at the round-trip frequency. This extends from about 25 cm^{-1} without injection to 54 cm^{-1} with 30 dBm injection. This extension is represented by the green area on the spectra with as boundaries the red dashed lines. Above the injection of 20 dBm (100 mW) the generation of new modes slows down, but we still observe a redistribution of energy between the modes. The FWM mechanism conducts to a broadening of the spectrum and the creation of a more homogeneous distribution of the amplitude among the modes. We studied this effect with a peak detection threshold within an amplitude of at least 1% and 10% of the maximum power of the optical peaks. Figure 5b records the increase of the number of modes as a function of the injected power. We define the total number of modes as the number of modes within an amplitude greater than 1% of the maximum amplitude. This quantity goes from about 25, without injection, to more than 120 for an injection at 30 dBm. The inset represents the percentage of modes within an amplitude of 90% of the highest peak, the proportion of peaks included in this ranges goes from 20% without injection to 60% of the optical modes with the RF injection. Figure 5c is a zoom-in, in linear scale, on the sideband generation between the free-running spectrum and the 0 dBm injection at the round-trip frequency. The net increase of number of longitudinal modes at low injected power corresponds to the redistribution of the energy of the principal cavity modes on their neighboring modes through the generation of sidebands, represented with different colors in the red spectrum. The relatively low overlap between the microwave mode and the active region and the high impedance mismatch between the source and the laser leads to an injection efficiency expected in the order of a few percent. Therefore, the observed effects on the spectra are generated with an injection power in the order of few tens of µW only. Due to the square roots dependence of the locking-range with the injected power, the optimization of the injection efficiency is crucial to achieving wider tunability of the FSR.

As the FWM is a frequency and phase sensitive process, this configuration has the potential to stabilize the frequency and phase of the modes generated.

The new generation of modes through the FWM process does not only have the ability to broaden the spectrum but also to compensate the dispersion. Indeed, the position of the new modes generated is placed at a frequency span described by the FSR,

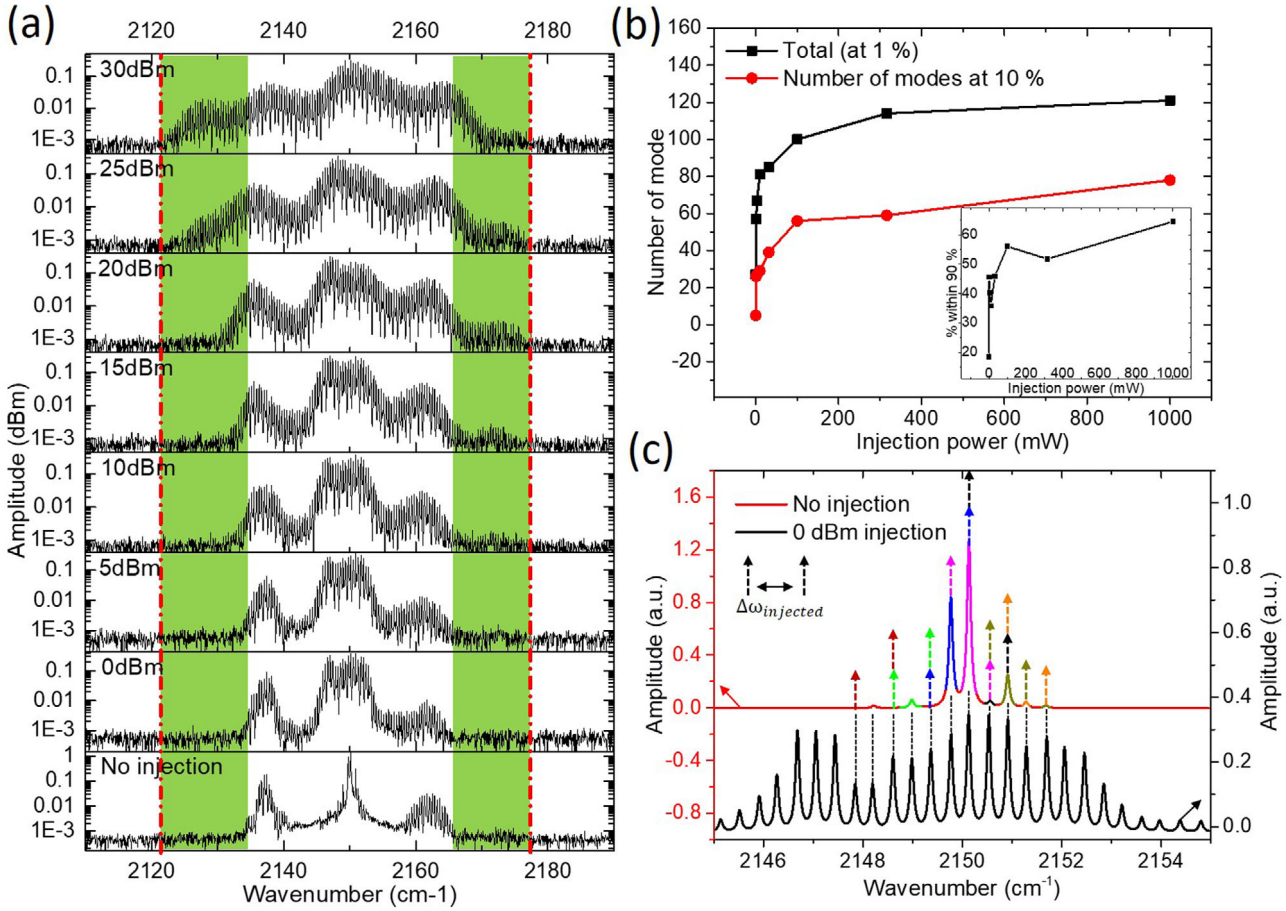

Figure 5. a) Evolution of the spectrum for several power injections for a 4 mm QCL at 4.7 μm with a current of 300 mA corresponding to 1.6 J_{th}; b) evolution of the number of optical modes for different injected power. The red curve is the number of optical modes with an amplitude of at least 10% of the maximum power and the black curve corresponds to an amplitude of at least 1%. The inset represents the percentage of the modes included in an amplitude of 90% of the highest peak. c) Evolution of the high-intensity group of modes under 0 dBm injection. The dashed arrow illustrates the sidebands generation.

i.e., exactly positioned as a comb spectrum. They are acting as a master oscillator and, in the case of a low-dispersion regime, will lock the existing dispersed-modes. In that sense, if the dispersion remains small enough, the modes stay efficiently coupled by the FWM and act as a comb operation.[24]

4. High-Resolution Study of the FSR

Each spectrum is recorded after the stabilization of the temperature. The parameters of the FTIR are set to achieve the highest resolution of the instrument described in the introduction. The acquisition time of the high-resolution spectra presented in the next studies was ≈20 min. No stabilization of the offset frequency was used for the measurements. The analyses of the single comb tooth for the high-resolution spectra show a Gaussian linewidth whose half width at half maximum is $\approx 5 \times 10^{-3}$ cm^{-1} (150 MHz). We do not observe an eventual frequency shift due to the current and temperature instabilities; moreover, the potential broadening of the FP modes due to these sources of noise would not influence the main results which are the peak frequencies of the modes.

The maximum of each optical mode is compared to the position of the previous and next modes, yielding the evolution of the FSR as a function of the mode number, or frequency. Since the FSR is related to the dispersion through the group refractive index n_g, a zero dispersion leads to a constant $n_g(\omega)$ and hence, a constant FSR. However, in the case of a nonzero dispersion, the peak position of each mode will be slightly shifted accordingly to the variation of the group refractive index and therefore, will introduce a frequency dependence of the FSR.

As described earlier, the wide waveguide used to reduce the dispersion allows the propagation of higher-order transverse modes with much lower intensities. Due to the finite resolution of the FTIR, the overlap between the fundamental and the high-order transverse modes of the cavity can result in a broadening of the comb tooth and therefore, an error in the peak frequency measurement. This phenomenon leads to a slight shift in the position of the maximum of the fundamental mode which produces an unwanted variation of the FSR.

This is usually observed at the edge of the spectra where the cavity modes have comparable amplitudes. This phenomenon has also been observed in other experiments.[26]

The use of high-resolution spectra allows us to see the dispersion into the MHz range and, therefore, reveals much more information than the basic observation of the beating signal. For instance, we can have a clear idea of the modes efficiently injected by the external modulation and master their FSR over a relatively large frequency span. **Figure 6**a is a zoom-in of the high-resolution spectra without injected (in gray) and with an injection at one of the extremities of the locking-range (in red). The upper part of Figure 6b–d represent the study of the FSR as a function of the wavenumber, while the lower part is the corresponding spectrum. The spectra are recorded for the QCL at a current of 400 mA with and without microwave modulation. An averaging is applied to the values of the FSR to smooth the oscillation due to the resolution. The red and green dashed lines and the yellow regions represent respectively, the frequency injected, the extremities of the locking-range and a frequency area of 10 MHz corresponding to approximately the resolution of the instrument. Figure 6b is the free-running spectrum without RF injection. Figure 6c,d represents a microwave modulation at 27 dBm for an injection in (red spectrum: M4) and out (green spectrum: M3) of the locking-range. We do not observe a variation of the modes spacing in the resolution of the FTIR, i.e., below 10 MHz. Nevertheless, the injection at the frequency 13 MHz lower than the beating signal is out of the locking-range (M3). In this case, only the small part of the spectrum indicated by the yellow region and the red dashed line is locked and follows the new FSR dictated by the microwave modulation. The next 70 modes are not locked and oscillate around a value following the not injected beatnote. The colored stars of Figure 6e displays the injection frequency (right axis) as a function of the average FSR measured over a stable area of the spectrum. The left axis corresponds to the colored histograms of the repartition of the FSR over the spectrum for each measurement (M2, M3, M4, and M5). The different microwave injections in the RF domain are represented in **Figure 7**a. The yellow area illustrates the locking-range of the laser at this injection power. For an RF injection detuned from the beating signal, we can observe the shift of the FSR correspondingly. Each bin size represents a frequency window of 6 MHz. As seen previously, for a microwave modulation in the locking-range, the FSR remains concentrated in the resolution. Nevertheless, for the measurements M3, out of the locking-range, we observe a significant broadening represented on the green histogram.

With or without injection in the locking-range, the high-resolution measurements do not show any dispersion within the resolution of the FTIR. Therefore, we can conclude that more than 90% of the optical power produced by the laser has a constant FSR within 10 MHz. Regardless of the thin beating signal of the free-running modes, the analysis of the mode spacing shows a frequency comb-like regime [2], for the free-running and injection-locked QCL. Nevertheless, a phase analysis of the modes is required to claim a frequency comb regime.

Similar measurements have been realized at different current densities and on QCLs emitting at 9 µm and draw the same conclusion.

5. Tunability of the FSR

The constant FSR over the spectrum is an important tool for many applications. Adding to that, the potential to tune the FSR over a range of frequency offers a new degree of freedom which opens the door to strong advantages in several applications, especially in multi-heterodyne measurements and dual-comb spectroscopy. In this study, we will further investigate the tunability of the FSR of our QCLs presented in the previous paragraph under microwave modulation. Figure 7a illustrates the measurements in the RF domain, with in solid gray arrow the beating signal of the free-running laser and in dashed colored arrows the frequencies of the different injections in and out of the locking-range. Each measurement is noted as M*X*, with *X* the number of the measurement (M1 corresponds to the spectrum without injection). The change of the FSR is investigated for injection at each extremity of the locking-range (M5 and M4), on the beatnote (M2) and out of the locking-range (M3).

To study the tunability of the FSR under a microwave modulation we compare the position of the optical mode N_i of the injected spectra with the equivalent optical mode of the noninjected spectrum as illustrated in Figure 7b. The first mode (N_1) is chosen arbitrarily from the beginning of the free-running spectrum as a reference. In an ideal case, the frequency of the mode with respect to the first mode N_1 is given by $\omega_i = \omega_1 + i \times \mathrm{FSR}$ with i an integer number. Upon RF injection, this relation translates to $\omega'_{i\_\mathrm{inj}} = \omega'_1 + i * \mathrm{FSR}_{\mathrm{inj}}$. ω_i and ω'_{i_inj} represent respectively the frequency of the ith mode for the free-running spectrum and the injected spectra. To simplified and remove the frequency offset we will shift all the injected spectra to the same first comb mode $\omega'_1 - \omega_1 = 0$. Hence, the shift between the injected and noninjected peak frequency, $\Delta\omega = \omega'_{i\_\mathrm{inj}} - \omega_i$, follows a linear relation given by $\Delta\omega = i \times (\mathrm{FSR}_{\mathrm{inj}} - \mathrm{FSR})$. Consequently, the variation of the frequency shift between two consecutive modes is proportional to the mode number. This proportionality coefficient is simply the frequency difference between the injected and free-running beatnotes. Figure 7c displays the analysis of the variation of the peak position under RF injection compared to the reference value without injection (ΔM*X*). The injection at a frequency higher than the beating signals increase the value of the FSR (in cm^{-1}), and thus, exhibits a positive slope corresponding to the difference of frequency between the beatnote of the free-running QCL and the RF injection. On the contrary, the injection at a lower frequency will decrease the value of the FSR and introduce a negative slope. We can noticeably observe the evolution of the peak position which shows the adaptation of the modes to the microwave modulation over the entire spectrum. Regarding the injection out of the locking-range, as observed previously, only the first modes are locked to the injected frequency. The dashed line corresponds to the slope expected for the injection, i.e., the variation of the FSR with the not injected spectrum. These values, along with the experimental slopes are recorded in **Table 1**.

For the injection in the locking-range all the modes follow the expected slopes, it implies that they have been efficiently locked at the frequency of the microwave modulation. As observed previously, the higher-order transverse modes are generating the breaks of the slopes noticed at the beginning and end of the curves. Table 1 lists the expected values of the slope

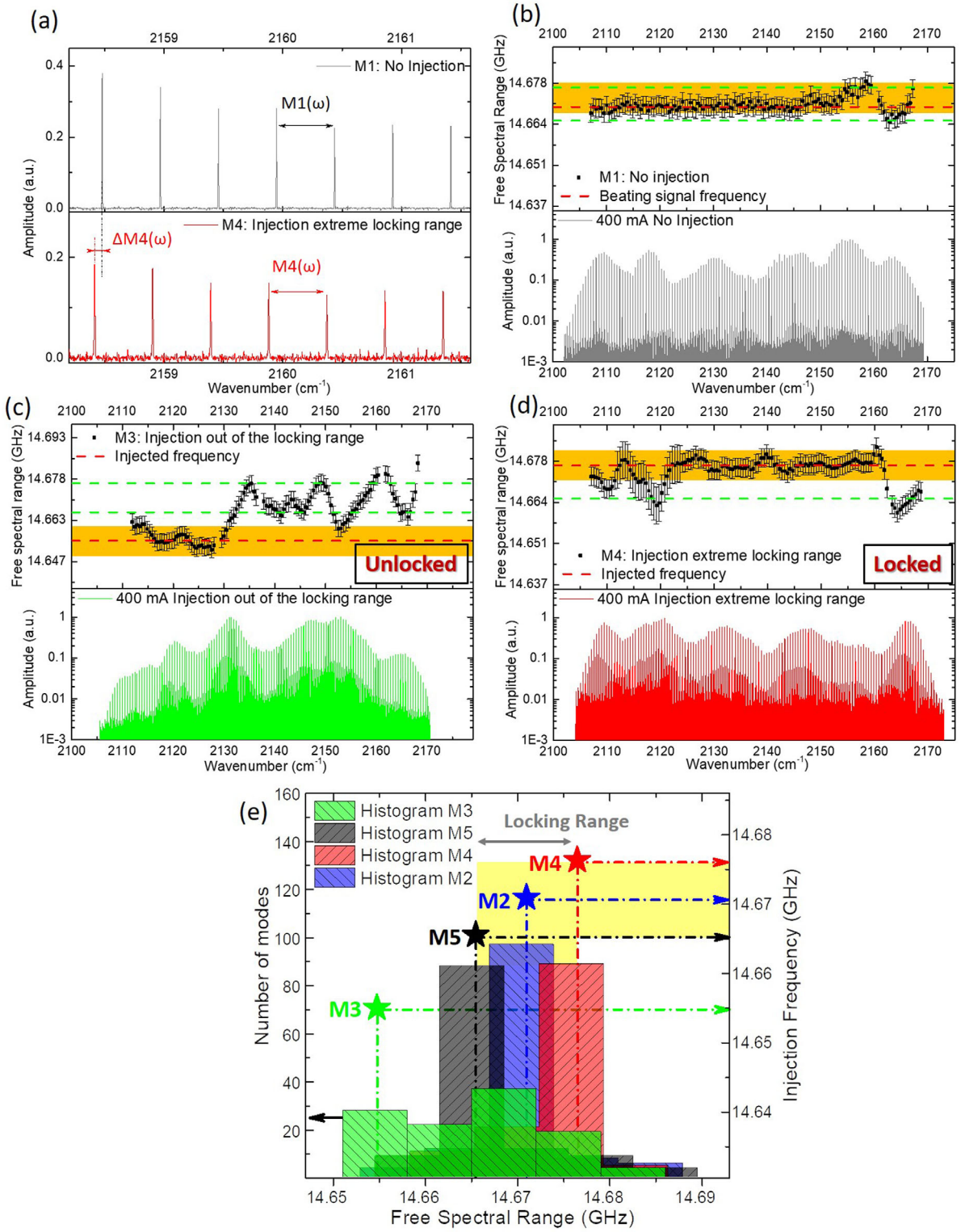

Figure 6. a) Zoom-in of the high-resolution spectra without injected (in gray) and with an injection at one of the extremities of the locking-range (in red). b–d) Analysis of the variation of the FSR over the spectra of a QCL emitting at 4.7 μm driven by a current of 400 mA with or without injection. The upper parts represent the FSR as a function of the wavenumber with the yellow region exhibiting a frequency area of 10 MHz and the lower parts showing the corresponding spectrum. b) The spectrum of the free-running QCL in gray, c,d) spectra with an RF injection, respectively, at the higher extremity of the locking-range in red and out of the locking-range in green. The injection frequencies and the extremities of the locking-range are indicated in dashed red and green lines. e) The right axis represents the injection frequency as a function of the average FSR measured over a stable area of the spectrum and the left axis is the histograms of the FSR repartition for each measurement. The yellow area represents the locking-range of the device.

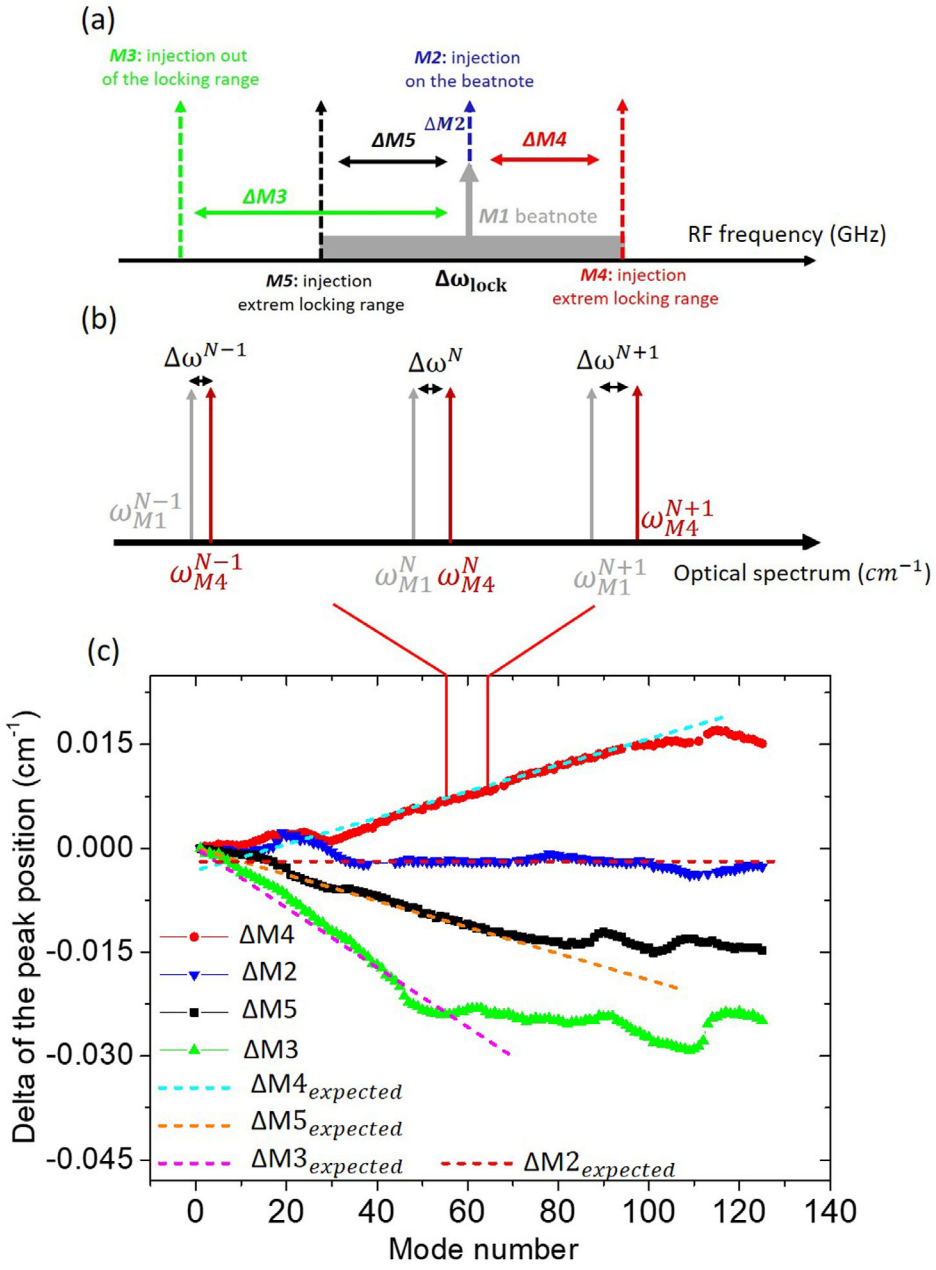

Figure 7. Measurements M1 without and M2, M3, M4, and M5 with RF injection at 27 dBm. a) Illustration of the measurement with RF injection at different frequencies in and out of the locking-range represented in gray, b) representation of the variation $\Delta\omega$ of the peak position between the free-running spectrum (gray) and injected spectrum (red). c) The variation of the peak position between the spectra injected (M2, M3, M4, or M5) and the spectrum noninjected taken as reference (M1) with the expected slope in dashed line (ΔM2, ΔM3, ΔM4, ΔM5).

Table 1. Experimental and calculated values of the shift of the FSR under microwave modulation.

Measurements	Slope expected [cm^{-1}]	Real slope [cm^{-1}]
ΔM5 (extreme low frequency of the range)	1.9×10^{-4} (5.7 MHz)	1.9×10^{-4} (5.6 MHz)
ΔM4 (extreme high frequency of the range)	-1.9×10^{-4} (–5.7 MHz)	-2.0×10^{-4} (–6 MHz)
ΔM2 (on the beatnote)	≈ 0 (0 MHz)	In the noise

corresponding to the ΔM*X* in Figure 7c and the experimental values given by a linear fit over the stable part of the spectrum for the analysis concerned. For the injection in the locking-range the experimental values are in an excellent agreement with the expected values. Moreover, we record a locking-range covering a frequency span of 13 MHz which is, as far as we know, the wider locking-range reported in MIR region. These results are consistent with the literature where the injection-locking of a THz comb QCL detuned from the beating signal introduces a shift of the dual-comb

multi-heterodyne frequencies in the MHz range.[14] Regarding the injection out of the locking-range (ΔM3), only a small portion of the spectrum is locked and follows the modulation. The slope expected (-4.3×10^{-4}) (–12.8 MHz)) is in accordance with the experimental slope (-4.7×10^{-4} (–14.1 MHz)) calculated over the modes locked (50 first modes). The remaining part of the spectrum does not follow this slope and, as seen previously, are not injected.

The external microwave modulation enables to tune the FSR over the locking-range. Same results have been found for different positions in the IV curve, lasers length, and for QCLs emitting at 9 µm. Beyond the advantages that bring too many applications, the fine study of the spectrum under an injection detuned from the beating signal can give important information on the dispersion and the correction of dispersion introduced by the FWM.

6. Conclusion

In conclusion, we have demonstrated high-speed QCL embedded in a microstrip line with a modulation band up to 30 GHz at cryogenic temperature where the highest frequency is limited by our test equipment. The modulation of the population inversion at the round-trip cavity, along with a design allowing low-dispersion, enable the generation of a large number of optical modes and a more homogenous distribution of the amplitude among the modes over the spectra, through FWM mechanism. The high-resolution spectra analysis shows no variation of the FSR within the resolution of the FTIR, (6 MHz), thereafter, showing a comb-like regime for free-running and RF injected operation over the entire spectrum. Furthermore, comparing the high-resolution spectra under microwave injection with the free-running spectrum, allows us to observe that the great majority of the longitudinal optical modes are separated by a frequency dictated by the master oscillator, which corresponds to a tunability of the FSR over the beat note locking-range. The ability of QCL to work as a comb-like regime and to tune FSR by microwave modulation makes them very promising for many applications in the atmospheric windows in the MIR, especially in heterodyne, dual comb spectroscopy and free-space communications.

Acknowledgements

The authors acknowledge Olivier Pirali for its help during the measurements of the QCLs emitting at 4.7 µm at Synchrotron Source Optimisée de Lumière d'Energie Intermédiaire du LURE (SOLEIL). Moreover, the authors would like to thank Fridolin Kwabia-Tchana and Xavier Landsheere for the measurements of the QCLs emitting at 9 µm at Laboratoire Inter-Universitaire des Systèmes Atmosphèrique (LISA). Furthermore, this work was supported by the Singapore National Research Foundation, Competitive Research Program (NRF-CRP18-2017-02) and Singapore Ministry of Education Tier 2 Program (MOE2016-T2-2-159).

Conflict of Interest

The authors declare no conflict of interest.

Keywords

injection locking, mid-infrared region, quantum devices, tunability of the free-spectral-range, ultrafast devices

Received: November 13, 2019
Revised: March 11, 2020
Published online:

[1] G. Villares, J. Faist, *Opt. Express* **2015**, *23*, 1651.
[2] A. Hugi, G. Villares, S. Blaser, H. C. Liu, J. Faist, *Nature* **2012**, *492*, 229.
[3] M. Singleton, P. Jouy, M. Beck, J. Faist, *Optica* **2018**, *5*, 948.
[4] F. Cappelli, L. Consolino, G. Campo, I. Galli, D. Mazzotti, A. Campa, M. Siciliani de Cumis, P. Cancio Pastor, R. Eramo, M. Rösch, M. Beck, G. Scalari, J. Faist, P. De Natale, S. Bartalini, *Nat. Photonics* **2019**, *13*, 562.
[5] F. Capasso, C. Sirtori, A. Y. Cho, *IEEE J. Quantum Electron.* **1994**, *30*, 1313.
[6] D. Walrod, S. Y. Auyang, P. a. Wolff, M. Sugimoto, *Appl. Phys. Lett.* **1991**, *59*, 2932.
[7] M. R. St-Jean, M. I. Amanti, A. Bismuto, M. Beck, J. Faist, C. Sirtori, *Opt. Express* **2017**, *25*, 1847.
[8] P. Friedli, H. Sigg, B. Hinkov, A. Hugi, S. Riedi, M. Beck, J. Faist, *Appl. Phys. Lett.* **2013**, *102*, 222104.
[9] Q. Y. Lu, M. Razeghi, S. Slivken, N. Bandyopadhyay, Y. Bai, W. J. Zhou, M. Chen, D. Heydari, A. Haddadi, R. McClintock, M. Amanti, C. Sirtori, *Appl. Phys. Lett.* **2015**, *106*, 1.
[10] J. Faist, *Quantum Cascade Lasers*, Oxford University, Oxford **2013**.
[11] H. Li, P. Laffaille, D. Gacemi, M. Apfel, C. Sirtori, J. Leonardon, G. Santarelli, M. Rösch, G. Scalari, M. Beck, J. Faist, W. Hänsel, R. Holzwarth, S. Barbieri, *Opt. Express* **2015**, *23*, 33270.
[12] L. Kuznetsova, C. Y. Wang, V. M. Gkortsas, L. Diehl, F. X. Kärtner, M. A. Belkin, A. Belyanin, X. Li, D. Ham, H. Schneider, H. C. Liu, F. Capasso, *Conf. Lasers Electro-Opt./Int. Quantum Electron. Conf.* **2009**, CMBB6.
[13] J. Hillbrand, A. M. Andrews, H. Detz, G. Strasser, B. Schwarz, *Nat. Photonics* **2019**, *13*, 101.
[14] L. Consolino, M. Nafa, F. Cappelli, K. Garrasi, F. P. Mezzapesa, L. Li, A. G. Davies, E. H. Linfield, M. S. Vitiello, P. De Natale, S. Bartalini, *Nat. Commun.* **2019**, *10*, 2938.
[15] E. Rodriguez, A. Mottaghizadeh, D. Gacemi, D. Palaferri, Z. Asghari, M. Jeannin, A. Vasanelli, A. Bigioli, Y. Todorov, M. Beck, J. Faist, Q. J. Wang, C. Sirtori, *ACS Photonics* **2018**, *5*, 3689.
[16] J. Pfeifle, V. Brasch, M. Lauermann, Y. Yu, D. Wegner, T. Herr, K. Hartinger, P. Schindler, J. Li, D. Hillerkuss, R. Schmogrow, C. Weimann, R. Holzwarth, W. Freude, J. Leuthold, T. J. Kippenberg, C. Koos, *Nat. Photonics* **2014**, *8*, 375.
[17] G. Villares, A. Hugi, S. Blaser, J. Faist, *Nat. Commun.* **2014**, *5*, 5192.
[18] Y. Wang, M. G. Soskind, W. Wang, G. Wysocki, *Appl. Phys. Lett.* **2014**, *104*, 031114.
[19] M. R. St-Jean, M. I. Amanti, A. Bernard, A. Calvar, A. Bismuto, E. Gini, M. Beck, J. Faist, H. C. Liu, C. Sirtori, *Laser Photonics Rev.* **2014**, *8*, 443.
[20] H. C. Liu, J. Li, M. Buchanan, Z. R. Wasilewski, *IEEE J. Quantum Electron.* **1996**, *32*, 1024.
[21] H. Schneider, H. C. Liu, *Quantum Well Infrared Photodetectors*, Springer Series in Optical Sciences, Springer, Berlin **2007**.
[22] B. Hinkov, A. Hugi, M. Beck, J. Faist, *Opt. Express* **2016**, *24*, 3294.
[23] A. Calvar, M. I. Amanti, M. Renaudat St-Jean, S. Barbieri, A. Bismuto, E. Gini, M. Beck, J. Faist, C. Sirtori, *Appl. Phys. Lett.* **2013**, *102*, 1.
[24] J. Faist, G. Villares, G. Scalari, M. Rösch, C. Bonzon, A. Hugi, M. Beck, *Nanophotonics* **2016**, *5*, 272.
[25] R. Adler, *Proc. IEEE* **1973**, *61*, 1380.
[26] M. Rösch, G. Scalari, M. Beck, J. Faist, *Nat. Photonics* **2015**, *9*, 42.

Bibliography

[A. Gomez 2008] A. Gomez, A. Nedelcu E. Costard X. Marcadet V. B. M. Carras C. M. Carras: Advantages of Quantum Cascade Detectors. In: *Proc. of SPIE* 6900 (2008), Nr. 69000J, S. 69000J–1–69000J–14

[A. rostami 2011] A. rostami, H. B. H. Rasooli R. H. Rasooli: *Terahertz technology*. Springer, 2011. – ISBN 1876–1100

[Adler et al. 2010] Adler, Florian ; Masłowski, Piotr ; Foltynowicz, Aleksandra ; Cossel, Kevin C. ; Briles, Travis C. ; Hartl, Ingmar ; Ye, Jun: Mid-infrared Fourier transform spectroscopy with a broadband frequency comb. In: *Optics Express* 18 (2010), sep, Nr. 21, 21861. http://dx.doi.org/10.1364/oe.18.021861. – DOI 10.1364/oe.18.021861

[Arthur 1968] Arthur, J. R.: Interaction of Ga and As2 Molecular Beams with GaAs Surfaces. In: *Journal of Applied Physics* 39 (1968), jul, Nr. 8, 4032–4034. http://dx.doi.org/10.1063/1.1656901. – DOI 10.1063/1.1656901

[Ayon 1999] Ayon, A. A.: Influence of Coil Power on the Etching Characteristics in a High Density Plasma Etcher. In: *Journal of The Electrochemical Society* 146 (1999), Nr. 7, 2730. http://dx.doi.org/10.1149/1.1392001. – DOI 10.1149/1.1392001

[Bai et al. 2011] Bai, Y. ; Bandyopadhyay, N. ; Tsao, S. ; Slivken, S. ; Razeghi, M.: Room temperature quantum cascade lasers with 27% wall plug efficiency. In: *Applied Physics Letters* 98 (2011), may, Nr. 18, 181102. http://dx.doi.org/10.1063/1.3586773. – DOI 10.1063/1.3586773

[Balaras and Argiriou 2002] Balaras, C.A. ; Argiriou, A.A.: Infrared thermography for building diagnostics. In: *Energy and Buildings* 34 (2002), feb, Nr. 2, 171–183. http://dx.doi.org/10.1016/s0378-7788(01)00105-0. – DOI 10.1016/s0378–7788(01)00105–0

[Barr 1961] Barr, E.Scott: The infrared pioneers—I. Sir William Herschel. In: *Infrared Physics* 1 (1961), mar, Nr. 1, 1–IN6. http://dx.doi.org/10.1016/0020-0891(61)90037-9. – DOI 10.1016/0020–0891(61)90037–9

[Bastard 1988] Bastard, G.: *Wave mechanics applied to semiconductor heterostructures*. Les Éditions de Physique, 1988 (Monographies de physique). https://books.google.fr/books?id=5rrvAAAAMAAJ. – ISBN 9780470217085

[Beck 2001] Beck, M.: Continuous Wave Operation of a Mid-Infrared Semiconductor Laser at Room Temperature. In: *Science* 295 (2001), dec, Nr. 5553, 301–305. http://dx.doi.org/10.1126/science.1066408. – DOI 10.1126/science.1066408

[Belenky et al. 2008] Belenky, Gregory ; Donetski, Dimitri ; Shterengas, Leon ; Hosoda, Takashi ; Chen, Jianfeng ; Kipshidze, Gela ; Kisin, Michail ; Westerfeld, David: Interband GaSb-based laser diodes for spectral regions of 2.3-2.4 m and

3-3.1 m with improved room-temperature performance. In: Sudharsanan, Rengarajan (Hrsg.) ; Jelen, Christopher (Hrsg.): *Quantum Sensing and Nanophotonic Devices V*, SPIE, feb 2008

[Bell 1880] Bell, Alexander G.: The Photophone. In: *Science* 1 (1880), sept, Nr. 11

[Bewley et al. 2013] Bewley, W. W. ; Kim, C. S. ; Canedy, C. L. ; Merritt, C. D. ; Vurgaftman, I. ; Abell, J. ; Meyer, J. R. ; Kim, M.: High-power, high-brightness continuous-wave interband cascade lasers with tapered ridges. In: *Applied Physics Letters* 103 (2013), sep, Nr. 11, 111111. http://dx.doi.org/10.1063/1.4821263. – DOI 10.1063/1.4821263

[Bharara et al. 2012] Bharara, Manish ; Schoess, Jeffrey ; Armstrong, David G.: Coming events cast their shadows before: detecting inflammation in the acute diabetic foot and the foot in remission. In: *Diabetes/Metabolism Research and Reviews* 28 (2012), jan, 15–20. http://dx.doi.org/10.1002/dmrr.2231. – DOI 10.1002/dmrr.2231

[Bhattacharya and Mi 2007] Bhattacharya, Pallab ; Mi, Zetian: Quantum-Dot Optoelectronic Devices. In: *Proceedings of the IEEE* 95 (2007), sep, Nr. 9, 1723–1740. http://dx.doi.org/10.1109/jproc.2007.900897. – DOI 10.1109/jproc.2007.900897

[Browning and Gurney 1999] Browning, K. A. ; Gurney, R. J.: Global Energy and Water Cycles. (1999), April

[Buffaz et al. 2010] Buffaz, A. ; Gomez, A. ; Carras, M. ; Doyennette, L. ; Berger, V.: Role of subband occupancy on electronic transport in quantum cascade detectors. In: *Physical Review B* 81 (2010), feb, Nr. 7. http://dx.doi.org/10.1103/physrevb.81.075304. – DOI 10.1103/physrevb.81.075304

[Bugajski et al. 2013] Bugajski, Maciej ; Pierscinski, Kamil ; Pierscinska, Dorota ; Szerling, Anna ; Kosiel, Kamil: Multimode instabilities in mid-infrared quantum cascade lasers. In: *Photonics Letters of Poland* 5 (2013), oct, Nr. 3. http://dx.doi.org/10.4302/plp.2013.3.02. – DOI 10.4302/plp.2013.3.02

[Butler et al. 1964] Butler, J. F. ; Calawa, A. R. ; Phelan, R. J. ; Harman, T. C. ; Strauss, A. J. ; Rediker, R. H.: PbTe DIODE LASER. In: *Applied Physics Letters* 5 (1964), aug, Nr. 4, 75–77. http://dx.doi.org/10.1063/1.1754062. – DOI 10.1063/1.1754062

[C. Koeniguer and Berger 2006] C. Koeniguer, A. G. G. Dubois D. G. Dubois ; Berger, V.: Electronic transport in quantum cascade structures at equilibrium. In: *PHYSICAL REVIEW B* 74 (2006), Nr. 23, S. 1–6

[Calvar et al. 2013] Calvar, A. ; Amanti, M. I. ; St-Jean, M. R. ; Barbieri, S. ; Bismuto, A. ; Gini, E. ; Beck, M. ; Faist, J. ; Sirtori, C.: High frequency modulation of mid-infrared quantum cascade lasers embedded into microstrip line. In: *Applied Physics Letters* 102 (2013), may, Nr. 18, 181114. http://dx.doi.org/10.1063/1.4804370. – DOI 10.1063/1.4804370

[Calvar 2013] Calvar, Ariane: *Design, engineering and processing of QC Lasers for high frequency modulation*, Université Paris Diderot, Diss., 2013

[Campbell and Madhukar 2007] Campbell, J.C. ; Madhukar, A.: Quantum-Dot Infrared Photodetectors. In: *Proceedings of the IEEE* 95 (2007), sep, Nr. 9, 1815–1827. http://dx.doi.org/10.1109/jproc.2007.900967. – DOI 10.1109/jproc.2007.900967

[Canedy et al. 2005] Canedy, C. L. ; Bewley, W. W. ; Lindle, J. R. ; Vurgaftman, I. ; Kim, C. S. ; Kim, M. ; Meyer, J. R.: High-power continuous-wave midinfrared type-II "W" diode lasers. In: *Applied Physics Letters* 86 (2005), may, Nr. 21, 211105. http://dx.doi.org/10.1063/1.1938256. – DOI 10.1063/1.1938256

[Capasso et al. 2002] Capasso, F. ; Paiella, R. ; Martini, R. ; Colombelli, R. ; Gmachl, C. ; Myers, T.L. ; Taubman, M.S. ; Williams, R.M. ; Bethea, C.G. ; Unterrainer, K. ; Hwang, H.Y. ; Sivco, D.L. ; Cho, A.Y. ; Sergent, A.M. ; Liu, H.C. ; Whittaker, E.A.: Quantum cascade lasers: ultrahigh-speed operation, optical wireless communication, narrow linewidth, and far-infrared emission. In: *IEEE Journal of Quantum Electronics* 38 (2002), jun, Nr. 6, 511–532. http://dx.doi.org/10.1109/jqe.2002.1005403. – DOI 10.1109/jqe.2002.1005403

[Casana et al. 2017] Casana, Jesse ; Wiewel, Adam ; Cool, Autumn ; Hill, Austin C. ; Fisher, Kevin D. ; Laugier, Elise J.: Archaeological Aerial Thermography in Theory and Practice. In: *Advances in Archaeological Practice* 5 (2017), sep, Nr. 04, 310–327. http://dx.doi.org/10.1017/aap.2017.23. – DOI 10.1017/aap.2017.23

[Chen 1975] Chen, Chuan-Chong: *Attenuation of Electromagnetic Radiation by Haze, Fog, Clouds, and Rain.* RAND Corporation, 1975 https://www.rand.org/pubs/reports/R1694.html

[Cho and Arthur 1975] Cho, A.Y. ; Arthur, J.R.: Molecular beam epitaxy. In: *Progress in Solid State Chemistry* 10 (1975), jan, 157–191. http://dx.doi.org/10.1016/0079-6786(75)90005-9. – DOI 10.1016/0079–6786(75)90005–9

[Combrie et al. 2005] Combrie, S. ; Bansropun, S. ; Lecomte, M. ; Parillaud, O. ; Cassette, S. ; Benisty, H. ; Nagle, J.: Optimization of an inductively coupled plasma etching process of GaInP GaAs based material for photonic band gap applications. In: *Journal of Vacuum Science & Technology B: Microelectronics and Nanometer Structures* 23 (2005), Nr. 4, 1521. http://dx.doi.org/10.1116/1.1993617. – DOI 10.1116/1.1993617

[Corrigan et al. 2009] Corrigan, Paul ; Martini, Rainer ; Whittaker, Edward A. ; Bethea, Clyde: Quantum cascade lasers and the Kruse model in free space optical communication. In: *Optics Express* 17 (2009), mar, Nr. 6, 4355. http://dx.doi.org/10.1364/oe.17.004355. – DOI 10.1364/oe.17.004355

[Culbert et al. 2015] Culbert, Julie ; Cozzolino, Daniel ; Ristic, Renata ; Wilkinson, Kerry: Classification of Sparkling Wine Style and Quality by MIR Spectroscopy. In: *Molecules* 20 (2015), may, Nr. 5, 8341–8356. http://dx.doi.org/10.3390/molecules20058341. – DOI 10.3390/molecules20058341

[D. Hofstetter and Blaser 2006] D. Hofstetter, T. Aellen J. Faist L. H. M. Graf G. M. Graf ; Blaser, S.: $23GHz$ operation of a room temperature photovoltaic quantum cascade detector at $5.35\mu m$. In: *Appl. Phys. Lett.* 89 (2006)

[Delga 2012] Delga, Alexandre: *Du phenomèene quantique au dispositif macroscopique, transport electronique dans les detecteurs inter-sousbandes.*, Universite Paris Diderot, Diss., 2012

[Delga et al. 2013] Delga, Alexandre ; Doyennette, Laetitia ; Berger, Vincent ; Carras, Mathieu ; Trinité, Virginie ; Nedelcu, Alexandru: Performances of quantum cascade detectors. In: *Infrared Physics & Technology* 59 (2013), jul, 100–107. http://dx.doi.org/10.1016/j.infrared.2012.12.022. – DOI 10.1016/j.infrared.2012.12.022

[Deng 2012] Deng, Ligang: Dry Etching of InP based Materials using a high density ICP plasma system. 7 (2012), December, Nr. 10

[Devi and Ebrahim-Zadeh 2017] Devi, Kavita ; Ebrahim-Zadeh, M.: Room-temperature, rapidly tunable, green-pumped continuous-wave optical parametric oscillator. In: *Optics Letters* 42 (2017), jun, Nr. 13, 2635. http://dx.doi.org/10.1364/ol.42.002635. – DOI 10.1364/ol.42.002635

[Dong et al. 2018] Dong, Ming ; Zhong, Guo qiang ; Miao, Shu zhuo ; Zheng, Chuan tao ; Wang, Yi ding: CO and CO2 dual-gas detection based on mid-infrared wideband absorption spectroscopy. In: *Optoelectronics Letters* 14 (2018), mar, Nr. 2, 119–123. http://dx.doi.org/10.1007/s11801-018-7248-1. – DOI 10.1007/s11801–018–7248–1

[Ebrahim-Zadeh 2008] Ebrahim-Zadeh, Majid: Mid-Infrared Optical Parametric Oscillators and Applications. In: Ebrahim-Zadeh, Majid (Hrsg.) ; Sorokina, Irina T. (Hrsg.): *Mid-Infrared Coherent Sources and Applications*. Dordrecht : Springer Netherlands, 2008. – ISBN 978–1–4020–6463–0, S. 347–375

[Eerdenbrugh and Taylor 2011] Eerdenbrugh, Bernard V. ; Taylor, Lynne S.: Application of mid-IR spectroscopy for the characterization of pharmaceutical systems. In: *International Journal of Pharmaceutics* 417 (2011), sep, Nr. 1-2, 3–16. http://dx.doi.org/10.1016/j.ijpharm.2010.12.011. – DOI 10.1016/j.ijpharm.2010.12.011

[Emmanuel Rosencher 2002] Emmanuel Rosencher, P. G. P. Borge Vinter V. Borge Vinter: *Optoelectronics*. 1. Cambridge University Press, 2002 http://gen.lib.rus.ec/book/index.php?md5=44A71C0E59B3363376914F63D765019F. – ISBN 0521771293,9780521771290,9780511016479,0521778131

[Faist et al. 1994] Faist, J. ; Capasso, F. ; Sivco, D. L. ; Sirtori, C. ; Hutchinson, A. L. ; Cho, A. Y.: Quantum Cascade Laser. In: *Science* 264 (1994), apr, Nr. 5158, 553–556. http://dx.doi.org/10.1126/science.264.5158.553. – DOI 10.1126/science.264.5158.553

[Faist 2013] Faist, Jérôme: *Quantum Cascade Lasers*. OUP Oxford, 2013

[Feit et al. 1996] Feit, Z. ; McDonald, M. ; Woods, R. J. ; Archambault, V. ; Mak, P.: Low threshold PbEuSeTe/PbTe separate confinement buried heterostructure diode lasers. In: *Applied Physics Letters* 68 (1996), feb, Nr. 6, 738–740. http://dx.doi.org/10.1063/1.116726. – DOI 10.1063/1.116726

[Flesch 1983] Flesch, Udo: titleThe Application Of Infrared-Sensors In Medicine/title. In: Besson, Jean (Hrsg.): *Advanced Infrared Sensor Technology*, SPIE, nov 1983

[Forge 2008] Forge, Simon: *Military Communications: From Ancient Times to the 21st Century20081Edited by Christopher H. Sterling. Military Communications: From Ancient Times to the 21st Century. Santa Barbara, CA: ABC-CLIO 2007. 565 pp. $95.00*. Emerald, 2008

[Garcia-Belmonte 2010] Garcia-Belmonte, Germà: Temperature dependence of open-circuit voltage in organic solar cells from generation–recombination kinetic balance. In: *Solar Energy Materials and Solar Cells* 94 (2010), dec, Nr. 12, 2166–2169. http://dx.doi.org/10.1016/j.solmat.2010.07.006. – DOI 10.1016/j.solmat.2010.07.006

[Gellie et al. 2010] Gellie, Pierre ; Barbieri, Stefano ; Lampin, Jean-François ; Filloux, Pascal ; Manquest, Christophe ; Sirtori, Carlo ; Sagnes, Isabelle ; Khanna, Suraj P. ; Linfield, Edmund H. ; Davies, A. G. ; Beere, Harvey ; Ritchie, David: Injection-locking of terahertz quantum cascade lasers up to 35GHz using RF amplitude modulation. In: *Optics Express* 18 (2010), sep, Nr. 20, 20799. http://dx.doi.org/10.1364/oe.18.020799. – DOI 10.1364/oe.18.020799

[Gendron et al. 2004] Gendron, L. ; Carras, M. ; Huynh, A. ; Ortiz, V. ; Koeniguer, C. ; Berger, V.: Quantum cascade photodetector. In: *Applied Physics Letters* 85 (2004), oct, Nr. 14, 2824–2826. http://dx.doi.org/10.1063/1.1781731. – DOI 10.1063/1.1781731

[Gendron et al. 2005] Gendron, L. ; Koeniguer, C. ; Berger, V. ; Marcadet, X.: High resistance narrow band quantum cascade photodetectors. In: *Applied Physics Letters* 86 (2005), mar, Nr. 12, 121116. http://dx.doi.org/10.1063/1.1884257. – DOI 10.1063/1.1884257

[Giapis et al. 1990] Giapis, Konstantinos P. ; Scheller, Geoffrey R. ; Gottscho, Richard A. ; Hobson, William S. ; Lee, Yong H.: Microscopic and macroscopic uniformity control in plasma etching. In: *Applied Physics Letters* 57 (1990), sep, Nr. 10, 983–985. http://dx.doi.org/10.1063/1.103532. – DOI 10.1063/1.103532

[Giordmaine and Miller 1965] Giordmaine, J. A. ; Miller, Robert C.: Tunable Coherent Parametric Oscillation in LiNbO3at Optical Frequencies. In: *Physical Review Letters* 14 (1965), jun, Nr. 24, 973–976. http://dx.doi.org/10.1103/physrevlett.14.973. – DOI 10.1103/physrevlett.14.973

[Giorgetta et al. 2009] Giorgetta, Fabrizio R. ; Baumann, Esther ; Graf, Marcel ; Yang, Quankui ; Manz, Christian ; Kohler, Klaus ; Beere, Harvey E. ; Ritchie, David A. ; Linfield, Edmund ; Davies, Alexander G. ; Fedoryshyn, Yuriy ; Jackel, Heinz ; Fischer, Milan ; Faist, JÉrÔme ; Hofstetter, Daniel: Quantum Cascade Detectors. In: *IEEE Journal of Quantum Electronics* 45 (2009), aug, Nr. 8, 1039–1052. http://dx.doi.org/10.1109/jqe.2009.2017929. – DOI 10.1109/jqe.2009.2017929

[Goossen et al. 1988] Goossen, K. W. ; Lyon, S. A. ; Alavi, K.: Photovoltaic quantum well infrared detector. In: *Applied Physics Letters* 52 (1988), may, Nr. 20, 1701–1703. http://dx.doi.org/10.1063/1.99022. – DOI 10.1063/1.99022

[Graf 2006] Graf, Marcel: *Design and characterisation of far and mid infrared quantum cascade detectors*, Universite de Neuchatel, Diss., 2006

[Graf et al. 2006] Graf, Marcel ; Hoyler, Nicolas ; Giovannini, Marcella ; Faist, Jérôme ; Hofstetter, Daniel: InP-based quantum cascade detectors in the mid-infrared. In: *Applied Physics Letters* 88 (2006), jun, Nr. 24, 241118. http://dx.doi.org/10.1063/1.2210088. – DOI 10.1063/1.2210088

[Graf et al. 2004] Graf, Marcel ; Scalari, Giacomo ; Hofstetter, Daniel ; Faist, Jérôme ; Beere, Harvey ; Linfield, Edmund ; Ritchie, David ; Davies, Giles: Terahertz range quantum well infrared photodetector. In: *Applied Physics Letters* 84 (2004), jan, Nr. 4, 475–477. http://dx.doi.org/10.1063/1.1641165. – DOI 10.1063/1.1641165

[Grant et al. 2006] Grant, P. D. ; Dudek, R. ; Buchanan, M. ; Liu, H. C.: Room-Temperature Heterodyne Detection up to 110 GHz With a Quantum-Well Infrared Photodetector. In: *IEEE Photonics Technology Letters* 18 (2006), nov, Nr. 21, 2218–2220. http://dx.doi.org/10.1109/lpt.2006.884267. – DOI 10.1109/lpt.2006.884267

[Gunapala and Bandara 1995] Gunapala, SD ; Bandara, KMSV: *Advances in Research and Development: Homojunction and Quantum-Well Infrared Detectors: Homojunction and Quantum-Well Infrared Detectors*. Bd. Volume 21. 1995. – ISBN 0–12–533021–9

[Gunapala and Bandara 1999] Gunapala, S.D. ; Bandara, S.V.: Chapter 4 Quantum Well Infrared Photodetector (QWIP) Focal Plane Arrays. Version: 1999. http://dx.doi.org/10.1016/s0080-8784(08)60307-5. In: *Semiconductors and Semimetals*. Elsevier, 1999. – DOI 10.1016/s0080–8784(08)60307–5, 197–282

[Gunapala et al. 2005] Gunapala, S.D. ; Bandara, S.V. ; Liu, J.K. ; Hill, C.J. ; Rafol, S.B. ; Mumolo, J.M. ; Trinh, J.T. ; Tidrow, M.Z. ; LeVan, P.D.: Development of mid-wavelength and long-wavelength megapixel portable QWIP imaging cameras. In: *Infrared Physics & Technology* 47 (2005), oct, Nr. 1-2, 67–75. http://dx.doi.org/10.1016/j.infrared.2005.02.012. – DOI 10.1016/j.infrared.2005.02.012

[Guo et al. 2016] Guo, Yizhen ; Wang, Jingjuan ; Lu, Lina ; Sun, Suqin ; Liu, Yang ; Xiao, Yao ; Qin, Youwen ; Xiao, Lijuan ; Wen, Haoran ; Qu, Lei: Application of mid-infrared spectroscopy in analyzing different segmented production of Angelica by AB-8 macroporous resin. In: *Journal of Molecular Structure* 1103 (2016), jan, 61–69. http://dx.doi.org/10.1016/j.molstruc.2015.09.003. – DOI 10.1016/j.molstruc.2015.09.003

[H. C. Liu 2000] H. C. Liu, F. C.: *Intersubband transitions in quantum wells: Physics and device applications I*. Academic Press, 2000. – ISBN 0–12–752171–2

[H. Schneider 2007] H. Schneider, H. C. L.: *Quantum well infrared photodetectors Physics and applications*. Springer, 2007. – ISBN 0342–4111

[Harrison 2011] Harrison, Paul: *Quantum Wells, Wires and Dots: Theoretical and Computational Physics of Semiconductor Nanostructures*. Wiley, 2011

[Helm et al. 1989] Helm, M. ; England, P. ; Colas, E. ; DeRosa, F. ; Allen, S. J.: Intersubband emission from semiconductor superlattices excited by sequential resonant tunneling. In: *Physical Review Letters* 63 (1989), jul, Nr. 1, 74–77. http://dx.doi.org/10.1103/physrevlett.63.74. – DOI 10.1103/physrevlett.63.74

[Helm 1999] Helm, Manfred: Chapter 1 The Basic Physics of Intersubband Transitions. Version: 1999. http://dx.doi.org/10.1016/s0080-8784(08)60304-x. In: *Semiconductors and Semimetals*. Elsevier, 1999. – DOI 10.1016/s0080–8784(08)60304–x, 1–99

[Hemmati 2006] Hemmati: *Deep Space Optical Communications*. Wiley-Interscience, 2006 (Deep-space communications and navigation series). http://gen.lib.rus.ec/book/index.php?md5=4BA37AADD28C6A6AF2B9686F32009A50. – ISBN 0470040025,9780470040027

[Henderson et al. 2018] Henderson, Ben ; Khodabakhsh, Amir ; Metsälä, Markus ; Ventrillard, Irène ; Schmidt, Florian M. ; Romanini, Daniele ; Ritchie, Grant A. D. ; Lintel Hekkert, Sacco te ; Briot, Raphaël ; Risby, Terence ; Marczin, Nandor ; Harren, Frans J. M. ; Cristescu, Simona M.: Laser spectroscopy for breath analysis: towards clinical implementation. In: *Applied Physics B* 124 (2018), jul, Nr. 8. http://dx.doi.org/10.1007/s00340-018-7030-x. – DOI 10.1007/s00340–018–7030–x

[Henini and Razeghi 2002] Henini, M. ; Razeghi, M.: *Handbook of Infrared Detection Technologies*. Elsevier, 2002. http://dx.doi.org/10.1016/b978-1-85617-388-9.x5000-x. http://dx.doi.org/10.1016/b978-1-85617-388-9.x5000-x

[Hildebrandt et al. 2010] Hildebrandt, Carolin ; Raschner, Christian ; Ammer, Kurt: An Overview of Recent Application of Medical Infrared Thermography in Sports Medicine in Austria. In: *Sensors* 10 (2010), may, Nr. 5, 4700–4715. http://dx.doi.org/10.3390/s100504700. – DOI 10.3390/s100504700

[Hinds et al. 2011] Hinds, Sean ; Buchanan, Margaret ; Dudek, Richard ; Haffouz, Sofiane ; Laframboise, Sylvain ; Wasilewski, Zbigniew ; Liu, H. C.: Near-Room-Temperature Mid-Infrared Quantum Well Photodetector. In: *Advanced Materials* 23 (2011), nov, Nr. 46, 5536–5539. http://dx.doi.org/10.1002/adma.201103372. – DOI 10.1002/adma.201103372

[Hoff et al. 1996] Hoff, J. R. ; Razeghi, M. ; Brown, Gail J.: Effect of the spin split-off band on optical absorption inp-typeGa1-xInxAsyP1-yquantum-well infrared detectors. In: *Physical Review B* 54 (1996), oct, Nr. 15, 10773–10783. http://dx.doi.org/10.1103/physrevb.54.10773. – DOI 10.1103/physrevb.54.10773

[Hofstetter et al. 2010] Hofstetter, D. ; Giorgetta, F. R. ; Baumann, E. ; Yang, Q. ; Manz, C. ; Köhler, K.: Mid-infrared quantum cascade detectors for applications in spectroscopy and pyrometry. In: *Applied Physics B* 100 (2010), mar, Nr. 2, 313–320. http://dx.doi.org/10.1007/s00340-010-3965-2. – DOI 10.1007/s00340–010–3965–2

[Hou and Zhang 2015] Hou, Chen Y. Wu J. R. ; Zhang, H.: A Brief Survey of Optical Wireless Communication. In: Javadi, B. (Hrsg.) ; Garg, S.K. (Hrsg.): *13th Australasian Symposium on Parallel and Distributed Computing (AusPDC 2015)* Bd. 163. Sydney, Australia : ACS, 2015 (CRPIT), 41-50

[Howard and Garing 1962] Howard, J.N. ; Garing, J.S.: The transmission of the atmosphere in the infrared—A review. In: *Infrared Physics* 2 (1962), jul, Nr. 3, 155–173. http://dx.doi.org/10.1016/0020-0891(62)90048-9. – DOI 10.1016/0020–0891(62)90048–9

[Iga 2000] Iga, K.: Surface-emitting laser-its birth and generation of new optoelectronics field. In: *IEEE Journal of Selected Topics in Quantum Electronics* 6 (2000), nov, Nr. 6, 1201–1215. http://dx.doi.org/10.1109/2944.902168. – DOI 10.1109/2944.902168

[Jain et al. 2013] Jain, Vk ; Kaushal, Hemani ; , A.Vats : *Free space optical communication: laser sources, modulation schemes and detection techniques*. 02 2013

[Kapon and Sirbu 2009] Kapon, Eli ; Sirbu, Alexei: Power-efficient answer. In: *Nature Photonics* 3 (2009), jan, Nr. 1, 27–29. http://dx.doi.org/10.1038/nphoton.2008.266. – DOI 10.1038/nphoton.2008.266

[Karunasiri 1996] Karunasiri, Gamani: Thermionic emission and tunneling in InGaAs/GaAs quantum well infrared detectors. In: *J. Appl. Phys.* 79 (1996), May, Nr. 10, S. 8121–8123. http://dx.doi.org/10.1063/1.362372. – DOI 10.1063/1.362372

[Kastalsky et al. 1988] Kastalsky, A. ; Duffield, T. ; Allen, S. J. ; Harbison, J.: Photovoltaic detection of infrared light in a GaAs/AlGaAs superlattice. In: *Applied Physics Letters* 52 (1988), apr, Nr. 16, 1320–1322. http://dx.doi.org/10.1063/1.99147. – DOI 10.1063/1.99147

[Kastenmeier et al. 1996] Kastenmeier, B. E. E. ; Matsuo, P. J. ; Beulens, J. J. ; Oehrlein, G. S.: Chemical dry etching of silicon nitride and silicon dioxide using CF4/O2/N2 gas mixtures. In: *Journal of Vacuum Science & Technology A: Vacuum, Surfaces, and Films* 14 (1996), sep, Nr. 5, 2802–2813. http://dx.doi.org/10.1116/1.580203. – DOI 10.1116/1.580203

[Kazarinov and Suris 1971] Kazarinov, R. F. ; Suris, R. A.: Possibility of the amplification of electromagnetic waves in a semiconductor with a superlattice. In: *Sov. Phys. Semicond.* 5 (1971), S. 707

[Kemsley et al. 1992] Kemsley, E.K. ; Zhuo, Li ; Hammouri, M.K. ; Wilson, R.H.: Quantitative analysis of sugar solutions using infrared spectroscopy. In: *Food Chemistry* 44 (1992), Nr. 4, 299–304. http://dx.doi.org/10.1016/0308-8146(92)90054-6. – DOI 10.1016/0308–8146(92)90054–6

[Kim et al. 2016] Kim, Dae-Yong ; Cho, Byoung-Kwan ; Lee, Seung H. ; Kwon, Kyungdo ; Park, Eun S. ; Lee, Wang-Hee: Application of Fourier transform-mid infrared reflectance spectroscopy for monitoring Korean traditional rice wine 'Makgeolli' fermentation. In: *Sensors and Actuators B: Chemical* 230 (2016), jul, 753–760. http://dx.doi.org/10.1016/j.snb.2016.02.076. – DOI 10.1016/j.snb.2016.02.076

[Kosterev et al. 1999] Kosterev, A. A. ; Curl, R. F. ; Tittel, F. K. ; Gmachl, C. ; Capasso, F. ; Sivco, D. L. ; Baillargeon, J. N. ; Hutchinson, A. L. ; Cho, A. Y.: Methane concentration and isotopic composition measurements with a mid-infrared quantum-cascade laser. In: *Optics Letters* 24 (1999), dec, Nr. 23, 1762. http://dx.doi.org/10.1364/ol.24.001762. – DOI 10.1364/ol.24.001762

[Krishna et al. 2007] Krishna, S. ; Gunapala, S.D. ; Bandara, S.V. ; Hill, C. ; Ting, D.Z.: Quantum Dot Based Infrared Focal Plane Arrays. In: *Proceedings of the IEEE* 95 (2007), sep, Nr. 9, 1838–1852. http://dx.doi.org/10.1109/jproc.2007.900969. – DOI 10.1109/jproc.2007.900969

[Lahiri et al. 2012] Lahiri, B.B. ; Bagavathiappan, S. ; Jayakumar, T. ; Philip, John: Medical applications of infrared thermography: A review. In: *Infrared Physics & Technology* 55 (2012), jul, Nr. 4, 221–235. http://dx.doi.org/10.1016/j.infrared.2012.03.007. – DOI 10.1016/j.infrared.2012.03.007

[Larry C. Andrews 2005] Larry C. Andrews, Ronald L. P.: *Laser Beam Propagation through Random Media, Second Edition*. 2nd. SPIE Publications, 2005 (SPIE Press Monograph Vol. PM152). http://gen.lib.rus.ec/book/index.php?md5=5D259BFF35ECFE3234414F1FBAB3ABDD. – ISBN 0819459488,9780819459480

[Lawson et al. 1959] Lawson, W.D. ; Nielsen, S. ; Putley, E.H. ; Young, A.S.: Preparation and properties of HgTe and mixed crystals of HgTe-CdTe. In: *Journal of Physics and Chemistry of Solids* 9 (1959), mar, Nr. 3-4, 325–329. http://dx.doi.org/10.1016/0022-3697(59)90110-6. – DOI 10.1016/0022–3697(59)90110–6

[Le et al. 2003] Le, D.T. ; Morath, C.P. ; Norton, H.E. ; Cardimona, D.A. ; Raghavan, S. ; Rotella, P. ; Stintz, S.A. ; Fuchs, B. ; Krishna, S.: High responsivity, LWIR dots-in-a-well quantum dot infrared photodetectors. In: *Infrared Physics & Technology* 44 (2003), oct, Nr. 5-6, 517–526. http://dx.doi.org/10.1016/s1350-4495(03)00171-3. – DOI 10.1016/s1350–4495(03)00171–3

[Levine 1993] Levine, B. F.: Quantum-well infrared photodetectors. In: *Journal of Applied Physics* 74 (1993), oct, Nr. 8, R1–R81. http://dx.doi.org/10.1063/1.354252. – DOI 10.1063/1.354252

[Levine et al. 1988] Levine, B. F. ; Bethea, C. G. ; Choi, K. K. ; Walker, J. ; Malik, R. J.: Bound-to-extended state absorption GaAs superlattice transport infrared detectors. In: *Journal of Applied Physics* 64 (1988), aug, Nr. 3, 1591–1593. http://dx.doi.org/10.1063/1.341794. – DOI 10.1063/1.341794

[Levine et al. 1987] Levine, B. F. ; Choi, K. K. ; Bethea, C. G. ; Walker, J. ; Malik, R. J.: New 10 m infrared detector using intersubband absorption in resonant tunneling GaAlAs superlattices. In: *Applied Physics Letters* 50 (1987), apr, Nr. 16, 1092–1094. http://dx.doi.org/10.1063/1.97928. – DOI 10.1063/1.97928

[Lin et al. 2010] Lin, Wei-Hsun ; Tseng, Chi-Che ; Chao, Kuang-Ping ; Kung, Shu-Yen ; Lin, Shih-Yen ; Wu, Meng-Chyi: Broadband Quantum-Dot Infrared Photodetector. In: *IEEE Photonics Technology Letters* 22 (2010), jul, Nr. 13, 963–965. http://dx.doi.org/10.1109/lpt.2010.2048425. – DOI 10.1109/lpt.2010.2048425

[Linker] Linker, Raphael: Soil Classification Via Mid-infrared Spectroscopy. http://dx.doi.org/10.1007/978-0-387-77253-0_48. In: *Computer And Computing Technologies In Agriculture, Volume II*. Springer US. – DOI 10.1007/978–0–387–77253–$0_4$8,1137 – –1146

[Liu et al. 1998] Liu, H. C. ; Buchanan, M. ; Wasilewski, Z. R.: How good is the polarization selection rule for intersubband transitions? In: *Applied Physics Letters* 72 (1998), apr, Nr. 14, 1682–1684. http://dx.doi.org/10.1063/1.121151. – DOI 10.1063/1.121151

[Liu et al. 2001] Liu, H. C. ; Gao, M. ; McCaffrey, J. ; Wasilewski, Z. R. ; Fafard, S.: Quantum dot infrared photodetectors. In: *Applied Physics Letters* 78 (2001), jan, Nr. 1, 79–81. http://dx.doi.org/10.1063/1.1337649. – DOI 10.1063/1.1337649

[Liu et al. 1996] Liu, H. C. ; Li, Jianmeng ; Buchanan, M. ; Wasilewski, Z. R.: High-frequency quantum-well infrared photodetectors measured by microwave-rectification technique. In: *IEEE Journal of Quantum Electronics* 32 (1996), June, Nr. 6, S. 1024–1028. http://dx.doi.org/10.1109/3.502380. – DOI 10.1109/3.502380. – ISSN 0018–9197

[Liu et al. 2008] Liu, H. C. ; Luo, Hui ; Song, Chun ying ; Wasilewski, Zbig R. ; SpringThorpe, A. J. ; Cao, J. C.: Terahertz Quantum Well Photodetectors. In: *IEEE Journal of Selected Topics in Quantum Electronics* 14 (2008), Nr. 2, 374–377. http://dx.doi.org/10.1109/jstqe.2007.910710. – DOI 10.1109/jstqe.2007.910710

[Liu 2000] Liu, H.C.: *Intersubband Transitions in QuantumWells: Physics and Device Applications II, volume vol.65 of Semiconductors and Semimetals*. academic press, 2000

[Luna et al. 2013] Luna, Aderval S. ; Silva, Arnaldo P. ; Ferré, Joan ; Boqué, Ricard: Classification of edible oils and modeling of their physico-chemical properties by chemometric methods using mid-IR spectroscopy. In: *Spectrochimica Acta Part A: Molecular and Biomolecular Spectroscopy* 100 (2013), jan, 109–114. http://dx.doi.org/10.1016/j.saa.2012.06.034. – DOI 10.1016/j.saa.2012.06.034

[Lundin 1985] Lundin, R.: A handbook formula for the inductance of a single-layer circular coil. In: *Proceedings of the IEEE* 73 (1985), Sept, Nr. 9, S. 1428–1429. http://dx.doi.org/10.1109/PROC.1985.13304. – DOI 10.1109/PROC.1985.13304. – ISSN 0018–9219

[Lyakh et al. 2009] Lyakh, A. ; Maulini, R. ; Tsekoun, A. ; Go, R. ; Pflügl, C. ; Diehl, L. ; Wang, Q. J. ; Capasso, Federico ; Patel, C. Kumar N.: 3 W continuous-wave room temperature single-facet emission from quantum cascade lasers based on nonresonant extraction design approach. In: *Applied Physics Letters* 95 (2009), oct, Nr. 14, 141113. http://dx.doi.org/10.1063/1.3238263. – DOI 10.1063/1.3238263

[Mahato et al. 2017] Mahato, Somnath ; Biswas, Debaleen ; Gerling, Luis G. ; Voz, Cristobal ; Puigdollers, Joaquim: Analysis of temperature dependent current-voltage and capacitance-voltage characteristics of an Au/V2O5/n-Si Schottky diode. In: *AIP Advances* 7 (2017), aug, Nr. 8, 085313. http://dx.doi.org/10.1063/1.4993553. – DOI 10.1063/1.4993553

[Manginas et al. 2007] Manginas, A. ; Andreanidis, E. ; Leontiadis, E. ; Sfirakis, P. ; Kokkinos, D.V. ; Alivizatos, P.A.: 454: First human application of right ventricular endocardial thermography in transplanted and coronary artery disease patients. In: *The Journal of Heart and Lung Transplantation* 26 (2007), feb, Nr. 2, S224. http://dx.doi.org/10.1016/j.healun.2006.11.477. – DOI 10.1016/j.healun.2006.11.477

[Mederer et al.] Mederer, F. ; Steinle, G. ; Kristen, G. ; Michalzik, R. ; Riechert, H. ; Egorov, A.Y. ; Ebeling, K.J.: Up to 10 Gbit/s data transmission with 1.3 m wavelength InGaAsN VCSELs. In: *Proceedings 27th European Conference on Optical Communication (Cat. No.01TH8551)*, IEEE

[Mele 1984] Mele, T. C.: Selective and anisotropic reactive ion etch of LPCVD silicon nitride with CHF3 based gases. In: *Journal of Vacuum Science & Technology B: Microelectronics and Nanometer Structures* 2 (1984), Nr. 4, 684. http://dx.doi.org/10.1116/1.582863. – DOI 10.1116/1.582863

[Melngailis 1963] Melngailis, I.: MASER ACTION IN InAs DIODES. In: *Applied Physics Letters* 2 (1963), may, Nr. 9, 176–178. http://dx.doi.org/10.1063/1.1753832. – DOI 10.1063/1.1753832

[Nalwa 2002] Nalwa, Hari S.: *Handbook of Thin Films*. Elsevier, 2002. http://dx.doi.org/10.1016/b978-0-12-512908-4.x5000-0. http://dx.doi.org/10.1016/b978-0-12-512908-4.x5000-0. – ISBN 978–0–12–512908–4

[Ng 2009] Ng, E.Y.-K.: A review of thermography as promising non-invasive detection modality for breast tumor. In: *International Journal of Thermal Sciences* 48 (2009), may, Nr. 5, 849–859. http://dx.doi.org/10.1016/j.ijthermalsci.2008.06.015. – DOI 10.1016/j.ijthermalsci.2008.06.015

[Palaferri et al. 2018] Palaferri, Daniele ; Todorov, Yanko ; Bigioli, Azzurra ; Mottaghizadeh, Alireza ; Gacemi, Djamal ; Calabrese, Allegra ; Vasanelli, Angela ; Li, Lianhe ; Davies, A. G. ; Linfield, Edmund H. ; Kapsalidis, Filippos ; Beck, Mattias ; Faist, Jérôme ; Sirtori, Carlo: Room-temperature nine-μm-wavelength photodetectors and GHz-frequency heterodyne receivers. In: *Nature* 556 (2018), mar, Nr. 7699, 85–88. http://dx.doi.org/10.1038/nature25790. – DOI 10.1038/nature25790

[Pan et al. 1998] Pan, Dong ; Towe, Elias ; Kennerly, Steve: Normal-incidence intersubband (In, Ga)As/GaAs quantum dot infrared photodetectors. In: *Applied Physics Letters* 73 (1998), oct, Nr. 14, 1937–1939. http://dx.doi.org/10.1063/1.122328. – DOI 10.1063/1.122328

[Patel 1964] Patel, C. K. N.: Continuous-Wave Laser Action on Vibrational-Rotational Transitions of CO2. In: *Physical Review* 136 (1964), nov, Nr. 5A, A1187–A1193. http://dx.doi.org/10.1103/physrev.136.a1187. – DOI 10.1103/physrev.136.a1187

[Pavelchek et al. 2004] Pavelchek, Andrew ; Trissel, Richard G. ; Plante, James ; Umbrasas, Saul: Long-wave infrared (10-m) free-space optical communication system. In: Voelz, David G. (Hrsg.) ; Ricklin, Jennifer C. (Hrsg.): *Free-Space Laser Communication and Active Laser Illumination III*, SPIE, jan 2004

[Perrin Walker 1991] Perrin Walker, William H.: *Handbook of metal etchants*. CRC Press, 1991. – ISBN 0–8493–3623–6

[Phelan et al. 1963] Phelan, R. J. ; Calawa, A. R. ; Rediker, R. H. ; Keyes, R. J. ; Lax, B.: INFRARED InSb LASER DIODE IN HIGH MAGNETIC FIELDS. In: *Applied Physics Letters* 3 (1963), nov, Nr. 9, 143–145. http://dx.doi.org/10.1063/1.1753905. – DOI 10.1063/1.1753905

[Phillips et al. 1998] Phillips, J. ; Kamath, K. ; Bhattacharya, P.: Far-infrared photoconductivity in self-organized InAs quantum dots. In: *Applied Physics Letters* 72 (1998), apr, Nr. 16, 2020–2022. http://dx.doi.org/10.1063/1.121252. – DOI 10.1063/1.121252

[Planck and Masius 1914] Planck, M. ; Masius, M.: *The Theory of Heat Radiation*. Blakiston, 1914 http://books.google.co.uk/books?id=2PR_AAAAMAAJ

[Plank et al. 2012] Plank, Thomas ; Leitgeb, Erich ; Pezzei, Pirmin ; Ghassemlooy, Zabih: Wavelength-selection for high data rate Free Space Optics (FSO) in next generation wireless communications. In: *2012 17th European Conference on Networks and Optical Communications*, IEEE, jun 2012

[Preier 1990] Preier, H: Physics and applications of IV-VI compound semiconductor lasers. In: *Semiconductor Science and Technology* 5 (1990), mar, Nr. 3S, S12–S20. http://dx.doi.org/10.1088/0268-1242/5/3s/004. – DOI 10.1088/0268–1242/5/3s/004

[Ravikumar et al. 2013] Ravikumar, Arvind P. ; Chen, Guopeng ; Zhao, Kuaile ; Tian, Yue ; Prucnal, Paul ; Tamargo, Maria C. ; Gmachl, Claire F. ; Shen, Aidong: Room

Temperature and High Responsivity Short Wavelength II-VI Quantum Well Infrared Photodetector. In: *CLEO: 2013*, OSA, 2013

[Razeghi et al. 2007] Razeghi, M. ; Evans, A. ; Nguyen, J. ; Bai, Y. ; Slivken, S. ; Darvish, S. R. ; Mi, K.: High-power mid- and far- wavelength infrared lasers for free space communication. In: Serpengüzel, Ali (Hrsg.) ; Badenes, Gonçal (Hrsg.) ; Righini, Giancarlo C. (Hrsg.): *Photonic Materials, Devices, and Applications II*, SPIE, may 2007

[Reiland et al. 1986] Reiland, W. ; Englisch, W. ; Endemann, M.: Optical Intersatellite Communication Links: State of CO 2 Laser Technology. In: Bhasin, Kul B. (Hrsg.): *Optical Technologies for Communication Satellite Applications*, SPIE, may 1986

[Renaudier et al. 2017] Renaudier, J. ; Meseguer, A. C. ; Ghazisaeidi, A. ; Tran, P. ; Muller, R. R. ; Brenot, R. ; Verdier, A. ; Blache, F. ; Mekhazni, K. ; Duval, B. ; Debregeas, H. ; Achouche, M. ; Boutin, A. ; Morin, F. ; Letteron, L. ; Fontaine, N. ; Frignac, Y. ; Charlet, G.: First 100-nm Continuous-Band WDM Transmission System with 115Tb/s Transport over 100km Using Novel Ultra-Wideband Semiconductor Optical Amplifiers. In: *2017 European Conference on Optical Communication (ECOC)*, IEEE, sep 2017

[Richards et al. 2003] Richards, Roger K. ; Hutchinson, Donald P. ; Bennett, Charles A.: Room-temperature QWIP detection at 10 m. In: Andresen, Bjorn (Hrsg.) ; Fulop, Gabor F. (Hrsg.) ; Strojnik, Marija (Hrsg.): *Infrared Technology and Applications XXVIII*, SPIE, jan 2003

[Richter et al. 2002] Richter, Dirk ; Erdelyi, Miklos ; Curl, Robert F. ; Tittel, Frank K. ; Oppenheimer, Clive ; Duffell, Hayley J. ; Burton, Mike: Field measurements of volcanic gases using tunable diode laser based mid-infrared and Fourier transform infrared spectrometers. In: *Optics and Lasers in Engineering* 37 (2002), feb, Nr. 2-3, 171–186. http://dx.doi.org/10.1016/s0143-8166(01)00094-x. – DOI 10.1016/s0143–8166(01)00094–x

[Rodriguez et al. 2018] Rodriguez, Etienne ; Mottaghizadeh, Alireza ; Gacemi, Djamal ; Palaferri, Daniele ; Asghari, Zahra ; Jeannin, Mathieu ; Vasanelli, Angela ; Bigioli, Azzurra ; Todorov, Yanko ; Beck, Mattias ; Faist, Jerome ; Wang, Qi J. ; Sirtori, Carlo: Room-Temperature, Wide-Band, Quantum Well Infrared Photodetector for Microwave Optical Links at 4.9 m Wavelength. In: *ACS Photonics* 5 (2018), jul, Nr. 9, 3689–3694. http://dx.doi.org/10.1021/acsphotonics.8b00704. – DOI 10.1021/acsphotonics.8b00704

[Rogalski 2012] Rogalski, A.: History of infrared detectors. In: *Opto-Electronics Review* 20 (2012), jan, Nr. 3. http://dx.doi.org/10.2478/s11772-012-0037-7. – DOI 10.2478/s11772–012–0037–7

[Rogalski et al. 2016] Rogalski, A ; Martyniuk, P ; Kopytko, M: Challenges of small-pixel infrared detectors: a review. In: *Reports on Progress in Physics* 79 (2016), mar, Nr. 4, 046501. http://dx.doi.org/10.1088/0034-4885/79/4/046501. – DOI 10.1088/0034–4885/79/4/046501

[Rommel et al. 2002] Rommel, Sean L. ; Jang, Jae-Hyung ; Lu, Wu ; Cueva, Gabriel ; Zhou, Ling ; Adesida, Ilesanmi ; Pajer, Gary ; Whaley, Ralph ; Lepore, Allen ; Schellanbarger, Zane ; Abeles, Joseph H.: Effect of H[sub 2] on the etch profile of InP/InGaAsP alloys in Cl[sub 2]/Ar/H[sub 2] inductively coupled plasma reactive

ion etching chemistries for photonic device fabrication. In: *Journal of Vacuum Science & Technology B: Microelectronics and Nanometer Structures* 20 (2002), Nr. 4, 1327. http://dx.doi.org/10.1116/1.1486232. – DOI 10.1116/1.1486232

[Rosencher et al. 2002] Rosencher, E. ; Vinter, B. ; Piva, P.G.: *Optoelectronics*. Cambridge University Press, 2002 (Optoelectronics). https://books.google.fr/books?id=x54JBfP800AC. – ISBN 9780521778138

[Saint-Jean 2015] Saint-Jean, Margaux R.: *Laser à cascade quantique dans un guide micro-onde pour la réalisation d'un peigne de fréquence*, Université Paris Diderot, Diss., 2015

[Schneider 1993] Schneider, H.: Optimized performance of quantum well intersubband infrared detectors: Photovoltaic versus photoconductive operation. In: *Journal of Applied Physics* 74 (1993), oct, Nr. 7, 4789–4791. http://dx.doi.org/10.1063/1.354352. – DOI 10.1063/1.354352

[Schneider and Liu 2007] Schneider, H. ; Liu, H.C.: *Quantum well infrared photodetectors: physics and applications*. Springer, 2007 (Springer series in optical sciences). https://books.google.fr/books?id=ciRRAAAAMAAJ. – ISBN 9783540363231

[Schneider et al. 1997] Schneider, H. ; Schönbein, C. ; Walther, M. ; Schwarz, K. ; Fleissner, J. ; Koidl, P.: Photovoltaic quantum well infrared photodetectors: The four-zone scheme. In: *Applied Physics Letters* 71 (1997), jul, Nr. 2, 246–248. http://dx.doi.org/10.1063/1.119510. – DOI 10.1063/1.119510

[Schneider et al. 2000] Schneider, Harald ; Walther, Martin ; Fleissner, Joachim ; Rehm, Robert ; Diwo, E. ; Schwarz, K. ; Koidl, Peter ; Weimann, Guenter ; Ziegler, Johann ; Breiter, Rainer ; Cabanski, Wolfgang A.: Low-noise QWIPs for FPA sensors with high thermal resolution. In: Andresen, Bjorn F. (Hrsg.) ; Fulop, Gabor F. (Hrsg.) ; Strojnik, Marija (Hrsg.): *Infrared Technology and Applications XXVI*, SPIE, dec 2000

[Schwarz et al. 2017] Schwarz, Benedikt ; Reininger, Peter ; Harrer, Andreas ; MacFarland, Donald ; Detz, Hermann ; Andrews, Aaron M. ; Schrenk, Werner ; Strasser, Gottfried: The limit of quantum cascade detectors: A single period device. In: *Applied Physics Letters* 111 (2017), aug, Nr. 6, 061107. http://dx.doi.org/10.1063/1.4985711. – DOI 10.1063/1.4985711

[Siegman 1986] Siegman, A.: *Lasers*. University Science Book, 1986

[Snekhalatha et al. 2018] Snekhalatha, U ; Mir, Nida ; Khan, Mehvish ; Raj, Parimal ; ., Vimaladhithan ; Choden, Yeshi: Facial thermography: a potential complimentary tool for evaluation of dental disorders. In: *International Journal of Engineering & Technology* 7 (2018), mar, Nr. 2.8, 175. http://dx.doi.org/10.14419/ijet.v7i2.8.10353. – DOI 10.14419/ijet.v7i2.8.10353

[Soda et al. 1979] Soda, Haruhisa ; Iga, Ken ichi ; Kitahara, Chiyuki ; Suematsu, Yasuharu: GaInAsP/InP Surface Emitting Injection Lasers. In: *Japanese Journal of Applied Physics* 18 (1979), dec, Nr. 12, 2329–2330. http://dx.doi.org/10.1143/jjap.18.2329. – DOI 10.1143/jjap.18.2329

[Stefano Barbieri and Sirtori 2007] Stefano Barbieri, Sukhdeep S. D. Wilfried Maineult M. Wilfried Maineult ; Sirtori, Carlo: 13GHz direct modulation of terahertz quantum cascade lasers. In: *Appl. Phys. Lett.* 91 (2007), Nr. 14, S. 143510. http://dx.doi.org/10.1063/1.2790827. – DOI 10.1063/1.2790827

[Sun et al. 2016] Sun, Lan ; Hsiung, Chang ; Pederson, Christopher G. ; Zou, Peng ; Smith, Valton ; Gunten, Marc von ; O'Brien, Nada A.: Pharmaceutical Raw Material Identification Using Miniature Near-Infrared (MicroNIR) Spectroscopy and Supervised Pattern Recognition Using Support Vector Machine. In: *Applied Spectroscopy* 70 (2016), mar, Nr. 5, 816–825. http://dx.doi.org/10.1177/0003702816638281. – DOI 10.1177/0003702816638281

[Svilen Dimitrov 2015] Svilen Dimitrov, Harald H.: *Principles of LED Light Communications: Towards Networked Li-Fi*. Cambridge University Press, 2015 http://gen.lib.rus.ec/book/index.php?md5=77C4C6CDBE64BADA17E598CC280C8922. – ISBN 1107049423,9781107049420

[Szajowski et al. 1999] Szajowski, Paul F. ; Nykolak, Gerald ; Auborn, James J. ; Presby, Herman M. ; Tourgee, G. E. ; Korevaar, Eric J. ; Schuster, John J. ; Kim, Isaac I.: title2.4-km free-space optical communication 1550-nm transmission link operating at 2.5 Gb/s: experimental results/title. In: Korevaar, Eric J. (Hrsg.): *Optical Wireless Communications*, SPIE, jan 1999

[Sze and Ng 2006] Sze, S.M. ; Ng, K.K.: *Physics of Semiconductor Devices*. Wiley, 2006 https://books.google.fr/books?id=o4unkmHBHb8C. – ISBN 9780470068304

[Theocharous et al. 2005] Theocharous, Evangelos ; Ishii, Juntaro ; Fox, Nigel P.: A comparison of the performance of a photovoltaic HgCdTe detector with that of large area single pixel QWIPs for infrared radiometric applications. In: *Infrared Physics & Technology* 46 (2005), apr, Nr. 4, 309–322. http://dx.doi.org/10.1016/j.infrared.2004.05.002. – DOI 10.1016/j.infrared.2004.05.002

[Tittel et al.] Tittel, Frank K. ; Richter, Dirk ; Fried, Alan: Mid-Infrared Laser Applications in Spectroscopy. http://dx.doi.org/10.1007/3-540-36491-9_11. In: *Topics in Applied Physics*. Springer Berlin Heidelberg. – DOI 10.1007/3–540–36491–9_11,458 – –529

[Todorov et al. 2010] Todorov, Y. ; Tosetto, L. ; Teissier, J. ; Andrews, A. M. ; Klang, P. ; Colombelli, R. ; Sagnes, I. ; Strasser, G. ; Sirtori, C.: Optical properties of metal-dielectric-metal microcavities in the THz frequency range. In: *Optics Express* 18 (2010), jun, Nr. 13, 13886. http://dx.doi.org/10.1364/oe.18.013886. – DOI 10.1364/oe.18.013886

[Tsai et al. 2015] Tsai, Wen-Shing ; Lu, Hai-Han ; Li, Chung-Yi ; Lu, Ting-Chieh ; Liao, Chen-Hong ; Chu, Chien-An ; Peng, Peng-Chun: A 20-m/40-Gb/s 1550-nm DFB LD-Based FSO Link. In: *IEEE Photonics Journal* 7 (2015), dec, Nr. 6, 1–7. http://dx.doi.org/10.1109/jphot.2015.2506172. – DOI 10.1109/jphot.2015.2506172

[Unger et al. 2006] Unger, J.K. ; Lemke, A.-J. ; Grosse-Siestrup, C.: Thermography as potential real-time technique to assess changes in flow distribution in hemofiltration. In: *Kidney International* 69 (2006), feb, Nr. 3, 520–525. http://dx.doi.org/10.1038/sj.ki.5000143. – DOI 10.1038/sj.ki.5000143

[Villares et al. 2014] Villares, Gustavo ; Hugi, Andreas ; Blaser, Stéphane ; Faist, Jérôme: Dual-comb spectroscopy based on quantum-cascade-laser frequency combs. In: *Nature Communications* 5 (2014), oct, Nr. 1. http://dx.doi.org/10.1038/ncomms6192. – DOI 10.1038/ncomms6192

[Vitiello et al. 2015] Vitiello, Miriam S. ; Scalari, Giacomo ; Williams, Benjamin ; Natale, Paolo D.: Quantum cascade lasers: 20 years of challenges. In: *Optics*

Express 23 (2015), feb, Nr. 4, 5167. http://dx.doi.org/10.1364/oe.23.005167. – DOI 10.1364/oe.23.005167

[Vurgaftman et al. 2015] Vurgaftman, I ; Weih, R ; Kamp, M ; Meyer, J R. ; Canedy, C L. ; Kim, C S. ; Kim, M ; Bewley, W W. ; Merritt, C D. ; Abell, J ; Höfling, S: Interband cascade lasers. In: *Journal of Physics D: Applied Physics* 48 (2015), mar, Nr. 12, 123001. http://dx.doi.org/10.1088/0022-3727/48/12/123001. – DOI 10.1088/0022–3727/48/12/123001

[Wadell 1991] Wadell, Brian C.: *Transmission Line Design Handbook*. Artech Print on Demand, 1991 (Artech House Antennas and Propagation Library). http://gen.lib.rus.ec/book/index.php?md5=5EC9F7AD92DDD4A91EEFFC1673135EF5. – ISBN 9780890064368,0890064369

[WALTHER and KRYSA 2017] WALTHER, T. ; KRYSA, A.B.: Transmission electron microscopy of AlGaAs/GaAs quantum cascade laser structures. In: *Journal of Microscopy* 268 (2017), oct, Nr. 3, 298–304. http://dx.doi.org/10.1111/jmi.12655. – DOI 10.1111/jmi.12655

[Webster and Eren 2017] Webster, J.G. ; Eren, H.: *Measurement, Instrumentation, and Sensors Handbook: Electromagnetic, Optical, Radiation, Chemical, and Biomedical Measurement*. CRC Press, 2017 https://books.google.fr/books?id=TglEDwAAQBAJ. – ISBN 9781351833332

[West and Eglash 1985a] West, L. C. ; Eglash, S. J.: First observation of an extremely large-dipole infrared transition within the conduction band of a GaAs quantum well. In: *Applied Physics Letters* 46 (1985), jun, Nr. 12, 1156–1158. http://dx.doi.org/10.1063/1.95742. – DOI 10.1063/1.95742

[West and Eglash 1985b] West, L. C. ; Eglash, S. J.: First observation of an extremely large-dipole infrared transition within the conduction band of a GaAs quantum well. In: *Appl. Phys. Lett.* 46 (1985), June, Nr. 12, S. 1156–1158. http://dx.doi.org/10.1063/1.95742. – DOI 10.1063/1.95742

[Wilson and Tapp 1999] Wilson, R.H. ; Tapp, H.S.: Mid-infrared spectroscopy for food analysis: recent new applications and relevant developments in sample presentation methods. In: *TrAC Trends in Analytical Chemistry* 18 (1999), feb, Nr. 2, 85–93. http://dx.doi.org/10.1016/s0165-9936(98)00107-1. – DOI 10.1016/s0165–9936(98)00107–1

[Winzer et al. 2018] Winzer, Peter J. ; Neilson, David T. ; Chraplyvy, Andrew R.: Fiber-optic transmission and networking: the previous 20 and the next 20 years [Invited]. In: *Optics Express* 26 (2018), aug, Nr. 18, 24190. http://dx.doi.org/10.1364/oe.26.024190. – DOI 10.1364/oe.26.024190

[Wu et al. 2018] Wu, Donghai ; Slivken, Steven ; Lu, Quanyong ; Razeghi, Manijeh: Review of high power frequency comb sources based on InP: from MIR to THz at CQD. In: Razeghi, Manijeh (Hrsg.) ; Baranov, Alexei N. (Hrsg.): *Terahertz Emitters, Receivers, and Applications IX*, SPIE, sep 2018

[Yang 1999] Yang, R.Q.: Mid-infrared interband cascade lasers based on type-II heterostructures. In: *Microelectronics Journal* 30 (1999), oct, Nr. 10, 1043–1056. http://dx.doi.org/10.1016/s0026-2692(99)00061-0. – DOI 10.1016/s0026–2692(99)00061–0

[Ye et al. 2016] Ye, Weilin ; Li, Chunguang ; Zheng, Chuantao ; Sanchez, Nancy P. ; Gluszek, Aleksander K. ; Hudzikowski, Arkadiusz J. ; Dong, Lei ; Griffin, Robert J. ; Tittel, Frank K.: Mid-infrared dual-gas sensor for simultaneous detection of methane and ethane using a single continuous-wave interband cascade laser. In: *Optics Express* 24 (2016), jul, Nr. 15, 16973. http://dx.doi.org/10.1364/oe.24.016973. – DOI 10.1364/oe.24.016973

[Yoshikawa et al.] Yoshikawa, M. ; Murakami, A. ; Sakurai, J. ; Nakayama, H. ; Nakamura, T.: High power VCSEL devices for free space optical communications. In: *Proceedings Electronic Components and Technology, 2005. ECTC '05.*, IEEE

[Yu.A. and Schmidt 1999] Yu.A., Goldberg ; Schmidt, N.M.: *Handbook Series on Semiconductor Parameters*. World Scientific, 1999. – ISBN 981–02–1420–0

[Yuhong Zhou and Wang 2016] Yuhong Zhou, Fengjiao Wang JungLiu Fengqi Liu Shuman Liu Jinchuan Zhang Ning Zhuo Lijun W. Shenqiang Zhai Z. Shenqiang Zhai ; Wang, ZhanGuo: High-speed, room-temperature quantum cascade detectors at 4.3μm. In: *AIP Advances* 6 (2016)

[Zaidi 2016] Zaidi, Salam Nazhan Ahmed A.: *OPTICAL AND ELECTRICAL CHARACTERISTICS OF VERTICAL-CAVITY SURFACE-EMITTING LASERS FOR FREE SPACE OPTICAL COMMUNICATIONS*, University of Northumbria at Newcastle, Diss., 2016

[Zuev 1976] In: Zuev, V. E.: *Laser-light transmission through the atmosphere*. Berlin, Heidelberg : Springer Berlin Heidelberg, 1976. – ISBN 978–3–540–38239–3, 29–69